The Propagation and Growth of Polygonal Fault Systems



James King
University College
Department of Earth Sciences
University of Oxford

A thesis submitted for the degree of
Doctor of Philosophy

Trinity 2021

This thesis is dedicated to
my parents, Sean and Michelle, and my sister, Emma,
for all of their love and support whilst completing my studies.

Contents

Acknowledgements **v**

Abstract **vii**

1 An Introduction to Polygonal Fault Systems **1**

1.1 An Overview of Polygonal Fault Systems 1

1.2 An Overview of the Growth of Normal Faults 4

1.3 Characteristics of Polygonal Fault Systems 13

1.3.1 PFS tiers, dimensions, and displacements 13

1.3.2 PFS planform geometries and stress perturbations 15

1.3.3 PFSs and facies changes 17

1.3.4 PFSs and the opal-A/CT boundary 17

1.3.5 Proposed PFS genetic mechanisms 21

1.3.6 The growth and kinematics of polygonal fault systems 24

1.3.7 The importance of polygonal fault systems 26

1.4 Research Aims 28

2 High-Resolution Fault Throw Analysis in Seismic Reflection Data: A Novel Methodology to Minimise and Quantify Fault Throw Uncertainty **29**

2.1 Abstract 30

2.2 Introduction 31

2.3 Fault Throw Analysis Uncertainties in Seismic Reflection Data 34

2.3.1 Fault drag 36

2.3.2 Seismic reflection peak interpolation uncertainty 36

2.3.3 Manual measurement picking uncertainty 37

2.3.4 Compaction-driven throw loss 38

2.4 Methodology to Minimise and Quantify Fault Throw Measurement Uncertainty 39

2.4.1 Spline interpolation of sample points . . . 39
2.4.2 Interpolated reflection peak auto-picking . . . 40
2.4.3 Quantifying reflection peak TWT uncertainty . . . 40
2.4.4 Determining the amplitude quantization interval . . . 41
2.4.5 Quantifying the reflection peak interpolation uncertainty . . . 42
2.5 Results – Seismic Reflection Peak Interpolation Uncertainty . . . 46
2.5.1 Amplitude and reflection peak interpolation uncertainty . . . 48
2.5.2 Depth (TWT) and reflection peak interpolation uncertainty . 49
2.5.3 Frequency and reflection peak interpolation uncertainty . . . 49
2.5.4 A comparison of fault throw measurement methodologies . . . 52
2.6 Conclusions . . . 54

3 The Spatial, Temporal, and Kinematic Evolution of a Polygonal Fault System 55
3.1 Abstract . . . 55
3.2 Introduction . . . 57
3.3 Data and Methods . . . 61
3.3.1 Data . . . 61
3.3.2 Measuring Fault Throw . . . 63
3.4 Geological Setting & Lithological Descriptions . . . 64
3.4.1 Development of the Vøring Basin . . . 64
3.4.2 Description of the PFS host strata . . . 64
3.4.2.1 Sedimentation rate estimates . . . 65
3.4.2.2 Stratigraphic wedges . . . 66
3.4.2.3 Opal-A/CT boundary . . . 66
3.4.2.4 Physical properties of the PFS host strata . . . 67
3.5 Fault Analysis . . . 72
3.5.1 Description of the PFS . . . 72
3.5.2 Growth packages . . . 73
3.5.3 Polygonal fault types . . . 74
3.5.4 Throw profile trends . . . 75
3.5.5 Scaling relationships and spatial distributions . . . 76
3.5.6 Throw at temporal markers . . . 77
3.5.7 Upper and lower tip gradients . . . 77
3.6 Discussion . . . 92
3.6.1 Temporal and kinematic evolution of the PFS . . . 92

3.7 Conclusions . . . 98

4 Ultra-Slow Throw Rates of Polygonal Fault Systems 99

4.1 Abstract . . . 100
4.2 Introduction . . . 101
4.3 Geological Setting . . . 103
4.4 Methods . . . 105
4.5 Results . . . 107
4.6 Discussion . . . 109
4.7 Conclusions . . . 113

5 Numerical Modelling of the Growth of Polygonal Fault Systems 114

5.1 Abstract . . . 115
5.2 Introduction . . . 116
5.3 Methodology . . . 122
5.3.1 Computational Framework . . . 122
5.3.2 Constitutive Model . . . 123
5.3.3 Model Setup . . . 124
5.3.3.1 Modelling strategy . . . 124
5.3.3.2 Boundary conditions . . . 125
5.3.3.3 Material characterisation . . . 125
5.3.3.4 Model outputs . . . 127
5.3.3.5 Kinematic justification . . . 130
5.4 Results . . . 132
5.4.1 Material compaction and fault throw . . . 132
5.4.2 Dip angles and fault throw . . . 138
5.4.3 Residual friction angles and fault throw . . . 139
5.4.4 Throw versus height profiles . . . 140
5.4.5 Throw rates . . . 141
5.4.6 Stress field perturbations . . . 143
5.5 Discussion . . . 157
5.5.1 Upscaling computational models to heterogeneous PFSs . . . 157
5.5.2 Factors governing the evolution of PFS growth . . . 158
5.5.3 Implications . . . 159
5.6 Conclusions . . . 161

6 Summary and Discussion **162**
6.1 Introduction . . . 162
6.2 Summary of Results . . . 164
6.3 The Evolution of Polygonal Fault Systems . . . 168
6.3.1 Nucleation . . . 168
6.3.2 Propagation and Growth . . . 169
6.3.2.1 Kinematics and propagation . . . 169
6.3.2.2 PFS growth – accommodating displacement in laterally-pinned conditions . . . 172
6.3.2.3 Factors that govern the growth of PFSs . . . 174
6.3.2.4 Growth rates . . . 177
6.3.3 Cessation . . . 179
6.4 Future Work . . . 181

7 Conclusions **182**

A Supplementary Material for "Ultra-Slow Throw Rates of Polygonal Fault Systems" **186**
A.1 Chronostratigraphic Calibration . . . 186
A.2 Biostratigraphy – Calcareous Nannofossils . . . 187
A.3 Paleomagnetics . . . 188
A.4 Seismic-Well Calibration . . . 189
A.5 Measuring Throw Rates . . . 190

B Numerical modelling methodology **196**
B.1 Computational framework . . . 197
B.1.1 ELFEN . . . 197
B.2 Constitutive model . . . 198
B.2.1 SoftRock 3 (SR3) state boundary surface . . . 198
B.2.2 Flow rule definition . . . 201
B.2.3 Volume change . . . 203
B.2.4 Hardening law and poro-elasticity . . . 204
B.2.5 Elastoplastic stress update . . . 206
B.2.6 Regularisation of the material softening . . . 210

C SEGY Peak Picking MATLAB Script **211**

References **224**

Acknowledgements

I feel very fortunate to have learnt from and been supported by several world-class mentors who have been influential in my development as a researcher, critical thinker, and communicator over the course of my studies.

First and foremost, I would like to thank my DPhil supervisor Joe Cartwright. I feel incredibly privileged to have undertaken my DPhil research under Joe's tutelage. Many of the most enjoyable moments of my research took place with nothing more than a few sheets of A4 paper, a pen, and hours of thought-provoking sketching and discussion with Joe. Words do not do justice to how grateful I am for Joe's unwavering encouragement and support.

I wish to thank my co-supervisor Bruce Levell for his advice and support throughout my DPhil. I have always admired Bruce's ability to make the most complex of concepts seem simple, which is a skill I have tried to emulate in my research.

I wish to thank Dan Roberts and his colleagues at Rockfield Global, for supporting my numerical modelling research and for their warm welcome on my visits to Swansea. Dan's can-do attitude and unwavering support were instrumental throughout the development of the modelling framework that was used in this research – which went through seemingly endless iterations and fresh starts.

The final version of this thesis benefitted from thoughtful discussion with my thesis examiners John Walsh and Richard Walker, who I wish to thank for their insightful suggestions and positive feedback.

I also wish to thank my friends and colleagues from the 3D Lab and Department of Earth Sciences: Benedict, Claudia, Ethan, Israa, José Alfredo, Matteo, Michael, Reybi, and Victoria. They were always on hand to discuss research questions or pop up to the research common room for an overly-long coffee break. Special thanks in particular to Martino Foschi

for teaching me various quantitative approaches to investigate geological problems and for sharing his passion for Italian cooking – including his golden rule of using no more than five ingredients, and to Chris Kirkham whom I have considered not only a great friend but also a role model and mentor, and whose boundless enthusiasm made the lab a fun and vibrant place to work.

I had the honour of being a recipient of the Oxford Radcliffe Scholarship and received funding from the Natural Environment Research Council as part of their Centre for Doctoral Training, both of which made this research possible and provided opportunities for me grow as a scholar. I am also grateful to University College Oxford, CASP, and AAPG for their support in funding field-trips and my attendance at international conferences.

Outside of work I feel especially fortunate to have met some truly incredible people in Oxford and made some very special friendships. Judy, Sam, Maj, Nick, Ed, and many more. This experience was immeasurably more fun shared with all of you.

Finally, I owe a special thanks to my family for all of their love and support, and for always encouraging me to do my best.

James King
April 2021

Abstract

Polygonal fault systems (PFSs) are laterally-pinned arrays of multi-directional nontectonic normal faults that develop in fine-grained sedimentary sequences. PFSs have been documented in over 150 basins globally, since they were first reported in early three-dimensional seismic reflection datasets in the late 1980's. The structural characteristics of PFSs are well documented, yet despite over three decades of research and wide debate within the published literature, the processes that govern the growth of polygonal faults are poorly understood.

This thesis investigates the propagation and growth of polygonal fault systems through spatial, temporal, and kinematic analysis of surface-breaching polygonal faults in the Vøring Basin, Norwegian Sea, and numerical modelling simulations. This thesis documents the first recorded throw rates from a PFS globally. These ultra-slow rates range between 1.4-10.9 m/m.y. and mark the lower limit of a continuous spectrum of extensional fault displacement rates, that are as much as three orders of magnitude slower than those of the fastest-growing tectonic faults. This thesis also establishes, through numerical modelling, that the growth of polygonal faults can be explained solely by gravity-driven differential compaction of unconsolidated fine-grained sediments at residual friction angles less than ~9°. These findings elucidate our understanding of the growth of these widespread and fascinating geological structures.

Chapter 1

An Introduction to Polygonal Fault Systems

1.1 An Overview of Polygonal Fault Systems

Polygonal Fault Systems (PFSs) are laterally extensive arrays of layer-bound nontectonic normal faults with a generally polygonal planform geometry. PFSs are widely developed in many continental margin basins around the world and are almost exclusively hosted in fine-grained sedimentary tiers (Fig. 1.1).

Soft-sediment layer-bound faults were first recognised by Buckley and Grant (1985) and Henriet et al. (1988) in low-resolution two-dimensional seismic reflection lines from the northern Atlantic Ocean and the southern North Sea. The onshore extent of the layer-bound faults identified in the southern North Sea were studied in west Flandrian (Belgium) quarries exposing Ypresian clay outcrops by Verschuren (1992). However, limited outcrop continuity and coarse two-dimensional seismic spacing meant that the classic interconnected *'polygonal'* fault network of these layer-bound faults was not discovered until the advent of conventional three-dimensional seismic reflection data in the early 1990's. Cartwright (1994a,b) pioneered the use

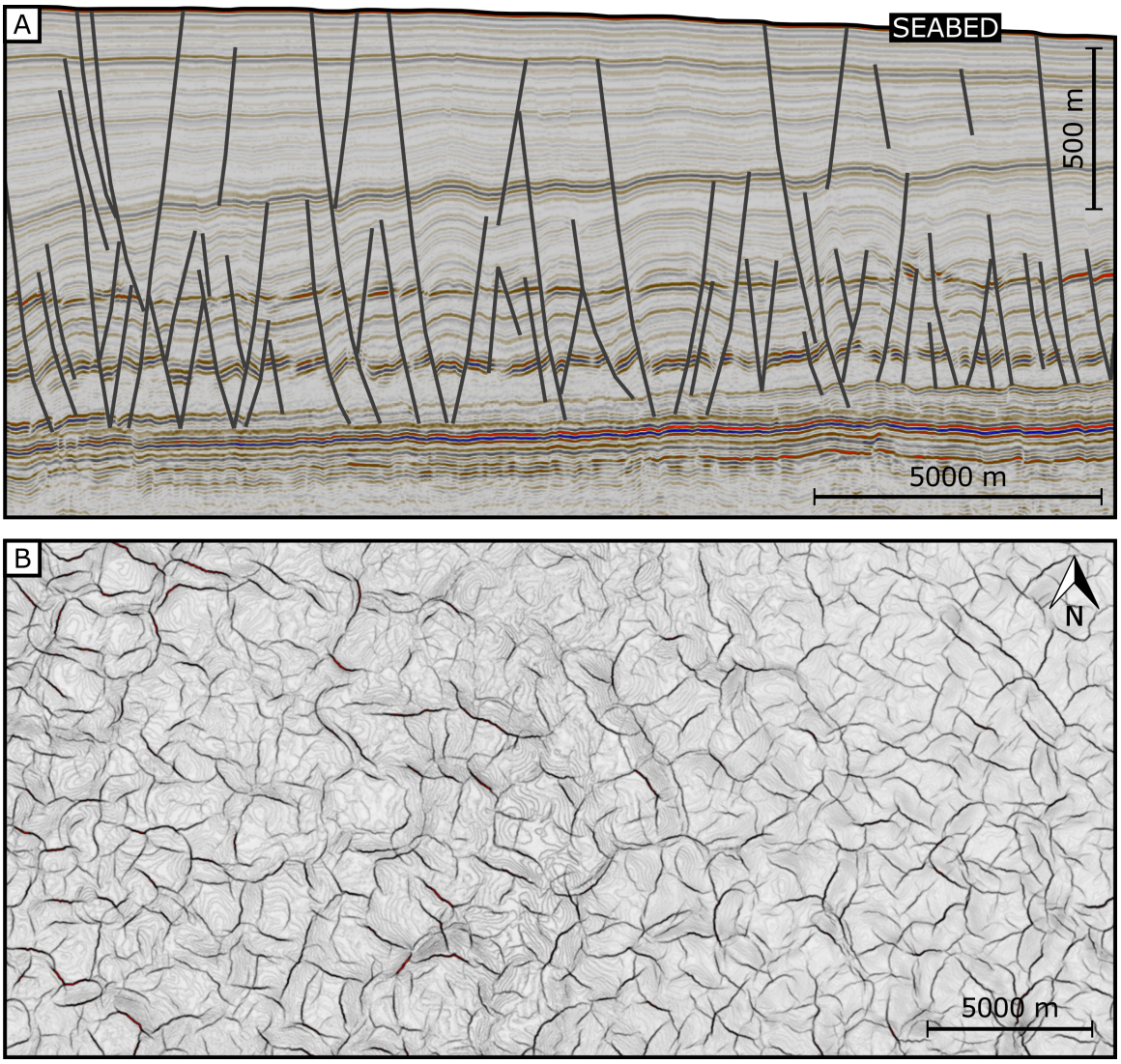


Figure 1.1: A seismic cross-section (A) and mapped horizon (B) through a polygonal fault system.

of early three-dimensional seismic reflection datasets to research layer-bound fault systems from the North Sea, and coined the term *'polygonal fault systems'* after their striking multi-directional network patternology and complex interlinking geometries. Since the early 1990's an abundance of global three-dimensional seismic reflection data acquisition has led to the discovery of polygonal fault systems in over 150 basins around the world (Fig. 1.2).

The nontectonic nature of polygonal faults was established concurrently with their

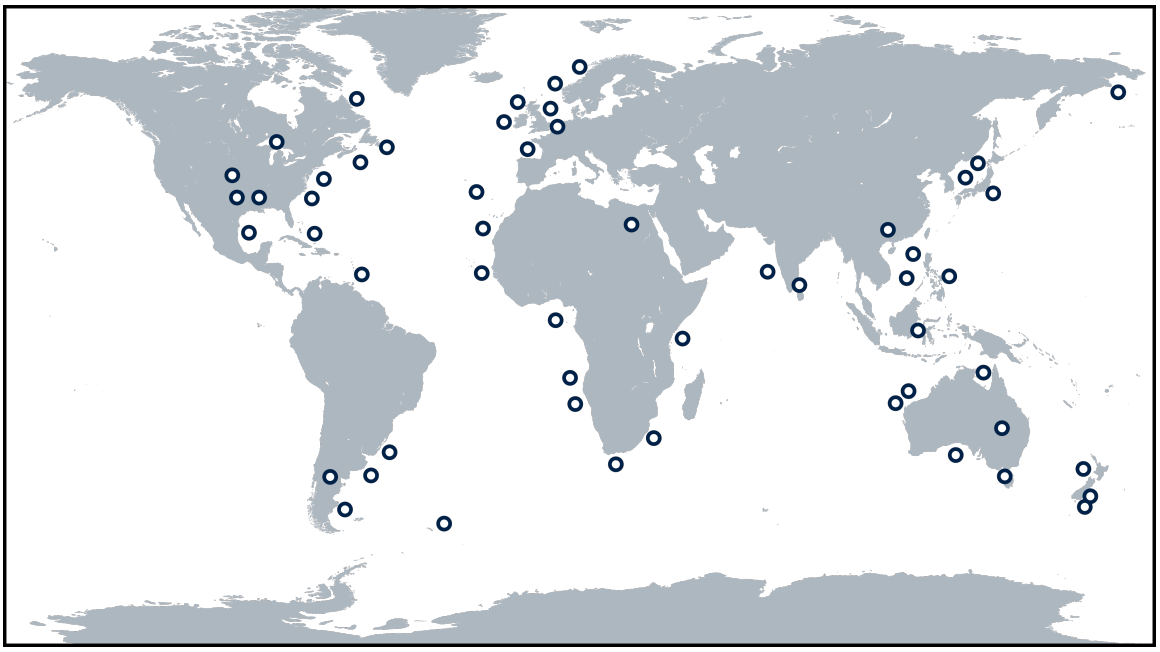


Figure 1.2: Global distribution map of polygonal fault systems, adapted from Cartwright (2011).

discovery, because of their development in well-defined layer-bound *'tiers'*. However, it has proved difficult to substantiate any genetic mechanism(s) that can explain the nucleation and subsequent growth of polygonal fault systems. Several mechanisms have been widely debated since the discovery of polygonal fault systems and much of the field's cumulative research effort over the past three decades has focused on this enigma (Cartwright et al., 2003; Goulty, 2008; Cartwright, 2011). The merits and shortfalls of these mechanisms are outlined in section 1.3.5.

Although relatively little is known about the initiation and temporal evolution of polygonal fault systems, their structural characteristics are well documented and described in an array of fine-grained sedimentary tiers ranging in composition from smectitic-rich mudstones to nannofossiliferous oozes (Cartwright, 2011). The wide ranging compositions of PFS host sediments has led many researchers to rule out a lithological control as a universal PFS formation mechanism. However, the sheer lateral extent of polygonal fault systems, in some cases spanning over two million

square kilometres (Cartwright, 2011), suggests that a single universal genetic mechanism would have to apply on a basin-wide and inter-basin scale or alternatively several different genetic mechanisms could give rise to polygonal fault systems. The logic supporting a single universal genetic mechanism is reflected in the current leading PFS nucleation hypotheses and also the subsequent growth hypotheses, which are rooted in basin-wide processes and sediment physical properties. Namely, the *'gravitational loading'* growth hypothesis, which applies Mohr Coulomb theory to show that a pre-existing fault hosted in fine-grained sediments with low coefficients of residual friction (μ_r) and high K_0 values (where K_0 is the coefficient of earth pressure at rest, measured as the ratio of the horizontal principle stress to the vertical principle stress) will propagate proportionally with sediment loading (Goulty, 2001a), and the *'diagenetically-induced shear failure'* nucleation hypothesis, which both experimental and computational models have shown can explain the nucleation and growth of shear-failures in sediments that undergo grain-framework volume reductions (Shin et al., 2008; Cartwright, 2011; Roberts et al., 2014). A quantitative investigation of the drivers of polygonal fault growth forms the focus of Chapter 5.

1.2 An Overview of the Growth of Normal Faults

Defining normal faults

Polygonal faults are an enigmatic class of nontectonic normal faults. Normal faults, often referred to as extensional faults, are shear fractures that form in settings where the vertical stress induced by the overburden (σ_1) is greater than the two perpendicular horizontal stresses ($\sigma_1 > \sigma_2 > \sigma_3$). Anderson (1905) first coined this traditional explanation which distinguishes normal, reverse, and strike-slip faults from each other in terms of stress (Fig. 1.3). There are three types of normal faults; *'tectonic normal faults'* which form directly through active regional tectonic processes, *'gravitational*

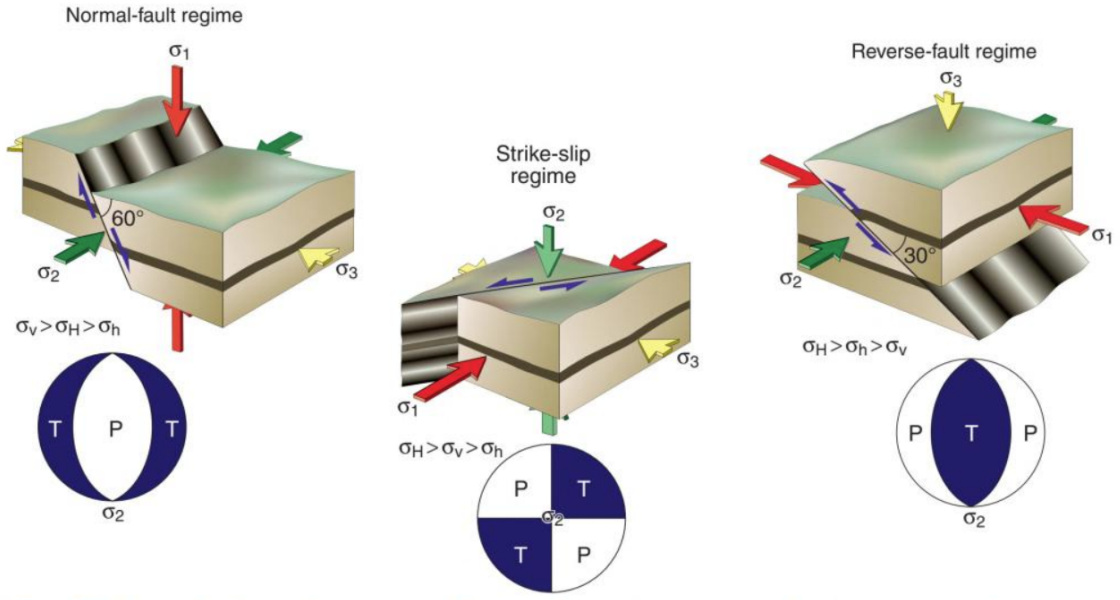


Figure 1.3: Relationships between the orientation of the principal stresses and tectonic regimes according to Anderson (1905). Equal area spherical projections show fields of compression (P) and tension (T). σ_v = vertical stress, σ_H = maximum horizontal stress, σ_h = minimum horizontal stress. Figure from Fossen (2016).

slope normal faults' which form in slope settings as a response to gravitational instabilities, and *'polygonal faults'* which are the focus of this thesis.

Differentiating blind and surface-breaching normal faults

Significant advances in our understanding of the fundamental kinematics, dimensions, displacements, scaling-laws, and growth of normal faults were made in the 1980's and 1990's. Muraoka and Kamata (1983) pioneered early normal fault research with their cutting edge fault length versus displacement graphs and field defining 'C' and 'M' fault types which characterise the two end-member fault displacement plot patterns. The displacement on C-type faults increases linearly from the fault tips to an apex in the central region of the fault, whereas, M-type faults have a pronounced flat zero-gradient profile. The characteristic flat profile of M-type faults can occur as the result of two separate fault growth styles, namely, *'blind'* and *'surface-breaching'* fault growth (Fig. 1.4) (Muraoka and Kamata, 1983; Peacock and Sanderson, 1991; Nicol

et al., 1996; Baudon and Cartwright, 2008a). An M-type displacement profile can be the signature of a blind fault that has propagated through a rigid, mechanically-competent unit, or the signature of a period of fault inactivity on a surface-breaching fault.

It is thus important to know if a fault is blind or surface-breaching (Fig. 1.4) when analysing displacement profiles. Blind faults propagate without intersecting the Earth's surface (Watterson, 1986). Theoretically an idealised blind fault nucleates at its point of maximum displacement and grows radially with an elliptical tip line (Watterson, 1986; Barnett et al., 1987). The upper tip gradients (measured as the change in throw with depth of the uppermost portion of a fault) of blind faults are low and typically in the range of 0.001-0.2 (Barnett et al., 1987; Walsh and Watterson, 1989; Wibberley et al., 1999). The upper tip line of surface-breaching faults, often referred to as *'growth faults'* or *'syn-sedimentary faults'* intersect the Earth's surface and thus the change in thickness of sediments across the fault records the difference in elevation of the depositional surface on the footwall and hanging wall through time (Childs et al., 2003). With chronostratigraphic calibration the offset of dated-marker beds offers a means to measure the displacement rate of surface-breaching faults (Nicol et al., 1997; Cartwright et al., 1998; Mouslopoulou et al., 2009; Dutton and Trudgill, 2009; Pochat et al., 2009; Jackson, 2018). The upper tip gradients of surface-breaching faults are typically >0.3, however, the lowest values of upper tip gradients on surface-breaching faults overlap with those of blind faults (Childs et al., 2003; Baudon and Cartwright, 2008a; Cartwright, 2011).

In addition to the occurrence of growth packages, which can sometimes be smaller than the vertical stratigraphic resolution of conventional seismic reflection data and therefore not imaged, the geometry of concentric 3D throw contours can be used as a diagnostic to differentiate blind and previously surface-breaching faults that have been subsquently buried (Baudon and Cartwright, 2008a). Surface-breaching faults

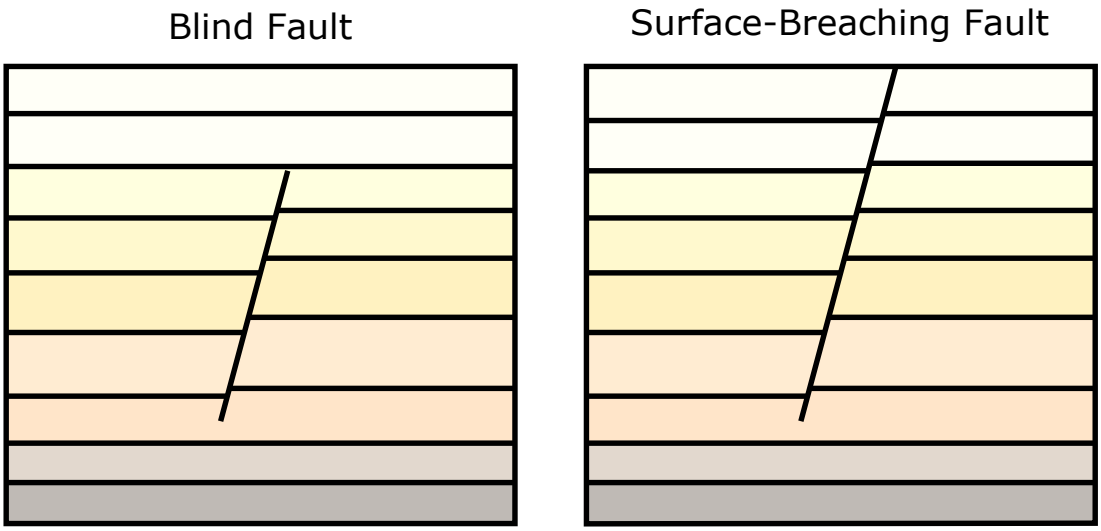


Figure 1.4: Blind faults (left) propagate at depth, whereas surface-breaching faults (right) propagate at the free surface. Absolute fault displacement rates can be calculated for surface-breaching faults which offset age-dated horizons, whereas only minimum displacement rate estimates can be calculated for blind faults, because a blind fault could have propagated at any point in time post-deposition of the age-calibrated host strata.

typically have sub-horizontal throw contours in the upper tip portion of the fault, whereas blind faults typically have elliptical throw contours (Fig. 1.5) (Baudon and Cartwright, 2008a).

Both blind and surface-breaching faults can have C-type profiles (Baudon and Cartwright, 2008a). As is the case with all qualitative classifications, the difference between end-members can become nuanced with complexity. It is common to find displacement profiles described as 'symmetric' or 'asymmetric', or as 'L', 'B', or 'Z' types in the literature e.g. Turrini et al. (2017) and Wrona et al. (2017) (Fig. 1.6), however, regardless of the 'fault type' displacement profiles are primarily controlled by differences in mechanical properties or changes in the displacement rate. As such, displacement profiles yield important insights into the kinematic and temporal evolution of fault growth.

The difference between blind and surface-breaching fault propagation is usually obvious for tectonic and gravity-driven faults which have large throws. Large surface-

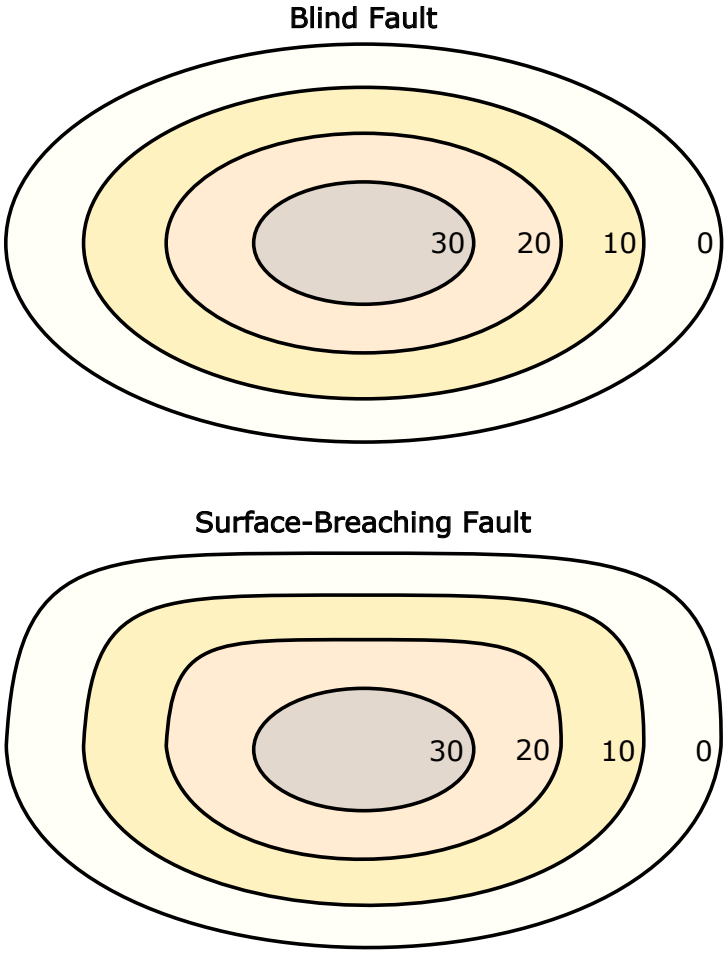


Figure 1.5: Schematic showing the idealised throw contours of a blind (top) and surface-breaching (bottom) fault. Blind faults typically have elliptical throw contours in the upper third of the fault, whereas surface-breaching faults typically have sub-horizontal throw contours that are influenced by the interaction of the upper tipline with the free surface. Numbers represent arbitrary throw values for respective contours.

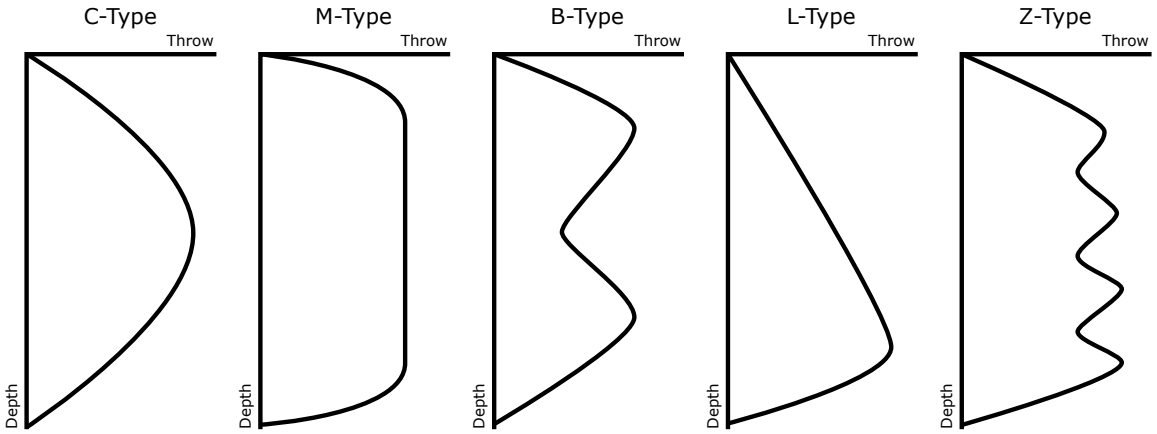


Figure 1.6: End-member throw profile types.

breaching faults (i.e.: surface breaking faults for at least part of their growth history) exhibit well-defined growth packages illustrated by stratigraphic thickening towards the fault plane in the hanging wall block. For faults with smaller throws, such as polygonal faults, the distinction between blind and surface-breaching faults can be ambiguous as the size of growth packages may be beneath the stratigraphic resolution of conventional three-dimensional seismic reflection data. However, examples of PFSs with clear syn-sedimentary growth packages have been documented by Cartwright (1994a), Cartwright and Lonergan (1996), Stuevold et al. (2003), Cartwright (2011), Laurent et al. (2012), Carruthers et al. (2013), and Wrona et al. (2017) (Fig. 1.7).

Normal fault growth models

There are two classical models for the growth of normal faults, the first often described as the *'conventional growth model'* suggests that faults grow as the result of systematic increases in both maximum displacement and length (Watterson, 1986; Walsh and Watterson, 1988; Cowie and Scholz, 1992; Nicol et al., 2005a). The *'alternative model'* proposed by Walsh et al. (2002) suggests that *"fault lengths are near-constant from an early stage and growth is achieved by an increase in cumulative displacement"*.

Differences between the two models are addressed by Nicol et al. (2005b) (Fig.

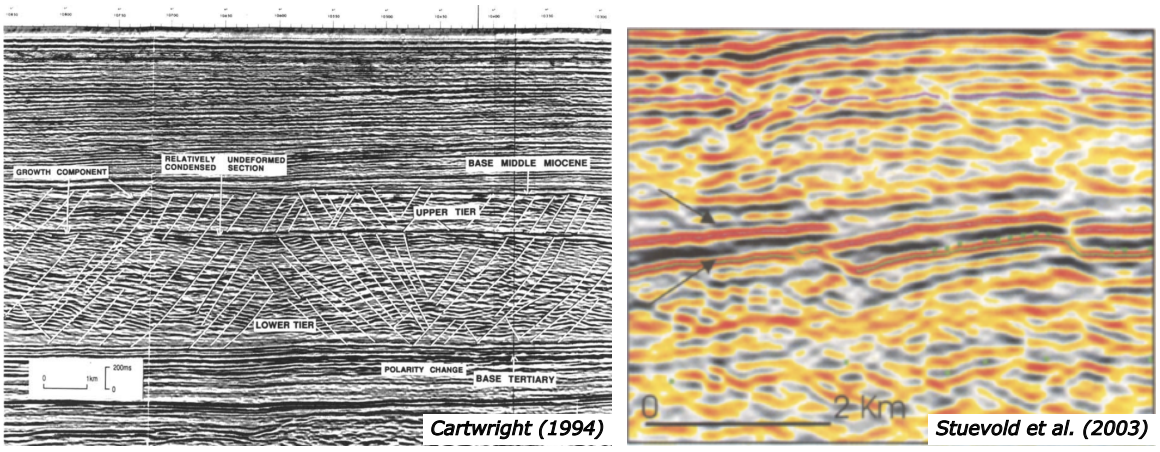


Figure 1.7: Polygonal fault systems with hanging-wall growth packages from (Left) the North Sea (Cartwright, 1994a) and (Right) Ormen Lange, Norwegian Sea (Stuevold et al., 2003).

1.8). The 'alternative model' neatly explains displacement accumulation on faults with retarded lateral propagation. This 'alternative model' may be applied to the growth of polygonal faults in a mature PFS with high degrees of fault linkage, and to buried polygonal fault systems capped by mechanical barriers whose fault tip lines are fixed. However, the upwards propagation of surface-breaching polygonal fault systems such as those located in the Norwegian Sea, offshore-Angola, offshore-Indonesia, and offshore-western Ireland do not conform to the 'alternative growth model' and are better explained by Morgan et al. (2015)'s adaptation of the 'conventional growth model'. Using 3D seismic data from the West African margin Morgan et al. (2015) investigated the perturbation of polygonal faults by pockmarks throughout the PFS tier and established that polygonal faults can nucleate early in the basal third of the tier and propagate upwards with basal tips restricted by an underlying mechanically competent unit. Morgan et al. (2015) suggests that the locus of displacement shifts with continued polygonal fault growth, such that the final displacement distributions are *"more axio-symmetrically disposed with respect to the base and top of the tier"* (Fig. 1.9).

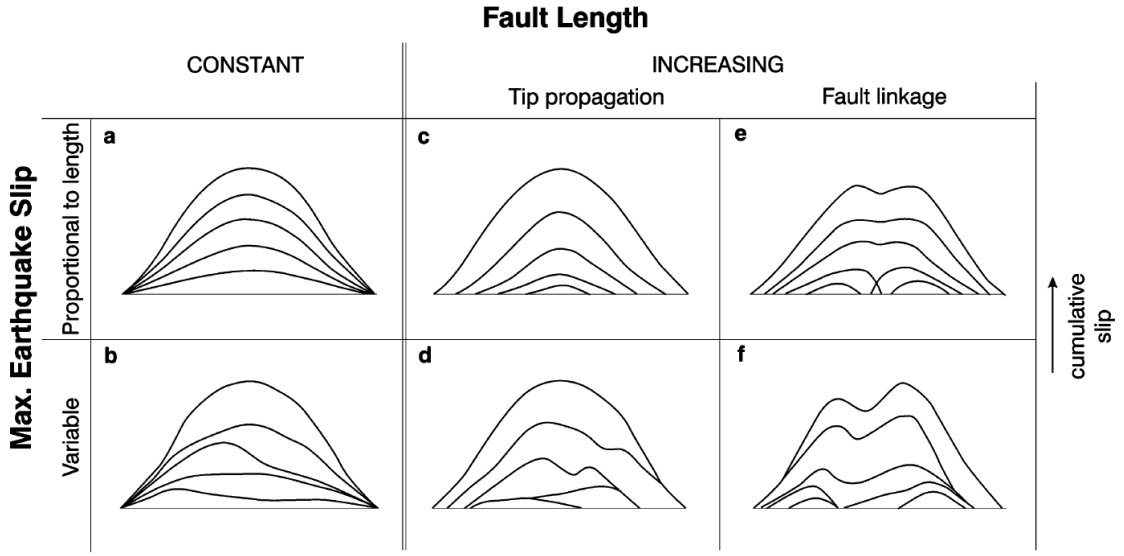


Figure 1.8: Schematic from Nicol et al. (2005b) showing variations on the growth styles of faults according to the 'constant-length' and 'increasing-length' models of isolated and linked faults. Cumulative displacement decreases from the central region of the fault to the tipline.

Normal fault scaling laws

The dimensions, growth rates, and earthquake recurrence intervals of normal faults can be expressed quantitatively. Maximum displacement (D) often scales with fault length (L) following the expression:

$$D = cL^n, \tag{1.1}$$

where the value of n is typically between 1 and 1.5 and c is a constant (Watterson, 1986; Walsh and Watterson, 1988; Cowie and Scholz, 1992; Gillespie et al., 1993; Walsh et al., 2002). Similiarly, a linear scaling relationship has been suggested for polygonal faults, where the maximum throw is ∼3-6% of the fault height (Shin et al., 2010; Cartwright, 2011).

Several authors have established a correlation between fault displacement rates and regional strain rates (Nicol et al., 1997, 2005a), and a positive relationship be-

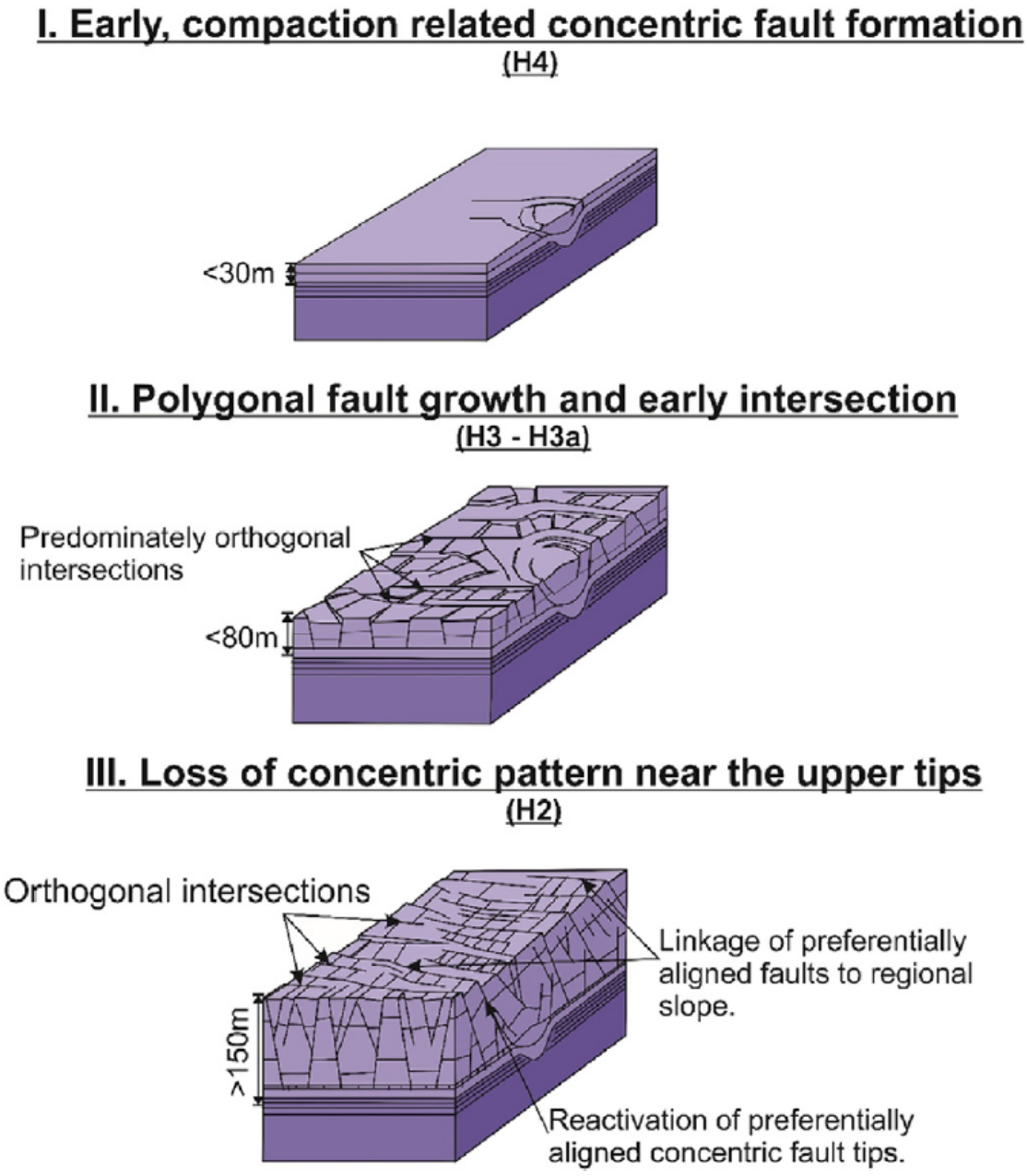


Figure 1.9: Polygonal fault growth model from Morgan et al. (2015).

tween fault displacement rates and fault lengths (Mouslopoulou et al., 2009). Differences between regional strain rates are accommodated by near-proportional differences in fault displacement rates rather than by different active fault densities (Nicol et al., 1997). Tectonic fault slip recurrence intervals and displacement rates are primarily controlled by basin-wide strain rates and fault dimensions, with fault interactions and intra-basinal variations in strain rate as important secondary factors (Nicol et al., 2005b).

Normal fault growth rates

There have been several studies on the propagation rates and displacement rates of syn-sedimentary tectonic and gravity-driven normal faults. Childs et al. (2003) measured lateral tip-line propagation for a series of gravity-driven and tectonic faults and found maximum propagation rates of 15 km/My and 3 km/My respectively. The rate of lateral fault propagation decreases with elapsed time as isolated faults intersect and form relay zones with neighbouring faults (Childs et al., 2003).

The displacement rates of tectonic and gravity-driven faults typically range between 10-3000 m/m.y. (Nicol et al., 1997; Cartwright et al., 1998; Childs et al., 2003; Dutton and Trudgill, 2009; Mouslopoulou et al., 2009; Pochat et al., 2009; Jackson, 2018). These displacement rates serve as an interesting comparison for the displacement rates of polygonal faults which are investigated and discussed in Chapter 4.

1.3 Characteristics of Polygonal Fault Systems

1.3.1 PFS tiers, dimensions, and displacements

Polygonal faults are layer-bound and confined to fine-grained sedimentary tiers. PFS host tiers can have variable geometries ranging from uniform tabular tiers with regu-

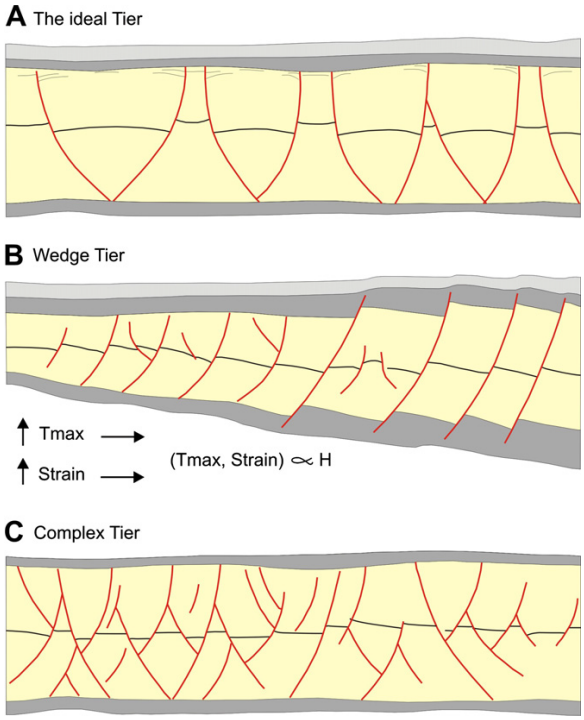


Figure 1.10: Schematic cross-sections from Cartwright (2011) showing an 'idealised' tabular tier (A) with regularly spaced faults dipping in opposing directions, a wedge-shaped tier (B) hosting faults with a preferred dip direction, and a complex tier (C) hosting faults of varying sizes with complex intersections and only a few 'master faults' which span the entire height of the tier.

larly spaced faults, to wedge-shaped tiers with preferential fault dip directions. PFS tiers are often complex and host faults of varying sizes with only a few *'master faults'* spanning the entire height of the tier (Fig. 1.10) (Cartwright, 2011).

Polygonal faults have trace lengths that range from a few tens of meters to several kilometers and they span stratigraphic intervals a few meters thick to well over a kilometer (Lonergan et al., 1998a; Cartwright et al., 2003). Polygonal faults have modest maximum displacements that generally scale with fault height (Cartwright et al., 2003; Shin et al., 2010; Cartwright, 2011) (Fig. 1.11). There is no typical polygonal fault displacement profile. Displacement versus depth plots from the same polygonal fault system can exhibit an array of profiles as highlighted by Neagu et al. (2010a) and in the Turrini et al. (2017) Uruguay PFS study.

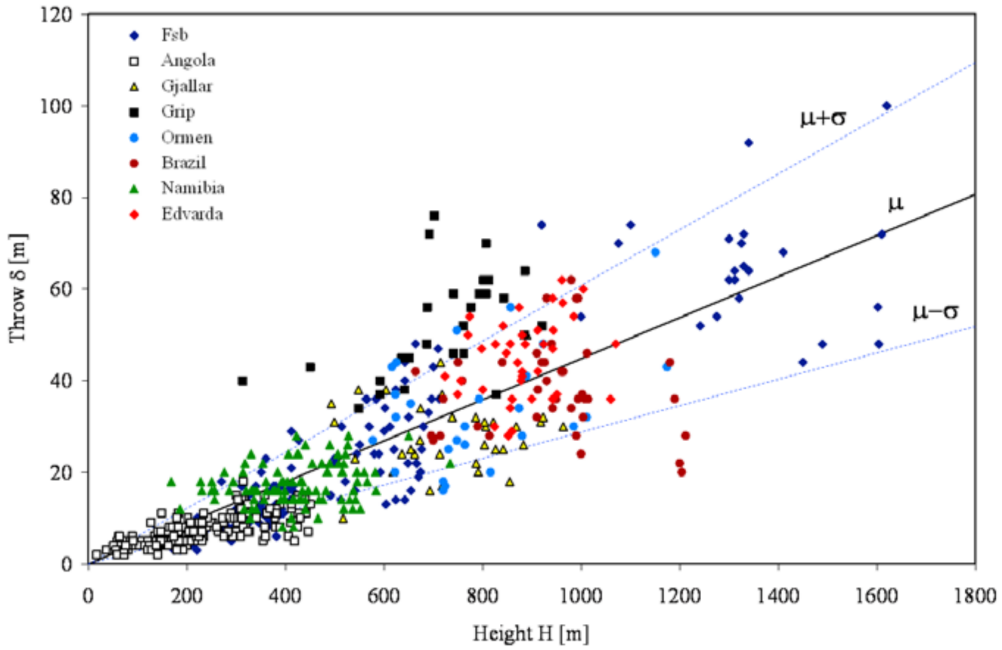


Figure 1.11: Maximum throw versus height plot from 629 individual polygonal faults with upper tips buried within 20-300 m of the seabed. From Shin et al. (2010) and Cartwright (2011)

.

1.3.2 PFS planform geometries and stress perturbations

The lateral extent of polygonal fault systems typically spans $> 10^5$ km^2 (Cartwright and Dewhurst, 1998), and in the case of the Eromanga Basin, Australia, the PFS spans over 2,000,000 km^2 (Cartwright, 2011). The vast lateral extent of polygonal fault systems is accompanied by a broad array of planform patterns. Typically polygonal cells are a few hundred meters to around a kilometer in diameter. Complex fault intersections and local stress perturbations influence the planform geometry and polygonal fault orientations are often polarised by neighbouring faults and pre-existing structures (Lonergan et al., 1998a; Hansen et al., 2004; Nelson, 2006).

Salt diapirs, pockmarks, tectonic faults, and pre-existing basement structures are all known to create local stress anisotropies which influence the orientations of polygonal faults (Fig. 1.12) (Hansen et al., 2004; Cartwright, 2011; Carruthers, 2012; Car-

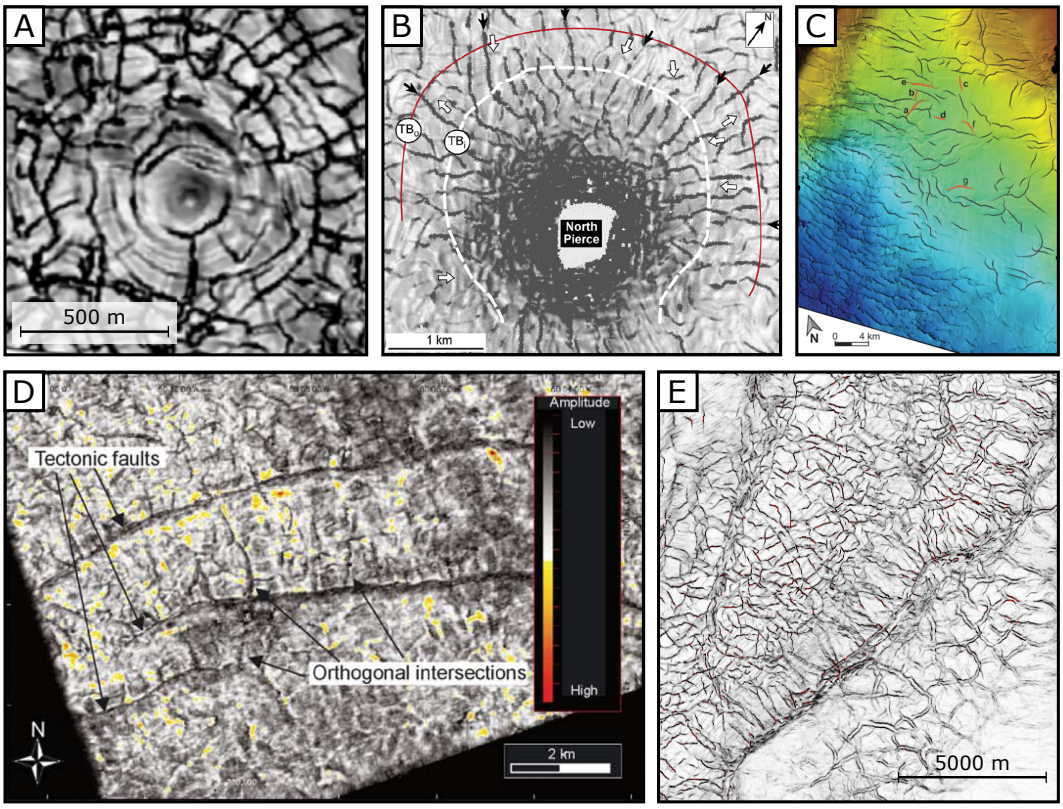


Figure 1.12: 'Polarised' PFS planform geometries. Polygonal faults orientated radially around (A) a pockmark (from Morgan et al. (2015)) and (B) a salt diapir (from Carruthers et al. (2013)). (C) Layer-bound faults from Ghalayini et al. (2017) which formed in an anisotropic stress regime. Polygonal faults polarised perpendicular to pre-existing tectonic structures (D) from Hansen et al. (2004) and (E) from the Bonaventure 3D survey, Exmouth Plateau, NWS Australia.

ruthers et al., 2013; Morgan et al., 2015; Morgan, 2016). An unusual non-polygonal layer-bound fault system hosted in fine-grained sediments in the Eastern Mediterranean has been documented by Ghalayini et al. (2017). These layer bound faults hosted in the Levant Basin, conform to many of the characteristics of polygonal fault systems, however, they have formed in an anisotropic horizontal stress regime and therefore lack the typical multi-directional planform geometry of conventional PFSs. Roberts (2014) modelled the role of stress anisotropies on PFS planform geometries and found that a difference between the maximum and minimum horizontal stress of just 3% aligns over 80% of fault strikes within $\pm 10^{\circ}$ of the maximum horizontal stress azimuth.

1.3.3 PFSs and facies changes

The lateral and vertical extent of polygonal fault systems are known to be heavily influenced by facies changes. Most notably, the transition from fine-grained to coarse-grained sediments, laterally or vertically, typically coincides with the death of a polygonal fault system. PFS regularly tip-out into mechanically competent facies at the base and top of tiers. Jackson et al. (2014) show that the lateral distribution and displacement profiles of polygonal faults can be used to map and identify coarse-grained reservoirs with fewer or no polygonal faults (1.13), and therefore PFS analysis can shed light on the first order geological characteristics of basins without stratigraphic well calibration. The vertical extent of the Espirito Santo Basin PFS, offshore Brazil, hosted in Early Miocene hemipelagic marls and siltstones is one such example of a PFS that 'dies out' vertically at the boundary with overlying turbiditic sands Fig. 1.14 (Carruthers, 2012). Locally, the lateral extent of polygonal fault systems can be influenced by contourite bodies, notably the Exmouth Plateau PFS, NW Shelf of Australia, the Norwegian Sea PFS (Laurent et al., 2012), and the Great South Basin PFS (Morley et al., 2017). In addition, trigger beds have been suggested as hypothetical facies that may have favourable properties to nucleate polygonal faults (Goulty, 2001a; Roberts, 2014).

1.3.4 PFSs and the opal-A/CT boundary

The physical properties of sedimentary units hosting PFSs can also change over time as the result of chemical diagenetic transitions. The most well-documented diagenetic reaction in PFS host tiers is the opal-A to opal-CT transformation (Davies et al., 1999; Davies and Cartwright, 2002; Davies, 2005; Davies and Cartwright, 2007; Davies et al., 2009; Davies and Ireland, 2011; Ireland et al., 2010, 2011; Neagu et al., 2010a,b; Cartwright, 2011). The chemical boundary between converted opal-CT and opal-

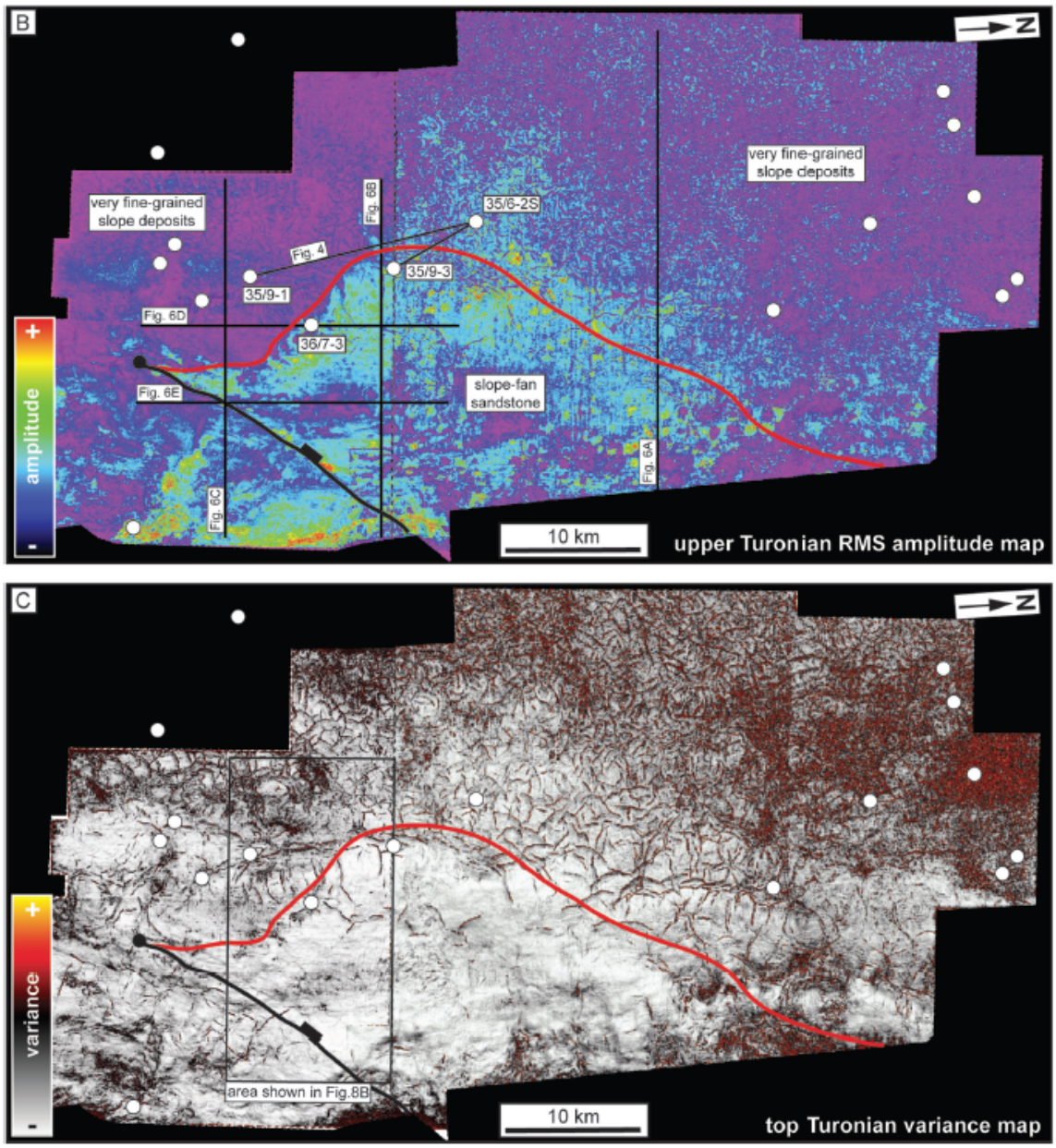


Figure 1.13: Amplitude (top) and variance (bottom) maps of the Top Turonian horizon through a PFS located on the Måløy slope, offshore Norway showing the lateral extent of the PFS is influenced by the occurrence of coarse-grained sediments. From Jackson et al. (2014).

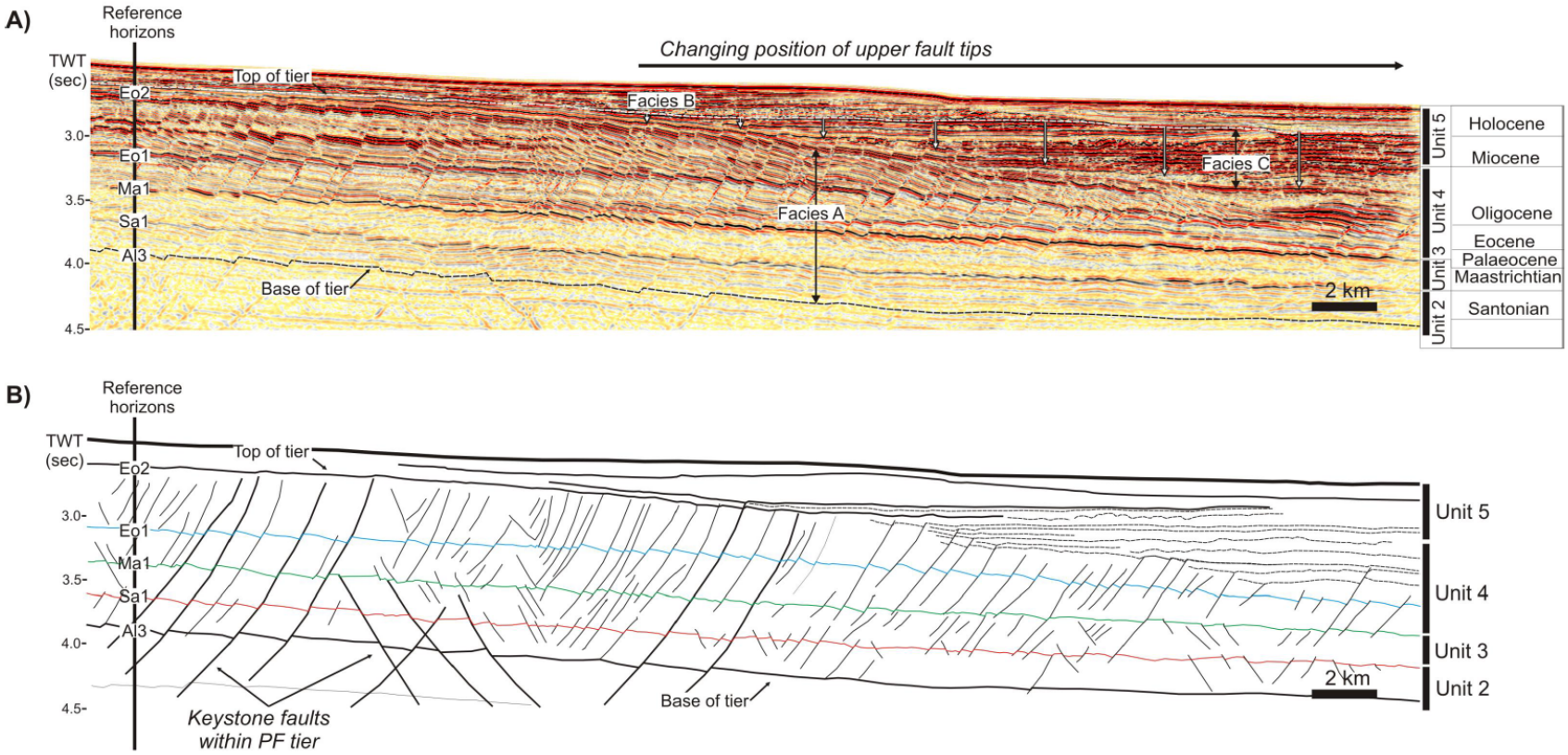


Figure 1.14: Seismic cross-section through the Espirito Santo Basin PFS, offshore Brazil, showing the changing position of upper PFS tips correlate with changing facies. Facies A comprises hemipelagic marls and siltstones, whereas Facies C hosts turbiditic sands. From Carruthers (2012).

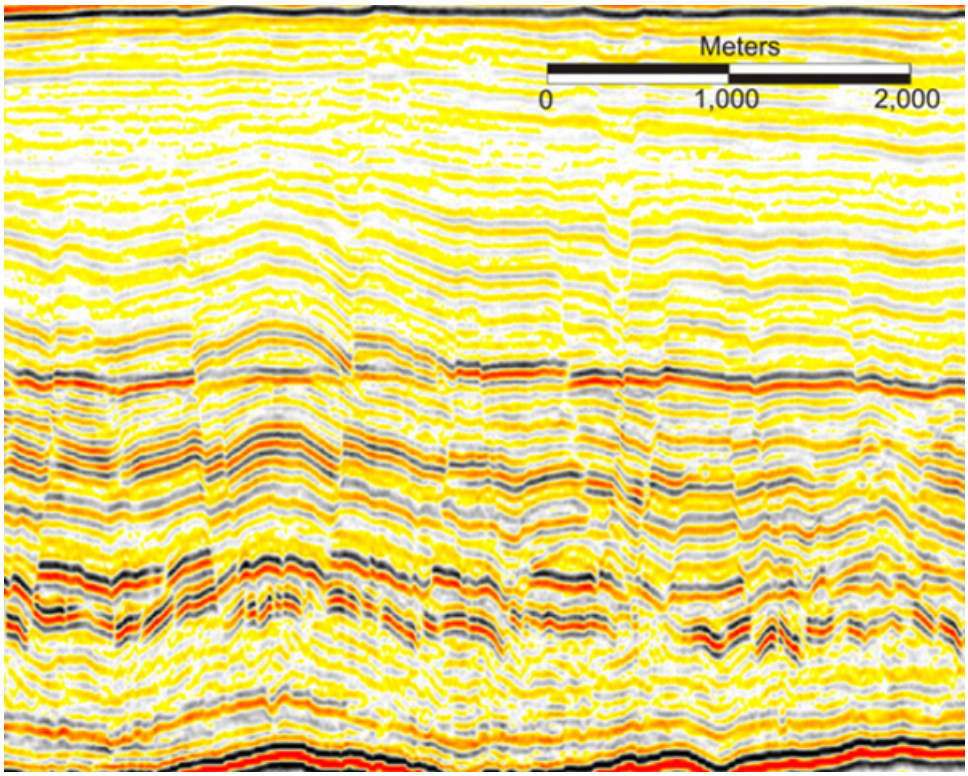


Figure 1.15: A PFS tier which has undergone opal-A/CT diagenesis. The opal-A/CT boundary is the sub-horizontal high amplitude reflector which cross-cuts stratigraphy located in the central region of the PFS tier. (From Cartwright (2011)).

A sediments has a strong acoustic impedence contrast and, as such, can be clearly imaged in seismic reflection data over vast areas (Fig. 1.15). The opal-A to opal-CT reaction takes place as a function of temperature, pressure, and time (Hein et al., 1978). The transition from opal-A to opal-CT can occur at temperatures as low as 25°C and in the first kilometer of burial (Davies and Cartwright, 2002; Ireland et al., 2011). The opal-A/CT transition creates a net volume reduction which has been associated causally with the nucleation and growth of polygonal fault systems (Shin et al., 2008, 2010; Cartwright, 2011; Roberts, 2014; Roberts et al., 2014). The opal-A/CT diagenetic transition may facilitate and drive polygonal fault growth in some basins, however, there are countless examples of PFSs that do not host this transition and therefore opal-A/CT diagenesis cannot be considered as a universal genetic mechanism.

1.3.5 Proposed PFS genetic mechanisms

Despite three decades of research, a universal PFS genetic mechanism remains elusive. Several mechanisms have been proposed since the discovery of polygonal fault systems, each of which has been widely debated in the literature (Henriet et al., 1988, 1991; Cartwright, 1994a; Cartwright and Lonergan, 1996; Cartwright and Dewhurst, 1998; Dewhurst et al., 1999; Watterson et al., 2000; Goulty, 2001a; Cartwright et al., 2003; Goulty and Swarbrick, 2005; James et al., 2006; Goulty, 2008; Cartwright, 2011).

Early mechanisms — density inversion, gravitational sliding, and overpressure

Henriet et al. (1988, 1991) proposed two early hypotheses to explain the formation of polygonal fault systems. They first applied the concept of Rayleigh-Taylor instabilities to explain PFS formation through density inversion. Secondly, they proposed overpressure as a mechanism to initiate a PFS as a network of hydraulic fractures. Overpressure was subsequently furthered as a mechanism by Cartwright (1994a,b) who suggested polygonal faults formed as basin-wide hydrofractures. Higgs and McClay (1993) used analogue sandbox models to suggested gravitational collapse on a slope as a mechanism to explain the layer-bound faults observed in two-dimensional seismic data.

Several observations from different polygonal fault systems around the world disprove density inversion and gravitational collapse as universal genetic mechanisms. Firstly, there are several active PFS tiers that have a systematically increasing density versus depth profiles. Secondly, the gravitational sliding mechanism can be ruled out as a universal mechanism because there are many PFSs located around the world that form on sub-horizontal plateaus. However, these mechanisms may drive the growth

of some PFSs in specific conditions.

Overpressure is more difficult to rule out completely. Overpressure in shallow fine-grained sediments typically forms through undercompaction of rapidly deposited low-permeability sediments, where the pore fluids are unable to dissipate fast enough for pore pressure to achieve an equilibrium hydrostatic pressure. As a result, the effective stresses do not increase with depth as porosity reduction is inhibited by overpressure (Goulty, 2001a). Goulty (2001a, 2008) highlights that this style of undercompation-driven overpressure preserves a constant ratio between the effective vertical and horizontal stresses during burial such that the stress state does not move towards failure. As overpressures can build up readily in basins that host PFS, its role as a contributor to the growth of PFSs should not be ruled out completely and it is possible that elevated fluid pressures may reactivate PFS growth (c.f. Bolton et al., 1998; and Watterson et al., 2000).

Current leading mechanisms — gravitational loading, and diagenetically-induced shear failure

There are currently two leading genetic mechanisms summarised by Goulty (2008) and Cartwright (2011) which explain significant aspects of the development of PFSs. These are *'gravitational loading'* (Goulty, 2001a, 2008) and *'diagenetically-induced shear failure'* (Shin et al., 2008, 2010; Cartwright, 2011). However, both have caveats that undermine their universal applicability as genetic models.

The gravitational loading mechanism proposed by Goulty (2001a) elegantly explains the growth of a pre-existing fracture through sediment loading. The mechanism is unique to fine-grained sediments which have intrinsically high K_0 values ($K_0 > 0.7$) and low coefficients of residual friction ($\mu_r < 0.18$). This mechanism is lithology-independent and can work on a basin-wide scale, however, it does not explain the nucleation of polygonal faults or how displacement is accommodated in

laterally-pinned conditions, and it requires specific sediment physical properties. It is nonetheless a simple mechanism to explain polygonal fault growth that could be applied universally across all PFSs (Fig. 1.16). However, Shin et al. (2010) tested the mechanics of this model through computational simulations and found that *"surprisingly low"* sediment bulk stiffness values were required to achieve the observed PFS maximum throw to fault height ratios. Shin et al. (2010) conclude... *"our results strongly imply that gravitational loading cannot by itself account for the significant deformations observed in polygonal faults, even for very low residual friction angles"* and instead consider diagenetic dissolution as a contributing mechanism (c.f. Shin et al. (2008)).

Cartwright and Dewhurst (1998) and Dewhurst et al. (1999) first explored the role of chemical diagenetic reactions as a mechanism to explain PFS nucleation. They suggested that syneresis, which can be defined as *'the spontaneous contraction of a gel-like substance'*, can create a shrinkage phenomena of colloidal fine-grained sediments that could cause the nucleation of polygonal faults. Syneresis can elegantly explain the nucleation of polygonal faults, however, it does not explain the subsequent fault propagation and growth. Furthermore, syneresis is lithology dependent and although it could occur in some clay-rich sediments, it cannot explain the nucleation of polygonal faults hosted in clean carbonate-rich oozes and chalks. Therefore, syneresis does not hold as a universal genetic mechanism, but it may have a role in the early pre-lithification stages of clay-rich PFS tiers. This mechanism can be classified as a physico-chemical process and can thus be considered as a subset of the diagenetically-induced shear failure mechanism.

Alternative diagenetic reactions which induce a net volume reduction have been suggested as drivers of PFS nucleation and growth, principally the transformation of opal-A to opal-CT, smectite to illite, and diagenetic alteration of volcanic ash (Dewhurst et al., 1999; Davies, 2005; Herrera et al., 2007; Shin et al., 2008, 2010; Ireland

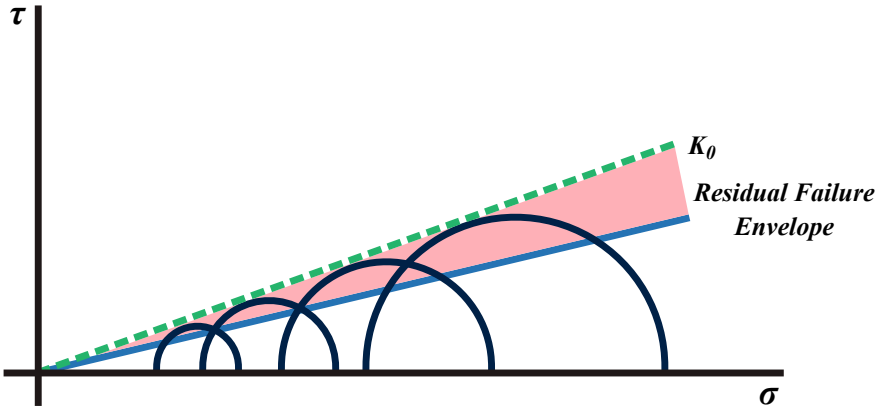


Figure 1.16: Schematic adapted from Goulty (2001a) showing that a pre-existing fracture will propagate under loading if the K_0 gradient is steeper than the residual failure envelope governed by the coefficient of residual friction (μ_r). x-axis label (σ) is the normal stress and y-axis label (τ) is the shear stress.

et al., 2010; Neagu et al., 2010a; Cartwright, 2011; Davies and Ireland, 2011). Laboratory experiments undertaken by Shin et al. (2008) show that shear failure can be accommodated by grain framework volumetric reductions, similar to the dissolution of salt grains in a glass bead sediment framework. However, as with the syneresis mechanism these diagenetically-induced volumetric reduction reactions are lithology specific and in the case of the smectite-illite transformation the burial depths required to meet the conditions for the reaction to take place are significantly deeper than the burial depths of many PFSs. Diagenetic volume reduction reactions can theoretically initiate polygonal fault nucleation, as shown by Roberts (2014) and Roberts et al. (2014), and also drive subsequent fault growth whilst creating accommodation space for displacement in laterally-pinned conditions (Fig. 1.17).

1.3.6 The growth and kinematics of polygonal fault systems

The growth and kinematics of polygonal fault systems has received relatively little attention in the published literature, primarily because of a lack of temporal constraints. Stuevold et al. (2003) presented some of the earliest analysis of the distribution of

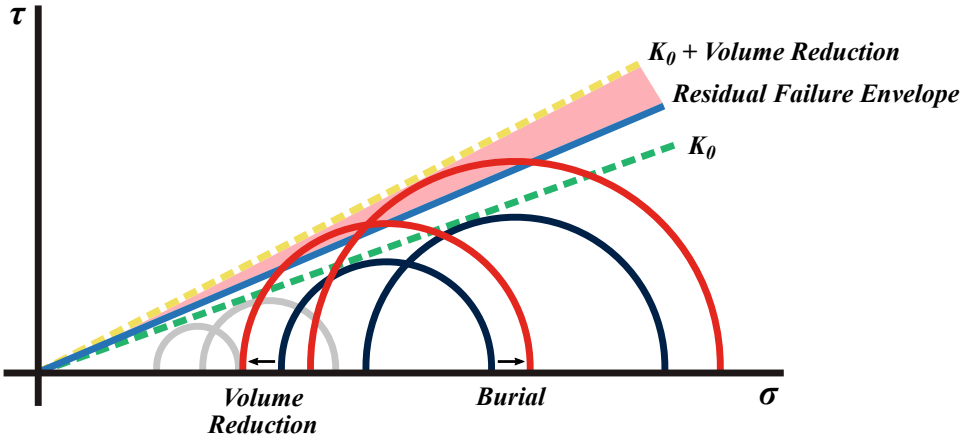


Figure 1.17: Schematic showing that the residual failure envelope can be met as a result of diagenetic volume reductions which simultaneously reduces σ_3 as σ_1 increases with burial. Theoretically diagenetic volume reduction can increase the size of the mohr circle from the K_0 gradient to the failure envelope. This has been shown experimentally (Shin et al., 2008) and through computational modelling (Roberts, 2014). x-axis label (σ) is the normal stress and y-axis label (τ) is the shear stress.

throw on polygonal faults, and established that the PFS hosted in Late Cretaceous fine-grained sediments of the Møre Basin, offshore Norway, grew by upward propagation and experienced a period of Eocene reactivation. Gay and Berndt (2007) investigated the cessation and reactivation of polygonal faults in the Vøring Basin, Norwegian Sea and attributed changes in regional sedimentation and rapid emplacement of debris flows to the cessation and reactivation of polygonal faults. Morgan et al. (2015) show evidence, from a wedge shaped PFS tier in the Lower Congo Basin, that polygonal faults can nucleate in the basal third of the tier at an early stage of burial and propagate upwards. This kinematic inference fits well with PFSs hosted in several basins around the world. Wrona et al. (2017) undertook a kinematic analysis of the Northern North Sea PFS and constrained the timing of fault growth to broad geological epochs. However, absolute displacement velocities for polygonal fault systems have remained elusive, unlike the displacement rates of tectonic and gravity-driven faults which typically grow at several tens to thousands of meters per million years (Nicol et al., 1997; Childs et al., 2003; Mouslopoulou et al., 2009). This

presents a major gap in our understanding of polygonal fault systems and is therefore a key research focus of this thesis. A spatial, temporal, and kinematic investigation of the Vøring Basin PFS forms the focus of Chapter 3 and a detailed investigation of the throw rates of the same PFS forms the focus of Chapter 4.

Furthermore, the processes and physical properties that drive and facilitate polygonal fault growth are poorly understood. A few pioneering studies have computationally investigated the geometrical characteristics of PFS in terms of physical properties. Shin et al. (2010) used the scaling relationship between polygonal fault height and maximum throw as a benchmark to investigate the validity of Goulty (2001a)'s *'gravitational loading'* mechanism. Shin et al. (2010) found that the bulk sediment stiffness values required to achieve the maximum throw values observed in seismic reflection data purely through sediment loading are unrealistically low, and they therefore favour a diagenetic mechanism. Following on from this work Roberts et al. (2014) investigated the role of diagenesis on polygonal fault growth in three-dimensional finite element simulations. Roberts et al. (2014) found that diagenetic processes that induce a volumetric shrinkage can create multi-directional faults in a three-dimensional laterally-pinned sedimentary tier. However, the main physical property drivers and inhibitors, and their relative magnitudes with respect to one another, are unknown. A numerical modelling investigation of the growth of PFSs forms the focus of Chapter 5.

1.3.7 The importance of polygonal fault systems

Polygonal fault systems have puzzled geoscientists for over three decades and answers to the most fundamental questions regarding their formation and growth have remained elusive. For example, the nucleation of polygonal faults defies classical soil mechanical theory in that they form during early burial, under conditions of net zero lateral strain, yet represent shear failure of unconsolidated granular materials (Shin

et al., 2010). Understanding the growth of polygonal fault systems is, however, more than just an academic curiosity. Polygonal fault systems have attracted considerable attention because of their ubiquity in many fine-grained slope depositional systems and they thus play an important role in the sealing integrity of petroleum systems, and the geological storage of CO_2 and high-grade nuclear waste. Furthermore, the spatial extent of PFS can also been used to guide the search for deep-water clastic reservoirs in in frontier basins (Jackson et al., 2014; Turrini et al., 2017). Understanding the kinematics and growth of polygonal faults even has as far-reaching interest to the study of polygonal fractures identified on the surface of Mars (Moscardelli et al., 2012; Oehler and Allen, 2012).

1.4 Research Aims

The primary aim of this thesis is:

To establish the temporal evolution of the growth of polygonal fault systems.

This aim is achieved through:

1. Spatial, temporal, and kinematic analysis of a polygonal fault system from the Norwegian Sea, using high-resolution throw versus depth measurements – Chapter 3.

2. Quantitative fault throw analysis of active polygonal faults in age-calibrated seismic reflection data, to derive the first measurements of throw rates for polygonal faults – Chapter 4.

3. Computational modelling of an isolated fault hosted in laterally-pinned conditions, to determine the mechanism and drivers of polygonal fault growth – Chapter 5.

Chapter 2

High-Resolution Fault Throw Analysis in Seismic Reflection Data: A Novel Methodology to Minimise and Quantify Fault Throw Uncertainty

The methodology developed and outlined in this chapter was used to collect results presented throughout this thesis. This methodology removes the manual picking error and quantifies the interpolation uncertainty. It is worth noting that in most cases the interpolation uncertainty is less than the fault drag uncertainty, but it is nonetheless an important component of the total fault throw measurement uncertainty.

2.1 Abstract

Seismic reflection data are used to identify, map, and measure geological bodies and structures in a wide range of industrial and academic fields. Understanding the geophysical uncertainty in the two-way traveltime (TWT) location of seismic reflection peaks is important for high-precision fault throw analysis and 3-D auto-tracking techniques that are used for horizon mapping. This study presents a novel methodology to explicitly quantify the interpolation uncertainty of reflection peaks (and troughs) in TWT, whilst simultaneously removing the manual picking uncertainty associated with traditional methods. This methodology enables high-precision fault displacement analysis with minimal and quantifiable uncertainty, which is particularly useful when analysing small faults such as those ubiquitous in thin caprocks. We show that interpolation uncertainties are lowest on reflection peaks with high amplitude values, irrespective of the spatial resolution of the seismic reflection data. The improved accuracy and precision of fault measurements using this methodology compared with those of traditional methods may help to de-risk the sealing integrity of fault-saturated caprocks in hydrocarbon and CO_2 storage systems. A MATLAB script that performs the methodology on SEGY data is attached in Appendix C.

2.2 Introduction

The abundance, quality, and spatial resolution of seismic reflection data has greatly improved over recent decades (Brown, 2011). The increased spatial resolution of three-dimensional seismic reflection data has led to the large-scale discovery of a variety of geological and diagenetic structures that were traditionally deemed only observable at field-outcrop scale (Posamentier and Kolla, 2003; Cartwright and Huuse, 2005; Hansen and Cartwright, 2006; Davies and Cartwright, 2007; Løseth et al., 2009). Understanding the geophysical uncertainty associated with the processing of field seismic data to laterally continuous seismic reflections has importance to a number of high-precision fields, such as, reservoir mapping, 3-D horizon map auto-tracking, and fault throw analysis (Bond, 2015).

Deriving the absolute uncertainty in the two-way traveltime (TWT) location of processed reflection peaks is non-trivial because the processing methodology involves several steps, including, deconvolution, stacking, and migration (Yilmaz, 2001). However, the relative TWT difference between any two adjacent reflection peaks can be calculated accurately (with respective upper and lower uncertainty bounds), because uncertainties that are derived from seismic processing can be assumed to be equal within the vicinity of adjacent seismic traces.

Often, the vertical resolution of seismic reflection data (Widess, 1973) is mistakenly cited as having a bearing on the resolution of fault throw measurements. In some studies, plus or minus the sample interval of the seismic data is quoted as the maximum error in throw measurements (Baudon and Cartwright, 2008b,a). However, a methodology to calculate the exact uncertainty of individual fault throw measurements, as opposed to a generalised blanket maximum uncertainty, has remained absent from academic literature. Without a methodology to explicitly calculate fault throw uncertainty, it is not possible to robustly analyse fault throw values that are

less than two times the sample interval of the seismic reflection data from which they are measured. Therefore, limiting the ability to confidently analyse and draw insight from the throw-versus-depth measurements of small faults that are important in the seal de-risking of caprocks in petroleum, CO_2, and nuclear waste storage systems globally.

We present a novel methodology that: (1) removes the picking error introduced through the manual positioning of a computer mouse cursor in traditional methods; (2) explicitly calculates the upper and lower reflection peak interpolation uncertainty in TWT; (3) can be used to plot uncertainty bars for fault throw measurements taken from seismic reflection data.

A glossary of terms used throughout the manuscript is presented in Table 2.1.

Term	Definition
Amplitude	The magnitude of the deviation of a seismic wiggle trace from the null point.
Quantization interval	The spacing between seismic reflection amplitude values in SEGY file format. The quantization interval is used as a measure of the uncertainty of sample point amplitude values.
Fault throw	The vertical component of fault displacement, measured between an offset fault footwall and hanging wall.
Frequency	The inverse of the time (milliseconds) to complete a wavecycle, i.e. the time between two peaks. Higher frequency values have smaller distances between seismic reflection peaks.
Interpolation uncertainty	The difference between the range of seismic waveforms that can be interpolated through the uncertainty bars of seismic sample points.
Reflection peak	Refers to the apex of peaks and troughs along a seismic wiggle trace.
Sample interval	The vertical spacing in TWT (milliseconds) between sample points.
Sample points	Discrete amplitude values spaced at a regular interval that enable the reconstruction of a continuous seismic wave through interpolation.
Seismic wiggle trace	The display of amplitude versus TWT as an oscillating curve about a null point.
Spline interpolation	Interpolation method to produce a smooth continuous curve, used to construct seismic wiggles from sample points.
TWT (Two-Way Traveltime)	The elapsed time for a seismic wave to travel from its source to a given reflector and return to its receiver.

Table 2.1: A glossary of terminology used throughout this chapter.

2.3 Fault Throw Analysis Uncertainties in Seismic Reflection Data

Fault throw analysis in seismic reflection datasets involves measuring the vertical offset of seismic reflections that can be correlated across a fault footwall and hanging wall. In order to quantify the total uncertainty associated with fault throw measurements, a complete understanding of the contributors to the uncertainty is required. The main sources of uncertainty in fault throw measurements taken from seismic reflection data are (Figure 2.1):

1. The incomplete imaging of fault drag (Walsh and Watterson, 1987; Mansfield and Cartwright, 1996).

2. Reflection peak interpolation uncertainty.

3. Manual measurement picking uncertainty.

4. Although not unique to seismic reflection data, compaction-driven throw loss (Mansfield and Cartwright, 1996; Cartwright et al., 1998; Taylor et al., 2008) is a potential source of uncertainty for all faults measured both through geophysical methods or at field outcrop.

To maximise measurement precision, care should be taken when choosing the vertical seismic cross-section that transects a fault in 3-D seismic reflection data. A seismic cross-section parallel to the displacement vector azimuth should be chosen. In cases where the obliquity of the displacement vector is unknown, it is common practice to choose a cross-sectional transect perpendicular to the fault strike, which assumes dip-slip displacement.

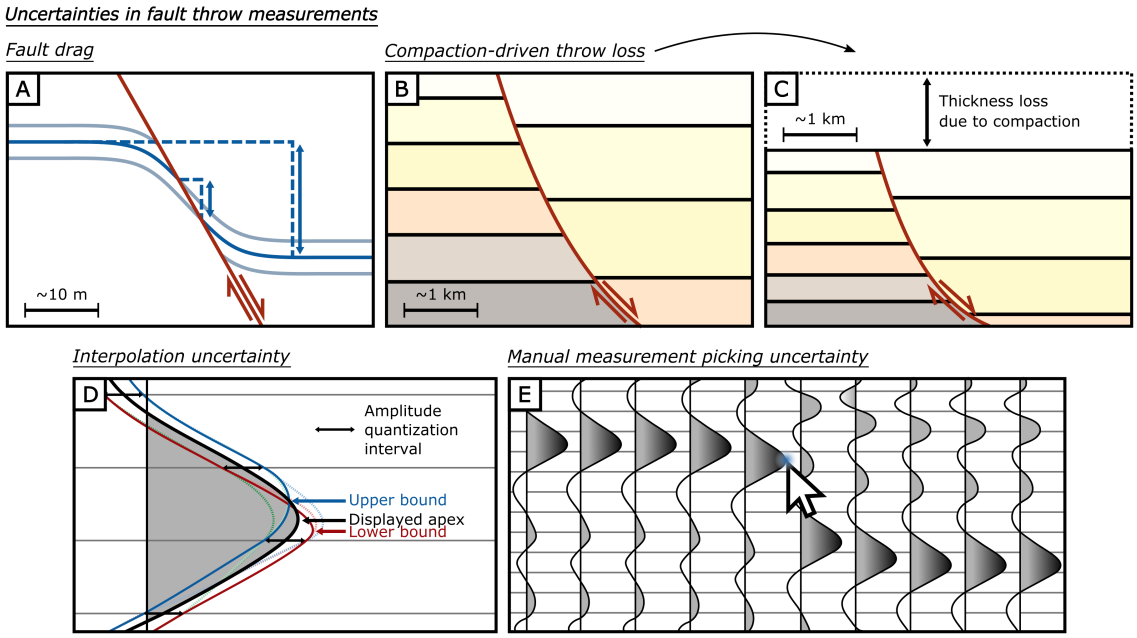


Figure 2.1: Schematic illustrations of uncertainties in fault throw measurements. (A) Maximum and minimum throw values can be measured from horizons with fault drag induced curvature. (B & C) The compaction of fine-grained sediments at depths greater than 1 km can reduce the true magnitude of throw values. In some cases, decompaction factors can be applied to estimate a range of pre-compaction throw values (adapted from Taylor et al. (2008)). (D) The seismic wiggle reflection peak interpolation uncertainty, which is the focus of this manuscript, is largely determined by the uncertainty of sample point amplitude values. (E) Manual measurement picking uncertainty is dependent upon the accuracy of human mouse cursor placement, and is typically within the sample interval.

2.3.1 Fault drag

Fault drag can introduce uncertainty to throw measurements in two ways (Walsh and Watterson, 1987; Mansfield and Cartwright, 1996). Firstly, the bending of seismic reflections in the footwall and/or hanging wall can create curved horizons from which a range of measurable throw values can be taken (Figure 2.1A). Depending on the magnitude of the curvature, the measured throw values can increase or decrease with distance (or more specifically – the number of seismic traces) from the fault plane. To capture a representative spectrum of deformation a seismic interpreter can measure both the minimum and maximum throw values of a fault-dragged seismic reflection. Secondly, as the throw decreases towards the upper tipline of a fault, the distinction between: a discrete fault offset; an upper tip monocline associated with fault propagation; pelagic drape above an arrested fault tip, and seismic imaging artefacts can become ambiguous. Drag folds with wavelengths less than 2-3 times the spatial resolution of the seismic reflection data cannot generally be distinguished from seismic imaging artefacts (Mansfield and Cartwright, 1996; Baudon and Cartwright, 2008b). The distinction between the aforementioned upper tip styles is most clear in high frequency seismic reflection data (>80 Hz) with a low bin size (<6.25 m). A typical 3-D seismic reflection dataset has a dominant frequency of ~40 Hz and a bin size of 12.5 m or 25 m.

2.3.2 Seismic reflection peak interpolation uncertainty

Smoothed reflection peaks displayed on workstation screens are interpolated from the amplitude values at sample points that have a regular TWT spacing (sample interval). During processing the amplitude values at each sample point are converted (through a signal processing method called quantization) from the original continuous values that are recorded at geo- or hydro-phones during acquisition to discretised values that

have a regular amplitude spacing called the quantization interval (Wood, 1974). Fault throw measurements cannot be read directly from the sets of discretised sample points in adjacent seismic traces because fault throw values are continuous and can therefore fall between sample points. Furthermore, the correlation across the fault uses the shape of the interpolated traces. Instead, fault throw measurements can be taken from the reflection trace which is produced from the interpolation of these sample points, specifically, the reflection peak or the zero-crossing because these have continuous TWT values and are consistent reference markers across seismic traces. However, the TWT value of a reflection peak or zero-crossing itself has an interpolation uncertainty determined in part by the amplitude quantization interval of the sample points (see section 2.4.4). The methodology to quantify this interpolation uncertainty is the main focus of this chapter and is outlined in section 2.4.4.

2.3.3 Manual measurement picking uncertainty

Traditional methods to measure fault throw values from seismic reflection data require manual placement of a computer mouse cursor over the reflection peak (or zero crossing) of a correlatable reflection in the footwall and hanging wall (Figure 2.1E). Errors occur in the consistency of the pick, and cursor positioning. Manually picked reflection peaks are typically accurate to within one sample interval of the seismic reflection data, however, the accuracy is largely dependent upon the level of screen magnification used by the interpreter. The precision of manual cursor positioning is low and, therefore, measurements are usually recorded to the nearest integer millisecond in TWT. Our methodology removes manual picking uncertainty from reflection peak measurements.

2.3.4 Compaction-driven throw loss

Although compaction-driven throw loss is a fault related uncertainty that is not caused or influenced by seismic reflection imaging, it is nonetheless a fault throw uncertainty that must be taken into account when undertaking fault analysis.

Throw loss can occur on faults due to the compaction of their host sediments (Figure 2.1 B&C) (Taylor et al., 2008). Compaction-driven throw loss is most significant on syn-sedimentary normal faults that are hosted in strata with a high component of fine-grained sediments (>70%) and post-faulting burial is large (>1 km) (Taylor et al., 2008). Decompaction correction factors can be estimated using porosity-versus-depth curves from nearby borehole data, to reconstruct the original magnitude of throw along a fault profile. However, good constraint on the timing of fault activity is also required to accurately apply decompaction factors, and even with good porosity data it is difficult to reduce the throw uncertainty on deeply buried faults hosted in fine-grained sediments.

In cases where compaction-drive throw loss is significant, an upper and lower decompaction correction factor should be applied to throw measurements to capture the range of uncertainty.

2.4 Methodology to Minimise and Quantify Fault Throw Measurement Uncertainty

The accuracy of fault throw measurements can be improved through computational picking of reflection peaks. We present a methodology that removes manual measurement picking uncertainty and quantifies the reflection peak interpolation uncertainty in TWT. The analysis that follows is based on trace analysis of 3-D migrated seismic data and our examples are time migrated data. As such, these data have been deconvolved, stacked and migrated and to varying degrees normalised. The resultant traces have a character that is a complex function of all these processes as well as the earth's reflection series. However, here we are dealing with the concept of resolution as it affects relative positioning of adjacent or near-adjacent traces and the measurement of time. On this basis, we argue that the analysis that follows is a justifiable method to determine the relative positioning uncertainties of reflection peaks in time across faults. The MATLAB code to run this methodology on seismic reflection data in SEGY file format is found in Appendix C.

2.4.1 Spline interpolation of sample points

Firstly, SEGY data must be loaded into MATLAB where an algorithm interpolates between the quantized sample points of each seismic trace sequentially using a spline interpolation method (Figure 2.2 – Step 1&2). The smoothness of the interpolated wiggle is determined by the spline interpolant interval. Based on trials, we selected an interpolant value of:

$$\text{Spline interpolant interval (ms)} = \frac{1}{\text{Sample interval (ms)} \times 10^2}$$

which produces a smooth interpolation that enables reflection peak values to be measured to two decimal places in TWT.

2.4.2 Interpolated reflection peak auto-picking

Once the seismic wiggles are interpolated, the reflection peaks can be isolated and automatically picked. The absolute amplitude values of the reflection peaks are used for the auto-picking (all values made positive) (Figure 2.2 – Step 3).

The apex of an interpolated reflection peak is picked at the spline interpolant point with an absolute amplitude value that is greater than that of the adjacent interpolant points both directly before and after it in TWT. The TWT values of thus-interpolated reflection peaks are computationally extracted and sequentially printed into a master matrix with their respective spatial coordinates (Figure 2.2 – Step 4). The reflection peak is the preferred reference point to measure fault throw, because each peak has an amplitude value that can be used as a proxy for interpolation uncertainty (interpolation uncertainty is lowest on high amplitude reflections) whereas the zero-crossing has no associated information.

2.4.3 Quantifying reflection peak TWT uncertainty

Steps 1-4 are then repeated for the interpolation uncertainty curves as illustrated in Figure 2.1D. The suite of uncertainty curves captures the minimum and maximum reflection peak TWT values that can be interpolated through the uncertainty bars of sample point amplitude values. The sample point amplitude uncertainty bars are determined by the quantization interval (outlined below, section 2.4.4).

2.4.4 Determining the amplitude quantization interval

Processed seismic reflection data goes through several steps of deconvolution, stacking, and migration before it is exported to SEGY file format. The acoustic waves that are reflected from geological strata are still predominantly recorded by geo- or hydrophones as continuous analogue values and are then converted into discretised digital amplitude values using a technique called quantization. This means the originally recorded analogue amplitude values at each TWT sample are rounded to the nearest discrete quantization value, and therefore the maximum amplitude uncertainty at any sample point is bound by ± half of the quantization interval. Any number of different reflection curves can be interpolated through the amplitude uncertainty bars of the sample points, and these curves give a spread of different reflection peak apex positions in TWT. However, the interpolations that define the upper and lower limits of the reflection peak apex in TWT can be described by the two extreme members of this family of curves – the earliest and the latest interpolation uncertainty curves in TWT as illustrated in Figure 2.1D. Which two of the six interpolation uncertainty curves that define the upper and lower reflection peak TWT values depends on the relative geometry of the sample points in amplitude-TWT space with respect to one another, and therefore is in principle different for each reflection peak along a single trace.

Interpolation uncertainty exists for any curve or surface that is interpolated from sample points with uncertain values. In the case of seismic reflection data, the TWT location of sample points is fixed at a regular grid spacing (the sample interval) and therefore has zero uncertainty. However, the amplitude value at each sample point has uncertainty equal to ± half of the quantization interval. The amplitude quantization interval is rarely available and needs to be determined for each survey empirically by plotting a histogram (with a large number of bins) of amplitudes for a seismic trace

(Figure 2.3). The quantization interval can be measured from the histogram as the interval between bins.

In some cases, particularly on high-resolution seismic data with low sample intervals, the histogram of amplitudes for each trace can appear almost continuous without a regular bin spacing. In these cases, a dynamic quantization has been applied during processing. To determine the quantization interval for the desired section of a seismic trace, the smallest spacing between amplitude values on sample points within the near vicinity of each other (typically within 10-20 sample points) should be used. As a crude rule of thumb based on our results, the amplitude quantization interval is approximately 8-15% of the median amplitude value of the seismic trace (or respective section of the seismic trace).

2.4.5 Quantifying the reflection peak interpolation uncertainty

The quantization interval is used to create amplitude uncertainty bars for each sample point. Six different spline curves are interpolated through the sample point uncertainty bars to find the upper and lower bounds of the interpolation uncertainty in TWT. The geometric positioning of the sample point amplitude values with respect to one another determines which of the six curves define the upper and lower interpolation uncertainty bounds for each reflection peak. The six interpolation uncertainty spline curves are interpolated from six individual amplitude-TWT matrices (Figure 2.2 – Step 5).

The reflection peaks for each of the six interpolation uncertainty spline curves are derived using the same method as above and are printed into six separate matrices (Figure 2.2 – Step 6). The TWT value of each reflection peak in the original interpolated SEGY data is then compared to those of six interpolation uncertainty values. Due to differences in the shapes of the interpolated uncertainty curves, there may not

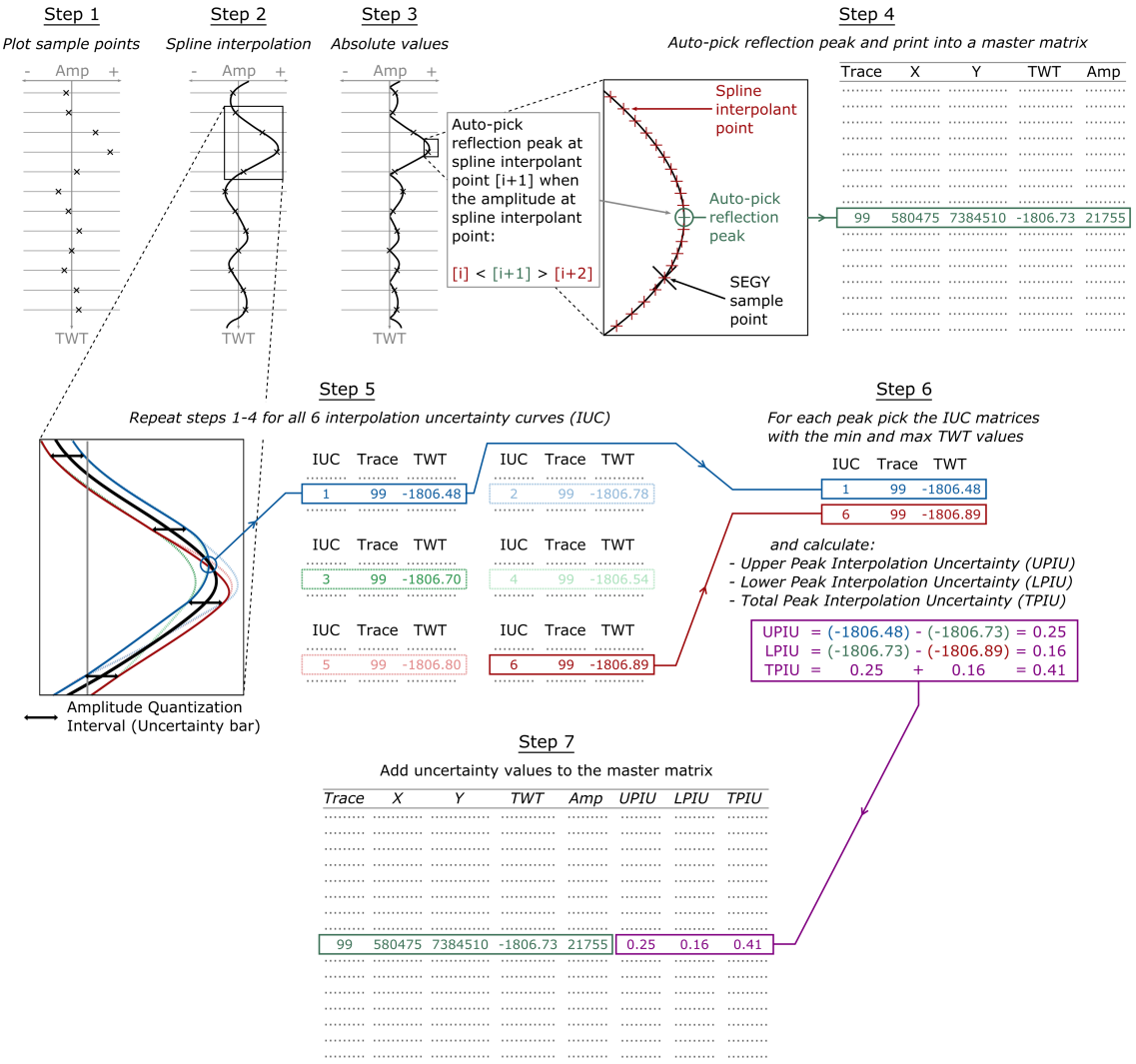


Figure 2.2: Automated reflection peak picking methodology with associated interpolation uncertainty, illustrated in a step by step guide for a single trace. The MATLAB code (Appendix C) runs through the SEGY traces sequentially adding new data to the master matrix. Amp = Amplitude, TWT = Two-Way Traveltime, IUC = Interpolation Uncertainty Curve.

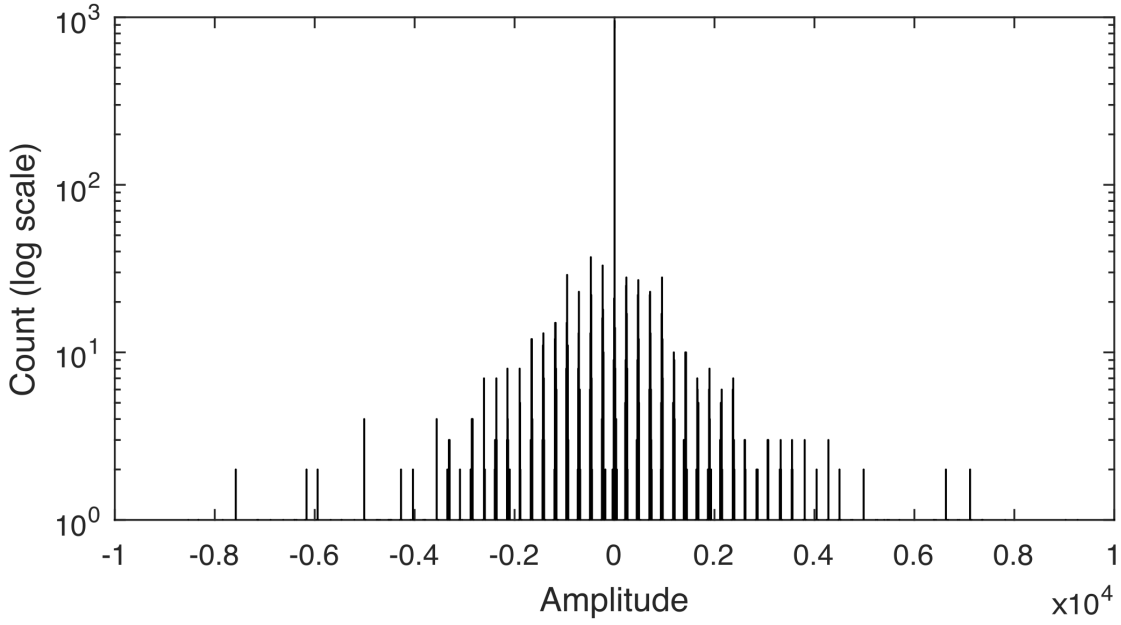


Figure 2.3: A histogram of amplitude values from a seismic reflection line. The regular interval between peaks on the histogram is the quantization interval.

be the same number of reflection peaks in each of the six interpolation uncertainty matrices. Therefore, reflection peak TWT values within ± one sample interval of the original SEGY data apex are concatenated into a new matrix. Within the newly concatenated matrix, for each reflection peak of the original seismic trace, the maximum and minimum TWT values of the six interpolation uncertainty curves are taken and the difference between the two values is printed as the interpolation uncertainty for that apex. The upper, lower, and total uncertainty values are added to the original matrix hosting the coordinates, TWT, and amplitudes (Figure 2.2 – Step 7). At this point the master matrix can be exported as a text file to be imported as point data in seismic interpretation software to overlay on top of the original seismic reflection line. Point data files require approximately 200 times the disk space of the original SEGY data. Alternatively, the seismic reflection data and newly created point data can be visualised together within MATLAB. The TWT and interpolation uncertainty for each reflection peak can be read directly from the point data and used to plot

fault-throw-versus-TWT graphs with uncertainty bars.

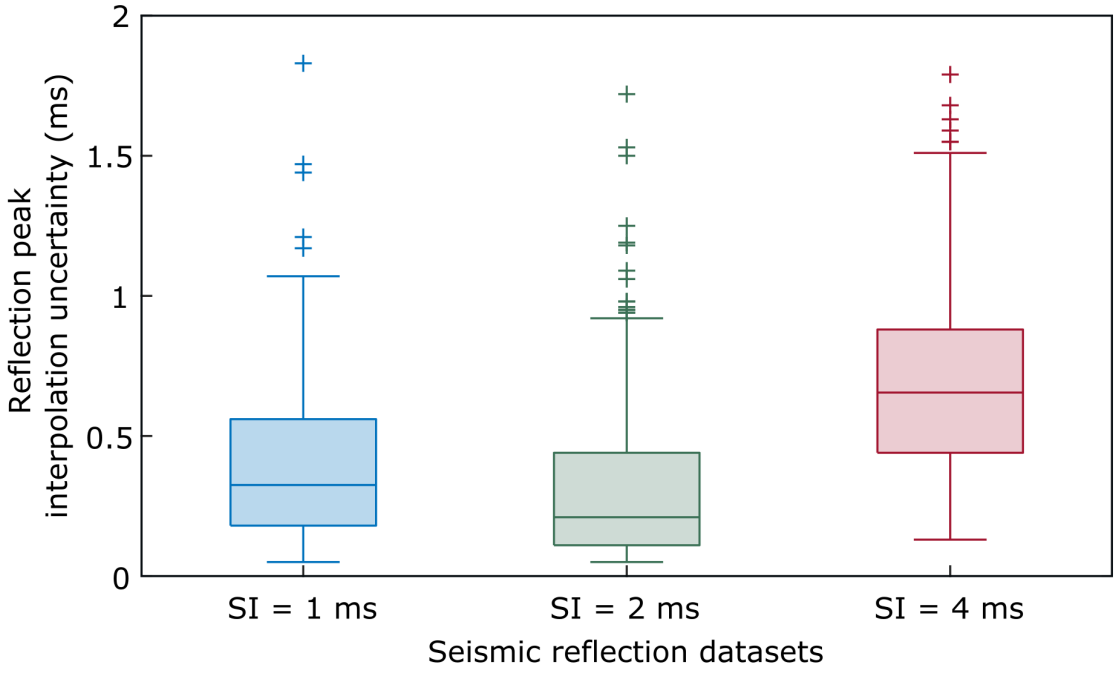


Figure 2.4: Box and whisker plots displaying the distribution of reflection peak interpolation uncertainty for seismic reflection lines with different sample intervals. SI = Sample Interval.

2.5 Results – Seismic Reflection Peak Interpolation Uncertainty

We applied the methodology (MATLAB code, Appendix C) to three separate seismic reflection datasets from the Vøring Basin of the Norwegian Sea with sample intervals of 1, 2, and 4 ms (Table 2.2) and recorded the reflection peak interpolation uncertainty with respect to amplitude, frequency, and TWT below the seafloor. We find that despite the three seismic reflection datasets having different sample intervals and spatial resolutions, the reflection peak interpolation uncertainty is bound by a remarkably similar range of values across all three datasets (Figure 2.4).

Parameter	**VBNS-SRL-SI1**	**VBNS-SRL-SI2**	**VBNS-SRL-SI4**
Sample interval (ms)	1	2	4
Dominant Frequency (Hz)	125	80	40
Vertical resolution estimate* (m)	4	6	12
Quantization interval	0.1	237.5	2175.5
(Mean Amplitude)/(Quantization Interval)	8.4	14.4	11.4

Table 2.2: The spatial resolution and geophysical parameters of the three seismic reflection lines used in our study. All three seismic reflection lines are from the Vøring Basin, Norwegian Sea. *Vertical resolution estimate based on a seismic velocity of ~2000 m/s.

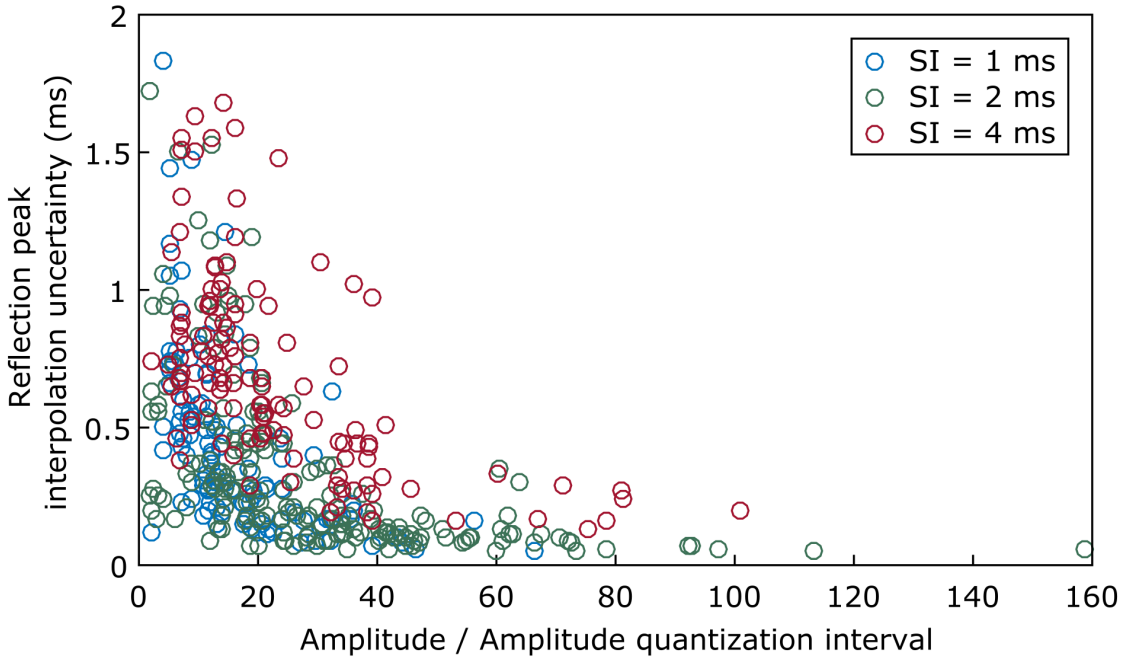


Figure 2.5: Scatter plot of reflection peak interpolation uncertainty versus amplitude normalised to the quantization interval. Seismic reflections with large amplitude values with respect to the amplitude quantization interval have lower reflection peak interpolation uncertainty. SI = Sample Interval.

2.5.1 Amplitude and reflection peak interpolation uncertainty

The reflection peak interpolation uncertainty decreases exponentially with increasing amplitude for each dataset (Figure 2.5). When amplitudes are normalised by dividing the amplitude by the quantization interval the reflection peak interpolation uncertainty for all three seismic reflection datasets plot in the same TWT vs normalised amplitude space (Figure 2.5). This shows a strong correlation between amplitude and reflection peak interpolation uncertainty for seismic reflection datasets.

2.5.2 Depth (TWT) and reflection peak interpolation uncertainty

The reflection peak interpolation uncertainty generally increases with increasing TWT below the seafloor (Figure 2.6). There is not a linear increase in reflection peak uncertainty with depth because amplitude values are a product of differences in acoustic properties of adjacent strata and tunings affects applied during processing to amplify weaker amplitudes at depth. The scatter plots of reflection peak interpolation uncertainty with increasing TWT for all datasets (Figure 2.6) show a systematic trend that we interpret to be due to the similar acoustic impedance response (in all three surveys) to the same geological formations in the Vøring Basin, Norwegian Sea.

2.5.3 Frequency and reflection peak interpolation uncertainty

The frequency of seismic reflection data is a geophysical parameter, like amplitude, that is varied during processing. There is a subtle trend of decreasing reflection peak interpolation uncertainty with increasing frequency (Figure 2.7), however, there is not a strong enough correlation to use frequency as a proxy for uncertainty.

Seismic reflection datasets with high frequencies have a larger number of reflection peaks per millisecond TWT. The higher number of reflections better image discrete displacement in upper fault tip regions, and decrease interpretive ambiguity of ductile and brittle deformation around fault tip-lines. Frequency is not a strong proxy for reflection peak interpolation uncertainty (Figure 2.7), however, seismic reflection datasets with higher frequency values and increased spatial resolution have less interpretative ambiguity as faults (and other geological structures) are more clearly imaged (Mansfield and Cartwright, 1996; Brown, 2011).

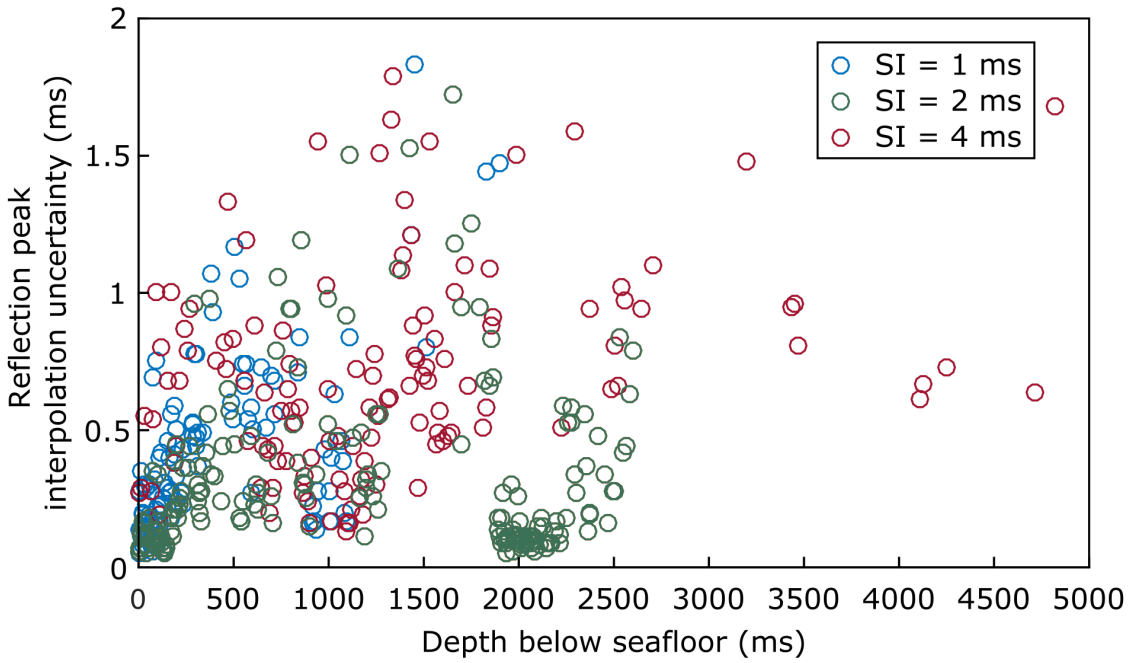


Figure 2.6: Scatter plot of reflection peak interpolation uncertainty versus the depth of the seismic reflection peak below the seafloor. Seismic reflection peak interpolation uncertainty generally increases with increasing depth, however, lithological acoustic impedance contrasts and geophysical tuning can boost seismic reflection amplitudes therefore reducing the interpolation uncertainty. The low uncertainty values at 1000 ms and 2000 ms below the seafloor are explained by all three seismic reflection datasets imaging the same formations in the Vøring Basin, Norwegian Sea. SI = Sample Interval.

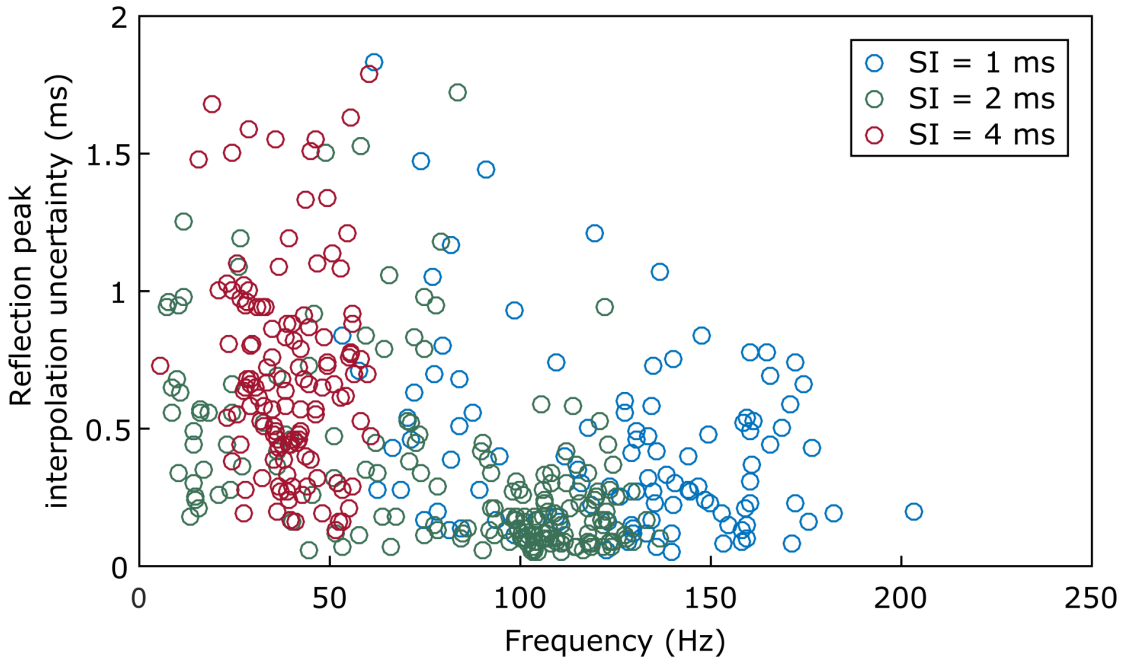


Figure 2.7: Scatter plot of reflection peak interpolation uncertainty versus frequency. SI = Sample Interval.

2.5.4 A comparison of fault throw measurement methodologies

Fault throw uncertainty bars produced using the method outlined in this manuscript are significantly smaller than blanket uncertainty bars defined by the sample interval as used in traditional methods (Figure 2.4). In some cases, fault throw uncertainty bars quantified using the methodology presented in this manuscript are up to eight-times smaller than those used in traditional methods. Differences between throw-versus-TWT graphs, typically used in fault analysis studies, produced using the methodology outlined in this manuscript and traditional methods are highlighted in Figure 2.8. Traditional methods are susceptible to artificial stepped profiles because measurements are accurate to the nearest integer millisecond TWT. Whereas faults measured using the auto-apex picking method outlined in this manuscript can be measured with greater precision and accuracy, therefore improving confidence and insight that can be drawn from throw-versus-TWT graphs. Artificial steps can be mis-interpreted as periods of fault inactivity on syn-sedimentary faults or changes in mechanical properties of blind faults. High resolution throw profiles are particularly important for the analysis of small faults, such as, those posing a sealing risk to regional caprocks and polygonal fault systems (Cartwright et al., 2003; Cartwright, 2011; King and Cartwright, 2020).

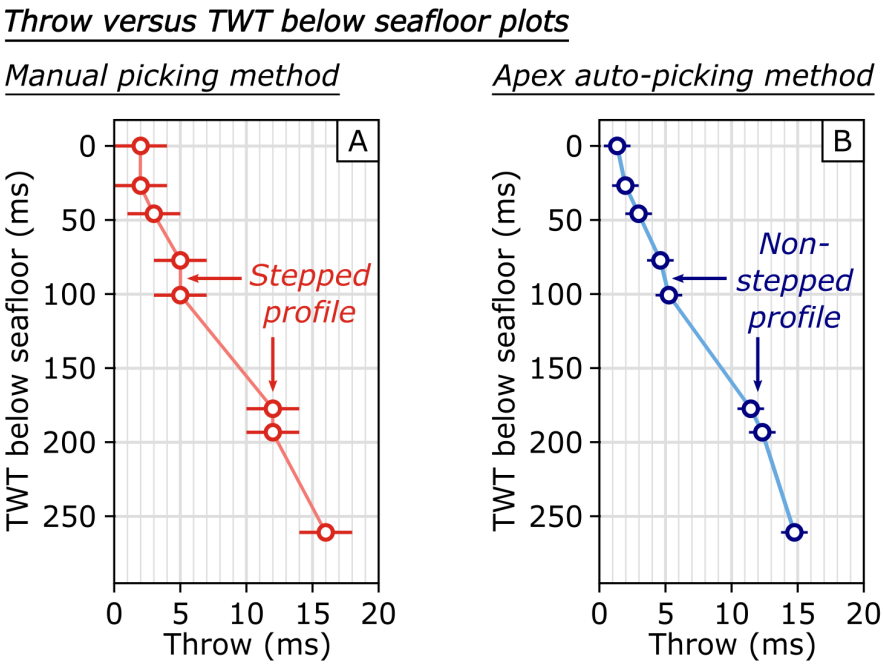


Figure 2.8: Comparative throw versus TWT (Two-Way Traveltime) below seafloor graphs for the traditional manual picking method (A) and the apex auto-picking method presented in this manuscript (B). Throw values measured to the nearest millisecond using the traditional manual method can produce artificial stepped profiles that can be interpreted as periods of inactivity on growth faults. However, when the same fault throws are measured using the apex auto-picking method the flat stepped profiles are smoothed to reveal continued fault activity.

2.6 Conclusions

We present a methodology to remove the manual picking uncertainty of reflection peak locations in TWT and explicitly quantify the associated interpolation uncertainty. The quantification of the reflection peak interpolation uncertainty can be used to plot accurate fault throw measurement uncertainty bars, that are up to 8 times smaller than uncertainty bars used in traditional methods.

We find that the reflection peak interpolation uncertainty is independent of the spatial resolution and sample interval of seismic reflection data. However, the seismic reflection peak interpolation uncertainty correlates strongly with the ratio of the reflection amplitude to quantization interval.

This methodology can significantly improve the accuracy of fault throw measurements, with particular importance to the analysis of small faults hosted in regional caprocks that may pose a sealing risk in petroleum, CO_2, and high-grade nuclear waste storage systems.

The methodology also has relevance to 3-D auto-tracking mapping techniques used in seismic interpretation software. The MATLAB code to apply this methodology to seismic reflection datasets in SEGY file format is found in Appendix C.

Chapter 3

The Spatial, Temporal, and Kinematic Evolution of a Polygonal Fault System

3.1 Abstract

Polygonal faults are a type of nontectonic normal fault that are found almost exclusively in fine-grained sedimentary tiers in over 150 basins around the world. The processes that govern the initiation, propagation, growth, and termination of Polygonal Fault Systems (PFSs) have been widely debated since they were first documented in early three-dimensional seismic reflection datasets in the late 1980's. Despite over three decades of research, our understanding of polygonal fault growth histories, the mechanisms that drive their growth, and their role as seal bypasses in petroleum and CO_2 storage systems remains elusive. This study investigates the kinematic evolution of 53 near-surface and surface breaching polygonal faults from the Vøring Basin, Norwegian Sea, that are hosted in age-calibrated fine-grained claystones and biosiliceous oozes. We find the largest polygonal faults (master faults), that span the

entire vertical extent of the tier, propagate upwards with sedimentation where they have been active at the seafloor since at least late Pliocene times. Analysis of throw versus height profiles reveal that the polygonal master faults exhibit macro-scale and small-scale throw gradient changes that may be the result of temporal changes in the amount of differential volumetric strain occurring at depth and/or mechanical property differences between different formations or intra-formational units.

3.2 Introduction

Polygonal faults are a class of meso-scale layer-bound nontectonic normal fault that are hosted in predominantly fine-grained sedimentary sequences often referred to as *'tiers'* (Cartwright, 1994a,b; Cartwright et al., 2003). Polygonal fault systems (PFSs) are found in over 150 basins around the world where they span large areal extents ranging from ~10^5-10^7 km^2 (Cartwright and Dewhurst, 1998; Cartwright et al., 2003). These nontectonic faults derived their namesake from their characteristic polygonal planform geometries (Figure 1.12, Chapter 1), that were first recorded with the advent of three-dimensional seismic reflection data in the late 1980's (Henriet et al., 1988, 1991; Cartwright, 1994a,b; Cartwright et al., 2003). Despite over three decades of research and wide debate in the academic literature (Dewhurst et al., 1999; Goulty, 2001a; Cartwright et al., 2003; Goulty and Swarbrick, 2005; James et al., 2006; Goulty, 2008; Cartwright, 2011), our understanding of the processes that govern the nucleation, propagation, and growth of polygonal faults remains elusive. Understanding the spatial, temporal, and kinematic evolution of polygonal faults has gained considerable interest in recent years because PFSs present an enigmatic leakage risk in many of the fine-grained *'sealing sequences'* of petroleum and CO_2 storage systems, in which they reside (Cartwright, 2011).

The three-dimensional geometries of polygonal faults are well documented from a number of basins, where several previous studies have revealed that polygonal faults exhibit a range of dip angles, network intersection geometries, and displacement distributions (Cartwright et al., 2003 and references therein - see Chapter 1 for detailed discussion). However, our understanding of the kinematics and underlying drivers of polygonal fault growth remains limited because of a lack of temporal constraints or physical analogues. Throw versus height profiles from several hundred polygonal faults across multiple study areas (Stuevold et al., 2003; Neagu et al., 2010a; Laurent

et al., 2012; Morgan et al., 2015; Ghalayini et al., 2017; Turrini et al., 2017; Wrona et al., 2017) have been used to infer the growth histories of PFS and oftentimes extended to speculate the underlying mechanism(s) that may drive their propagation and growth, albeit with limited constraints.

One critical kinematic constraint that has been widely recognised across several studies is the timing of fault initiation, which has been shown to occur in the early stages of burial (Cartwright, 1994a; Lonergan et al., 1998a; Berndt et al., 2003; Stuevold et al., 2003; Gay et al., 2004; Morgan et al., 2015). Results from several studies suggest that, following an early nucleation phase, polygonal faults often grow by upward propagation (Watterson et al., 2000; Stuevold et al., 2003; Gay and Berndt, 2007; Davies and Ireland, 2011; Morgan et al., 2015) and that their downward propagation is inhibited by either a change in mechanical properties caused by a lithological transition or through a detachment of the lower tip into a mobile basal layer (Cartwright et al., 2003; Cartwright, 2011).

A number of previous studies have also shown that the upward propagation of polygonal faults can be impeded by coarse-grained sedimentary facies (Lonergan and Cartwright, 1999; Cartwright et al., 2003; Stuevold et al., 2003; Carruthers, 2012; Turrini et al., 2017) and, because of this, the extent of polygonal faulting has been used as a mapping proxy to identify reservoir facies in frontier petroleum exploration basins (Jackson et al., 2014). A handful of pioneering computational studies have attempted to investigate the drivers of polygonal fault growth (Shin et al., 2010; Roberts et al., 2014; Roberts, 2014), however, without temporally constrained kinematic growth histories the processes that govern the growth of PFSs remain theoretical.

This study investigates the spatial, kinematic, and temporal evolution of near-surface and surface breaching polygonal faults located in the Vøring Basin, Norwegian Sea (Figure 3.1). The study area was chosen because it offers high-resolution three-dimensional seismic reflection data coverage and chronostratigraphic and phys-

ical property calibration provided by Ocean Drilling Program (ODP) and industry well data, to enable the investigation of the kinematic growth histories of an active PFS. We use a novel methodology (presented in Chapter 2) to measure high-resolution throw versus height profiles of 53 polygonal faults and present evidence to suggest the master faults that comprise the PFS have grown contemporaneously with sedimentation, since at least the late Pliocene.

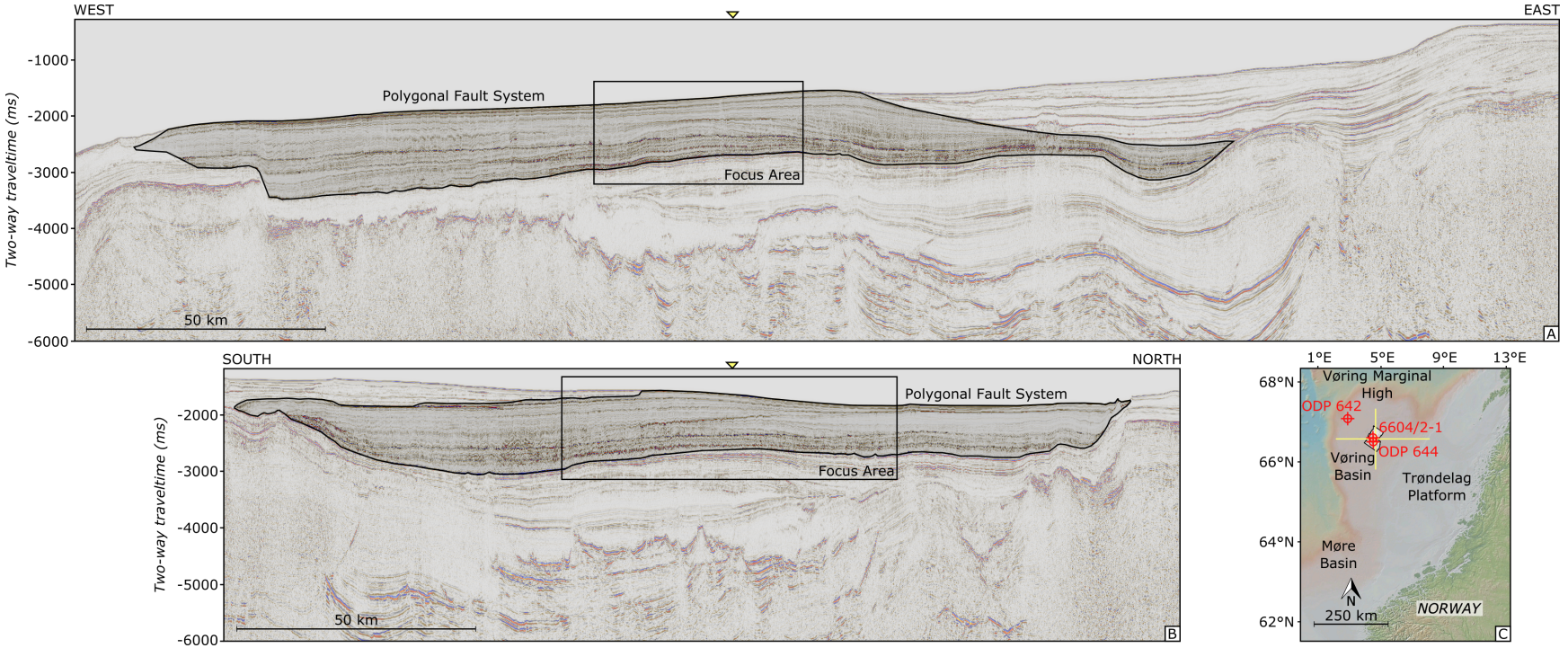


Figure 3.1: Two-dimensional seismic reflection cross-sections transecting the Vøring Basin showing the location of our focus area with respect to the regional extent of the polygonal fault system. Yellow triangles show the intersection plane on the (A) east-west and (B) north-south transects. (C) Locations of the cross-sections are shown with respect to our three-dimensional seismic reflection dataset coverage, ODP wells 642 and 644, hole 6604/2-1, and the Norwegian coastline.

3.3 Data and Methods

3.3.1 Data

The data used in this study consists of the BG0904 three-dimensional seismic reflection volume, the Ocean Drilling Program (ODP) well 644, and industry well 6604/2-1 (Figure 3.2). The BG0904 seismic survey covers ~2400 km^2 and is zero phased, time migrated, and displayed with positive American polarity (Brown, 2011). The sample interval is 4 milliseconds, the bin spacing is 25 metres, the dominant frequency is ~40 Hz, and the vertical resolution is ~10 metres based on an interval velocity of 1600 m/s as used by Shipboard Scientific Party (1987). A single ultra-high-resolution two-dimensional seismic line is used to measure the throw profile of the orthogonal striking fault NGull-053, which has a sample interview of 1 millisecond, a dominant frequency of ~125 Hz, and a vertical resolution of ~4 metres. The ODP 644 well samples ~250 m of sediments below the seafloor and provides lithological core descriptions and chronostratigraphic calibration for the uppermost portion of the PFS tier (Shipboard Scientific Party, 1987). The 6604/2-1 well spans the entire thickness of the PFS tier and provides lithological cuttings descriptions, regional geological formation boundary calibration, and a bulk density well log (BG Group, 2012) (available from the Norwegian Petroleum Directorate, http://www.npd.no). We used Schlumberger's Petrel software to visualise the seismic reflection data and produce maps of key horizons and isopachs across the study area, using standard three-dimensional auto-tracking techniques. The calibration of the BG0904 seismic reflection volume used in this study is illustrated in Figure 3.4. (See Appendix A for detailed chronostratigraphic calibration of the top 250 metres below the seabed, provided by ODP well 644 used in Chapters 3 & 4.)

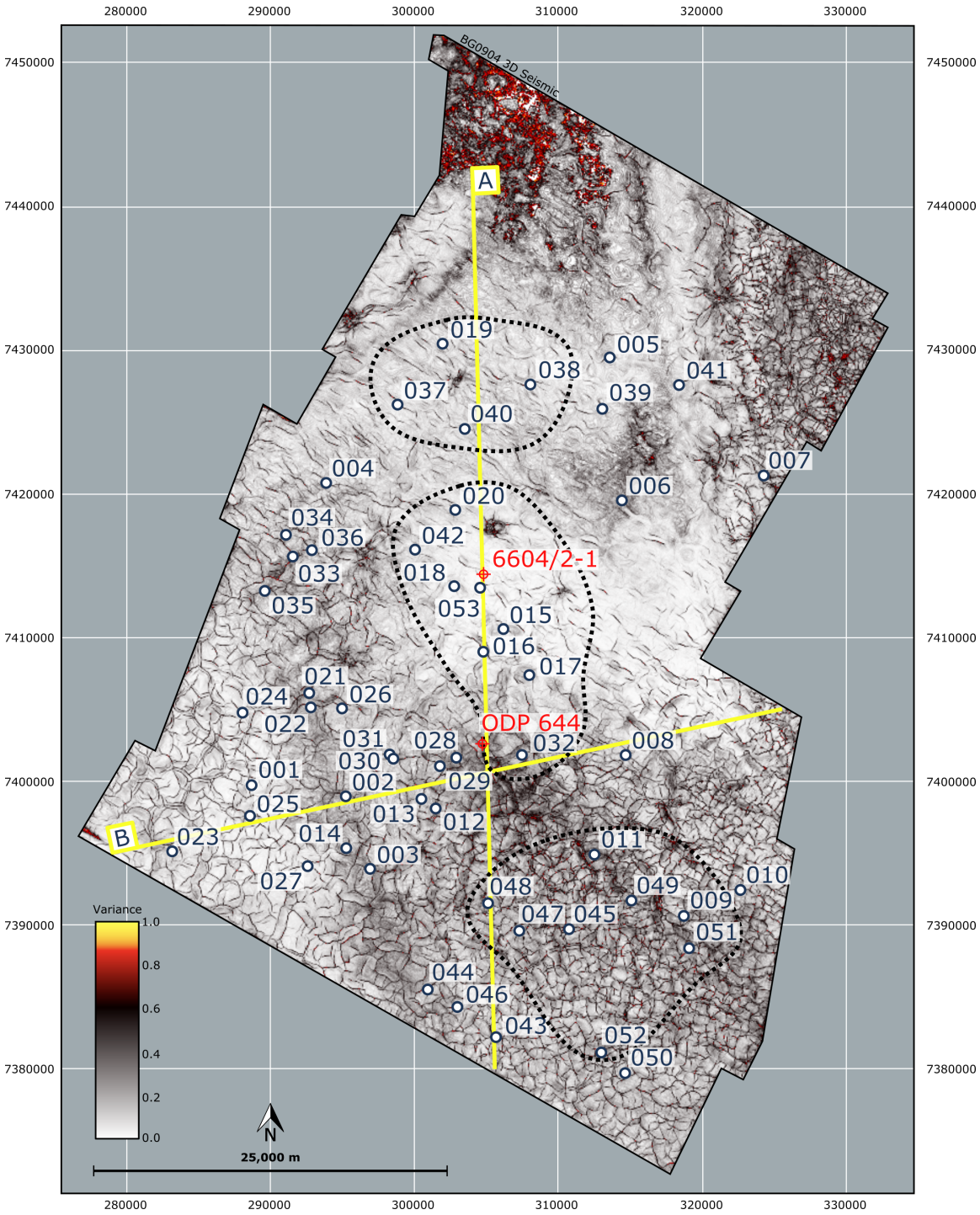


Figure 3.2: Location of faults NGull001-NGull053 measured and used in our analysis. Basemap is a seismic variance timeslice at -2775 ms. Yellow lines show the locations of seismic profiles in Figure 3.3. Black dotted polygons show the faults featured in Figures 3.14, 3.15, 3.16, 3.17, & 3.18 with throw versus height plots and accompanying seismic cross-sections.

3.3.2 Measuring Fault Throw

We measured fault throw values from 53 polygonal faults on seismic profiles oriented perpendicular to the fault strike that transected the central section of the fault where the maximum throw value was found. Throw values were taken as the difference, in Two-Way Traveltime (TWT), between the reflection peaks of the footwall and hanging wall respectively, where reflection peak locations in TWT were computationally extracted using the methodology described in Chapter 2. Throw values from as many as 70 seismic reflections were recorded from each fault in our study. It should be noted that the throw value recorded from the opal-A/CT boundary is not true stratigraphic throw, but is the vertical offset of the fossilised diagenetic boundary front (Neagu et al., 2010a). In the shallow stratigraphic section, calibrated by dated horizons, there is limited fault drag, however, where offset reflections are not approximately planar, measurements of throw have been consistently taken to minimise spurious measurement errors by measuring at least one seismic trace in from the fault plane where the apex locations of seismic traces either side are stable (Mansfield and Cartwright, 1996). Throw measurements recorded from the uppermost portions of polygonal fault tips that are less than ~8 milliseconds may in some cases be related to upper tip monoclines that could be the result of tipline propagation a few tens of metres below the surface, or discrete offset beyond the image resolution of the data. We plot throw in milliseconds against the Two-Way Traveltime below the seafloor location of the footwall, with measurement error within ± 1 ms (Townsend et al., 1998). We do not apply a decompaction factor (Taylor et al., 2008) to our throw measurements because the faults have experienced shallow burial conditions and the throw values recorded are low, therefore, our measurements may be considered as minimum values.

3.4 Geological Setting & Lithological Descriptions

3.4.1 Development of the Vøring Basin

Our study area is located in the Vøring Basin of the Norwegian Sea, situated approximately 500 km northwest of the Norwegian coastline (Figure 3.1 C). The Vøring Basin developed over three main tectonic phases from (1) the late Mid-Jurassic to Late Cenomanian, (2) Late Cenomanian to Early Paleocene, and (3) Early Paleocene to present (Shipboard Scientific Party, 1987; Brekke et al., 1999; Brekke et al., 2000). The Vøring Basin is bound to the east by a series of fault complexes separating it from the Trøndelag Platform and to the west by the Vøring Escarpment of the Vøring Marginal High (Brekke et al., 2000) (Figure 3.1). Much of the mud-dominated sedimentary basin fill, which is over 10 km thick in places, was supplied to the Vøring basin from erosion of both the Greenland and Fennoscandia continental shields during the second phase of rifting (Scheck-Wenderoth et al., 2007). The basin has experienced a complex tectonic development over the course of the latter two tectonic phases including extension, thermal uplift, and intermittent phases of compression/transpression (Blystad, 1995; Brekke et al., 1999). Large-scale igneous activity accompanied continental breakup in the North Atlantic during the Late Paleocene to Early Eocene, where a series of sills and dykes were injected into the Cretaceous strata (Skogseid et al., 1992).

3.4.2 Description of the PFS host strata

The PFS that forms the focus of our study extends across the Norwegian Sea, where it has been investigated and characterised in previous studies (Berndt et al., 2003; Gay and Berndt, 2007; Neagu et al., 2010a; Ireland et al., 2011; Laurent et al., 2012). The polygonal fault system is most prominent at the seabed within our study

area and neighbouring seismic reflection volumes in the Gjallar Ridge area, however, the upper PFS tier boundary can be found within the top 100 or so metres of the seabed across much of the Vøring Basin. The PFS tier is hosted within a sequence of Eocene-Present aged hemipelagic sediments that span the Brygge, Kai, and Naust Formations (Berndt et al., 2003; Gay and Berndt, 2007; Ireland et al., 2010; Neagu et al., 2010a; Laurent et al., 2012; BG Group, 2012) (Figure 3.4).

Within the study area, industry well 6604/2-1 calibrates the geological formations that host the PFS tier through wireline log curves and cuttings descriptions. The Brygge Formation comprises ~800 m of biosiliceous ooze in its upper most section and claystones with occasional thin and closely-space limestones in the lower parts of the section (BG Group, 2012). The Kai Formation unconformably overlies the Brygge Formation and comprises ~175 m of interbedded ooze and claystone (BG Group, 2012). The Naust Formation which unconformably overlies the Kai Formation comprises ~175 of claystone and fine-grained glacial deposits (Shipboard Scientific Party, 1987; BG Group, 2012).

3.4.2.1 Sedimentation rate estimates

The Brygge Formation was deposited from the Ypresian through to the early Miocene (~40 m.y.), the Kai Formation was deposited from the early Miocene to the late Pliocene (~15 m.y.), and the Naust Formation was deposited between the late Pliocene to the present day (~3 m.y.), respectively (Dalland et al., 1988; Eidvin et al., 2007; Chand et al., 2011; Eidvin et al., 2014; BG Group, 2012). These broad depositional time periods and thicknesses recorded at the 6604-2/1 well give sedimentation estimates of ~20 m/m.y for the Brygge Formation, ~10 m/m.y. for the Kai Formation, and ~60 m/m.y. for the Naust Formation. Sedimentation rates for the Naust Formation recorded at ODP well 644 increase from ~50m/m.y. to ~100 m/m.y. uphole (Shipboard Scientific Party, 1987). It is worth noting that the Brygge Formation

sedimentation rate estimate is likely an underestimate because these units have been buried to greater depths than the Kai and Naust, where they have experienced mechanical compaction and diagenetic thickness changes that have not been accounted for. At the location of the 6604/2-1 well, these sedimentation rate estimates suggest that the loading rate halved during the deposition of the Kai interval before increasing by 6 fold in the Naust interval.

3.4.2.2 Stratigraphic wedges

The PFS that forms the focus of this study is hosted within a number of stratigraphic wedges across the wider Vøring Basin, which have been interpreted as contourite drift deposits (Laberg et al., 2001; Ottesen et al., 2009; Laurent et al., 2012; Eidvin et al., 2014). Within the study area, the PFS tier comprises wedge shaped stratigraphy within the Kai and Naust Formations (Figure 3.3). The Brygge Formation is roughly uniform in thickness across the study area, and it is unconformably overlaid by the Kai and Naust Formations that thicken southward. The Kai Formation comprises two stratigraphic wedges that thin in a north-south direction across the study area. One wedge thins southward from the northern region of the study area where it condenses in the central region of the study area near the 6604/2-1 well, and a second wedge overlays the thin end of the northern wedge and thickens southward from the central region of the study area. The Naust Formation unconformably overlies the Kai Formation where it thickens from north to south across the study area. The wedge shaped stratigraphy implies that the Naust and Kai Formations had a faster sedimentation rate in the south of the study area relative to the north.

3.4.2.3 Opal-A/CT boundary

A fossilised opal-A/CT boundary within the Miocene strata of the Brygge Formation is well imaged and documented across the entire extent of the Vøring Basin (Brekke

et al., 1999; Brekke et al., 2000). The opal A-CT boundary reflection cross-cuts the stratigraphic seismic reflections imaged within the Brygge Formation (Figures 3.4 & 3.3), and lies approximately parallel to the seismic reflection at the top of Kai Formation. The apparent discrepancy between the shallow burial depth of the opal-A/CT boundary and the present day geothermal gradient has been noted by several authors who have suggested that the reflector *'froze'* when the geothermal gradient was at least 50-60°C km^{-1} in the late Miocene/late Pliocene (Brekke et al., 1999; Brekke et al., 2000; Davies et al., 2009; Neagu et al., 2010a,b; Ireland et al., 2011).

3.4.2.4 Physical properties of the PFS host strata

Physical property calibration of the tier within the study area is limited to a single density log recorded in industry well 6604/2-1 (Figure 3.4) and porosity values recorded from the top 250 metres of the ODP hole 644 (Figure 3.5). Porosity measurements from the top 250 metres below the seafloor at ODP hole 644 range between 40-70%, where, bulk porosity values decrease from around 65% at the top of the Naust Formation to around 60% at its base before increasing to around 65% in the uppermost portion of the Kai Formation that is sampled by the well (Figure 3.5). This increase in porosity downhole from the Naust to the Kai Formation correlates with a change in lithology from clay-rich sediments in the Naust to biosiliceous oozes in the Kai (Shipboard Scientific Party, 1987; BG Group, 2012). The porosity fluctuates to values as low as 40% within the Naust Formation, which is likely the result of highly compressible intra-formational units layered between more competent units.

The 6604/2-1 downhole density log records values of ~1.7-2.0 g/cm^3 within the lower Naust and upper Kai Formations before decreasing to values of ~1.5 g/cm^3 in the lower Kai and upper Brygge Formations. These lower density values remain flat over the interval of biosiliceous ooze before increasing sharply at the opal-A/CT boundary to ~1.7-1.9 g/cm^3 that grade into values of ~2.0 g/cm^3 at the top of the

Tare Formation, which marks the base of the PFS tier. The low bulk density values recorded within the biosiliceous ooze interval above the opal-A/CT boundary are likely related to high porosity values, which suggests that the interval may have experienced only a nominal amount of compaction over the first 500 metres or so of burial. The bulk density profile decrease within the stratigraphy comprising biosiliceous ooze (well 6604/2-1 Figure 3.4) is also observed in the 6704/12-1 and 6704/12-2 wells located ~50 km north (Neagu et al., 2010a; Ireland et al., 2011; Laurent et al., 2012). This exceptional porosity preservation is characteristic of biosiliceous oozes (Praeger, 2009). The diagenetic transition from opal-A to opal-CT causes an increase in the bulk density values recorded in the base of the PFS tier, which has been attributed to a porosity reduction of ~10% in the nearby 6704/12-1 well (Neagu et al., 2010a). Neagu et al. (2010a) showed that this diagenetically-induced porosity reduction has caused significant vertical strain within the lower portion of the PFS tier, where it has caused compactional flattening of the lower polygonal fault plane dips.

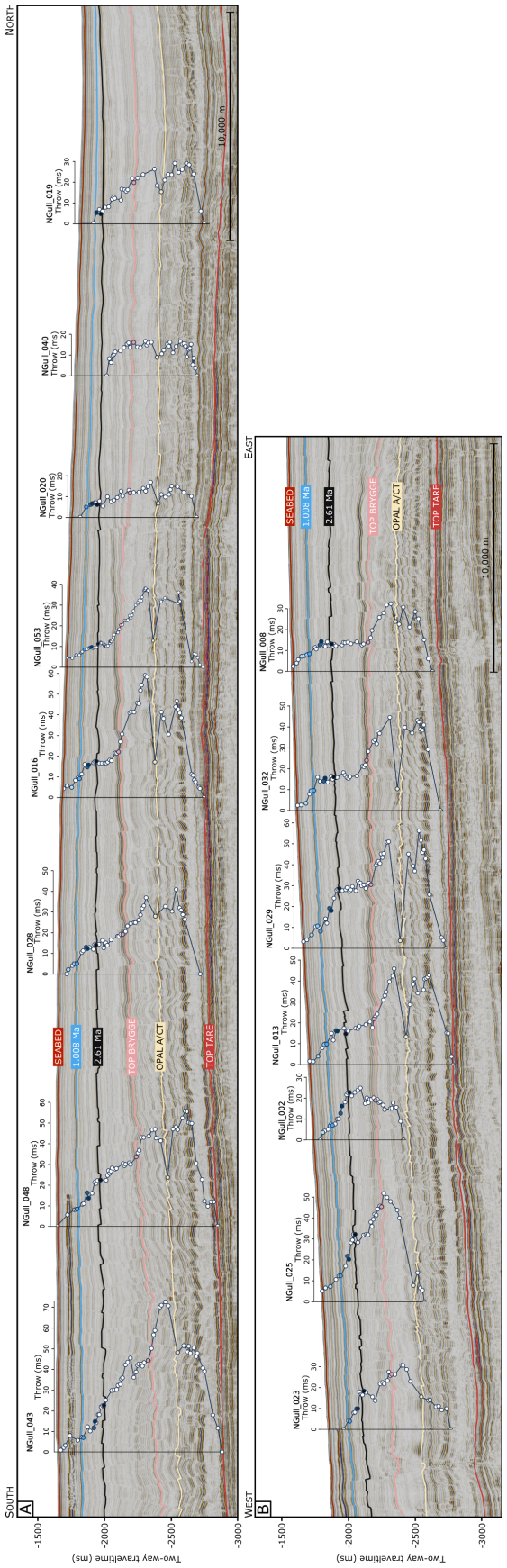


Figure 3.3: (A) North-south and (B) east-west seismic reflection cross-sections across the study area with superimposed fault throw-versus-depth profiles from nearby faults. See Figure 3.2 for the location of cross-sections. Vertical exaggeration ~x5.

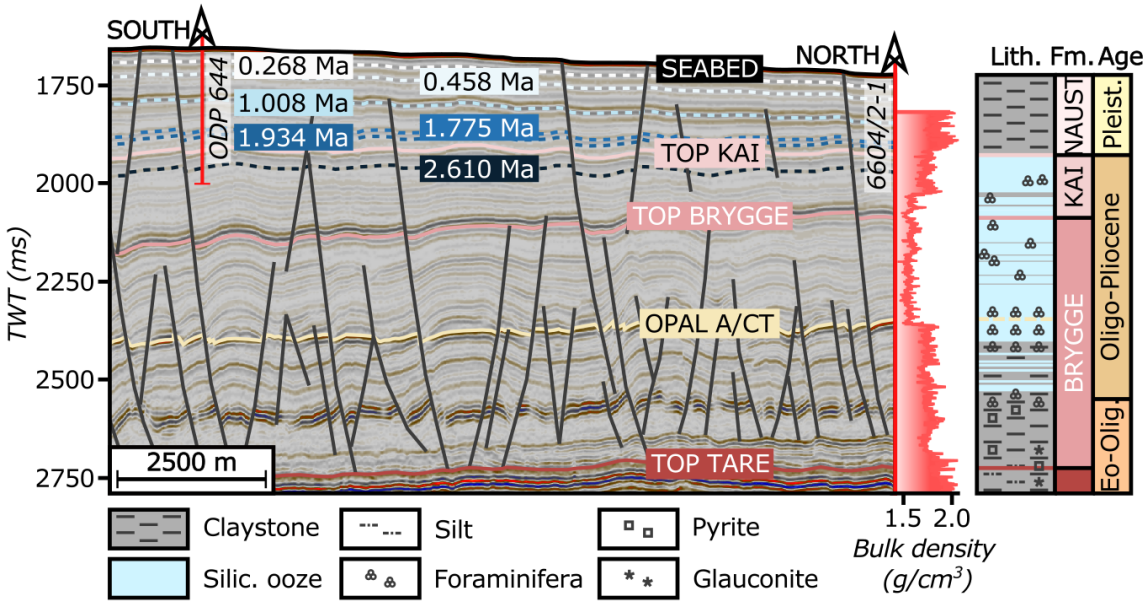


Figure 3.4: Seismic reflection cross-section transecting the Vøring Basin PFS through ODP well 664 and industry well 6604/2-1, with accompanying bulk density profile, stratigraphic column, age-calibrated reflections, formation boundaries, and the fossilised opal-A/CT reflection.

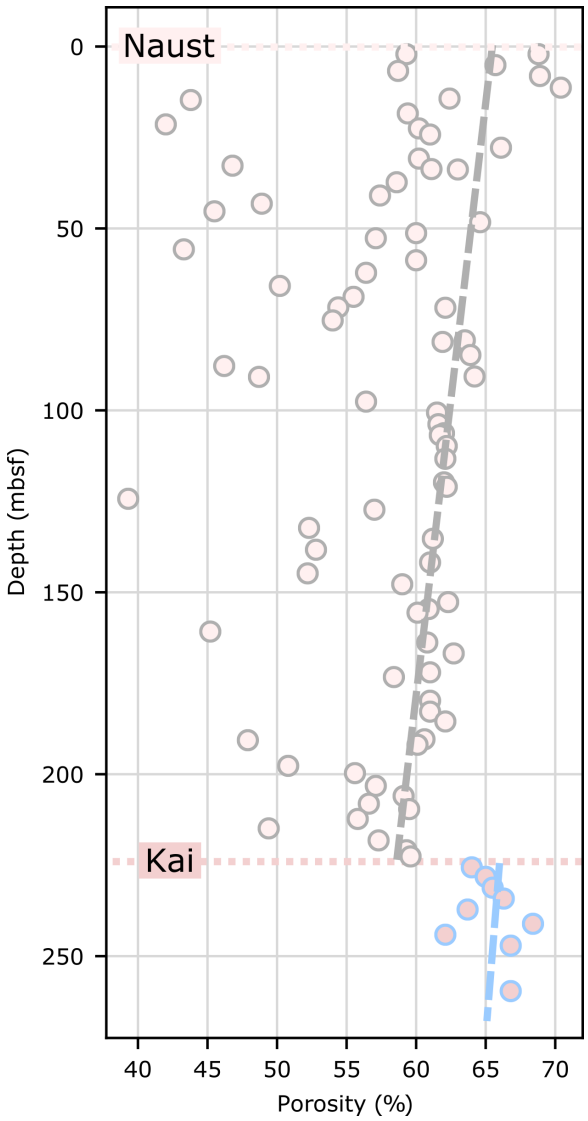


Figure 3.5: Porosity versus depth profile from ODP hole 644 (Shipboard Scientific Party, 1987). Naust and Kai Formations are coloured coded, respectively. Grey and blue coloured dashed lines represent the macro-scale compaction trend of the formation.

3.5 Fault Analysis

Throw profiles for the 53 polygonal faults analysed in our study (Figure 3.2) are displayed in Figures 3.6, 3.7, and 3.8, where as many as 70 throw measurements were recorded on each fault. Faults with a range of dip directions were included in our sample population to eliminate the possibility of introducing an orientation bias (Figure 3.9 I). The majority of the faults analysed in our study are *master faults*, which are the largest polygonal faults that span the vertical extent of the PFS tier (Cartwright, 2011). These polygonal master faults intersect or tip out within a few seismic reflections of the present day seafloor. However, we also sampled a small number of smaller faults (e.g. NGull-001, NGull-023, NGull-035) that do not span the entire height of the tier for comparison. In addition, we present a series of maps (Figure 3.9) that show the spatial distribution of various attributes from our fault sample population, such as: maximum throw values; fault heights; upper and lower tip gradients; dip direction; throw at the opal-A/CT boundary; and throw at the 2.61 Ma horizon.

3.5.1 Description of the PFS

The PFS within our study area shares many of the characteristics of both the wider Vøring Basin PFS that has been described in several previous studies (Gay and Berndt, 2007; Neagu et al., 2010a; Ireland et al., 2011; Laurent et al., 2012), and PFSs from other basins around the world, such as those documented by Cartwright (1994a,b), Lonergan et al. (1998a,b), Cartwright and Dewhurst (1998), Gay et al. (2007), Berndt et al. (2012), Carruthers et al. (2013), Morgan et al. (2015), Turrini et al. (2017), and Wrona et al. (2017). Within the study area, the PFS comprises an array of multi-directional layer-bound normal faults that range in height from a few tens of metres to around one kilometre and range in width from a few hundred

metres to over two kilometres before intersecting a neighbouring fault. The PFS has a well-connected planform pattern (Figure 3.2), with both linear and curvi-linear fault traces that have a predominantly orthogonal intersection angle. This planform style is characteristic of the *irregular planform* end-member presented by Lonergan et al. (1998a).

The greatest fault density occurs in the lower portions of the tier (see greater fault density in the variance time-slice base map of Figure 3.9 H from the lower third of the tier compared to the variance time-slice base map of Figure 3.9 G which is from the upper third of the tier). The majority of lower polygonal fault tips terminate within a few reflections of the base of the Brygge Formation, whereas in marked contrast the upper tips terminate at a range of different horizons across the vertical extent of the tier (Figure 3.3). Less than half of the faults observed in the basal section of the PFS tier span the entire tier height. A small number of subordinate polygonal faults that neither tip out in the near vicinity of the lower tier boundary nor reach the present day seabed are also observed within the tier. These subordinate faults, which have sometimes been referred to as *space-filling* faults in other PFSs (Lonergan et al., 1998a), are less prominent throughout the tier as they are commonly intersected by larger neighbouring faults.

The polygonal faults within the tier exhibit a range of dip angles that shallow with depth in a similar fashion to those documented by Neagu et al. (2010a) in an adjacently located seismic reflection survey found less than 50 km north of our study area. Here, and in our study area, polygonal fault dip angles are as high as 50°-70° above the opal-A/CT boundary and as low as 30°-50° below it (Neagu et al., 2010a).

3.5.2 Growth packages

A series of small growth packages (units with greater thicknesses in the hanging wall relative to the footwall and that often have a wedge-shaped geometry that thickens

systematically towards the hanging wall cut off) that are typically no more than one seismic reflection thicker on the hanging wall side than the footwall side of the fault are observed sporadically within the tier. These growth packages are most commonly found within the Naust and Kai Formations, but a few growth packages are also observed within the Brygge Formation (Figures 3.10 & 3.11). Some faults exhibit a marked decrease in the throw values of seismic reflections that directly overlie the larger growth packages, but many of the growth packages cannot be identified in throw versus depth profiles without accompanying seismic reflection profiles (Figures 3.10 & 3.11).

3.5.3 Polygonal fault types

We categorise our fault throw profiles into the end-member types (C, M, L, B, Z, *see Chapter 1 - Figure 1.6*), as used in previous studies (Muraoka and Kamata, 1983; Stuevold et al., 2003; Baudon and Cartwright, 2008c; Jackson et al., 2014; Turrini et al., 2017), and hybrid types (C/M, C/Z, and L/M), where the letter on the left describes the macro-scale profile and the letter on the right describes portions of the profile.

Faults with C-type throw profiles have a cone-shaped throw distribution, where the greatest amount of throw is found in the central portion of a symmetrical profile. Faults with M-shaped throw profiles have a distinct flat central section where there is no significant change of slope, with abrupt changes in gradient either side towards the fault tips. Faults with L-shaped profiles have asymmetric throw distributions with greater throw values skewed to the lower portions of the fault. L-type faults have steeper lower tip gradients and shallower upper tip gradients. Faults with B-shaped profiles have two maximum throw peaks (one in the upper section of the fault and one in the lower section of the fault) separated by lower throw values in between. There are no B-type faults within our sample population, however, B-type faults

are often characteristic of two separate fault planes that have merged through dip-linkage. Faults with Z-shaped throw profiles have several increases and decreases in throw with depth. Many faults have small M-type sections within a larger C-type or L-type profile, and it is common for faults to have a number of small-scale increases and decreases in throw values within the larger macro-scale trend.

Our study comprises: L-type (43%); C-type (22%); L/M-type (13%); C/M-type (11%); M-type (6%); Z-type (4%); and C/Z-type (1%) (Figure 3.12), examples of which are illustrated in Figure 3.13.

3.5.4 Throw profile trends

Faults with L-type and L/M-type throw versus depth profiles, that have greater throw values skewed towards the lower third of the PFS tier, dominate the sample population. The L-type and L/M-type fault profiles typically span the full height of the tier and are often characterised by a marked increase in the amount of throw within the Brygge Formation. In contrast to the L-type and L/M-type faults, many of the C-type and M-type faults that comprise our sample population do not span the entire height of the tier (e.g. NGull-001, NGull-002, NGull-006, NGull-012, NGull-040) and they do not exhibit systematic patterns that can be traced from one fault to another.

Faults in the northern part of the study area are hosted in a thinner sequence of fine-grained sediments and are typically smaller in height than those found in the south of the study area. The faults located in the north of the study area have more symmetrically shaped throw profiles (Figure 3.14) than those found in the rest of the study area (Figure 3.3). The northern faults also span a different stratigraphic wedge within the Kai Formation compared to the faults found in the rest of the study area (Figure 3.3 A). Faults in the central part of the study area exhibit L/M-type throw profiles with quasi-linear trends within the Kai and Naust Formations, respectively,

where shallower throw gradients are observed within the Kai Formation compared to steeper throw gradients in the overlying Naust Formation and underlying Brygge Formation (Figure 3.15 & 3.16). The quasi-linear L/M-type trends within the Kai and Naust Formations and the accentuated bulging throw profile within the Brygge Formation exhibited on faults found in the central region of the study area grade into L-type throw profiles in the south and southeast of the study area, where throw profiles exhibit near-linear gradients from the upper fault tip to the top of Brygge Formation or in some cases to the locus of maximum throw (T_{max} position) (Figures 3.17 & 3.18). The grading of fault throw distributions and wedge-shaped stratigraphy can be traced across throw profiles that are superimposed on seismic cross-sections, such as those presented in Figure 3.3.

All of the 53 fault throw profiles exhibit some degree of small-scale fluctuations in throw values, where the throw increases and decreases by a few milliseconds within a macro-scale trend. Some of these small-scale steps in the throw profile can be seen across several faults. For example, a minor decrease in throw can be observed beneath the opal-A/CT marker at ~800-900 ms below the seafloor on several polygonal faults. However, most of the small-scale throw fluctuations on the upper portions of the fault profiles cannot be traced across the entire study area but they can sometimes be observed at the same horizon on neighbouring faults, such as the increase in throw by ~2 ms from the 1.934 Ma to the 1.775 Ma horizon on NGull-047 and NGull-048 (Figure 3.17).

3.5.5 Scaling relationships and spatial distributions

The faults with the greatest maximum throw values are found in the south of the area (Figure 3.9 A) where the tier is thickest and the faults are tallest (Figures 3.3 & 3.9 F). The PFS conforms to the global scaling relationship established by Shin et al. (2010), with maximum throw values ranging between 1.8-7.8% of the fault height with

a mean of 4.0% (Figure 3.19). There is no apparent clustering of faults with high or low *maximum throw to fault height* ratios across the study area (Figure 3.9 B). The vertical location of the locus of maximum throw is predominantly found in the lower portion of the faults (Figure 3.9 C). However, a smaller number of C-type faults in the north of the study area have loci of maximum throw values located closer to the central portion of the fault.

3.5.6 Throw at temporal markers

The throw values recorded at the 2.61 m.y. horizon broadly increase from north to south across the study area in a similar fashion to the trend of maximum throw values. Faults with the greatest recorded throw values at the 2.61 Myr horizon also have greater than average maximum throw to fault height ratios, however, these faults do not exhibit any systematic spatial clustering. The displacement of the opal-A/CT diagenetic boundary, which fossilised at around the same time as the deposition of the top Kai horizon (Neagu et al., 2010b), suggests that the faults have accumulated significant magnitudes of throw in their lower portions since the late Pliocene (Figure 3.20) (Neagu et al., 2010a). However, like Neagu et al. (2010a), we find no apparent systematic trend between the amount of throw at the opal-A/CT boundary and the amount of throw in the sediments that post-date the late Pliocene.

3.5.7 Upper and lower tip gradients

The upper and lower tip gradients of faults in our sample population range between 0.024-0.194 and 0.076-0.415, respectively, where the mean upper tip gradient is 0.069 and the mean lower tip gradient is 0.208. There is no apparent spatial clustering of faults with high or low upper tip gradients (Figure 3.9 G), however, lower fault tip gradients generally increase from north to south across the study area (Figure 3.9 H). The north-south increasing trend of lower tip gradients correlates strongly with

increasing maximum throw values on the largest faults that are found in the south of the study area, where the tier is at it thickest.

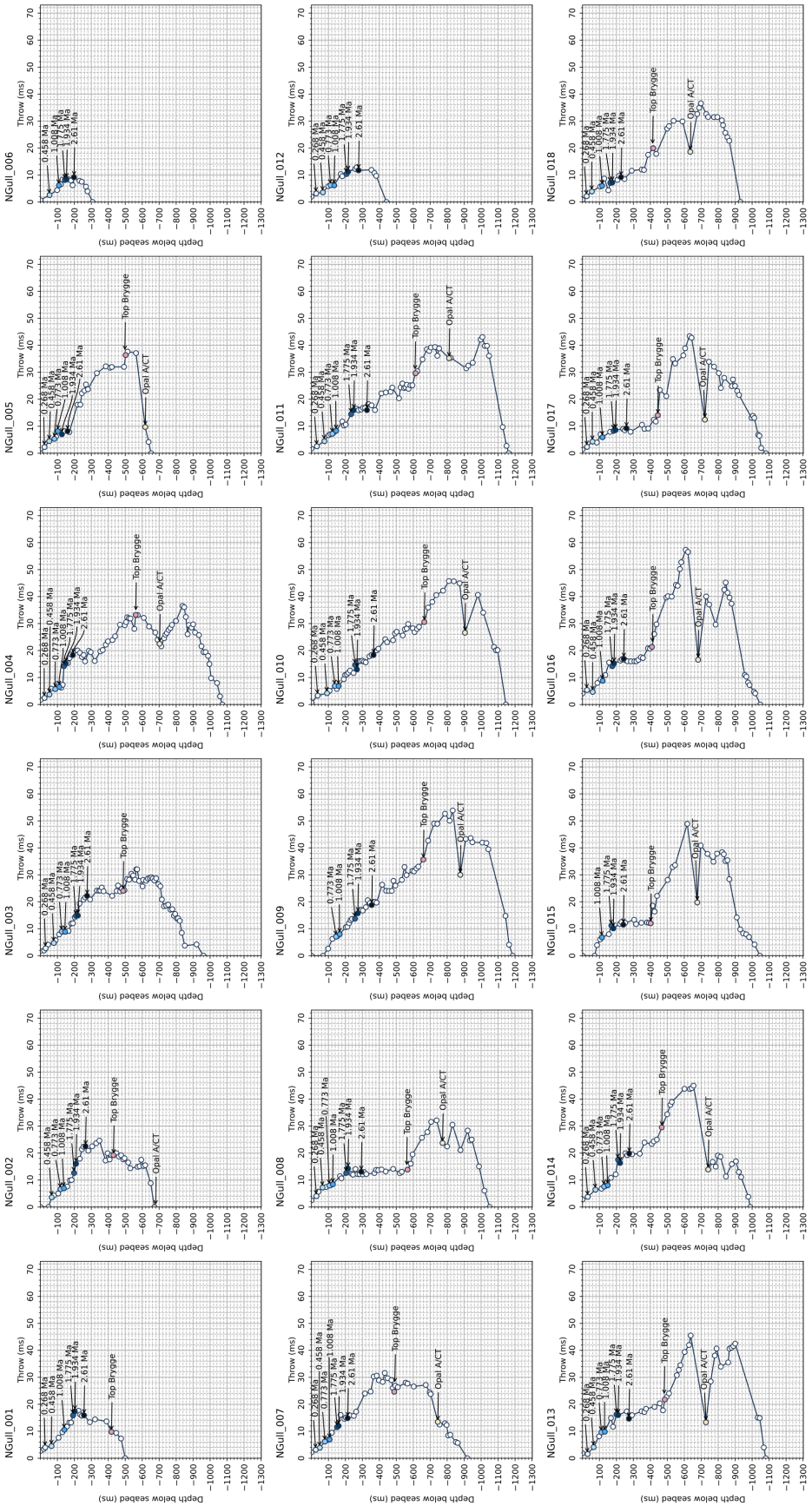


Figure 3.6: Throw versus depth plots with throw values labelled at age-dated horizons, the top of the Brygge Formation, and the Opal A-CT boundary. [1 of 3]

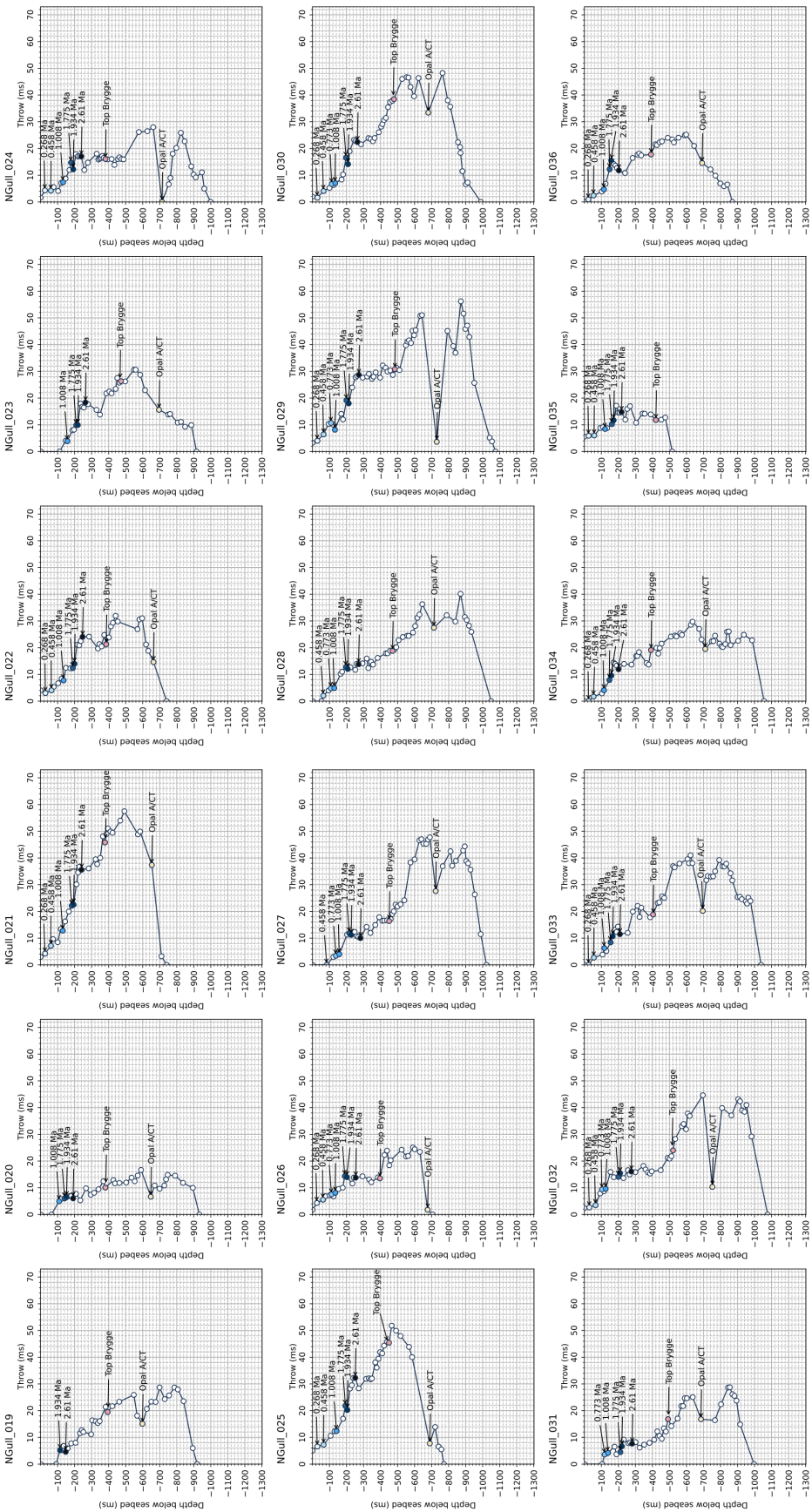


Figure 3.7: Throw versus depth plots with throw values labelled at age-dated horizons, the top of the Brygge Formation, and the Opal A-CT boundary. [2 of 3]

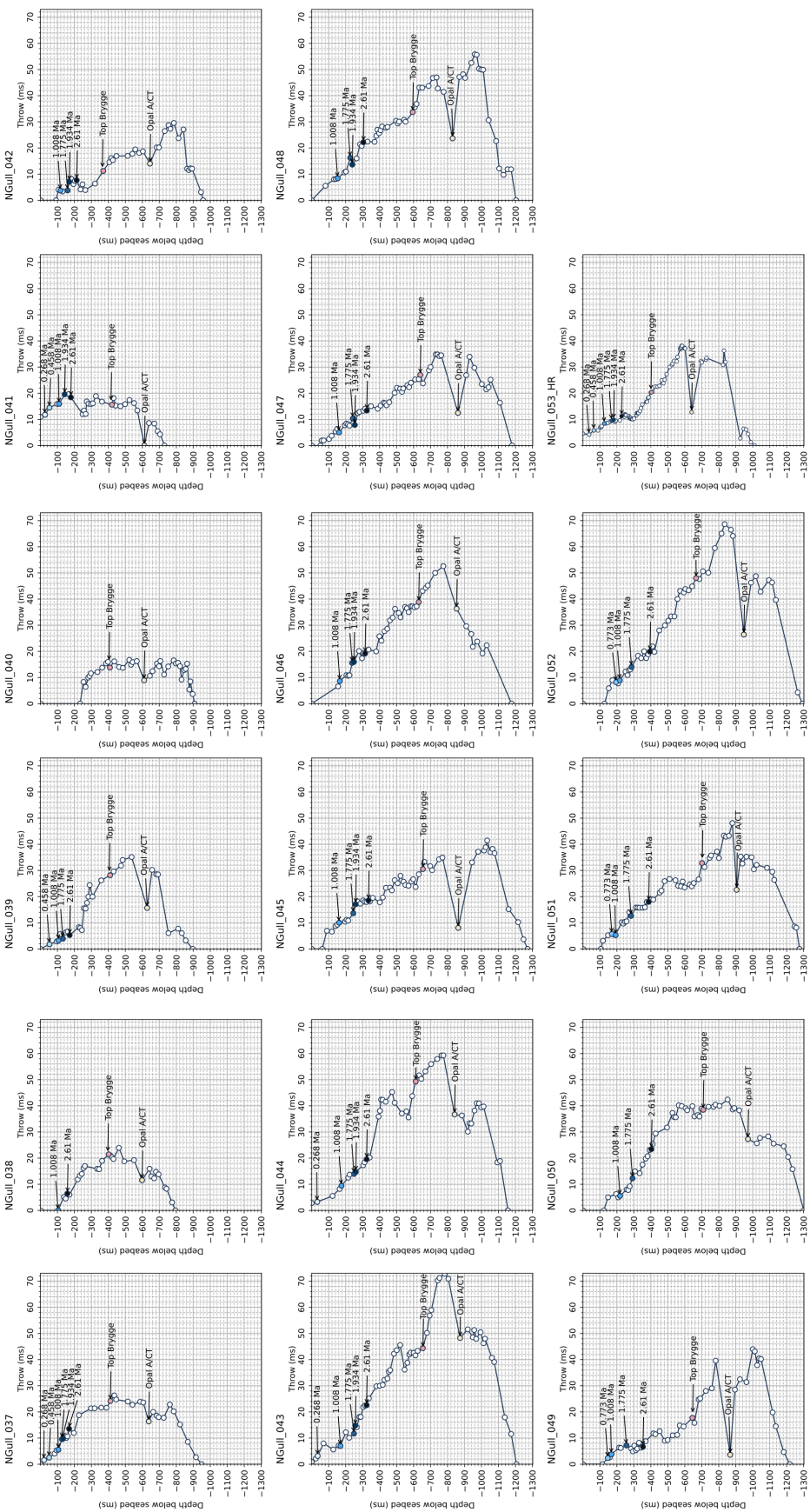


Figure 3.8: Throw versus depth plots with throw values labelled at age-dated horizons, the top of the Brygge Formation, and the Opal A-CT boundary. [3 of 3]

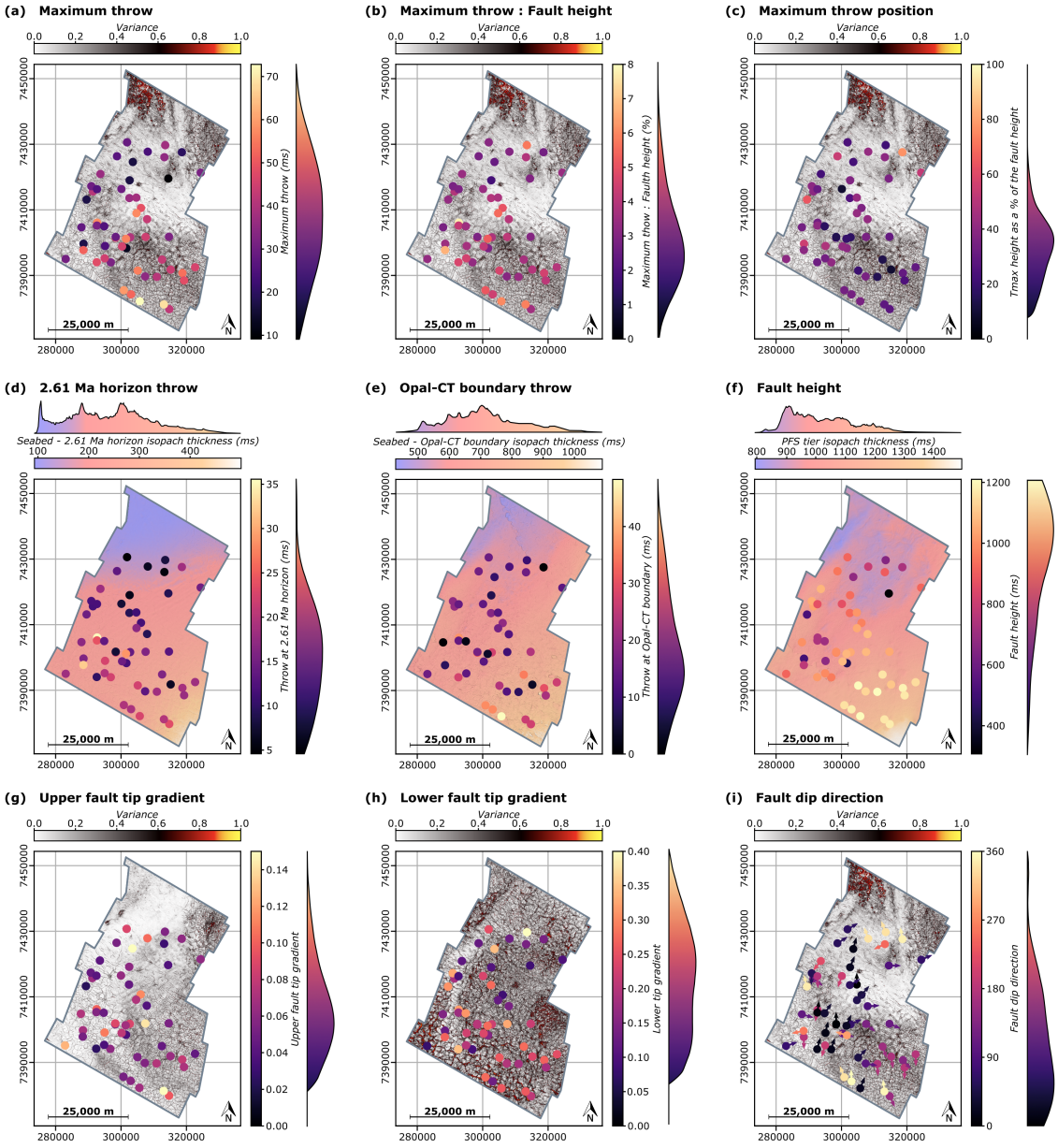


Figure 3.9: (a) Maximum throw values of polygonal faults across our study area. (b) Maximum throw values as a percentage of the fault height. (c) The height of the maximum throw position with respect to the height of the fault. (d) Throw at the 2.61 Ma horizon, overlain on an isopach thickness map between the seafloor and the 2.61 Ma horizon. (e) Throw at the opal-CT boundary, overlain on an isopach thickness map between the seafloor and the Opal-CT boundary. (f) Fault height values, overlain on an isopach thickness map of the PFS tier. (g) Upper fault tip gradients. (h) Lower fault tip gradients. (i) Fault dip direction. Figures (a), (b), (c), and (i) overlay a variance timeslice at -2075 ms. Figures (g) and (h) overlay variance timeslices at -2000 ms and -2500 ms respectively. Probability density distributions are presented at the edge of each subplot. T_{max} = maximum throw.

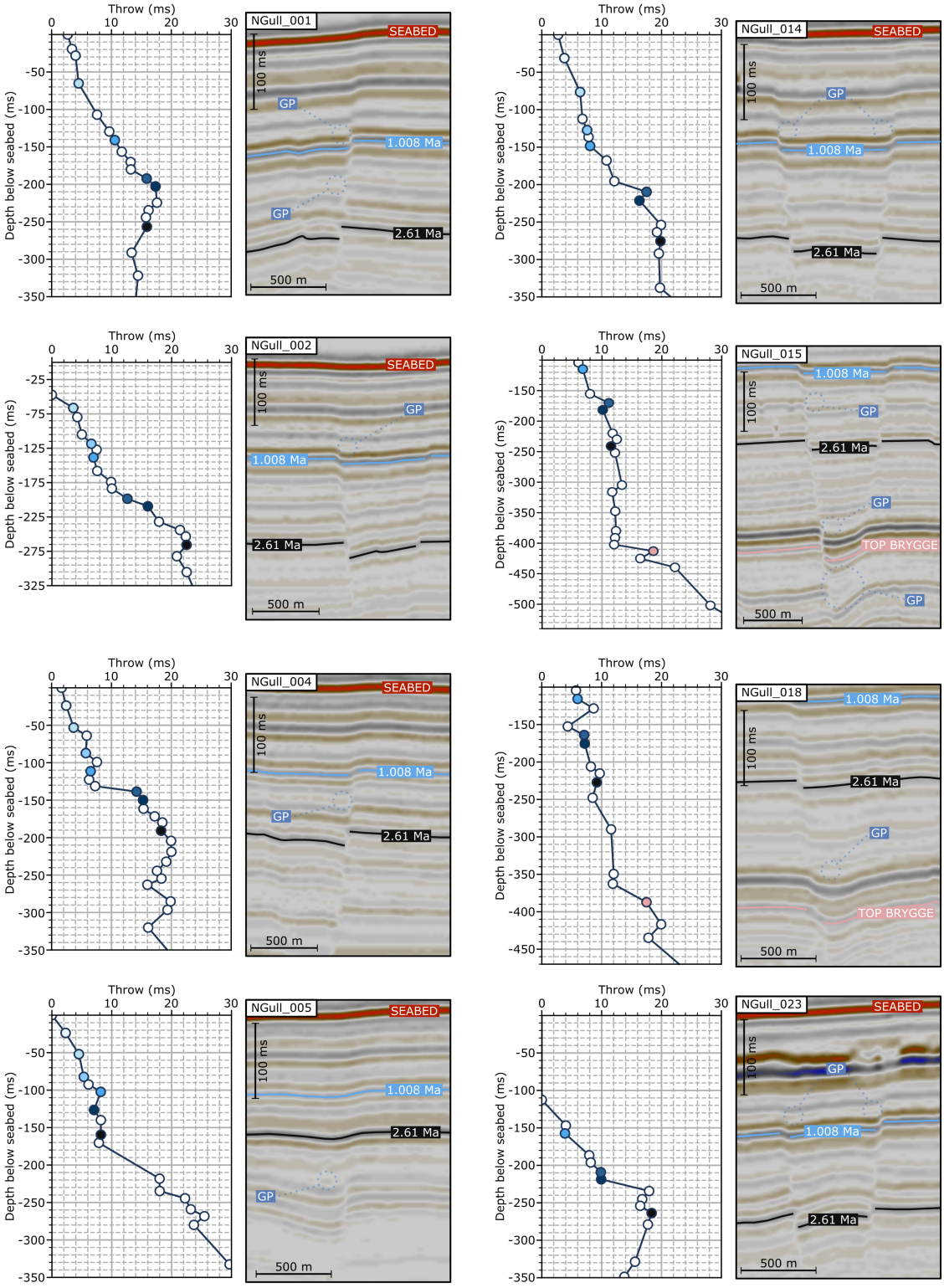


Figure 3.10: A selection of growth packages and accompanying throw-depth plots from faults within the BG0904 seismic reflection survey [1/2].

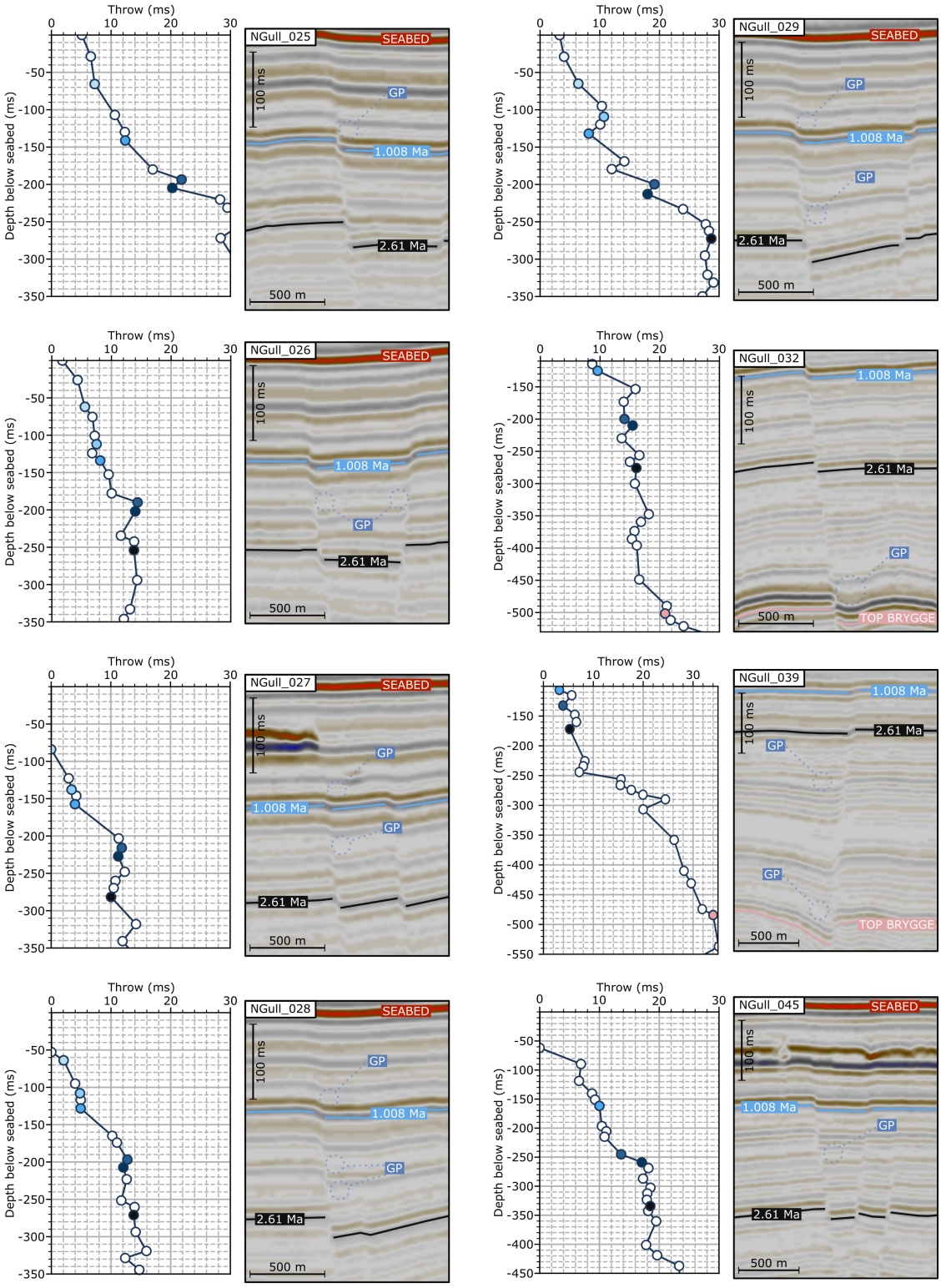


Figure 3.11: A selection of growth packages and accompanying throw-depth plots from faults within the BG0904 seismic reflection survey [2/2].

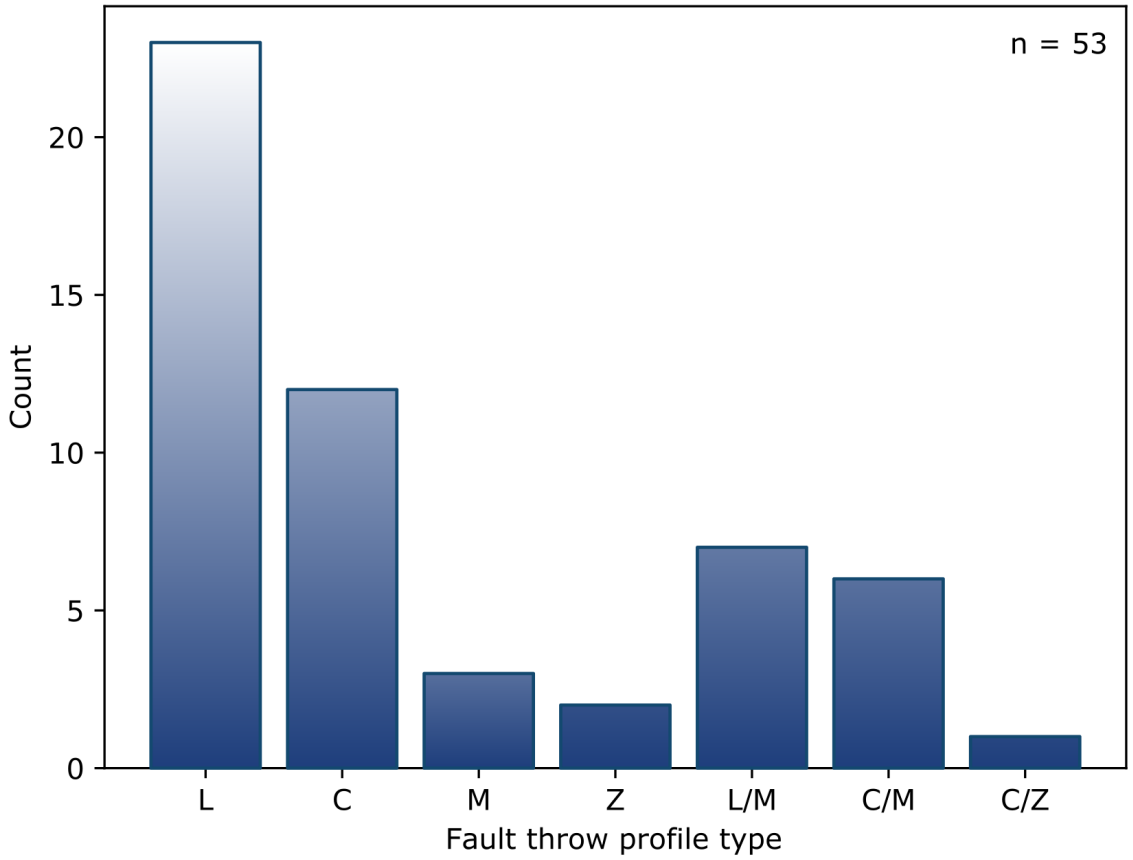


Figure 3.12: Bar chart showing the frequency of fault types within the fault sample population.

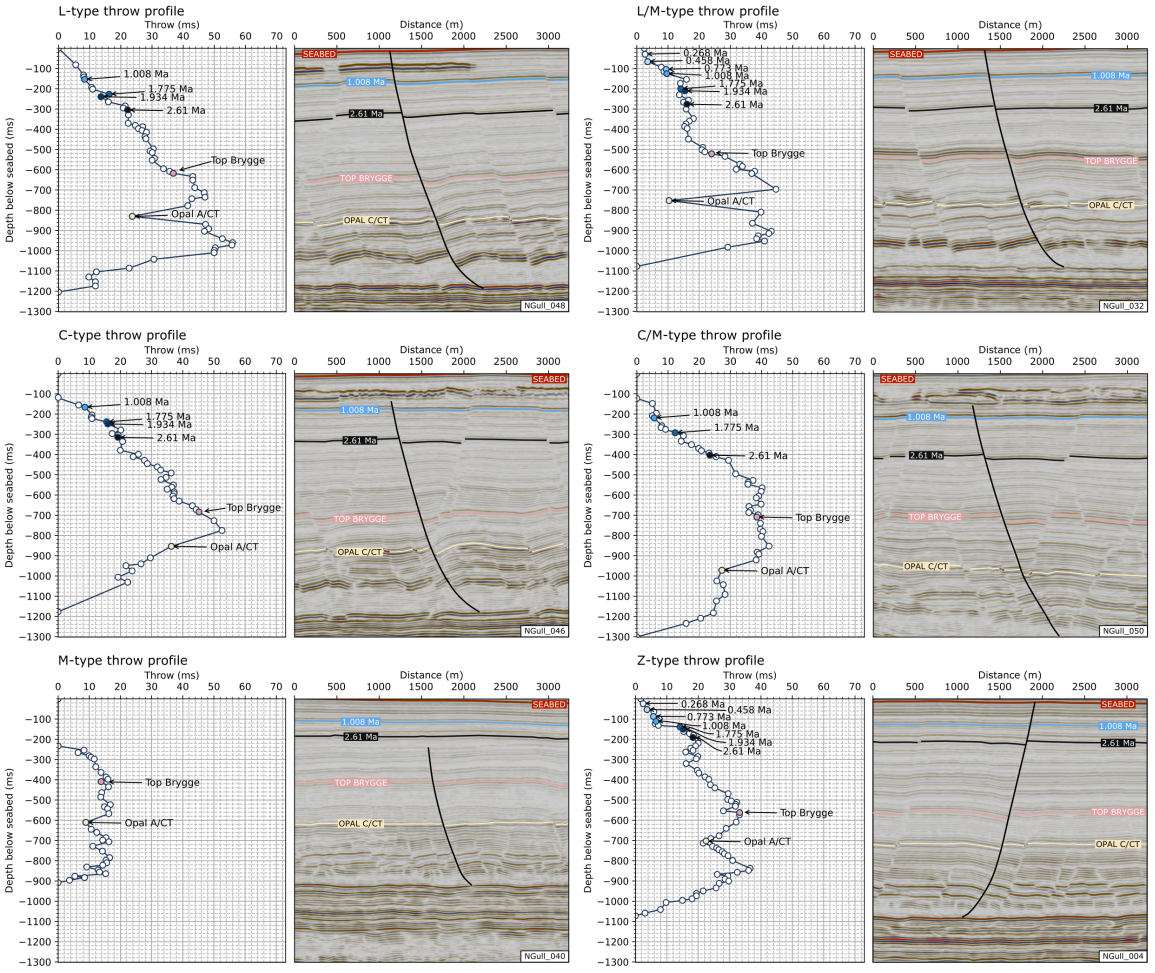


Figure 3.13: Examples of throw versus depth profiles and accompanying seismic reflection cross-sections for L-type, C-type, M-type, L/M-type, C/M-type, and Z-type faults from the study area.

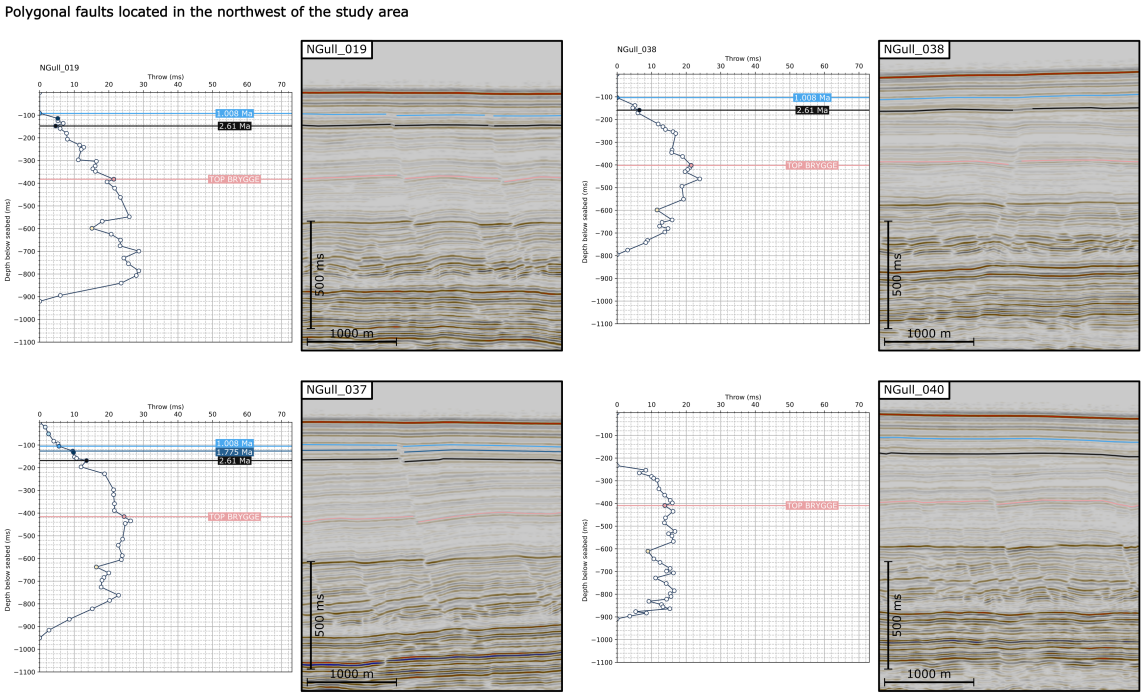


Figure 3.14: Throw-depth profiles with accompanying seismic reflection cross-sections and marker horizons for faults in the northwest of the study area. Faults NGull-037 and NGull-038 exhibit broadly symmetrical C-type profiles. NGull-040 has an upper tip which terminates within the upper Kai Formation and has a broadly M-type profile. NGull-019 has an L-type profile.

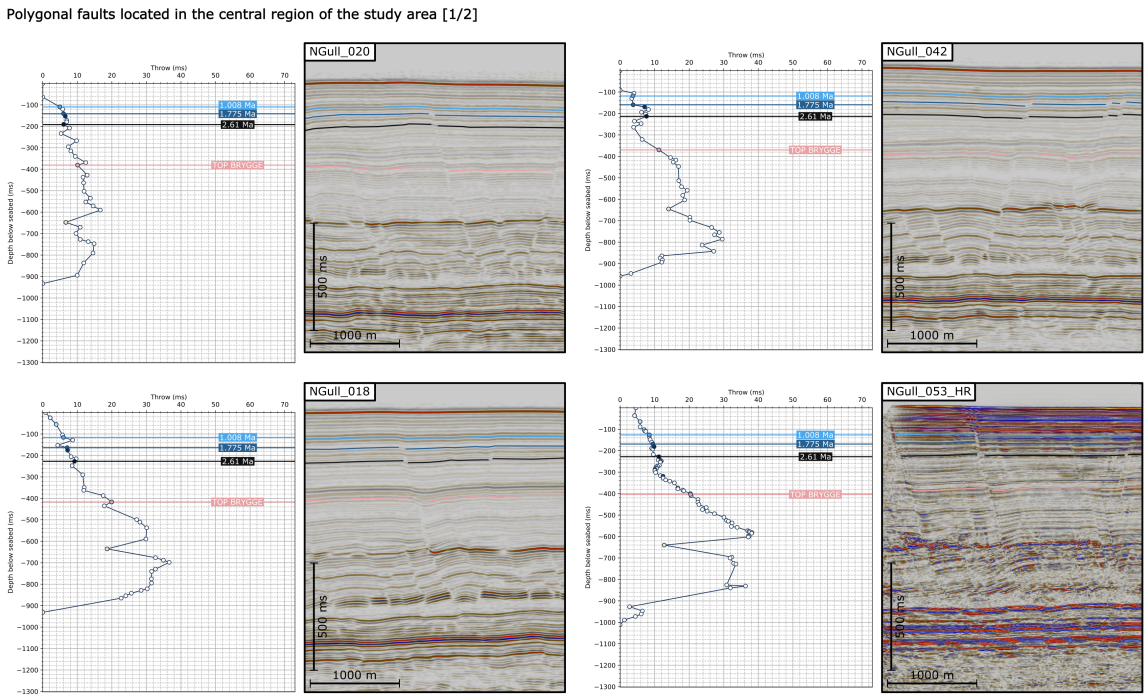


Figure 3.15: Throw-depth profiles with accompanying seismic reflection cross-sections and marker horizons for faults in the central part of the study area [1/2].

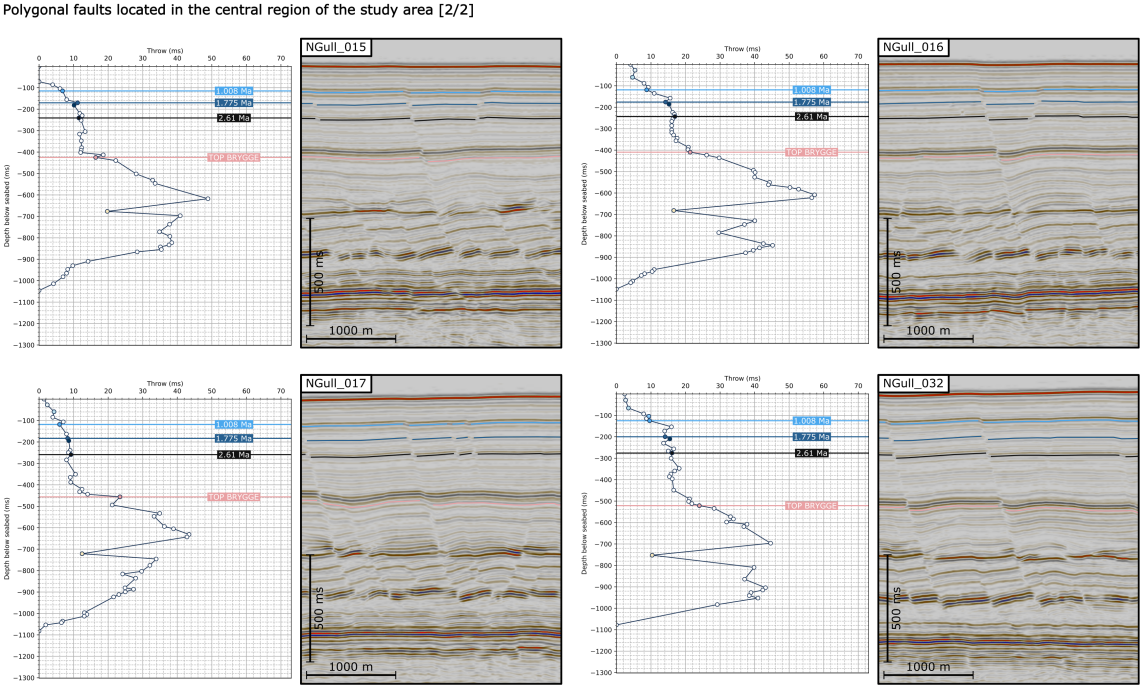


Figure 3.16: Throw-depth profiles with accompanying seismic reflection cross-sections and marker horizons for faults in the central part of the study area [2/2]. All four faults exhibit L/M-type profiles, with near zero gradients in the interval above the top Brygge and lowermost Naust.

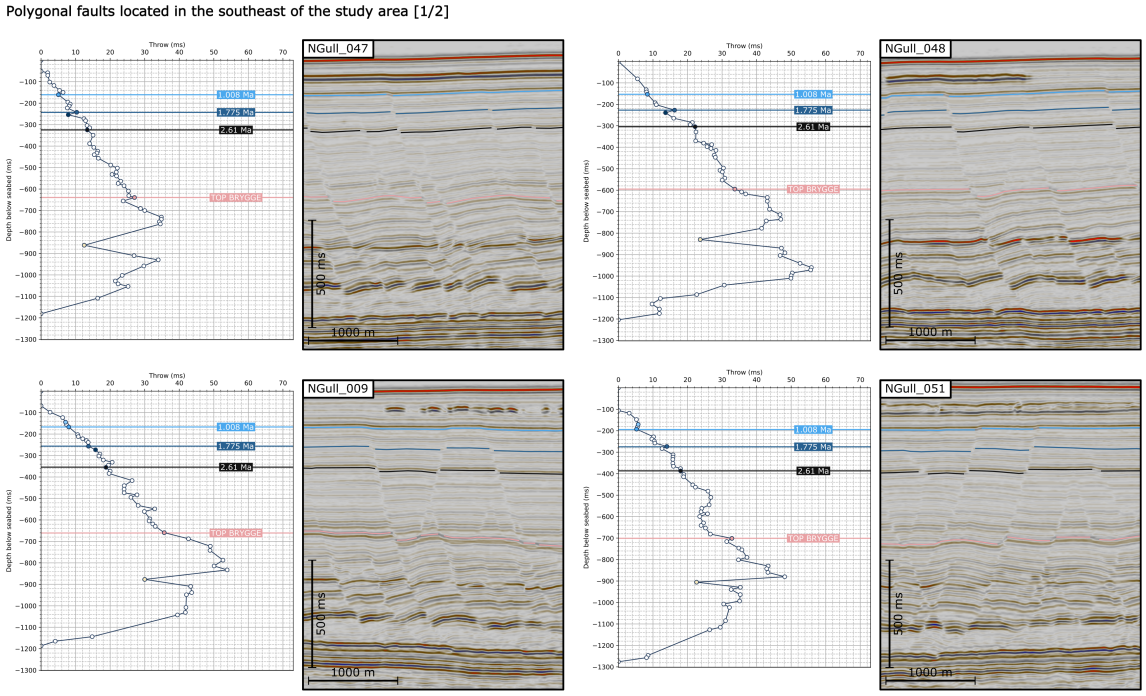


Figure 3.17: Throw-depth profiles with accompanying seismic reflection cross-sections and marker horizons for faults in the southeast of the study area [1/2].

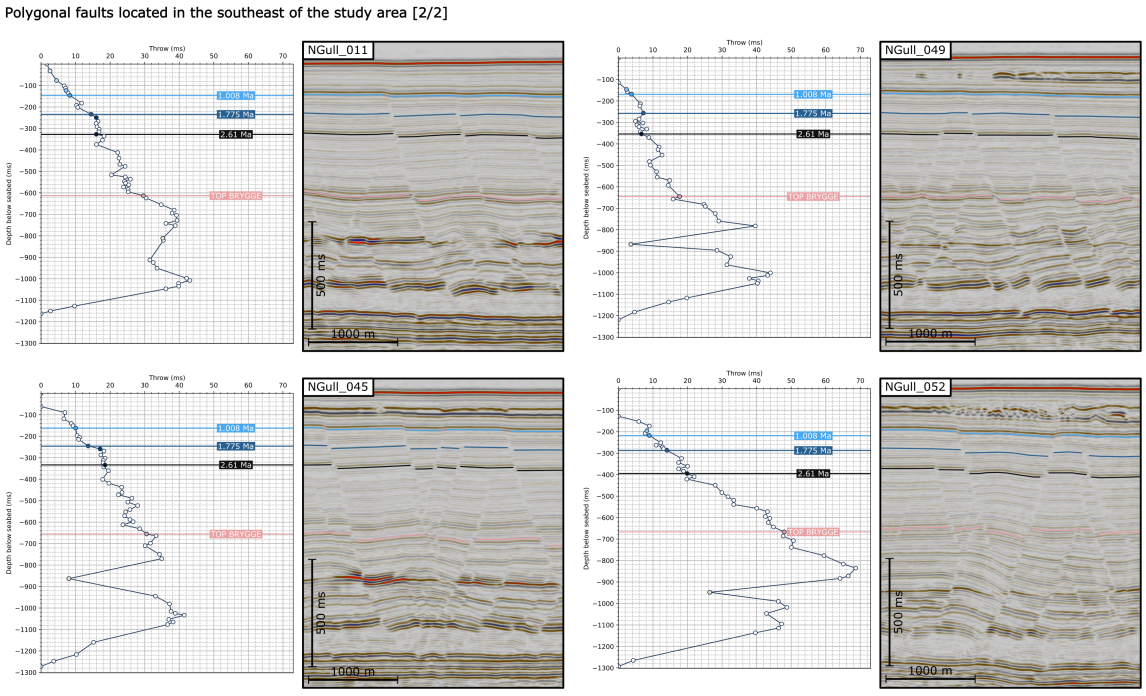


Figure 3.18: Throw-depth profiles with accompanying seismic reflection cross-sections and marker horizons for faults in the southeast of the study area [2/2].

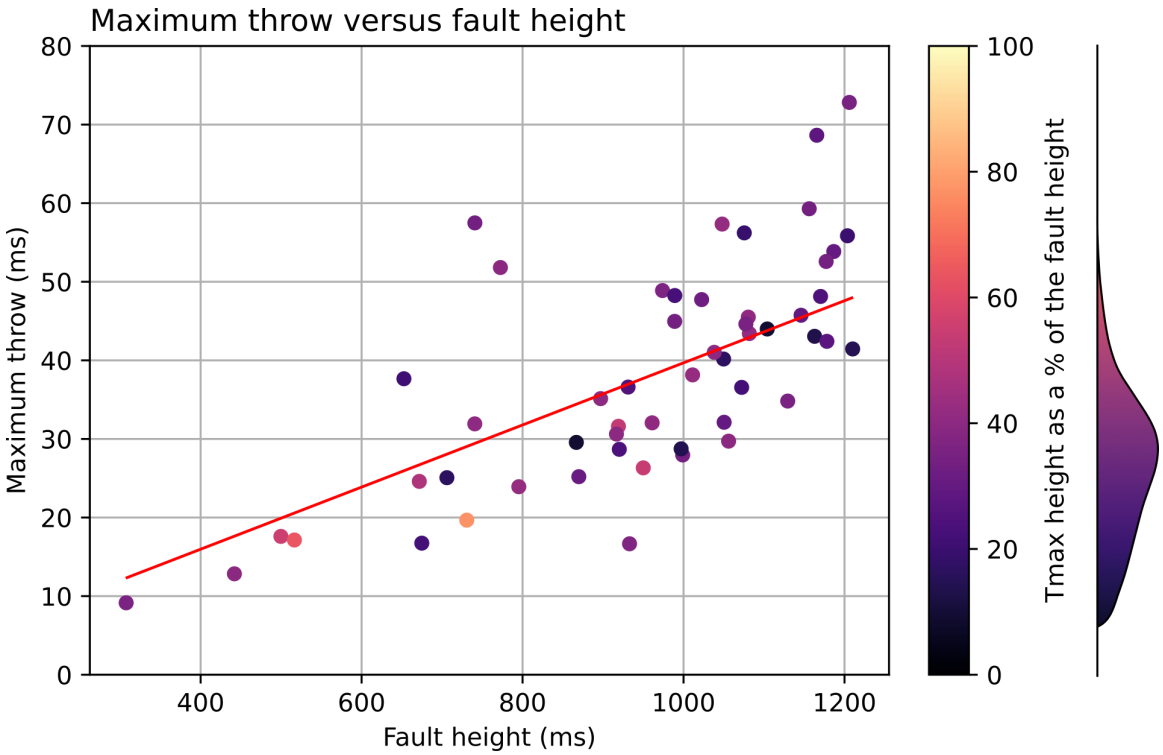


Figure 3.19: Maximum throw versus fault height for all 53 faults analysed in our study. The red line represents the mean ratio (i.e. a maximum throw value equal to 3.96% of the fault height). Points are coloured with respect to the height of the maximum throw location as a percentage of the fault height. Note that faults with smaller heights have higher T_{max} positions closer to the central section of the fault. T_{max} = maximum throw.

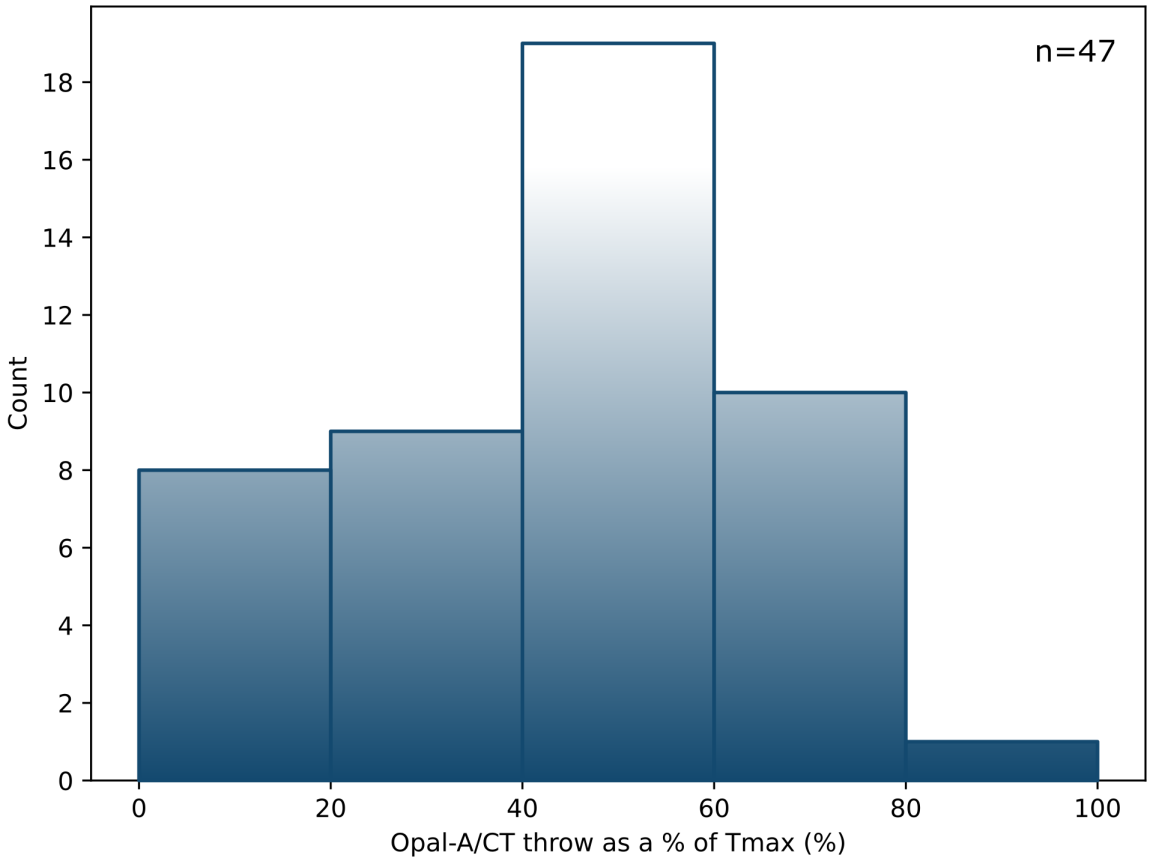


Figure 3.20: Histogram of throw at the opal-A/CT reflection boundary as a percentage of the maximum throw value (T_{max}) recorded on the fault. Note that the minimum = 0%, maximum = 82%, and mean = 43%.

3.6 Discussion

The large number of throw measurements recorded along the height of each polygonal fault in our sample population illuminated a number of patterns that are correlatable across the wedge-shaped stratigraphy of the PFS tier. The shape of throw versus depth profiles provide a useful diagnostic to interpret both the slip history of a fault and the mechanical competency of the faulted geological units (Muraoka and Kamata, 1983; Cartwright et al., 1998). Coupling the insights derived from the spatial analysis of throw versus depth plots with those derived from temporal markers within the PFS tier, such as: the offset opal-A/CT boundary; chronostratigraphically calibrated horizons in the uppermost portions of the tier; and observable growth packages, enable the kinematic growth history of the polygonal fault system to be constrained.

3.6.1 Temporal and kinematic evolution of the PFS

Three key factors enable the later stages of the growth of the PFS to be temporally constrained. Firstly, the chronostratigraphic calibration of the upper 250 metres of the tier provided by ODP hole 644 and the geological formation boundaries provided by industry well 6604/2-1 (Figure 3.4) constrain the age of the sediments that host the PFS. Secondly, the series of small growth packages within the upper portions of the PFS tier (Figure 3.10 & 3.11) indicate that the upper tips of the PFS have intersected or been in close proximity to the seabed since at least the late Pliocene and that the PFS has propagated upward with sedimentation over this time period. Furthermore, the absence of large syn-sedimentary wedges in the fault hanging walls suggests that the polygonal faults have propagated at a rate approximately equal to the sedimentation rate and that the rate of throw accumulation has not outpaced sedimentation. This propagation inference is in agreement with the propagation model suggested by Goulty (2001a), where fault propagation can be driven by gravitational loading

in sediments with high K_0 values and low coefficients of residual friction. Thirdly, the diagenetic opal-A/CT boundary, which fossilised in the late Pliocene around the time of deposition of the top Kai horizon (Brekke et al., 2000; Neagu et al., 2010b), post-dates the stratigraphic offset in the lower portion of the PFS tier, and therefore, offset at the opal-A/CT boundary implies that fault throw has accrued over the entire vertical extent of the polygonal fault planes since at least the late Pliocene (Neagu et al., 2010a). These three factors suggest that the PFS has been active at, or in close proximity to, the seafloor from at least the late Pliocene, since when the polygonal faults have propagated upwards with sedimentation.

One of the most striking findings from this study is the consistency with which throw profile gradient changes can be traced between neighbouring master faults across the study area (Figures 3.3, 3.14, 3.15, 3.16, 3.17, & 3.18). The predominately L-type master faults are characterised by throw profiles that commonly exhibit a prominent change in gradient that occurs close to the stratigraphic boundary separating the Kai and Brygge Formations. The faults situated closest to well 6604/2-1 in the central region of the study area have throw gradient changes that correlate with changes in lithology and bulk density that occur close to the Naust-Kai and Kai-Brygge Formation boundaries, respectively (Figures 3.3, 3.4, 3.15, & 3.16) (BG Group, 2012). The predominance of L-type throw profiles amongst the master polygonal faults, which have greater amounts of throw in the lower portions of the faults, also suggest that the PFS propagated upwards from the basal section of the tier, where throw has accumulated synchronously with upward propagation in association with a fixed or detached lower tip (c.f. Nicol et al. (1996)). The steeper lower tip gradients compared to shallower upper tip gradients suggest that much of the differential volumetric strain associated with the accommodation of fault displacement in laterally-pinned strata has occurred in the lower portion of the tier (Cartwright, 2011). The smaller subordinate polygonal faults within the tier may have experienced

different growth histories to those of the largest tier-spanning master faults, that have formed the focus of this study, where their continued propagation and growth was likely inhibited by fault intersections.

Given that throw has accrued over the vertical extent of the polygonal master faults throughout their upwards propagation, the throw values recorded at any given unit are therefore a measure of both the differential vertical strain of the unit and the differential vertical strain over the underlying units. The reduction in the throw gradient above the top Brygge may be the result of a reduction in the amount of differential vertical strain achievable in the sedimentary units found in Kai and Naust Formations compared to the Brygge Formation and/or a reduction in the amount of differential vertical strain occurring in the units that comprise the Brygge Formation during the continued growth of the PFS simultaneously with deposition of the Kai and Naust Formations. The changes in the throw gradients do not appear to coincide with clear erosional surfaces within the study area, however, it is possible that erosion during depositional hiatuses between the Brygge, Kai, and Naust Formations may account for some steps observed on the throw profiles of surface-breaching polygonal faults.

The differences between the porosity and bulk density properties of the claystone rich Naust and biosiliceous oozes of the lower Kai and upper Brygge Formations may explain the steeper throw gradients observed in the Naust interval compared to the Kai interval on many of the polygonal faults located in the central region of the study area. Similarly, the differences between the throw profiles of faults found in the north of the study area compared to the south of the study area may be related to physical property differences between the units that comprise the different stratigraphic wedges found within the tier. Throw gradients recorded at the uppermost tips of some polygonal faults imaged at the resolution limits of the three-dimensional seismic data may also be attributed to upper tip monoclines associated with upward propagating

fault tips that track sedimentation a few tens of metres below the seabed. These upper tip gradients are unlikely to be associated with pelagic drape above an arrested fault tip because the Naust Formation was deposited by hemipelagic and/or contouritic processes (Ottesen et al., 2009).

The throw gradient changes at or close to the Kai-Brygge Formation on the faults found in the central region of the study area may also be associated with a change in physical properties between the Kai and Brygge Formations (Bulk Density log, Figure 3.4). Alternatively, the reduction in the throw gradient within the Kai Formation compared to the Brygge Formation may be related to a temporal change in the amount of differential vertical strain in the lowermost units of the tier during earlier and later phases of PFS growth, respectively. A decrease in the amount of differential vertical strain during simultaneous deposition and fault propagation of the Kai Formation could be associated with the fossilisation of the opal-A to opal-CT transition. The greater amounts of throw in the Brygge Formation may be explained by an enhanced period of early growth driven by diagenetically-induced volumetric strain associated with the transition of opal-A to opal-CT (Cartwright, 2011; Davies and Ireland, 2011). The shallowing of the fault plane dips associated with diagenetic compaction may also reduce the amount of differential vertical strain that occurs in the lowermost units of the tier in the later stages of fault growth (Neagu et al., 2010a). Alternatively, the claystones in the base of the Brygge Formation may have experienced an initial phase of faster compaction before reaching a slower compaction plateau at a burial depth that coincided with slower sedimentation rates during the deposition of the Kai Formation. It is also possible that changes in the throw profile gradients may be associated with local variations in the fault friction angle. An investigation into the influence of different compaction profiles, fault dips, and residual friction angles on the accrual of polygonal fault throw forms the focus of Chapter 5.

Within the macro-scale throw profile gradients there are a series of small-scale

throw profile steps that in some cases can be traced across many of the faults across the study area. The most widespread of these small-scale patterns is found between the opal-A/CT boundary and the lower fault tip, where the throw decreases markedly in a small interval situated above a higher amplitude reflection in the lower Brygge Formation (NGull-015, NGull-016, NGull-017, NGull-032, NGull-042, NGull-048, NGull-051, NGull-052, Figures 3.14, 3.15, 3.16, 3.17, & 3.18). Most of the small-scale throw profile steps are associated with neighbouring fault intersections or the partitioning of strain on adjacent fault segments. Small throw gradient steps in the upper portions of polygonal faults are not found systematically at the same reflections across the entire study area, although some small-scale steps can be found on neighbouring faults. Small-scale increases in the amount of throw in the upper tip portions of some faults (e.g. throw at the 1.775 Ma horizon on neighbouring faults NGull-047 and NGull-048) may also reflect intra-formational differences in the compressibility of layered units (Figure 3.5). Alternatively, small-scale intervals in the upper tip regions with zero throw gradients may be interpreted as short periods of growth inactivity, because these small stasis intervals do not systematically coincide with stratigraphic horizons. However, the majority of departures from linear throw profiles are associated with strucutal complexities such as, conjugate and antithetic faults (NGull-017, NGull-052), fault relays (NGull-053), and drag (NGull-016, NGull-017).

The precise onset and trigger of PFS nucleation remains elusive, however, growth packages at the top Brygge horizon suggest that the PFS had formed before the early Miocene and the absence of polygonal faults in the Tare Formation indicate its initiation post-dates the late Paleocene. Our observations support previous studies which suggest the onset of PFS nucleation occurs in the early phases of burial within a few tens to hundred of metres of the seafloor (Cartwright et al., 2003; Morgan et al., 2015). It is possible that the early nucleation of the PFS tier within the study area may be related to diagenetically-induced volumetric strain associated with the opal-A

to opal-CT transition as computationally modelled by Roberts et al. (2014).

In summary, the kinematic growth history of the master faults within the PFS likely involved: (1) an initiation phase in the late Paleocene to early Miocene, where the system nucleated within a few tens to hundreds of metres of the paleo-seafloor; (2) an early phase of radial tipline propagation; (3) a period of lower and lateral fault tip abutment, where the lower tips arrested at a basal boundary and the lateral tips began to intersect neighbouring faults; (4) a period of upward fault propagation that continues to the present day, where the upper fault tip positions closely track the seafloor - sometimes developing small growth packages in the fault hanging walls. Throw appears to have accrued over the entire vertical extent of the fault planes throughout propagation. This upward kinematic growth model is consistent with that proposed by Morgan et al. (2015), who used the relationship of perturbed polygonal fault orientations with respect to temporally constrained pockmarks to infer an upward propagation history in the Lower Congo Basin PFS. The computational investigation of polygonal faults that forms the focus of Chapter 5 uses this upwards kinematic growth model to investigate the drivers of throw accumulation in laterally pinned conditions.

3.7 Conclusions

This study comprises a spatial, temporal, and kinematic investigation of polygonal faults located within the northern Vøring Basin in close proximity to ODP well 644 and industry well 6604/2-1. This analysis suggests that the PFS has propagated upward for much of its growth history, where master faults have been active at, or within a few tens of metres of, the seabed from at least the late Pliocene. The throw profiles of the polygonal master faults exhibit macro-scale gradient changes that may be the result of temporal changes in the amount of differential volumetric strain occurring at depth and/or differences in the mechanical properties of strata that comprises the PFS host tier. Small-scale steps observed on the throw profiles may represent short periods of growth inactivity and/or differences in the intrinsic physical properties of the intra-formational units.

Chapter 4

Ultra-Slow Throw Rates of Polygonal Fault Systems

This chapter was published in the 48th volume of Geology on 1st May 2020. This published chapter has an accompanying *Supplementary Material* file that outlines the chronostratigraphic calibration alongside seven supplementary figures and can be found in Appendix A. This *Supplementary Material* is available on the online GSA Data Repository (item 20200139) at http://www.geosociety.org/datarepository/2020/.

King, J. J., & Cartwright, J. A. (2020). "Ultra-slow throw rates of polygonal fault systems". *Geology*, 48(5), pp. 473-477. doi.org/10.1130/G47221.1

4.1 Abstract

Polygonal Fault Systems (PFSs) are an enigmatic class of small non-tectonic extensional faults. PFSs are predominantly hosted in fine-grained sedimentary tiers and are prevalent along many continental margin basins. The genesis of PFSs is widely debated and little is known about the time frame for polygonal fault growth. We present the first measurements of throw rates for polygonal faults by measuring the vertical offset of seven age-calibrated horizons mapped using three-dimensional seismic reflection data from the Norwegian Sea. Individual polygonal faults exhibit a range of throw rate profiles through time, ranging from near linear to singly or multiply stepped. The stepped profiles have a range of short-term throw rates ranging from 0 to 18 m/m.y. Time-averaged throw rates of 180 polygonal faults over the entire 2.61-0 Ma interval are normally distributed and range between 1.4-10.9 m/m.y. We convert our PFS throw rates to displacement rates and compare these to published displacement rates for gravity driven and tectonic normal faults. We find that the displacement rates of polygonal faults mark the lower limit of a continuous spectrum of extensional fault displacement rates; they are as much as two orders of magnitude slower than those of gravity-driven faults, and as much as three orders of magnitude slower than those of the fastest-growing tectonic faults. We attribute the ultra-slow kinematic behaviour to the nontectonic nature of polygonal faults, where throw accumulates primarily through dewatering of the largely fine-grained sediments comprising the host layers for the PFS, and differential volumetric strain between the fault footwalls and hanging walls.

4.2 Introduction

First identified as intra-formational faults within Eocene and Oligocene claystones of Belgium over 30 years ago (Henriet et al., 1988), polygonal faults are now recognised in over >150 basins worldwide, where they commonly extend over vast areas of $\sim 10^5 - 10^7$ km^2 (Cartwright et al., 2003; Cartwright, 2011). Polygonal Fault Systems (PFSs) have attracted considerable attention in recent years, partly because of their ubiquity in many fine-grained slope depositional systems, but also because of their importance as sealing sequences for petroleum, CO_2, and high grade nuclear waste (Cartwright, 2011). Polygonal faults can also be used to guide the search for deep-water clastic reservoirs (Jackson et al., 2014; Turrini et al., 2017). More fundamentally, PFSs are interesting as structures because they are a challenge for classical soil mechanical theory in that they form during early burial, under conditions of net zero lateral strain, yet represent shear failure of unconsolidated granular materials (Shin et al., 2010).

The structural characteristics of PFSs are well documented (see Cartwright (2011) and references therein). PFSs are developed in 'tiers', as laterally extensive arrays of layer-bound nontectonic normal faults. These arrays are typically characterised by multi-directional fault patterns in planform, hence the name 'polygonal fault systems'. Throw profiles on individual polygonal faults are relatively well documented from a number of different PFSs and exhibit similar variations to those seen on many small tectonic normal faults, albeit with modified forms due to the complex three-dimensional (3-D) intersection geometries resulting from the polygonal architecture (Nicol et al., 2003; Stuevold et al., 2003; Neagu et al., 2010a; Wrona et al., 2017). An empirical scaling relationship has been suggested for PFSs between the maximum throw and the height of a polygonal fault, where maximum throw values are around ~3-6% of the fault height (Shin et al., 2010).

Although the processes that govern the nucleation and propagation of polygonal faults are generally considered to be unrelated to far-field tectonic stresses (Cartwright et al., 2003; Goulty, 2008; Verschuren, 2019), there is as yet no agreement on their precise genetic evolution. Suggested mechanisms include gravity sliding, density inversion, overpressure, gravitational loading, and diagenetically-induced shear failure (Cartwright et al., 2003; Goulty, 2008; Cartwright, 2011; Verschuren, 2019). Advances in our understanding of PFSs have been hindered in part by a scarcity of field outcrop examples to provide sub-seismic observations of the fault zones and associated minor structures (Tewksbury et al., 2014; Verschuren, 2019). An additional, important unconstrained parameter to date has been the lack of any direct measurements of throw rates of polygonal faults.

Here we attempt to bridge this gap in knowledge by presenting the first direct measurements of throw rates for polygonal faults, using an exceptional seismic reflection and well data set from the Norwegian Sea. The key to measuring the throw rates is, firstly, identifying currently active faults, secondly, establishing that they propagated to the seabed at an earlier stage in their evolution, and thirdly, having good age calibration of horizons that are offset by the faults. These criteria are fulfilled by the combination of high-resolution 3-D seismic reflection and borehole data collected by the Ocean Drilling Program (ODP). Our results may not be fully representative of the entire spectrum of PFSs so far identified globally, but they at least provide direct constraints for those attempting to model the evolution of these extraordinary structures.

4.3 Geological Setting

The study area is located within the Vøring Basin on the outer part of the Norwegian continental margin (Figure 4.1 A), and extends over a small area of a laterally extensive PFS tier developed within Eocene-Pliocene hemipelagic sediments (Gay and Berndt, 2007; Ireland et al., 2010; Neagu et al., 2010a). Previous studies of this PFS in nearby areas have described the detailed geometry of the system and its relationship to the stratigraphy (Hansen et al., 2004; Gay and Berndt, 2007; Ireland et al., 2010; Neagu et al., 2010a). The PFS tier is almost uniform in thickness (∼1000 m) across the study area (Figure 4.1 B), but varies in thickness over the rest of the basin. Host strata comprise fine-grained siliceous mudstones and claystones of the Naust, Kai, and Brygge Formations, with a prominent diagenetic phase boundary between opal-A and opal-CT occurring in the lower third of the tier (Figure 4.1 B & 4.1 C) (Ireland et al., 2010; Neagu et al., 2010a).

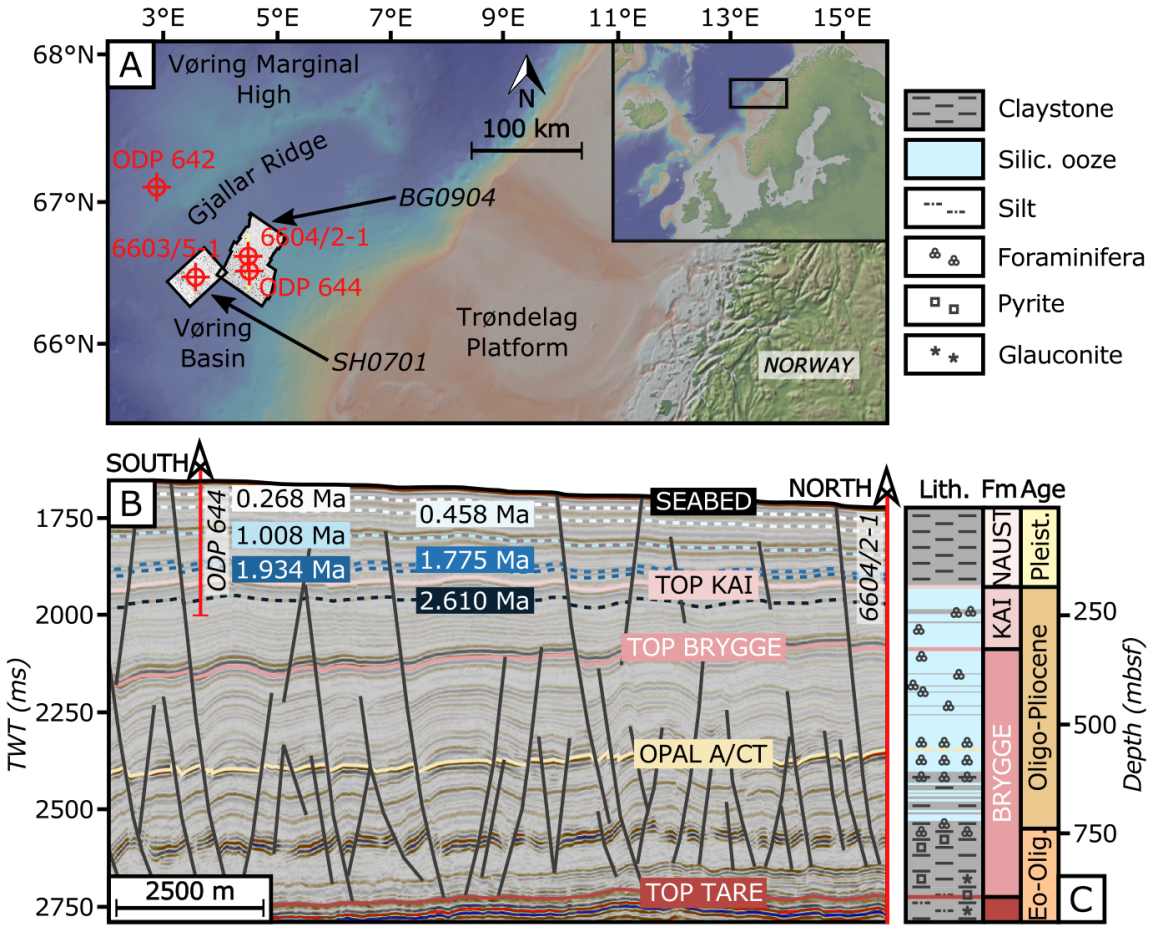


Figure 4.1: (A) Map of the study area located in the Vøring Basin of the Norwegian Sea, which includes two 3D seismic reflection volumes (SH0701 and BG0904) that are litho- and chrono-stratigraphically calibrated by two industry wells and Ocean Drilling Program (ODP) Hole 644. (B) Seismic profile of the polygonal fault system (PFS, solid black lines) tier through ODP Hole 644 and well 6604/2-1 showing dated horizons (from Shipboard Scientific Party, 1987) used in our analysis, alongside stratigraphic formation boundaries and the diagenetic phase boundary between opal-A and opal-CT. (C) Stratigraphic column of PFS host sediments. Lith.—lithology; Fm—formation; Pleist.—Pleistocene; Olig.—Oligocene; mbsf—meters below seafloor; Silic.—siliceous; TWT—two-way travel time.

4.4 Methods

We mapped the faults and horizons in the study area using two adjoining high-resolution 3-D seismic reflection surveys (Figure 4.1 A). These surveys (SH0701 and BG0904) have bin spacing of 6.25 m and 25 m, respectively, and a vertical resolution of ~6 m and ~10 m respectively in the uppermost sedimentary interval (see Fig. A.1 in the *Supplementary Material*, Appendix A). We plotted detailed throw profiles for 53 individual polygonal faults by measuring the vertical offset for as many as 70 horizons in two-way traveltime (TWT) (Figure A.3 in *Supplementary Material*, Appendix A). We transform the throw versus TWT plots into throw versus geologic age plots using seven bio- and magneto-stratigraphic dated marker horizons distributed throughout the 0-2.61 Ma interval, which is the focus of the study. We converted dated marker horizons and formation boundaries from two wells, ODP Hole 644 and well 6604/2-1, to milliseconds TWT from depth in meters using an internal velocity of 1600 m/s (Shipboard Scientific Party, 1987). The uncertainty in the depth conversion of the dated marker horizons on the seismic reflection data equates to ±0.1 m.y. for horizons <1 Ma and ±0.2 m.y. for horizons >1 Ma (for a detailed description, see *Supplementary Material* in Appendix A). Throw measurements of the age-calibrated horizons are considered accurate to ±1 m (c.f. Townsend et al. (1998)). Time-averaged throw rates are derived from the 2.61 Ma horizon to the present-day seabed by dividing the throw by the elapsed time.

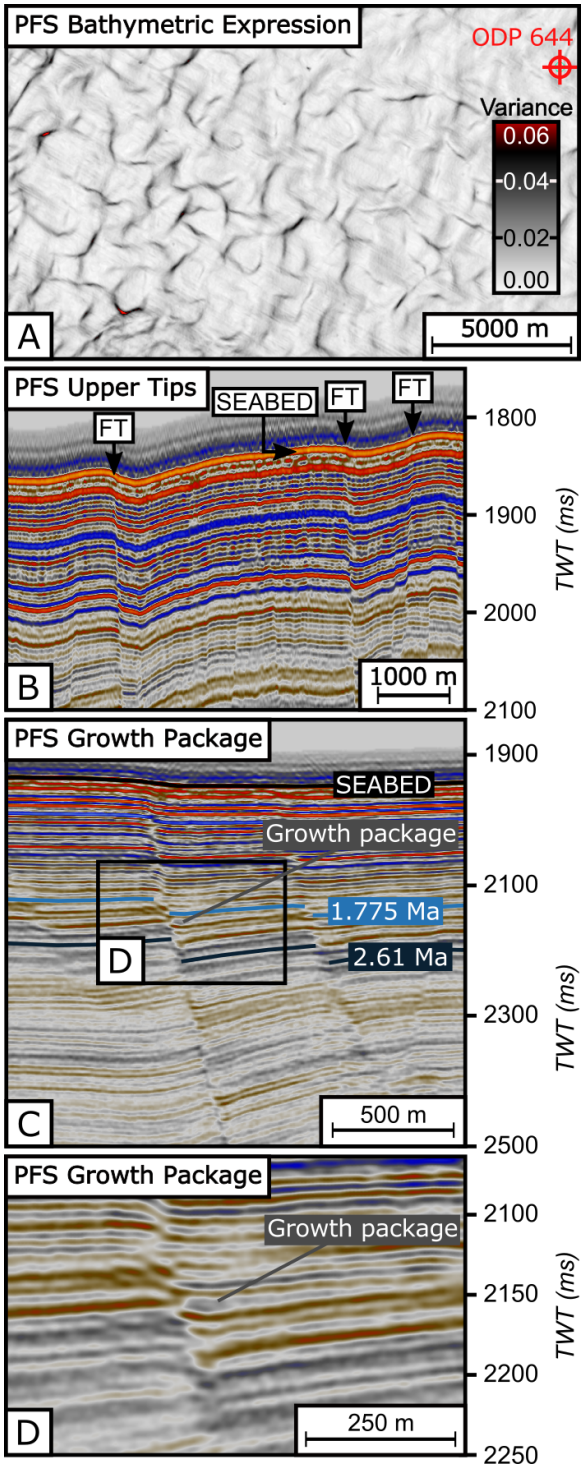


Figure 4.2: (A) Seabed variance map showing bathymetric expression of polygonal faults in the Vøring Basin, Norwegian Sea. ODP 644— Ocean Drilling Program Hole 644. (B) Seismic cross section showing bathymetric expression of polygonal fault upper tips (vertical exaggeration ~15×). Fault tips are labeled FT. (C,D) Syn-sedimentary growth package within age-calibrated stratigraphy. PFS—polygonal fault system; TWT—two-way traveltime.

4.5 Results

The base of the PFS tier is identified as the base of the Brygge Formation (Eocene-Oligocene) (Figure 4.1 B), and >90% of the basal fault tips occur at this horizon. In contrast, there is an upward reduction in fault density, and the polygonal fault upper tips terminate at a range of seismic reflections. Only the larger-throw faults continue upwards to tip out at or close to the modern seabed (Figures 4.1 B, 4.2 A, and 4.2 B). These polygonal faults have measurable bathymetric expression (Figure 4.2A) suggesting continued activity to the present day (c.f. Berndt et al. (2012)).

On a small number of the larger faults, reflection-bound intervals thicken noticeably across the faults in a manner typical of localised syn-sedimentary growth (Cartwright et al., 1998; Childs et al., 2003) (Figure 4.2 C and 4.2 D). These 'growth packages' are comparable to those identified elsewhere associated with polygonal faults (e.g. Stuevold et al. (2003) and Wrona et al. (2017)). They are not found at any specific horizon, but are sporadically distributed throughout the interval corresponding to the last 2.61 m.y. Average sedimentation rates outpace displacement rates by at least one order of magnitude during this interval (Figure A.5 in *Supplementary Material*, Appendix A). This may explain why growth packages are so uncommonly developed in the study area.

We constructed throw-versus-depth plots for 53 widely distributed polygonal faults whose upper tips are at or close to the present-day seabed. These plots (Figure A.3, *Supplementary Material*, Appendix A) show that throw increases downward from the seabed to a maximum value in the central third to lower third of the tier, and then decreases downward to the basal tips, in a similar manner to that previously described for polygonal faults (e.g. Neagu et al. (2010a)). The upper portions of these plots were transformed into throw-versus-geological age profiles, whose gradient changes reveal temporal changes in throw rate (Figure 4.3 A, and Figure A.4 in *Supplementary*

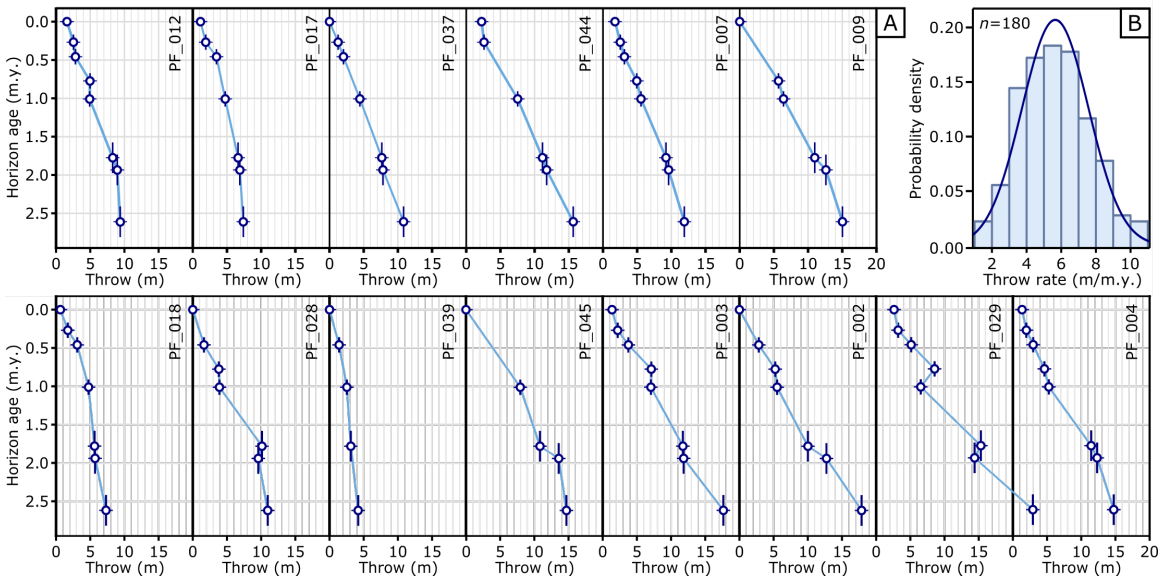


Figure 4.3: (A) Polygonal fault throw versus horizon age for 14 polygonal fault upper tips in the Vøring Basin, Norwegian Sea. (B) Probability density function of time-averaged polygonal fault system throw rates derived from the 2.61 Ma horizon for 180 faults.

Material, Appendix A).

Individual faults exhibit a range of profiles of throw with time, from almost linear profiles (constant throw rate with time; e.g., Figure 4.3 A, fault PF_037) to singly or multiply stepped (variable throw rate through time with zero-gradient stasis intervals, e.g., Figure 4.3 A, fault PF_029). Of the 53 faults, around 60% of profiles are approximately linear, or smoothly varying, and the remainder are stepped (Figure 4.3A). The stepped profiles exhibit a range of short-term throw rates ranging from 0 to 18 m/m.y.

In addition to the detailed throw-versus-age profiles, we derived time-averaged throw rates from a larger sample of 180 individual faults for the entire 2.61-0 Ma interval (Figure 4.3B). The measured throw rates are normally distributed and range between 1.4 and 10.9 m/m.y., with a mean and median of 5.7 m/m.y. and 5.6 m/m.y. respectively.

4.6 Discussion

In order to measure throw rates for faults from upper-tip geometries of the type presented above, it must be clear that the upper tips propagated in a syn-sedimentary fashion, i.e. with the tip at or close to the sediment-water interface (Childs et al., 2003; Baudon and Cartwright, 2008c). The throw rate data presented here all come from polygonal faults with upper tips at or within a few metres of the current seabed. The occurrence of small 'growth packages' within the age-calibrated stratigraphy (Figures 4.2 C and 4.2 D), albeit uncommon, and the presence of polygonal faults at or within a few meters of the modern seabed (Figure 4.1 B, 4.2 A and 4.2 B) indicate that the upper tips of the PFS have intersected the paleo-seabed throughout our chronostratigraphic study interval, and propagated upward with sedimentation in an active syn-sedimentary fashion. This interpretation is consistent with that of Neagu et al. (2010a), who dated fault activity on this PFS in relation to the fossilisation of the opal-A to opal-CT diagenetic boundary. Neagu et al. (2010a) used measured throw values of this boundary to argue for a post-fossilisation syn-sedimentary growth phase for the PFS in the Norwegian Sea. They dated the fossilisation as late Miocene to late Pliocene, which accords well with the oldest dated horizon in our study (2.61 Ma). Furthermore, we interpret stasis intervals across different polygonal fault throw profiles (Figure 4.3 A) as short periods of growth inactivity, rather than the mechanical response to blind fault propagation through competent stratigraphy, because of the their non-systematic occurrence relative to stratigraphic layering. It is possible that the PFS may have nucleated and propagated as an array of blind faults that became syn-sedimentary later in the evolution of the system (c.f. Baudon and Cartwright (2008c)). While we cannot rule out the possibility that some polygonal faults may have propagated to their current position as blind faults, we consider it is unlikely that the polygonal faults analysed in our study were blind faults over the last 2.61

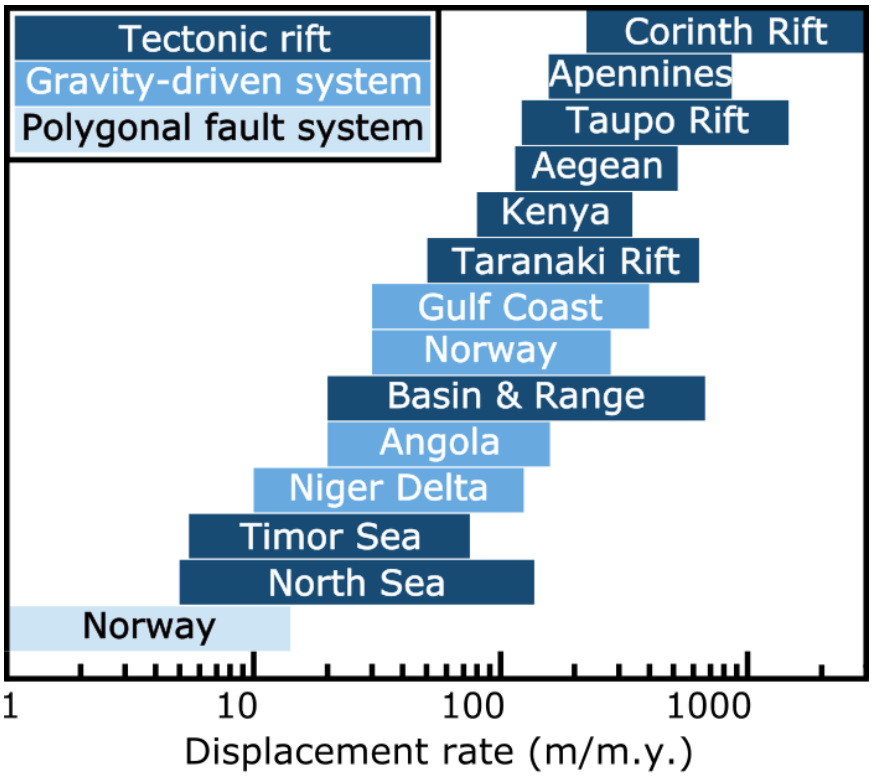


Figure 4.4: Log plot of displacement rates from extensional tectonic, gravity-driven, and polygonal fault systems (PFSs) from basins around the world. Tectonic and gravity-driven fault displacement rates are sourced from: Nicol et al. (1997), Mouslopoulou et al. (2009), Dutton and Trudgill (2009), Pochat et al. (2009), and Jackson (2018). PFSs time-averaged throw rates are converted to displacement rates using a conversion factor of 1.4.

m.y.

The measured throw rates both for short time increments and for the entire 2.61 m.y. period of the measured interval give comparable ranges in values, from 0 to 18 m/m.y. (Figure 4.3 B and Figure A.4 in *Supplementary Material*, Appendix A). To make a comparison with previously measured fault displacement rates, we can convert our throw rates to displacement rates if we assume that displacement vectors are dip slip, and by knowing the true dip of the fault planes. This correction factor amounts to 1.1 to 1.4 for faults dipping between 45° and 70°. Displacement rates for these polygonal faults compared to basement detached, gravity-driven, and tectonic faults from various rift settings shows that polygonal faults slip one to three orders

of magnitude more slowly (time averaged) than their tectonic counterparts (Figure 4.4). Our derived PFS displacement rates are the lowest ever measured for a fault array of any type globally. This comparison prompts interesting questions as to the slip mechanism: Do polygonal faults creep, or do they exhibit stick-slip behaviour as has been suggested (Tewksbury et al., 2014)?

Regardless of the underlying genetic mechanism, the accommodation of multidirectional extensional faults under net-zero lateral strain conditions requires a bulk volumetric reduction of the host tier. It is beyond the scope of the current study to attempt to explain the very slow slipping behaviour of polygonal faults. However, the ultra-slow nature of polygonal faults is not a complete surprise given the slow rates of geological processes that govern volumetric reductions in shallowly buried fine-grained sediments. These slow geological processes may include the rate of gravitational loading through sedimentation in deep-marine pelagic depositional environments, the rate of dewatering in low-permeability fine-grained sediments, and the rate of low temperature diagenetic reactions (Goulty, 2008; Cartwright, 2011). The negative throw gradients observed on the lower portions of throw-depth (t-z) plots of all polygonal faults measured to date strongly argue that there is a differential volumetric strain from footwall relative to hanging wall that accounts for a large part, if not all, of the displacement that accumulates along the fault throughout its growth history. We suggest that the ultra-slow rates presented in this study, point to a direct link between the displacement rate and the differential volumetric contractional strain rate between the footwall and hanging wall. This differential is in turn likely to be governed by bulk material properties such as stiffness, Poisson's ratio, and frictional coefficients (Shin et al., 2010; Roberts et al., 2014).

In isolation, the ultra-slow displacement rates do not explicitly favour one PFS genetic or growth mechanism over another. They do however, offer an initial temporal benchmark that may assist future computational modelling work to establish

the physical property conditions and mechanical evolution building on some pioneering attempts to model the growth of polygonal faults using finite element methods (Roberts et al., 2014).

4.7 Conclusions

1. We record the first throw rates for a polygonal fault system (PFS), from the Vøring Basin in the Norwegian Sea.

2. Our results from 180 polygonal faults show that time-averaged throw rates over the last 2.61 m.y. are normally distributed and range between 1.4 and 10.9 m/m.y.

3. Our derived PFS displacement rates mark the lower limit of a continuous spectrum of extensional fault displacement rates, where the displacement rates of polygonal faults are as much as three orders of magnitude slower than those of the fastest-growing tectonic faults.

4. The ultra-slow PFS throw rates are consistent with slow geological processes that drive differential bulk volumetric reductions between fault footwalls and hanging walls.

Chapter 5

Numerical Modelling of the Growth of Polygonal Fault Systems

This chapter has been prepared to submit for publication. The research presented in this chapter is my own work, however, it benefited from collaboration with Dan Roberts, who supported with the development of the finite element modelling approach, and Joe Cartwright and Bruce Levell, who supported with the research strategy.

5.1 Abstract

Normal faults require volume change to accommodate varying displacement of offset beds. Most tectonic and gravitational slope faults are associated with demonstrable lateral extension, whether they are driven by regional-scale plate tectonic forces or gravitational slope instabilities on passive margins, respectively. However, polygonal fault systems (PFSs) are a nontectonic class of normal faults that resemble the geometries of their tectonic counterparts but grow in laterally-pinned conditions, and therefore, must be explained by an altogether different mechanism. Despite over three-decades of active research and wide debate in the published literature, the mechanisms that govern the growth of polygonal faults are poorly understood. Here we investigate the growth of polygonal faults using a suite of geomechanical finite element forward models that couple dynamic fault propagation, sedimentation, and the mechanical compaction of unconsolidated granular sediment. We find that the growth of polygonal faults within laterally-pinned sedimentary tiers can be explained solely by gravity-driven differential compaction, where the magnitude of fault throw is governed by the relationship between the residual friction angle, the fault dip angle, and material compaction.

5.2 Introduction

The terms normal fault and extensional fault are often used interchangeably to describe fractures that vertically offset strata over length scales upward from a few millimetres to thousands of kilometres (Peacock et al., 2000; Fossen, 2016). This exchangeable nomenclature is used to describe tectonic and gravitational slope fault systems, which are driven by processes such as mantle convection and slope instabilities, respectively (McKenzie, 1978; Vendeville et al., 1987; McClay, 1990). However, a counter-intuitive class of nontectonic normal faults, called polygonal faults, that grow in laterally-pinned conditions must be explained by an altogether different mechanism (Henriet et al., 1988; Cartwright et al., 2003; Goulty, 2008; Cartwright, 2011).

Polygonal fault systems (PFSs) were first reported in the open literature in the late 1980's with the advent of three-dimensional seismic reflection datasets and have since been documented in over 150 basins around the world, where they span large areal extents of predominantly fine-grained sedimentary sequences (typically ~10^5-10^7 km^2) (Figure 5.1) (Henriet et al., 1988, 1991; Higgs and McClay, 1993; Cartwright, 1994a,b; Cartwright and Dewhurst, 1998; Cartwright et al., 2003; Cartwright, 2011). A typical PFS tier hosts an array of intersecting normal faults with multi-directional orientations and modest throws (< 100 m) that range in height from a few tens of metres to over a kilometre (Lonergan et al., 1998a; Cartwright et al., 2003). Within a single PFS, the majority of faults share a common basal termination boundary, whereas the upper tips of polygonal faults terminate at a range of different heights within the tier (Cartwright et al., 2003). The majority of polygonal faults are small (<1 km in height) and concentrate in the lower portion of the tier, where they terminate basally into a mechanically competent unit or detach into a mobile layer (Cartwright et al., 2003), however, a smaller number of *master faults* span the entire height of the tier where they tip out into a propagation barrier or intersect the

seabed (Cartwright et al., 2003; Cartwright, 2011). The widespread occurrence of PFSs within the shallow subsurface suggests they initiate early in the burial history of the host tier (Cartwright, 1994a,b; Berndt et al., 2003; Cartwright et al., 2003; Stuevold et al., 2003), and several studies have suggested that polygonal faults propagate upwards with sedimentation (Lonergan et al., 1998a; Goulty, 2001a; Stuevold et al., 2003; Gay and Berndt, 2007; Davies and Ireland, 2011; Tewksbury et al., 2014; Morgan et al., 2015; King and Cartwright, 2020) (Chapters 3 & 4). Polygonal faults are commonly characterised by listrically dipping fault planes with depth, where shallowly buried upper fault tips can exhibit dips in the range of 50°-80° and deeper buried portions of faults can exhibit dips as low as 30°-50° (Cartwright, 1994a; Cartwright and Lonergan, 1996; Lonergan et al., 1998b; Clausen et al., 1999; Cartwright et al., 2003; Shoulders et al., 2007; Sun et al., 2010). The maximum throw values of polygonal faults are usually located in the central third to lower third of their height, where maximum throw values scale at around 3-6% of the fault height (Shin et al., 2010; Cartwright, 2011). Recently, throw rates of polygonal faults were recorded for the first time from the upper tips of the Vøring Basin PFS, where they were found to range from 1.4-10.9 m/m.y. over an interval extending back some three million years from the present day (King and Cartwright, 2020) (Chapter 4).

Although the geometries, intersections, and distribution of PFSs are well studied and documented (Chapter 1), despite over three-decades of academic research, the processes that initiate and subsequently drive the growth of polygonal faults are poorly understood. Several mechanisms have been proposed to explain the nucleation and growth of PFSs, but most have been discounted as universal mechanisms because they cannot explain the formation or growth of all polygonal fault systems observed globally (Cartwright et al., 2003; Goulty, 2008; Cartwright, 2011). In recent years, 'gravitational loading' (Goulty, 2001a; Goulty and Swarbrick, 2005) and 'diagenetically-induced shear failure' (Shin et al., 2008, 2010; Cartwright, 2011) have

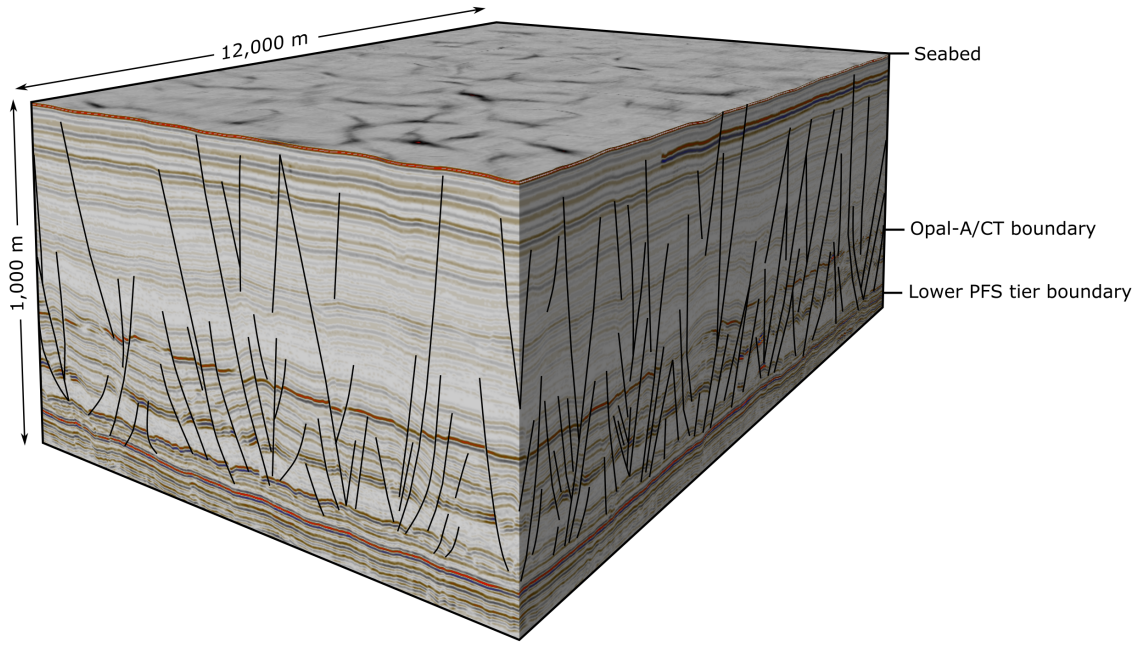


Figure 5.1: A three-dimensional visualisation of a portion of the Vøring Basin PFS, Norwegian Sea, showing the geometry of polygonal faults in cross-section and the classic polygonal planform pattern at the present-day seabed.

been favoured as mechanisms to explain specific aspects of the evolution of polygonal faults because, in theory, they are universally applicable across all PFSs. The gravitational loading mechanism provides an elegant geomechanical explanation of the simultaneous upward propagation of pre-existing fractures hosted within laterally-pinned fine-grained strata with increasing overburden stresses that build as a result of sedimentation (Goulty, 2001a,b; Goulty and Swarbrick, 2005; Goulty, 2008). In Mohr-Coulomb terms (Figure 5.2 A), the residual failure criterion of a pre-existing fault is breached under laterally-confined hydrostatic loading conditions, if it is hosted within a material with a sufficiently low residual friction angle and a high K_0 value. Where K_0 is the coefficient of lateral earth pressure 'at rest', calculated as the ratio of the horizontal stress over the vertical stress, which is typically ~0.3-0.4 for coarse-grained sediments and >0.7 for fine-grained sediments (Jones, 1994; Goulty, 2001a; Goulty and Swarbrick, 2005; Casey, 2014). However, the gravitational loading mechanism does not attempt to explain either the nucleation of polygonal faults or how

displacement is accommodated within laterally-pinned conditions. Alternatively, it has been suggested that a diagenetically-induced shear failure mechanism may explain the full evolution of a PFS, from genesis to fossilisation (Shin et al., 2008, 2010; Cartwright, 2011). In Mohr-Coulomb terms (Figure 5.2 B), a diagenetically-induced volumetric reduction causes a decrease in the minimum principal stress, which increases the size of the Mohr circle such that it intersects the initial failure criterion, thus nucleating a shear fracture. A diagenetic mechanism may lead to further fault propagation in laterally-confined hydrostatic conditions if the expanding size of the Mohr circle breaches the residual failure criterion. Furthermore, the volumetric reduction associated with such a diagenetic mechanism can create accommodation space for fault-related displacement in laterally-confined conditions (Shin et al., 2008). A diagenetic mechanism has gathered wide attraction because many PFS tiers contain diagenetically reactive sediments that undergo volumetric reductions, such as, opal-A to opal-CT, smectite to illite, and some volcanic ashes (Cartwright, 2011).

A limited number of studies have attempted to computationally investigate the gravitational loading and diagenetically-induced shear failure mechanisms. One of the main conclusions of the Shin et al. (2010) study was that the maximum throw to height scaling relationship of polygonal faults in laterally-pinned gravitational loading conditions were only achieved at exceptionally low material bulk stiffness values, that are between one and three orders of magnitude lower than those recorded from fine-grained sediments (Santamarina et al., 2001). Shin et al. (2010) attributed the exceptionally low bulk stiffness values to diagenetic grain dissolution, following results from earlier physical modelling work (Shin et al., 2008), and hence ruled out a purely gravitational model as the driver of throw accumulation on polygonal faults. However, the bulk material stiffness term used in the Shin et al. (2010) Drucker-Prager models does not explicitly incorporate gravity-driven mechanical compaction. Roberts et al. (2014) and Roberts (2014) used the *ELFEN* geomechanical code and a *SoftRock 3*

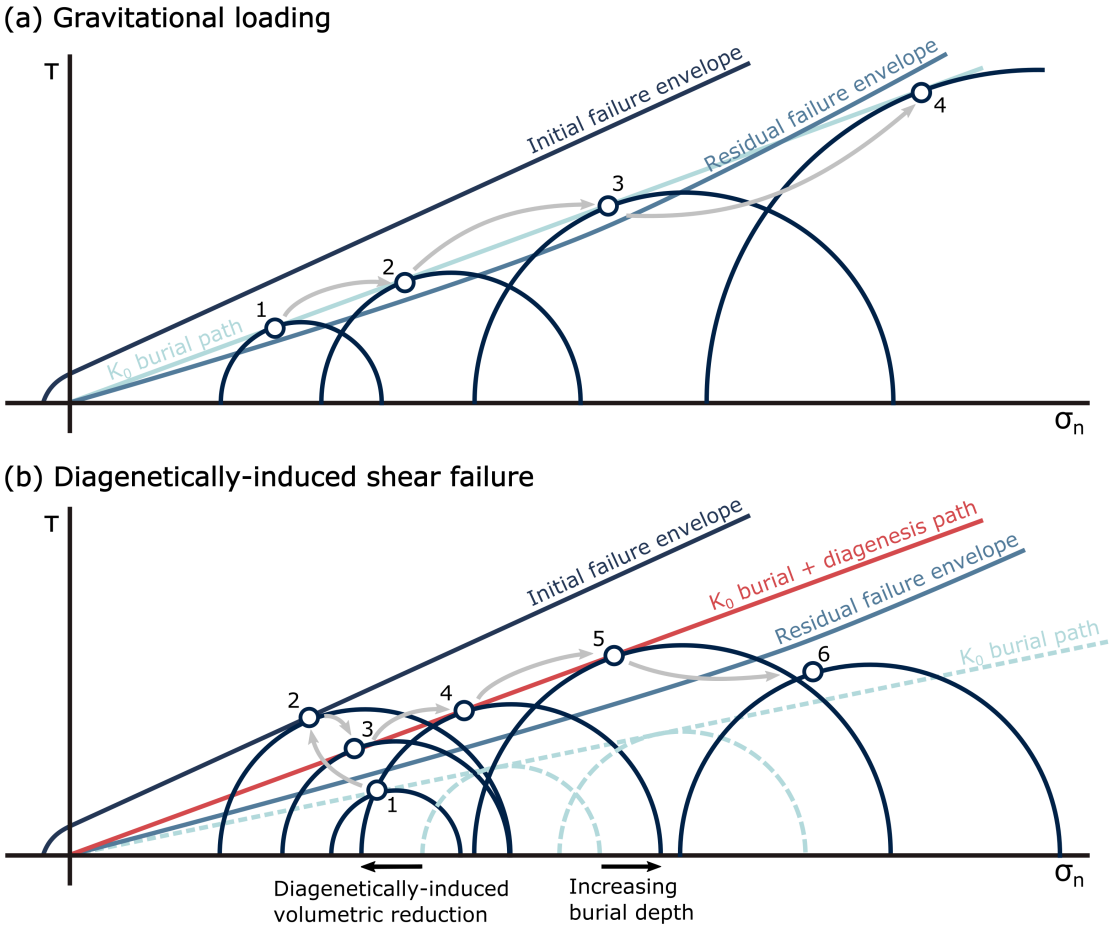


Figure 5.2: Illustrative representation of the (a) gravitational loading mechanism and (b) diagenetically-induced shear failure mechanism presented in terms of Mohr-Coulomb theory, with effective normal stress acting on the shear plane (σ_n) on the x-axis and shear stress (τ) on the y-axis. The K_0 burial stress path lies above the residual failure envelope if $K_0 < 1 - 2\mu_r \left(\sqrt{1+\mu_r^2} - \mu_r\right)$, where μ_r is the coefficient of residual friction, and $\mu_r = \tan\varphi_r$, where φ_r is the residual friction angle, and frictional sliding is achieved when the shear stress (τ) reaches the residual failure envelope defined by $\tau = c + \sigma_n \tan\varphi_r$, where c is the cohesion. The gravitational loading mechanism may explain the propagation of pre-existing fractures that are hosted within laterally-pinned materials with low intrinsic residual friction angles and high K_0 values. Diagenetically-induced volumetric shrinkage of laterally-pinned sediments may cause a reduction in the minimum principal stress such that the size of the Mohr circle increases to intersect the initial failure envelope, thus causing the nucleation of a shear fracture. Continued diagenetically-induced volumetric shrinkage with increasing burial may yield conditions that exceed the residual failure envelope until the cessation or slowing of diagenetic activity.

constitutive model to demonstrate that a diagenetically-triggered isotropic chemical porosity reduction, such as that caused by the transition of opal-A to opal-CT, of 5% was sufficient to localise and propagate shear fractures that resembled the geometries and network intersections of polygonal faults in two-dimensional cross-section and three-dimensional planforms. Roberts et al. (2014) and Roberts (2014) also showed that a horizontal stress anisotropy of just 3% was enough to align over 80% of fault orientations to within $\pm 10^{\circ}$ of the maximum horizontal stress. Despite the advances made by these pioneering studies, our understanding of the relative magnitudes of different drivers of PFS growth is limited, and the role of gravity-driven mechanical compaction may have been overlooked as a means of accommodating polygonal fault displacement.

In this study, we investigated the hypothesis that gravity-driven differential compaction can solely drive the propagation and accumulation of throw on pre-existing polygonal faults that are hosted in laterally-pinned unconsolidated sediments. To test this hypothesis, we developed a series of laterally-pinned finite element models using the *ELFEN* geomechanical code, to examine the evolution of a single fault that propagates synchronously with the deposition of granular compacting sediment. We investigated the sensitivity of the accrual of fault throw with respect to three main variables: (1) material compaction profiles, (2) residual friction angles, and (3) fault dip angles. Understanding what drives the growth of polygonal fault systems is important to assess the sealing integrity of polygonally faulted caprocks that are found in many petroleum and CO_2 storage systems (Cartwright, 2011). Furthermore, the process(es) that govern the growth of laterally-pinned fault systems may contribute to an unrecognised portion of the strain that accumulates on other fault systems that are traditionally solely associated with gravitational slope instabilities or tectonic processes.

5.3 Methodology

5.3.1 Computational Framework

To undertake our analysis, we used the *ELFEN* forward modelling geomechanical code, which is a finite strain, quasi-static, explicit finite element continuum formulation. The underlying computational methods are discussed extensively by Perić and Crook (2004) and Rockfield (2010) (see Appendix B for summary). This modelling framework has been used to solve a host of geological problems ranging from salt tectonics (Nikolinakou et al., 2014a,b) to regional fold and thrust belts (Albertz and Lingrey, 2012), as well as previous studies of polygonal fault systems (Roberts et al., 2014; Roberts, 2014). However, alternative modelling approaches such as the Discrete Element Method (DEM), which unlike the finite element continuum approach does not use a pre-defined material constitutive model but instead models the interaction of rock particle assemblages governed by Newton's laws of motion, have been used to solve similar geological problems (Finch et al., 2003; Schöpfer et al., 2009; Gray et al., 2014). We selected a finite element approach because the DEM approach can require excessively long solution times due to the searches needed to evaluate the particle interactions, which can therefore limit the model resolution (Yin et al., 2009), and the calibration of some DEM models can present challenges in obtaining values recorded from physical experiments (Schöpfer et al., 2009). The ability to pre-define the material behaviour in a continuum approach offered greater specificity when designing a sensitivity analysis of granular material compaction trends, and previous studies of PFSs using these modelling tools provided proof of concept prior to embarking on our study. However, both the finite element and discrete element methods offer valid approaches to the study of polygonal fault systems.

5.3.2 Constitutive Model

The constitutive model relates deformational strains and stresses through a set of equations (see Appendix B) that comprise material-specific parameters, such as frictional and dilational angles. We used the *SoftRock 3* (SR3) constitutive model, which is an advanced variant of the Modified Cam Clay model (Crook et al., 2006) that is derived from *Critical State Soil Mechanics* theory (Schofield and Wroth, 1968; Muir Wood, 1990), in our study because it explicitly incorporates the role of granular sediment compaction in material deformation. Alternative constitutive frameworks, such as the Mohr-Coulomb and Drucker-Prager models have been used in several computational geological studies (Schultz-Ela, 2003; Gradmann et al., 2009; Shin et al., 2010), however, they do not explicitly account for granular compaction and are therefore, better suited to the characterisation of lithified and crystalline rocks. Several previous studies have used an SR3 constitutive framework to model the elastoplastic deformation associated with salt diapirs rising through porous sediments (Nikolinakou et al., 2014a,b), and the investigation of polygonal faulting in unconsolidated fine-grained sediments (Roberts et al., 2014; Roberts, 2014).

The methodology and calibration of the *SoftRock 3* constitutive framework are discussed extensively by Crook et al. (2006) and Rockfield (2010). The full elastoplastic formulation is included in Appendix B, however, we use a reduced subset of its full capability in our analysis. Specifically, rather than determining the nucleation and propagation of the fault plane via the intersection of the material stress path with the state boundary surface as in the diagenetically-induced fault nucleation simulations undertaken by Roberts et al. (2014), we instead prescribe the fault with a frictional planar surface. In addition, the porous elastic law is included in our simulations, but its influence is negligible over the burial depths of our material models which are instead primarily deforming via compaction-related plastic strain determined by the

hardening law (Appendix B).

5.3.3 Model Setup

5.3.3.1 Modelling strategy

Our modelling strategy was designed to investigate the role of gravity-driven differential compaction facilitated by frictional sliding on a dipping fault plane with simultaneous sedimentation, as a mechanism to explain the accrual of fault throw in laterally-pinned conditions. To investigate this mechanism, we constructed a suite of two-dimensional field-scale finite element models that simulate the upward propagation of a pre-existing normal fault from a fixed lower tip with synchronous sedimentation in laterally-pinned hydrostatic plane-strain conditions, and undertook a sensitivity analysis of the accrual of fault throw with respect to three key variable parameters: (1) the compaction profile of the fault-hosting fine-grained granular sediment that was of uniform composition from the top to the bottom of the model; (2) the friction angle of the fault plane (residual friction angle); (3) the dip angle at which the fault plane propagates.

The models comprise a starting base unit that hosts a pre-existing fault plane which propagates upwards from a fixed lower tip, that resides a few tens of metres above the base of the model. The upward fault propagation occurs synchronously with the deposition of 1000 metres of unconsolidated granular material at a sedimentation rate of 100 m/m.y. over fifty 0.2 million-year time increments, simulating 10 million-years. Material compaction is fully coupled throughout all fifty depositional stages where we assume fully-drained conditions and do not build overpressure. Like the material compaction profile, the starting dip angle and residual friction angle of the fault plane are variable parameters that are prescribed in each model simulation, and their respective influences on fault throw are investigated via sensitivity analysis.

The material compaction profile with increasing burial depth is prescribed in each simulation, where we investigate four primary compaction curves (outlined in Section 5.3.3.3). The fault plane friction angle (residual friction angle) remains constant in each simulation, and is investigated over values of 5°, 7°, 9°, and 11°. The fault dip angle is prescribed on the upper tip segment that propagates at each 0.2 million-year time increment, however, the fault dip angle shallows dynamically with burial as a result of compaction creating a degree of fault dip listricity. We investigate initial dip angle values of 40°, 50°, 60°, 70°, and 80°, which when compacted shallow by as much as 15°-20° at depth.

5.3.3.2 Boundary conditions

The width of the models are set so that there is no interaction between fault-related deformations in the central portion of the model and the lateral boundary conditions, and vice versa. All models are 2000 metres wide with element sizes of ~5 metres, except for the investigation of a 40° dipping fault plane which requires a 3000 metre wide model to prevent edge effects. All of the models have frictionless boundary conditions at both their lateral edges and base, where elements at the model boundaries are confined but are able to slide freely.

5.3.3.3 Material characterisation

We characterised four materials, m1-m4, to capture a range of different compaction profiles that are exhibited by fine-grained sediments. All materials used in our analysis are characterised with the same underlying elastic physical property and SR3 property parameters (see Appendix B, Tables B.1 and B.2), however, each material has a unique compaction profile that is defined by a piecewise linear lambda-kappa parameter in the hardening law (Appendix B) all with an initial porosity value of 70%.

Over the shallow burial depths analysed in our models, gravitationally-driven volumetric strains of high porosity granular sediments are predominately plastic rather than elastic. We include the SR3 porous elastic laws (see Appendix B) in our material characterisation for completeness, however, our models are insensitive to changes in both the stiffness parameter value (E) and Poisson's ratio paramater value (ν) that fall within the range of those recorded from fine-grained sediments (Santamarina et al., 2001). Furthermore, the SR3 property parameters used to define the state boundary surface are included (Appendix B), however, fault plane propagation is prescribed in our models rather than determined via the intersection of the material stress path with the state boundary surface. The SR3 frictional and dilational parameters were chosen such that the material is characterised with a K_0 value of 0.7-0.72 typical of fine-grained sediments (Jones, 1994; Goulty and Swarbrick, 2005; Casey, 2014).

The compaction profiles that define each material (m1-m4) have been guided by consideration of compaction curves from shales and argillaceous sediments, experimental compaction curves derived from kaolinite-smectite aggregates, and porosity-versus-depth data from Ocean Drilling Program (ODP) wells that logged four different polygonal fault systems (Figure 5.3). Rather than using any specific study as a reference curve for our material compaction characterisations, we sought to define an array of materials with incremental differences in both the gradient of compaction with depth and the absolute amount of volumetric compaction. The m1, m2, and m3 materials are defined to capture the upper, middle, and lower ranges of compaction curve profiles recorded from fine-grained sediments in previous compaction studies (compiled in Mondol et al., 2007). The m4 material more closely traces the porosity versus depth profiles of biosiliceous fine-grained sediments recorded from ODP boreholes that transect known polygonal fault systems (Shipboard Scientific Party, 1987, 1990, 1996, 2001). After the first 150 metres of burial the compaction gradients of the m1 and m4 materials are approximately equal, which presents an opportunity

to compare the influence of the absolute magnitude and the gradient of volumetric reduction on the accrual of fault throw.

The material residual friction angle (fault friction angle) is a variable parameter that is investigated through sensitivity analysis over values between 5°-11°, that are based on low values recorded from ring shear, drained shear box, and rotary shear tests of claystones and siliceous mudstones compiled from published literature (Table 5.1).

5.3.3.4 Model outputs

From each sensitivity run, we produced a series of effective mean stress, effective mean stress perturbation, horizontal effective mean stress perturbation, and vertical effective mean stress perturbation contour plots with offset temporal stratigraphic markers. From these plots, we measured the throw at each stratigraphic marker along the fault plane each time the fault gained ~50 metres in height. Throw measurements were taken one element width (~5 metres) laterally from the fault plane for consistency with measurements taken from seismic reflection data that are typically taken one seismic trace away from the fault plane. From each throw versus height profile, we extracted the maximum throw value (T_{max}) to serve as an incremental measure of fault growth for cross-comparison across different sensitivity runs. We plot maximum throw against fault height for our suite of material compaction, residual friction angle, and fault dip angle sensitivity analyses and benchmark our results to the range of T_{max} versus height values recorded within one standard deviation of the mean of polygonal faults from basins around the world (dashed grey lines on Figure 5.4 B, C, and D) (Shin et al., 2010). We derive throw rates from each throw versus height plot, as the amount of throw at the stratigraphic marker deposited one million years before the present timestep. We also include a maximum and minimum principal stress vector plot with 50 metre spaced vectors that are scaled in size with respect to

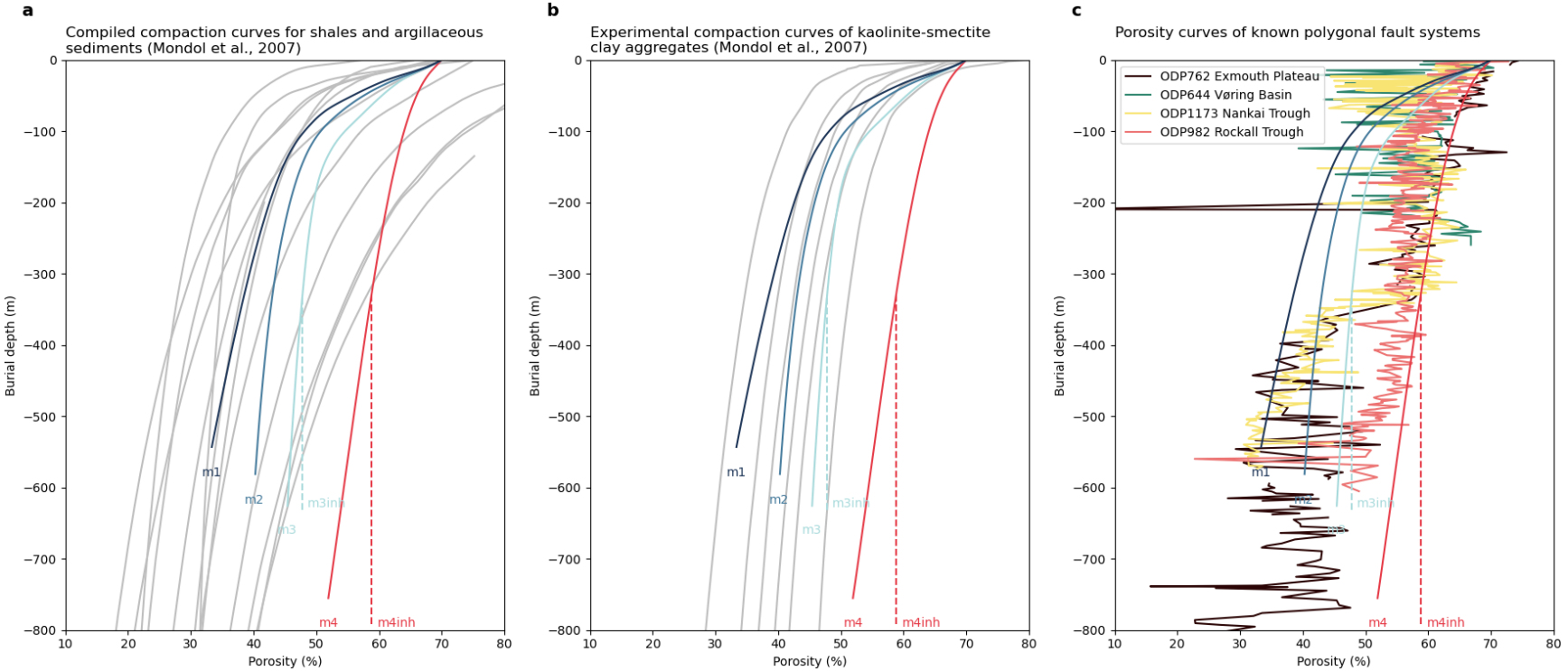


Figure 5.3: Compaction curves for the m1, m2, m3, m4, m3inh, and m4inh materials used in our sensitivity study superimposed on: (a) Compaction curves for shales and argillaceous sediments from several literature sources compiled in Mondol et al. (2007); (b) Experimental compaction curves of kaolinite-smectite clay aggregates from Mondol et al. (2007). Ratios of kaolinite:smectite aggregates of grey coloured compaction curves from left to right 100:0, 80:20, 60:40, 40:60, 20:80, 0:100.; (c) Porosity versus depth curves from Ocean Drilling Program (ODP) well sites that transect known polygonal fault systems that are hosted in fine-grained sediments ranging in lithology from claystone (upper ~300 m of Vøring Basin PFS), siliceous mudstone (Nankai Trough PFS), to calcareous ooze (Exmouth Plateau PFS).

Residual Friction Angle (°)	Lithology	Age	Location	Method	References
3.4	Wet Montmorillonite	–	–	Drained Triaxial Friction Experiments	Moore and Lockner (2007)
4.6	Claystone - Santa Clara Fm	Plio-Pleistocene	Santa Clara, California, USA	Drained Shear Box	Nelson (1992)
4.9	Siliceous Mudstone - Honorobe	–	Honorobe URL Site, Japan		Sanada et al. (2009)
5.0	Claystone	–	Chatfield Dam, Colorado, USA	Drained Ring Shear	Dewoolkar and Huzjak (2005)
5.0	Claystone	Plio-Pleistocene	Oahu, Hawaii	Drained Ring Shear	Wan and Kwong (2002)
5.1	Claystone	Lower Miocene	North Sea	Leak-off test estimate	Goulty and Swarbrick (2005)
5.7	Claystone - Cucaracha Shale	Early-Middle Miocene	Panama Canal	Drained Ring Shear and Drained Shear Box	LaGatta (1970) and Bishop et al. (1971)
6.0	Claystone - Weald Clay	Cretaceous	Kent, UK	Drained Shear Box	Cripps and Taylor (1981)
6.2	Claystone - Nankai Trough	–	Nankai Trough, offshore Japan	Rotary Shear	Ikari et al. (2018)
6.8	Claystone	Late Pleistocene	IODP Hole U1381, offshore Costa Rica	Rotary Shear	Namiki et al. (2014)
8.0	Claystone - Blue London Clay	Early Eocene	Wraysbury, UK	Drained Ring Shear	LaGatta (1970) and Bishop et al. (1971)
8.0	Claystone - Brown London Clay	Early Eocene	Walthamstow, UK	Drained Ring Shear	Bishop et al. (1971)
10.3	Claystone	Pliocene-Quaternary	Eastern Mediterranean ODP Leg 160	Drained Shear Box	Kopf et al. (1998)

Table 5.1: Low residual friction angle values recorded from fine-grained sediments compiled from published literature.

the magnitude of the maximum principal stress at each point.

5.3.3.5 Kinematic justification

The kinematics of our fault propagation models are based on previous studies that have shown: (1) polygonal faults nucleate in the lower portions of their tiers early in their burial history (Cartwright et al., 2003); (2) polygonal faults propagate in an upwards direction for much of their growth histories (Morgan et al., 2015) (Chapter 3), where their downward propagation is impeded by a basal mechanical barrier or a detachment into a mobile basal layer (Cartwright et al., 2003; Cartwright, 2011); (3) polygonal fault systems are found at the present day (Gay and Berndt, 2007; Berndt et al., 2012; Armandita et al., 2015; Morgan et al., 2015) and paleo-seabed, as evidenced by small growth packages (Cartwright, 1994a; Lonergan et al., 1998a; Stuevold et al., 2003; Cartwright, 2011; Laurent et al., 2012) (see also Chapter 3, Figures 3.10 & 3.11), which suggests that polygonal faults can propagate upwards at or near the seabed; (4) fault propagation may occur synchronously with gravitational loading in sediments with sufficiently high K_0 values and sufficiently low residual friction angles (Goulty, 2001a; Goulty and Swarbrick, 2005) (Figure 5.2 A); (5) hemipelagic sedimentation rates in deep marine depositional environments are low (~2-200 m/m.y.) (Cartwright and Dewhurst, 1998; Shipboard Scientific Party, 1987, 1990, 1996, 2001).

Geometrical and quantitative measures to compare our modelling results and test our hypothesis are offered by the maximum throw (T_{max}) versus height empirical scaling relationship established by Shin et al. (2010), a plethora of polygonal fault throw versus height profiles from multiple basins around the world (Neagu et al., 2010a; Turrini et al., 2017; Wrona et al., 2017) (Chapter 3), and the recently recorded throw rates from surface-breaching polygonal fault upper tips in the top 2.61 million-years of stratigraphy from the Vøring Basin (King and Cartwright, 2020) (Chapter 4). The kinematic growth model used in our analysis may not be representative of the

growth of all polygonal faults within all PFSs, however, it is consistent with temporal and kinematic observations of PFS master faults from several previous studies and the findings of Chapter 3.

5.4 Results

The results of our sensitivity study are illustrated in Figure 5.4, where we present a series of maximum throw (T_{max}) versus fault height graphs that show the influence of different material compaction profiles, residual friction angles, and fault dip propagation angles on the magnitude of throw that accumulates on a fault hosted in laterally-pinned conditions, throughout its temporal evolution. An example of the temporal evolution of a single sensitivity run, from which throw versus height measurements are taken, is illustrated in Figures 5.5 & 5.6 for the m1-fr5-d60 model (where m1 is the material model, fr5 represents the residual friction angle used was 5°, and d60 represents the fault propagated with a dip angle of 60°) at 2 million-year time increments. In addition to the contour plots, the corresponding principal stress vector plot for the m1-fr5-d60 model at the 10 million-year timestep is presented in Figure 5.7, which shows the rotation of the maximum and minimum stresses associated with frictional sliding on the fault plane. The stress field is unperturbed at the lateral edges of the models, where the effective mean stress increases monotonically with depth as the result of one-dimensional consolidation (Terzaghi and Peck, 1948). Effective mean stress perturbations are found on both sides of the fault plane, where they dissipate to ambient values within a few hundred metres of the fault plane (Figure 5.5).

5.4.1 Material compaction and fault throw

Faults hosted within each of the m1-m4 materials (Figure 5.4 A) yield different maximum throw values with respect to the fault height (Figure 5.4 B). All else being equal, the greatest maximum throw values accrue on faults hosted in the m1 material (Figure 5.4 B), which undergoes the greatest amount of gravity-driven mechanical compaction with burial depth of all our material characterisations (Figure 5.4 A). Faults

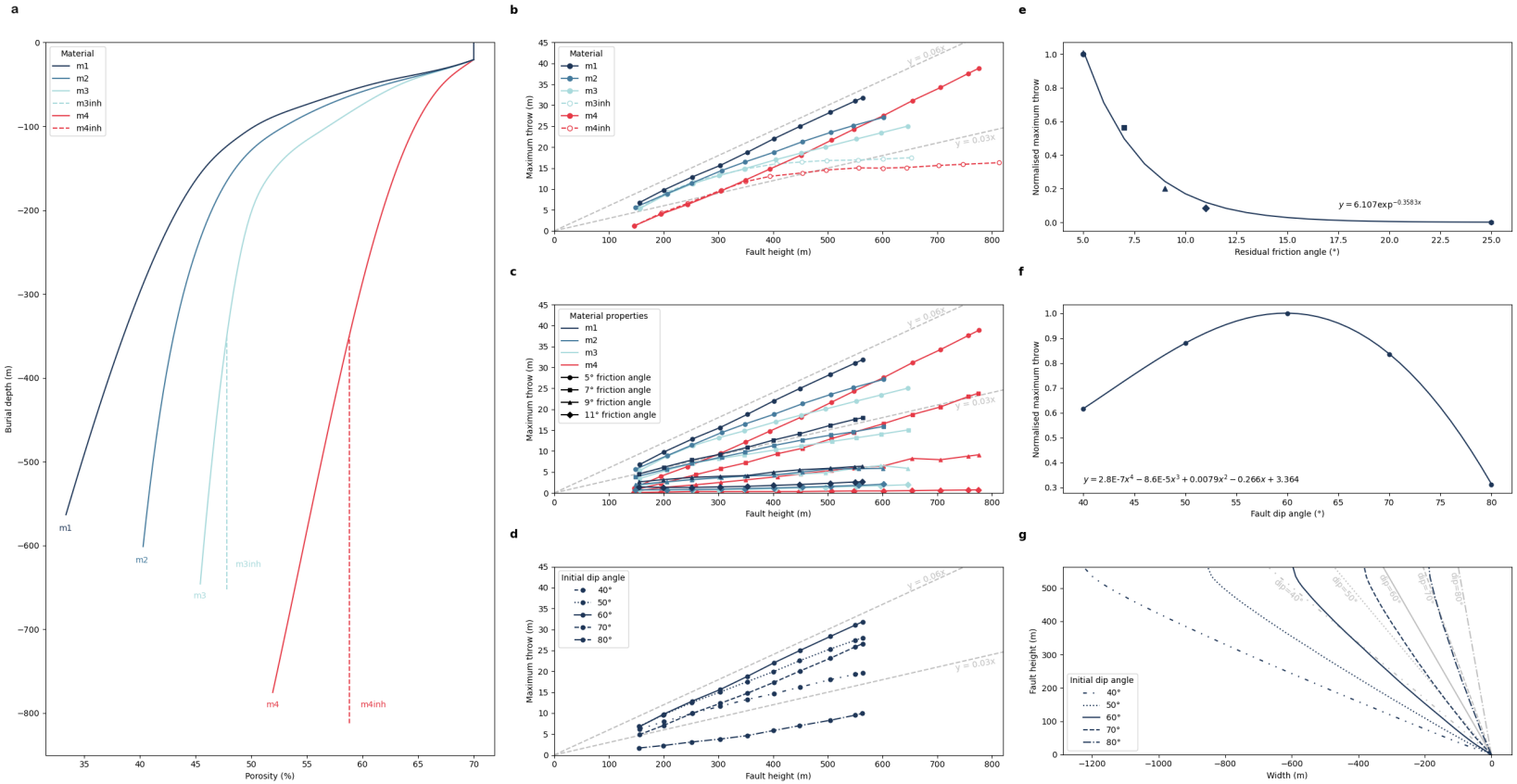


Figure 5.4: (a) Solid coloured lines display the compaction profiles of 1000 m of deposited sediment for the four materials, m1-m4, which are derived from published compaction curves for hemipelagic fine-grained sediments. Dashed lines represent inhibited compaction profiles beyond a burial depth of 350 meters for the m3inh and m4inh materials. (b) Sensitivity of maximum throw with respect to fault height for a range of compacting and incompressible materials for a fault plane with a propagating dip angle of 60° and a 5° residual friction angle. (c) Sensitivity of maximum throw on a fault plane with a propagating dip angle of 60° with respect to fault height for materials m1-m4 over residual friction angles of 5°, 7°, 9°, and 11°. (d) Sensitivity of maximum throw with respect to fault height for a fault with propagating dip angles between 40°-80° hosted in the m1 material with a 5° residual friction. (e) Normalised maximum throw values with respect to different residual friction angles on a fault with a propagating dip angle of 60° hosted in the m1 material with a peak friction angle of 25°. (f) Normalised maximum throw values with respect to different initial fault dip angles for a fault with a residual friction angle of 5° hosted in the m1 material. (g) Blue coloured lines show compacted fault dip angles used in our sensitivity analysis for the m1 material at true scale. Grey lines show the initial uncompacted dip angles for visual comparison.

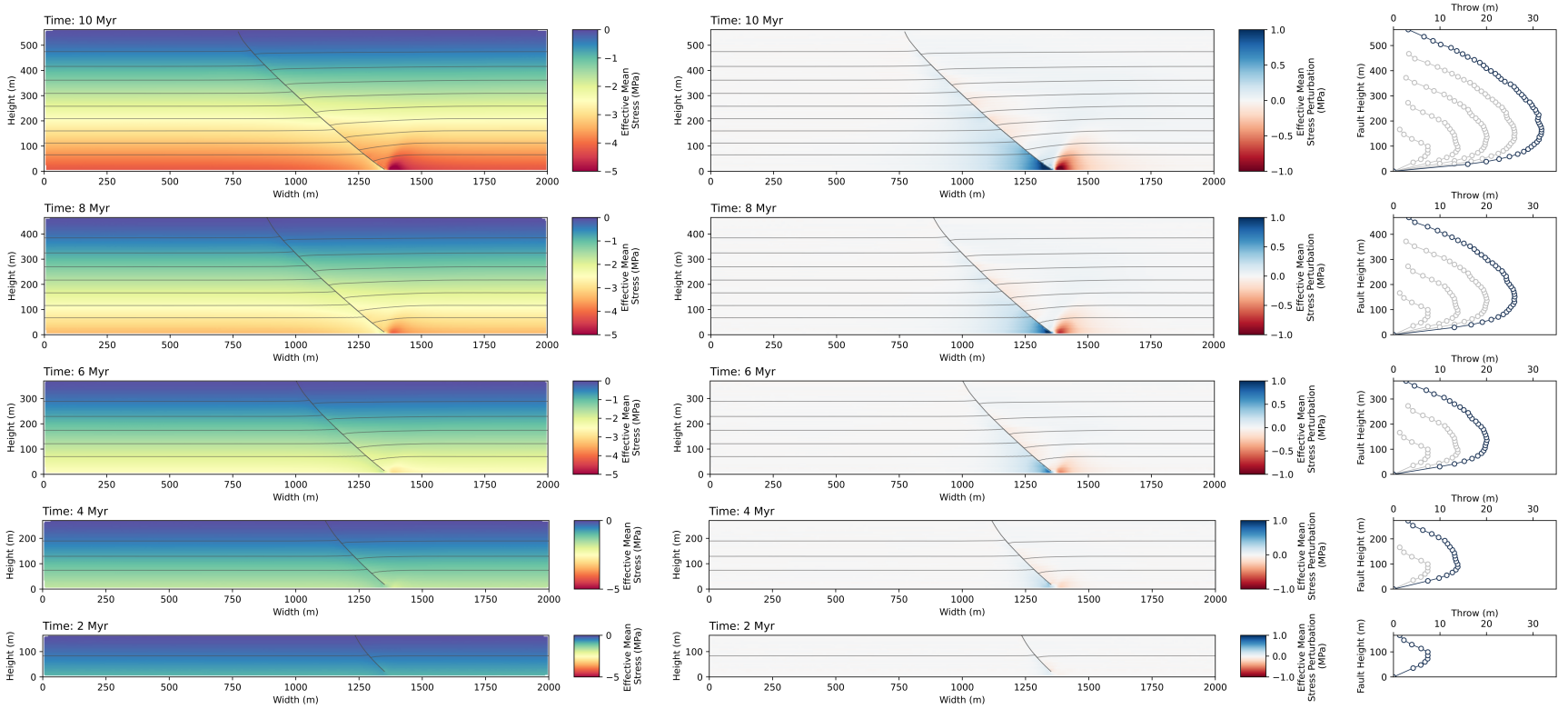


Figure 5.5: Effective mean stress and effective mean stress perturbation contour plots at 2 million-year time increments showing the evolution of a normal fault hosted in laterally-pinned conditions that propagates simultaneously with the deposition of granular sediment at a rate of 100 metres per million years. The fault propagates with an initial dip of 60° that shallows to ~40° with compaction. The residual friction angle is 5° and the host material is characterised by the m1 material compaction profile. Offset grey horizontal lines represent stratigraphic markers at 1 million-year time intervals. The throw versus height graphs that accompany the contour plots display the accrual of vertical displacement throughout the growth of this fault. Points represent throw measurements taken at stratigraphic markers with a 0.2 million-year depositional interval. Blue colours represent the throw profile for the timesteps in the adjacent contour plots and grey coloured profiles represent throw versus height profiles at previous timesteps to illustrate the evolution of fault growth.

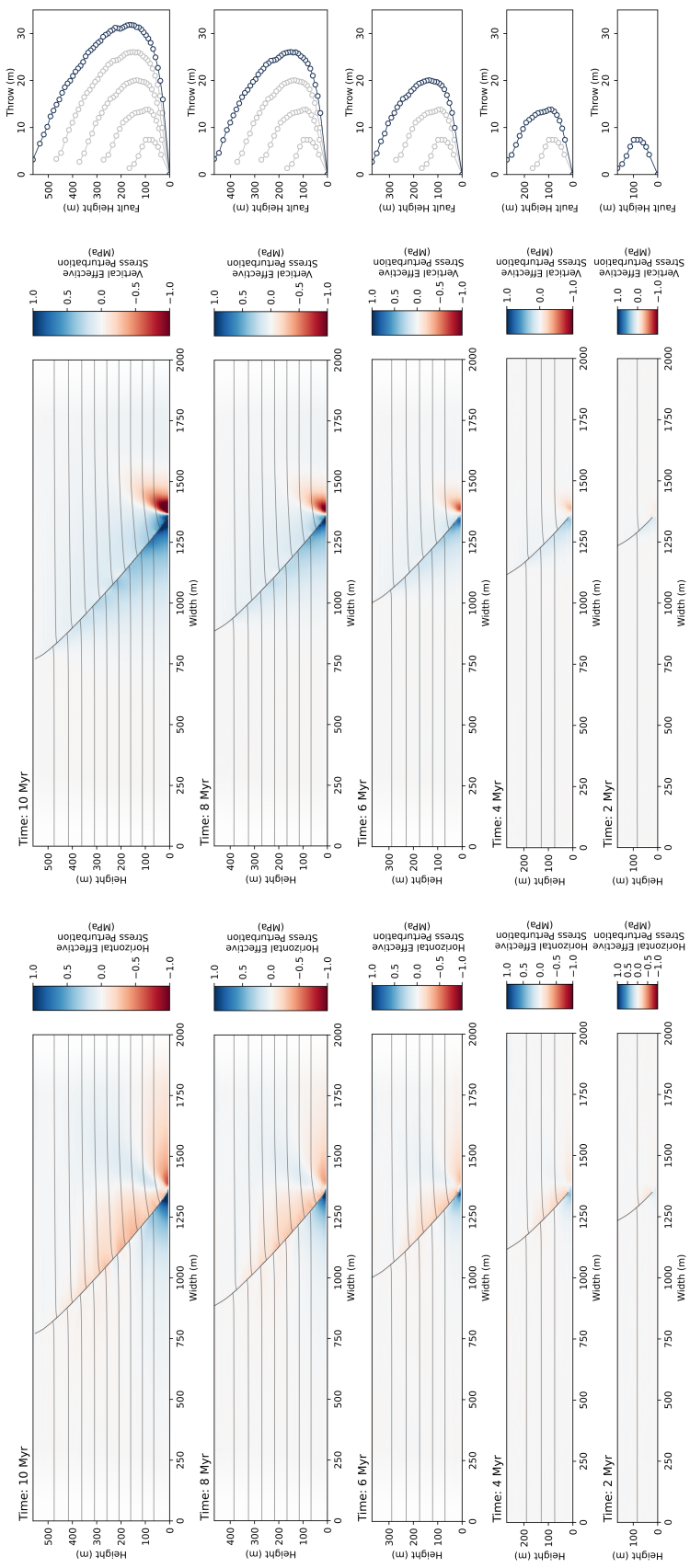


Figure 5.6: Horizontal and vertical effective mean stress perturbation contour plots at 2 million-year time increments showing the evolution of a normal fault hosted in laterally-pinned conditions that propagates simultaneously with the deposition of granular sediment at a rate of 100 metres per million years. The fault propagates with an initial dip of 60° that shallows to ~40° with compaction. The residual friction angle is 5° and the host material is characterised by the m1 material compaction profile. Offset grey horizontal lines represent stratigraphic markers at 1 million-year time intervals. The throw versus height graphs that accompany the contour plots display the accrual of vertical displacement throughout the growth of this fault. Points represent throw measurements taken at stratigraphic markers with a 0.2 million-year depositional interval. Blue colours represent the throw profile for the timesteps in the adjacent contour plots and grey coloured profiles represent throw versus height profiles at previous timesteps to illustrate the evolution of fault growth.

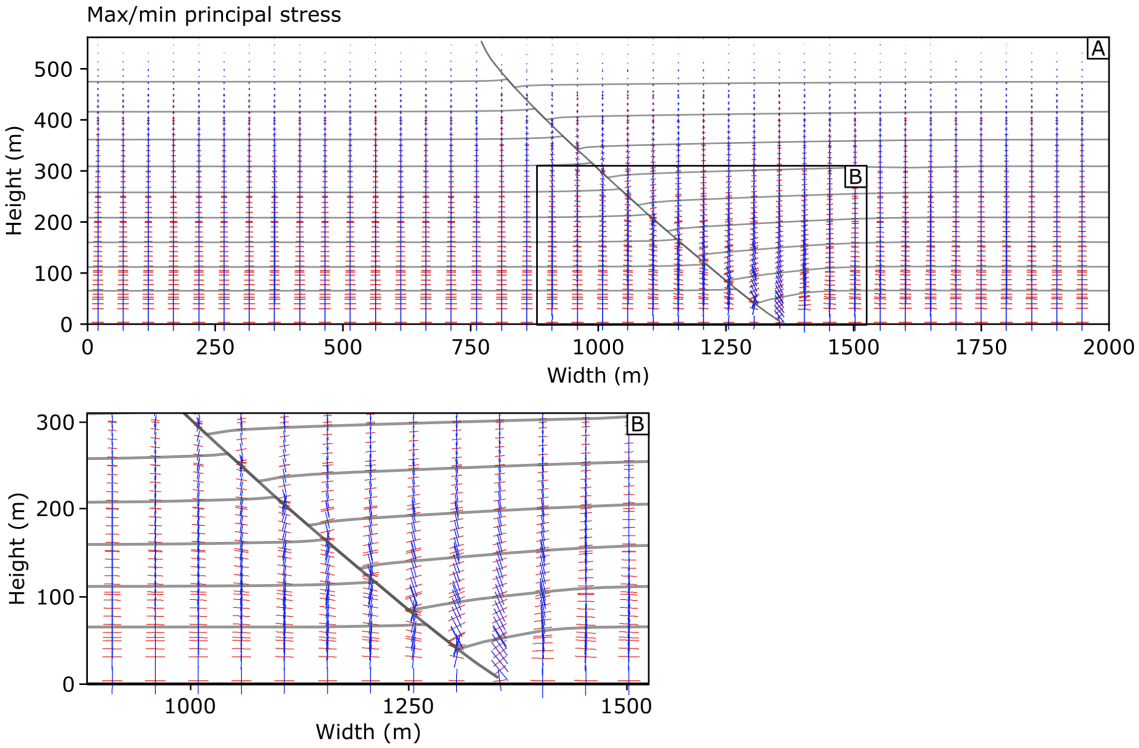


Figure 5.7: (A) Maximum (blue) and minimum (red) principal stress vectors at a 50 metre spacing for the m1-fr5-d60 model run at the final 10 million-year timestep. (B) Shows a zoomed in region centred on the lower fault tip exhibiting rotation of the principal stress axes. The size of the vector symbol scales with the magnitude of the stress, which increases with burial depth.

hosted in the m2 and m3 materials accrue lower maximum throw values compared to faults hosted in the m1 material (Figure 5.4 B), which reflects the incrementally lower amounts of mechanical compaction experienced by the m2 and m3 materials with burial depth, respectively (Figure 5.4 A). Interestingly, faults hosted in the m4 material initially accrue lower maximum throw values than faults hosted in the m2 and m3 materials at heights less than 450 m and 600 m, respectively. However, at fault heights greater than 450 m and 600 m, respectively, the maximum throw values are larger for faults hosted in the m4 material than their m2 and m3 counterparts (Figure 5.4 B). All else being equal, the gradient of the T_{max} versus fault height trends (Figure 5.4 B) for faults hosted in the m1 and m4 materials are approximately equal, which reflects the similarities in their compaction profile gradients at burial depths deeper than 150 m (Figure 5.4 A). However, faults hosted in the m1 material yield larger maximum throw values than those of faults hosted in our m4 material because of the differences in their compaction profiles in the first 150 m of burial below the surface.

The gradients of the T_{max} versus fault height trends (Figure 5.4 B) for faults hosted in the m2 and m3 materials decrease with increasing fault height in a curvilinear fashion as the rate of material compaction reduces with greater burial depth. Whereas, the near-constant gradients of the T_{max} versus fault height trends of faults hosted in the m1 and m4 materials reflect their respective near-constant compaction profiles with burial depths in excess of 150 metres (Figure 5.4 A). Once fault-hosting material ceases to undergo further compaction, as characterised by the m3inh and m4inh materials (Figure 5.4 A) at burial depths greater than ~350 m, the T_{max} versus fault height gradient decreases dramatically to near-zero with increasing fault height (Figure 5.4 B). The influence of inhibited material compaction with burial depth on the accrual of fault throw is seen most clearly in the effective stress contour plots and accompanying throw versus height plots illustrated in Figures 5.8, 5.9 & 5.10. Here

we see that throw continues to accumulate in the upper portions of the faults that are hosted in compacting stratigraphy at burial depths shallower than ~350 m, but fault throw ceases to accumulate on deeper portions of the faults that are hosted in stratigraphic intervals which do not undergo compaction (Figures 5.8 & 5.9). The throw versus height plots of the m3inh and m4inh simulations exhibit flat gradients across the central portion of the fault, where throw values are roughly constant – characteristic of *'M-style'* faults (Chapter 1, Figure 1.6) – and the locus of maximum throw climbs upward compared to the m3 and m4 uninhibited cases which have T_{max} values located in the lower to central third of the fault height and *'C-shaped'* throw versus height profiles (Figure 5.10) (Muraoka and Kamata, 1983). The m3inh and m4inh sensitivity runs also exhibit elevated effective mean stress perturbations in the lower portion of the tier compared to their m3 and m4 model counterparts (Figures 5.8 & 5.9).

5.4.2 Dip angles and fault throw

Polygonal fault systems exhibit an array of fault dip angles that range from as low as 30° at greater burial depths that have experienced high levels of compaction to as high as 80° in some shallowly buried upper tip regions (Clausen et al., 1999; Lonergan et al., 1998a; Cartwright et al., 2003; Shoulders et al., 2007). We investigate the sensitivity of the accumulation of throw on a fault hosted in the m1 material with a residual friction angle of 5° to different propagating dip angles, that shallow as a result of compaction throughout the evolution of our models (Figure 5.4 G & 5.13).

All else being equal, the greatest throw values accumulate on faults that propagate with an initial dip angle of 60° that shallows with compaction to a dip angle of ~40° at depth (Figures 5.13, 5.14, & 5.15). Lower throw values are measured on faults with both increasing and decreasing initial dip angles from the 60° dip reference case (Figure 5.4 D & F and Figure 5.14). At the conclusion of our 10 million-year

model simulations, the lowest maximum throw values accrue on fault planes with propagating dip angles of 80°, followed by 40°, then 70°, then 50°, with the highest throw values accrued on faults with a propagating dip angle of 60° (Figure 5.4 D and Figure 5.14). As a percentage of the maximum throw recorded on a fault with a propagating dip of 60° (hosted in the m1 material with a residual friction angle of 5°), faults with dip propagation angles of 40°, 50°, 70°, and 80° yield values of 61%, 87%, 83%, and 31% respectively (Figure 5.4 F). Our throw versus height plots reveal (Figures 5.14 & 5.15) that steeply dipping fault planes yield more evenly distributed *'C-shaped'* throw versus height profiles and shallower dipping fault planes yield *'L-shaped'* throw versus height profiles with greater throw values skewed to the lower portions of the fault (Chapter 1, Figure 1.6) (Muraoka and Kamata, 1983; Turrini et al., 2017).

At the maximum fault height achieved at the end of the m1 material simulations, the joint-steepest gradients of the T_{max} versus fault height trends are found on the faults with propagating dip angles of 60° and 70° (Figure 5.4 D). When taking account of compaction of the dip angle (Figure 5.4 G & 5.13), the average compacted dips of the 60° and 70° cases are ~40-50° and ~50-60° respectively. As the gradients of the T_{max} versus fault height trends decrease as the fault dip angle either increases or decreases from these values respectively, Figure 5.4 E suggests that that the greatest amount of throw occurs between these two cases – on a fault plane with a dip angle of ~45°. This is consistent with the stress decomposition of an overburden load with respect to a fracture plane, where the maximum shear stress occurs at a 45° angle to the maximum principal stress (Fossen, 2016).

5.4.3 Residual friction angles and fault throw

The residual friction angle sensitivity study was undertaken with a fault plane with a propagation dip of 60° hosted in each of the m1-m4 materials over residual friction

angles of 5°, 7°, 9°, and 11° based on values compiled from frictional studies of fine-grained sediments (Table 5.1). Our results show that all else being equal, throw values are highest on faults with lower residual friction angles (Figure 5.4 C). Maximum throw values decrease exponentially with increasing residual friction angles, reaching zero when the fault plane friction angle equals the host material peak friction angle (Figure 5.4 E).

At residual friction angles of 5°, all four of the material characterisations yield high maximum throw values with respect to the fault height, with values in the upper range of those recorded from polygonal fault systems (Shin et al., 2010). As the residual friction angle increases to 7°, the maximum throw values with respect to fault height derived from our four material models decrease by ~45%, with values in the mid-lower end of those recorded polygonal fault systems (Shin et al., 2010). An increase in the residual friction angle by a further two degrees to 9° yields maximum throw with respect to fault height values at and below the lowest values recorded from polygonal fault systems, and at residual friction angles of 11° and greater throw ceases to accumulate in substantial quantities across the fault plane (Figures 5.4 C and 5.16).

5.4.4 Throw versus height profiles

The throw versus height profiles derived from our model simulations (Figures 5.5, 5.8, 5.11, 5.14, 5.16, 5.18) share a striking resemblance to those derived from PFS studies from basins around the world (Morgan et al., 2015; Turrini et al., 2017; Wrona et al., 2017), including those presented in Chapter 3. Figure 5.18 shows the side-by-side comparison of throw versus height profiles for faults with different propagating dip angles, residual friction angles, and host material compaction profiles at the end of our 10 million-year simulations. A commonality across all of the simulated throw versus height profiles is the steeper lower tip gradient compared to the upper tip gradient

(Table 5.2 and Figure 5.18). A greater proportion of the throw that accumulates on the faults over the course of the 10 million-year simulation accrues in the lower third and central third of the tier. Fault throw versus height profiles have curved *'C-shaped'* or *'L-shaped'* geometries in all cases other than the m3inh and m4inh simulations which model the influence of non-compacting stratigraphy on the accrual of fault throw (Figure 1.6). In the m3inh and m4inh cases, the throw versus height profiles have a flatter *'M-shaped'* central portion and lower maximum throw with respect to fault height values (Table 5.2 and Figures 5.10 & 5.18).

Figure 5.5 illustrates an example of the temporal evolution of throw versus height profiles throughout the growth of a normal fault hosted in laterally-pinned conditions. Here fault throw accumulates proportionately with successive fault propagation and sedimentation throughout the temporal evolution of our models. Throw versus height plots have quasi-symmetric profiles in the earliest phases of growth ($\leq$2.5 million-years) that become more asymmetric with continued fault growth through time ($\geq$5 million-years), where greater throw values are skewed towards the lower third of the fault.

5.4.5 Throw rates

We measured the upper tip throw rate for each simulation run as the throw accumulated at the stratigraphic marker deposited 1 million-years earlier. Our measured throw rates range between 0-10.45 m/m.y., with the fastest throw rates recorded on the faults with the greatest T_{max} values as a percentage of the fault height (Table 5.2 and Figure 5.19). The measured throw rates increase temporally throughout the evolution of the model simulations, reflecting the greater amounts of throw that accumulate at each subsequent timestep because of the larger thickness of differentially compacting sediment in the footwall and hanging wall as the fault height increases (Figure 5.19). The throw rates recorded from our model simulations fall within the

Model simulation	**Upper Tip Gradient**	**Lower Tip Gradient**	**Maximum Throw (m)**	**Fault Height (m)**	**Maximum Throw / Fault Height**	**Throw Rate (m/m.y.)**
m1-fr5-d60	0.108	0.480	31.84	564	5.65%	10.45
m1-fr7-d60	0.063	0.258	17.96	564	3.18%	6.54
m1-fr9-d60	0.028	0.099	6.38	564	1.13%	3.25
m1-fr5-d40	0.055	0.362	19.64	564	3.48%	5.38
m1-fr5-d50	0.084	0.477	28.02	564	4.97%	7.56
m1-fr5-d70	0.093	0.357	26.59	564	4.71%	8.48
m1-fr5-d80	0.032	0.128	9.94	564	1.76%	2.33
m2-fr5-d60	0.098	0.378	27.12	602	4.50%	9.58
m3-fr5-d60	0.091	0.322	25.04	647	3.87%	9.09
m4-fr5-d60	0.096	0.398	38.86	776	5.00%	9.63
m3inh-fr5-d60	0.092	0.212	17.48	653	2.68%	4.63
m4inh-fr5-d60	0.060	0.139	16.29	813	2.00%	4.18

Table 5.2: Upper and lower tip gradients, maximum throw values, and throw rates for faults with different material compaction profiles, propagating dip angles, and residual friction angles from our sensitivity analysis. All values are measured at the conclusion of each respective simulation at the 10 million-year timestep.

same range of those recorded from the upper tips of the Vøring Basin PFS, in the Norwegian Sea where similar sedimentation rates are recorded to those used in our models (King and Cartwright, 2020) (Chapters 3 & 4).

5.4.6 Stress field perturbations

The series of contour plots produced from our simulations (Figures 5.5, 5.6, 5.8, 5.9, 5.11, 5.12, 5.14, 5.15, 5.16, 5.17) reveal effective mean stress perturbations in the fault footwalls and hanging walls. The lowermost footwalls exhibit reduced (blue colours) effective stress perturbations and are 'shadowed' from the full extent of the overburden, whereas the lower most hanging walls exhibit elevated (red colours) effective stress perturbations because frictional sliding on the fault plane facilitates a rotation of the principal stress axis (Figure 5.7). Elevated effective mean stress perturbations in the hanging walls are concentrated at the basal tier boundary, where values decrease in a fan shape away from a circular focal region located at the lower fault tip to ambient one-dimensional consolidation effective stress values within a few hundred metres of the fault. A lower amplitude region of elevated effective mean stress is also found in the central region of the fault plane, which dissipates within a hundred metres or so of the fault. The stress shadow found in the fault footwalls is greatest at the basal tier boundary, where the footwall effective stress perturbation dissipates in the triangular area underneath the fault plane within a few hundred metres of the lower tip.

The horizontal effective stress perturbations are elevated (red colours) in a triangular region adjacent to the fault plane and in a basal region at the lower tier boundary in the fault hanging wall. The horizontal effective stress perturbations are reduced (blue colours) in the lowermost footwall and in a dilational triangular zone in the hanging wall that separates the two aforementioned elevated areas, which is associated with the hinge of bed rotation caused by frictional sliding on the fault plane.

The vertical effective stress perturbations are elevated in a circular shaped focal region at the base of the fault hanging wall, and are reduced in a ~100 metre radius of the fault plane in both the footwall and hanging wall. The effective mean stress (and both the vertical and horizontal components) perturbations are greater in the m3inh and m4inh material models which stop compacting at depths in excess of ~350 metres. In these non-compacting cases, the focal regions of effective stress perturbations spread upward across the portion of the fault plane hosted within non-compacting strata (Figures 5.8 & 5.9). The lateral boundaries of all simulations exhibit unperturbed one-dimensional consolidation stress fields.

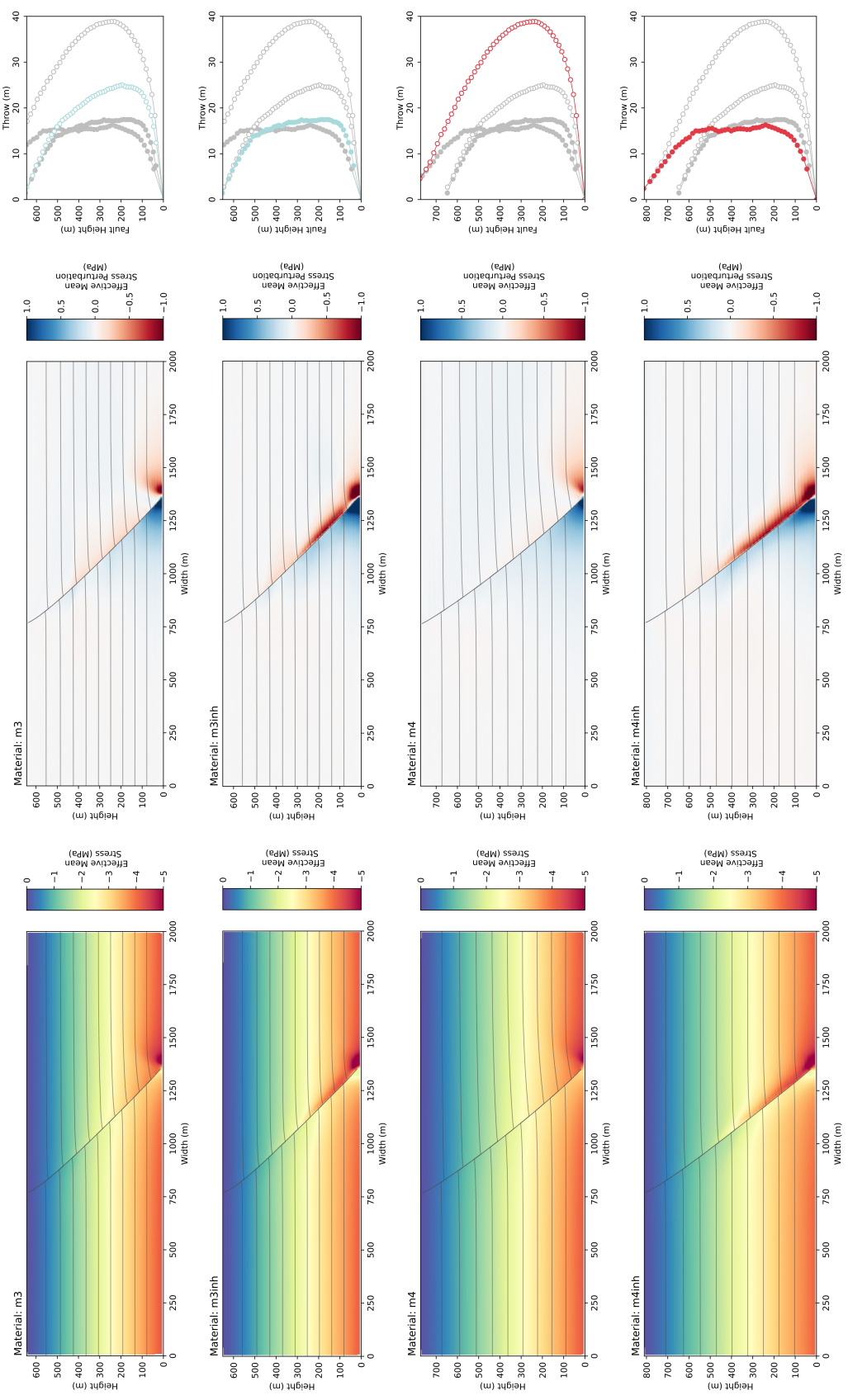


Figure 5.8: Effective mean stress and perturbation contour plots and accompanying throw versus height plots for faults with a propagating dip angle of 60° and a residual friction angle of 5° hosted in the m3, m3inh, m4, and m4inh materials at the conclusion of their respective 10 million-year simulations.

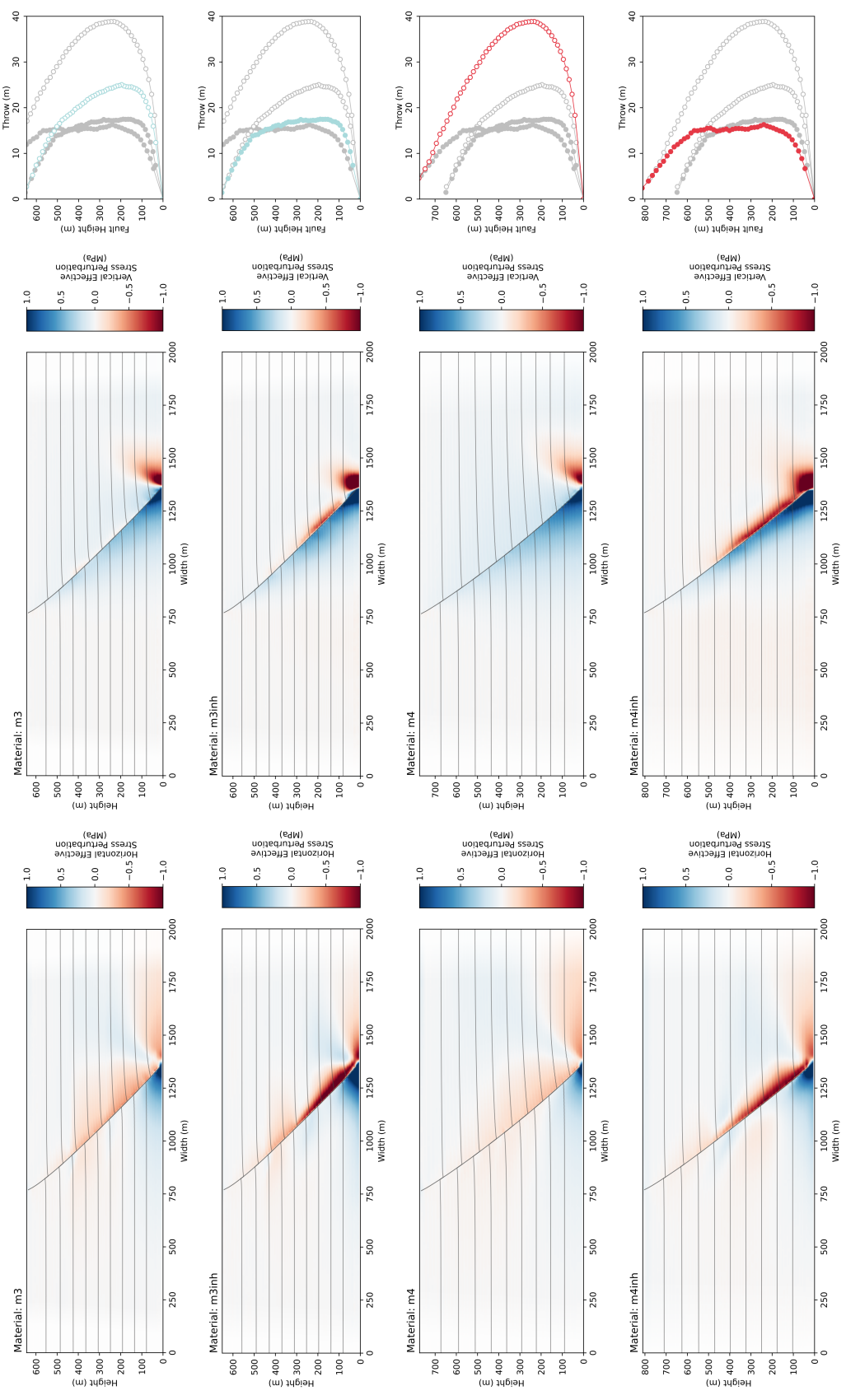


Figure 5.9: Horizontal and vertical effective stress perturbation contour plots and accompanying throw versus height plots for faults with a propagating dip angle of 60° and a residual friction angle of 5° hosted in the m3, m3inh, m4, and m4inh materials at the conclusion of their respective 10 million-year simulations.

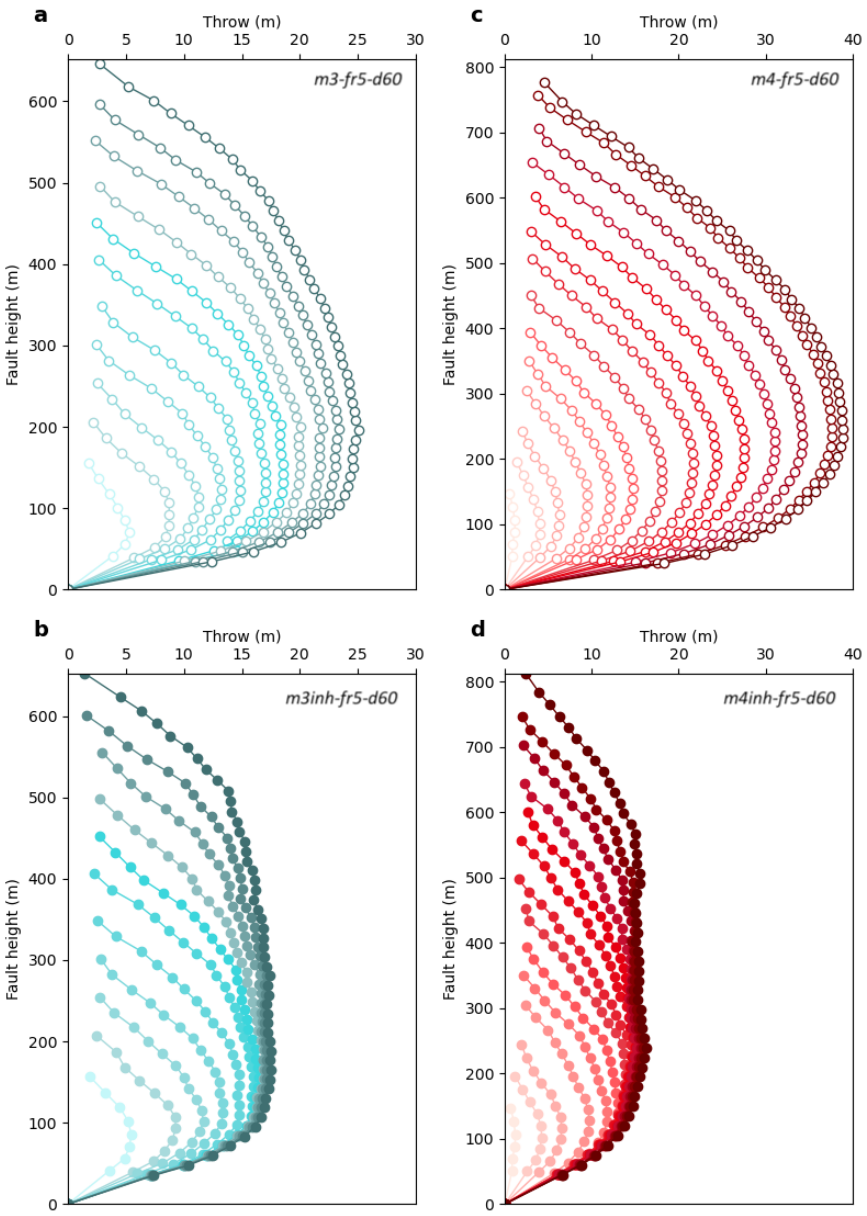


Figure 5.10: The evolution of throw versus height profiles for faults with a propagating dip angle of 60° and a residual friction angle of 5° hosted within compacting and non-compacting materials: (a) m3 material, (b) m3inh material, (c) m4 material, and (d) m4inh material.

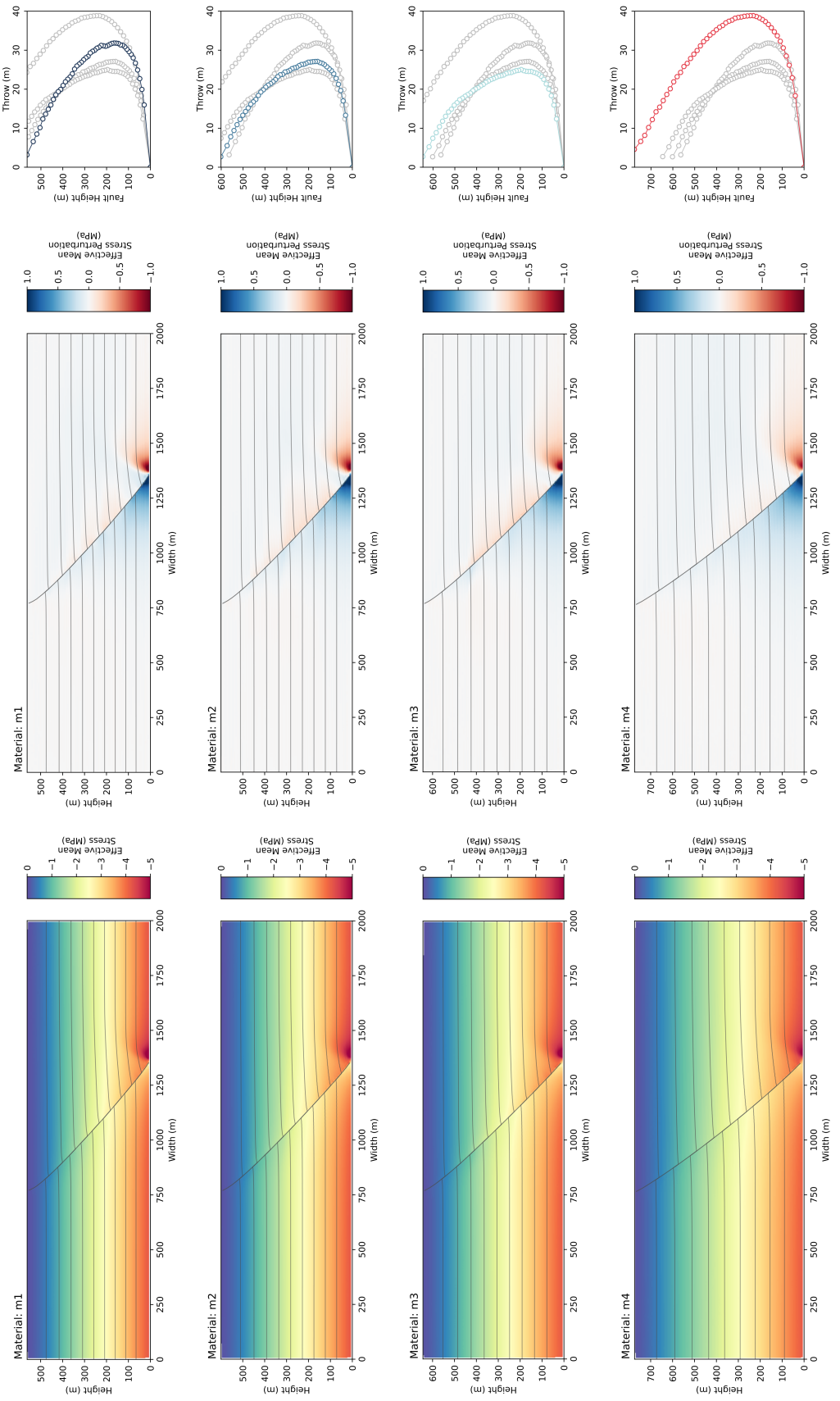


Figure 5.11: Effective mean stress and perturbation contour plots and accompanying throw versus height plots for faults with a propagating dip angle of 60° and a residual friction angle of 5° hosted in the m1, m2, m3, and m4 materials at the conclusion of their respective 10 million-year simulations.

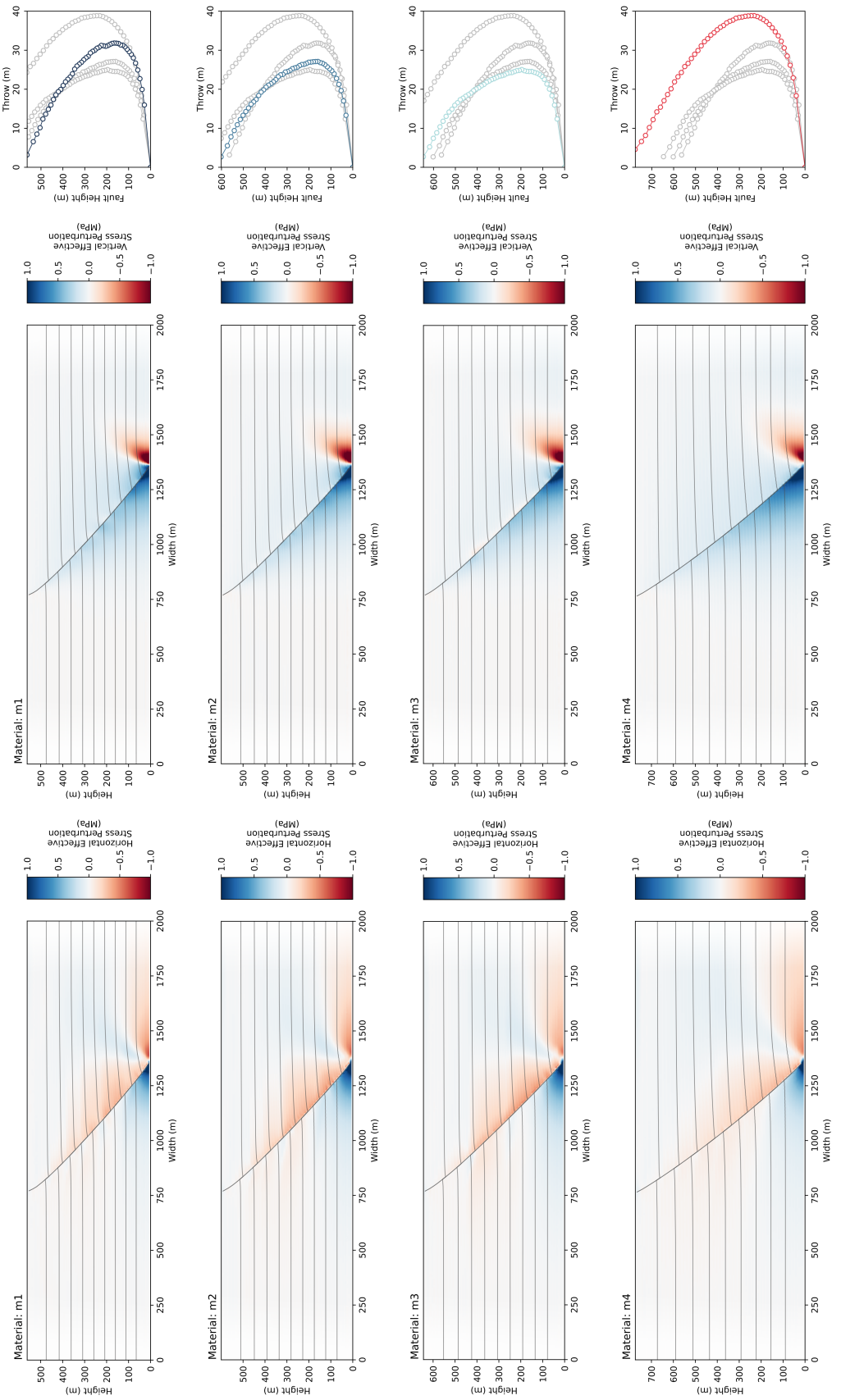


Figure 5.12: Horizontal and vertical effective stress perturbation contour plots and accompanying throw versus height plots for faults with a propagating dip angle of 60° and a residual friction angle of 5° hosted in the m1, m2, m3, and m4 materials at the conclusion of their respective 10 million-year simulations.

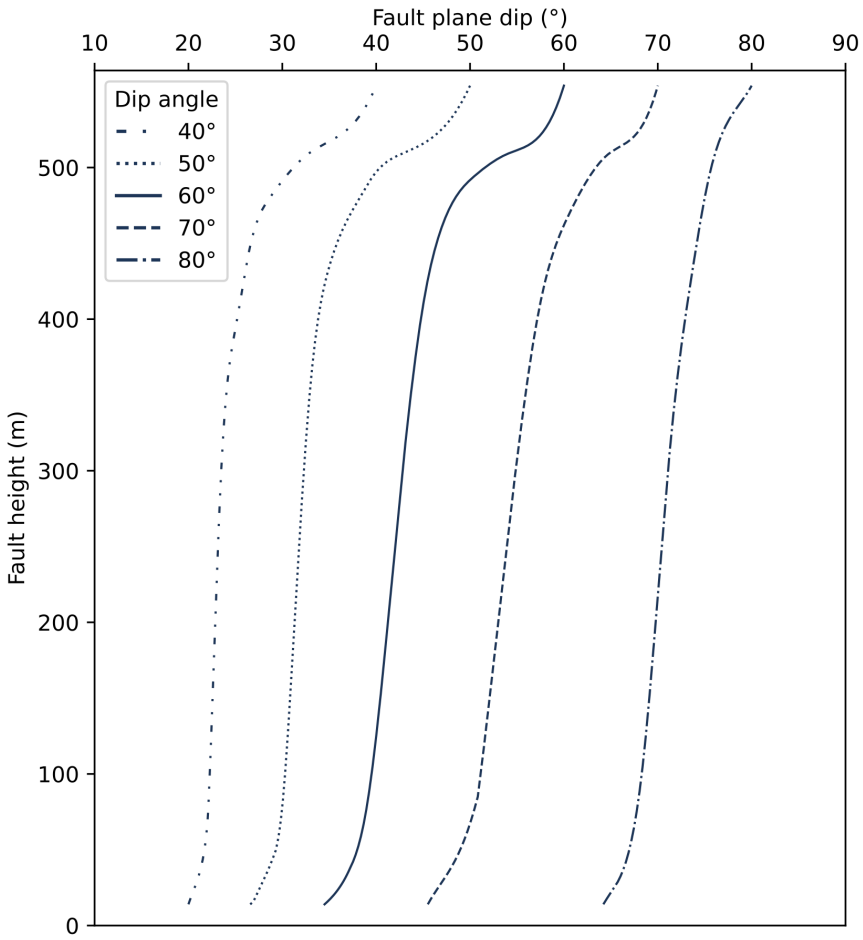


Figure 5.13: Fault plane dip versus fault height for faults with different propagating dip angles hosted in the m1 material at the conclusion of the 10 million-year simulations.

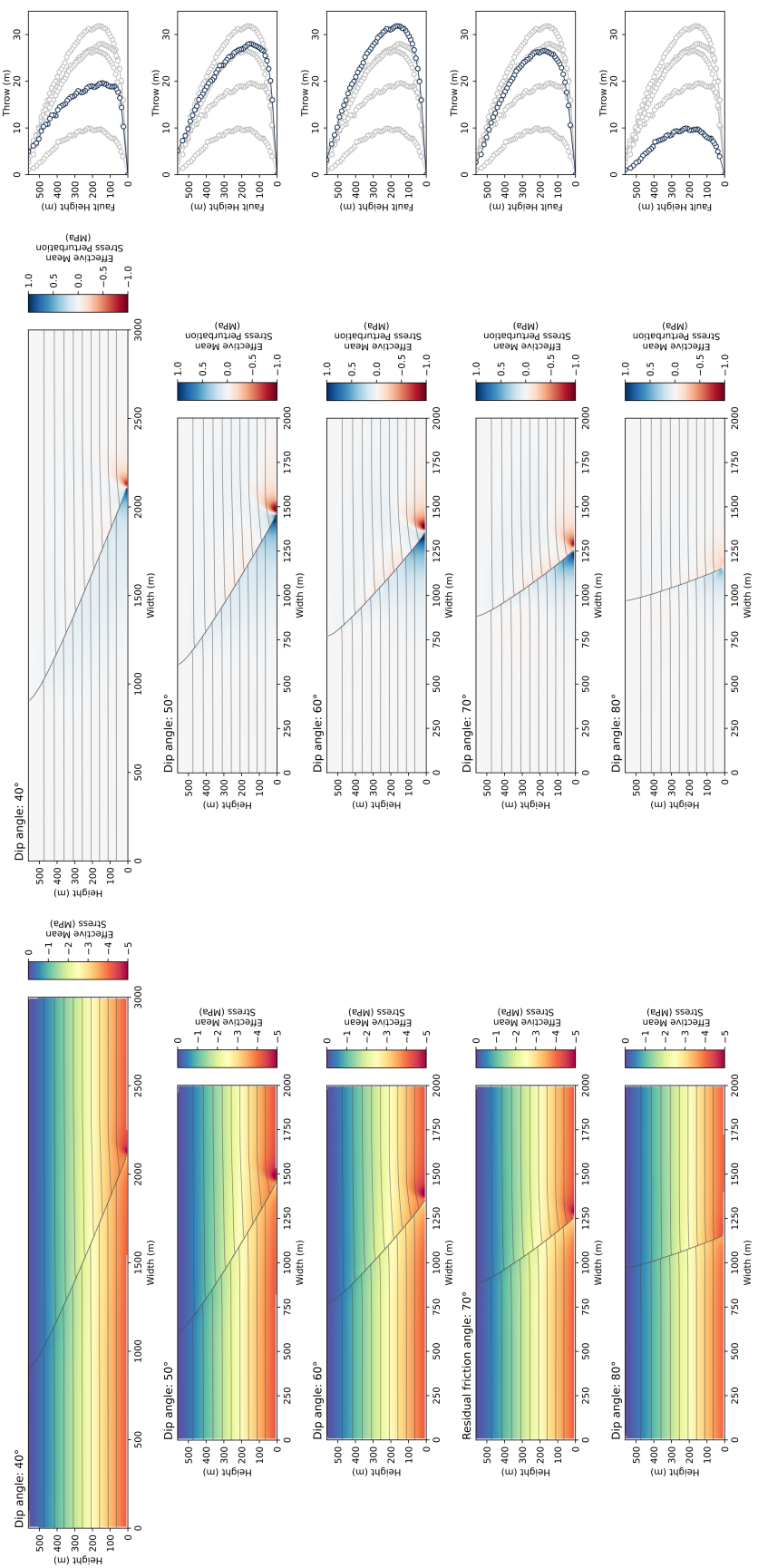


Figure 5.14: Effective mean stress and perturbation contour plots and accompanying throw versus height plots for faults hosted in the m1 material and a residual friction angle of 5°, 50°, 60°, 70°, and 80° at the conclusion of their respective 10 million-year simulations.

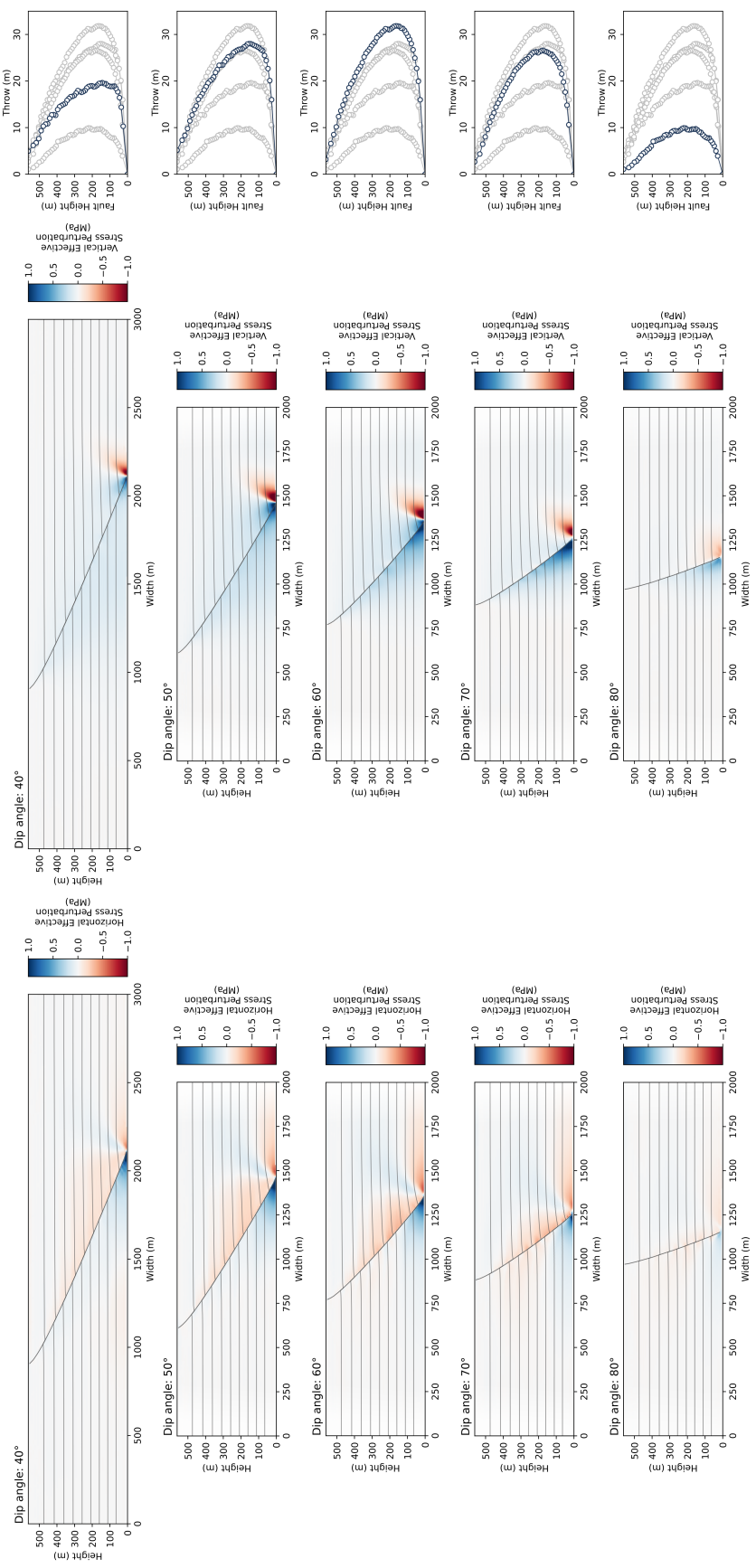


Figure 5.15: Horizontal and vertical effective stress perturbation contour plots and accompanying throw-versus-height plots for faults hosted in the m1 material and a residual friction angle of 5° with starting dip angles of 40°, 50°, 60°, 70°, and 80° at the conclusion of their respective 10 million-year simulations.

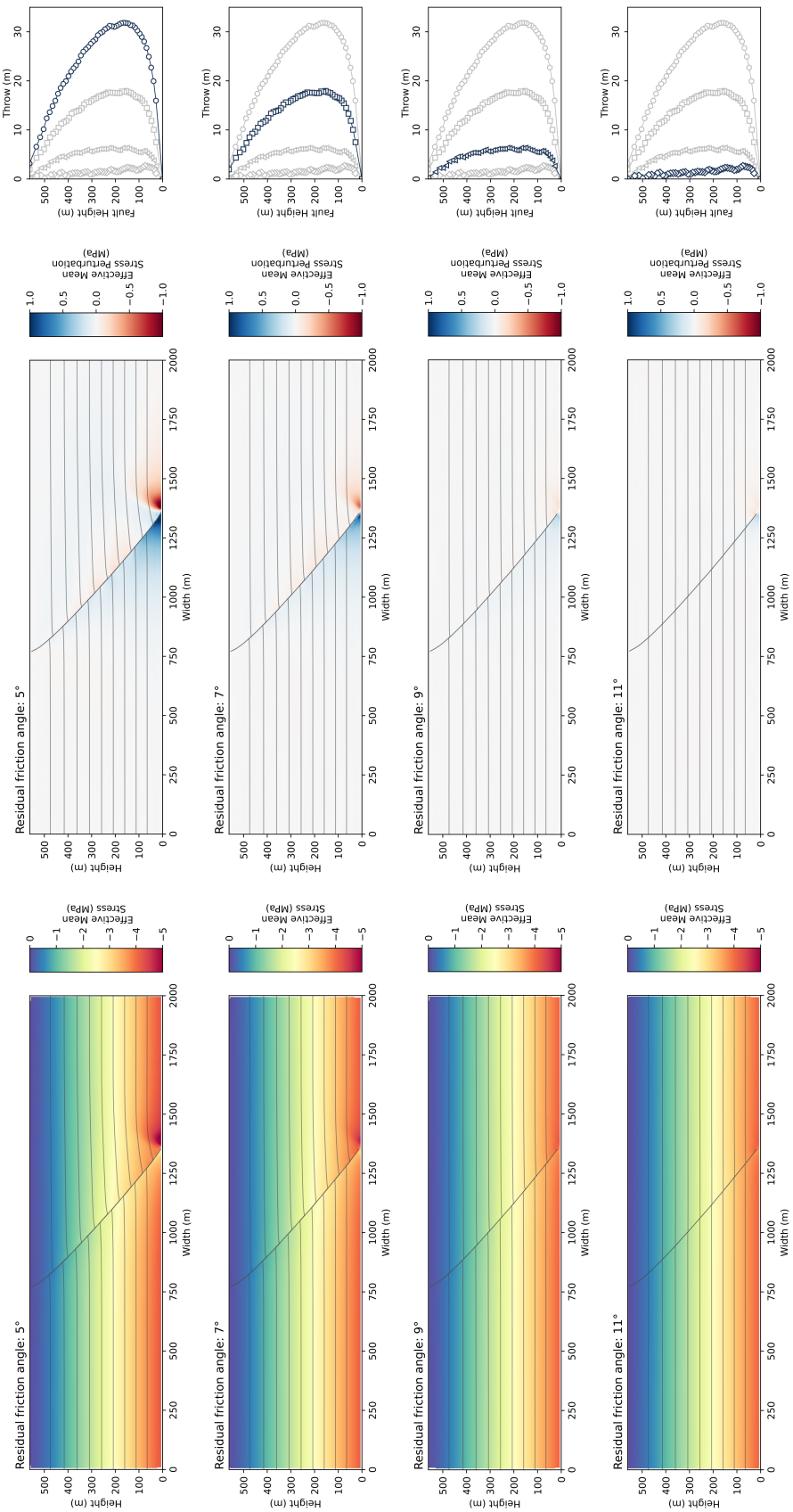


Figure 5.16: Effective mean stress and perturbation contour plots and accompanying throw versus height plots for faults hosted in the m1 material with a propagating dip angle of 60° and residual friction angles of 5°, 7°, 9°, and 11° at the conclusion of their respective 10 million-year simulations.

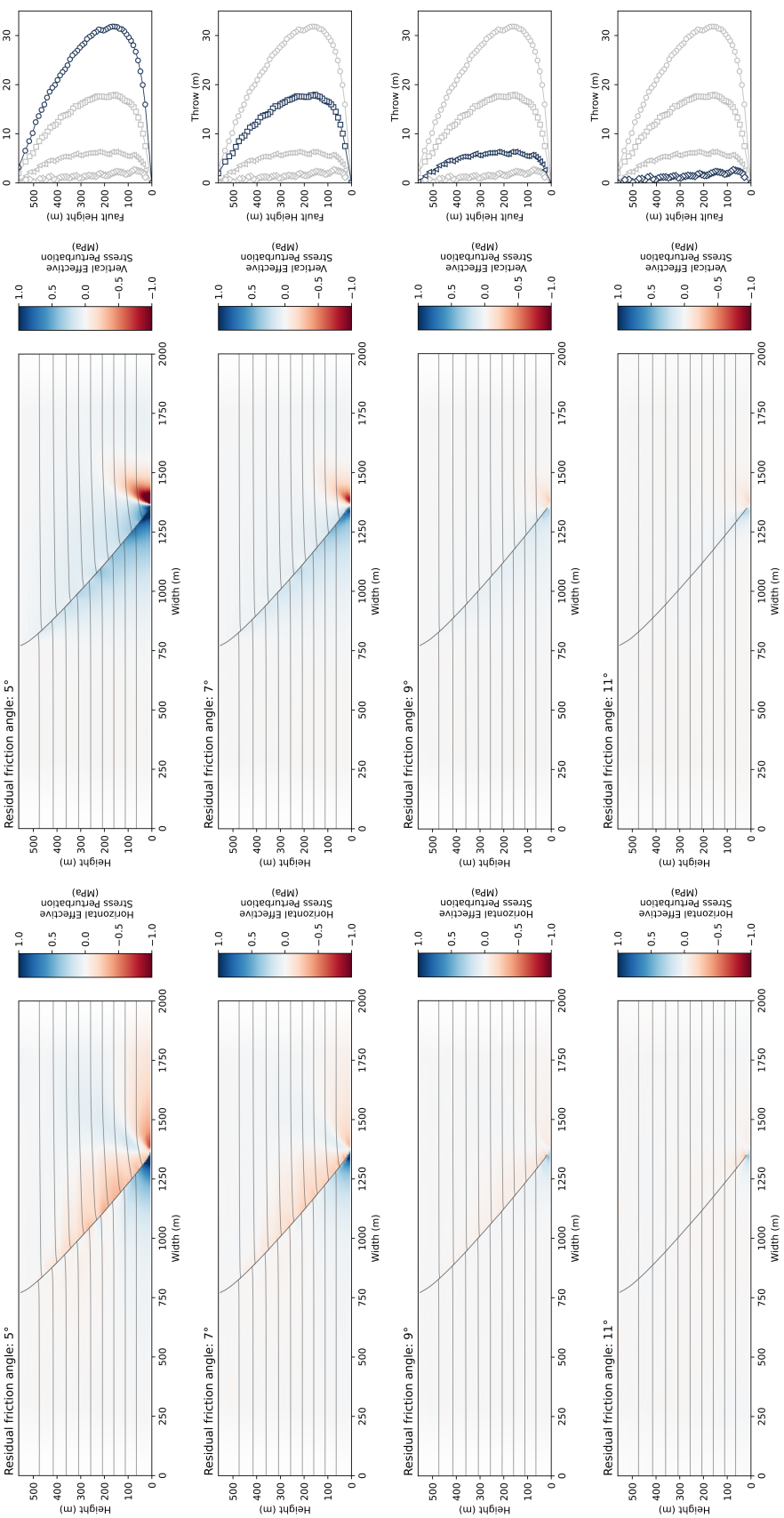


Figure 5.17: Horizontal and vertical effective stress perturbation contour plots and accompanying throw versus height plots for faults hosted in the m1 material with a propagating dip angle of 60° and residual friction angles of 5°, 7°, 9°, and 11° at the conclusion of their respective 10 million-year simulations.

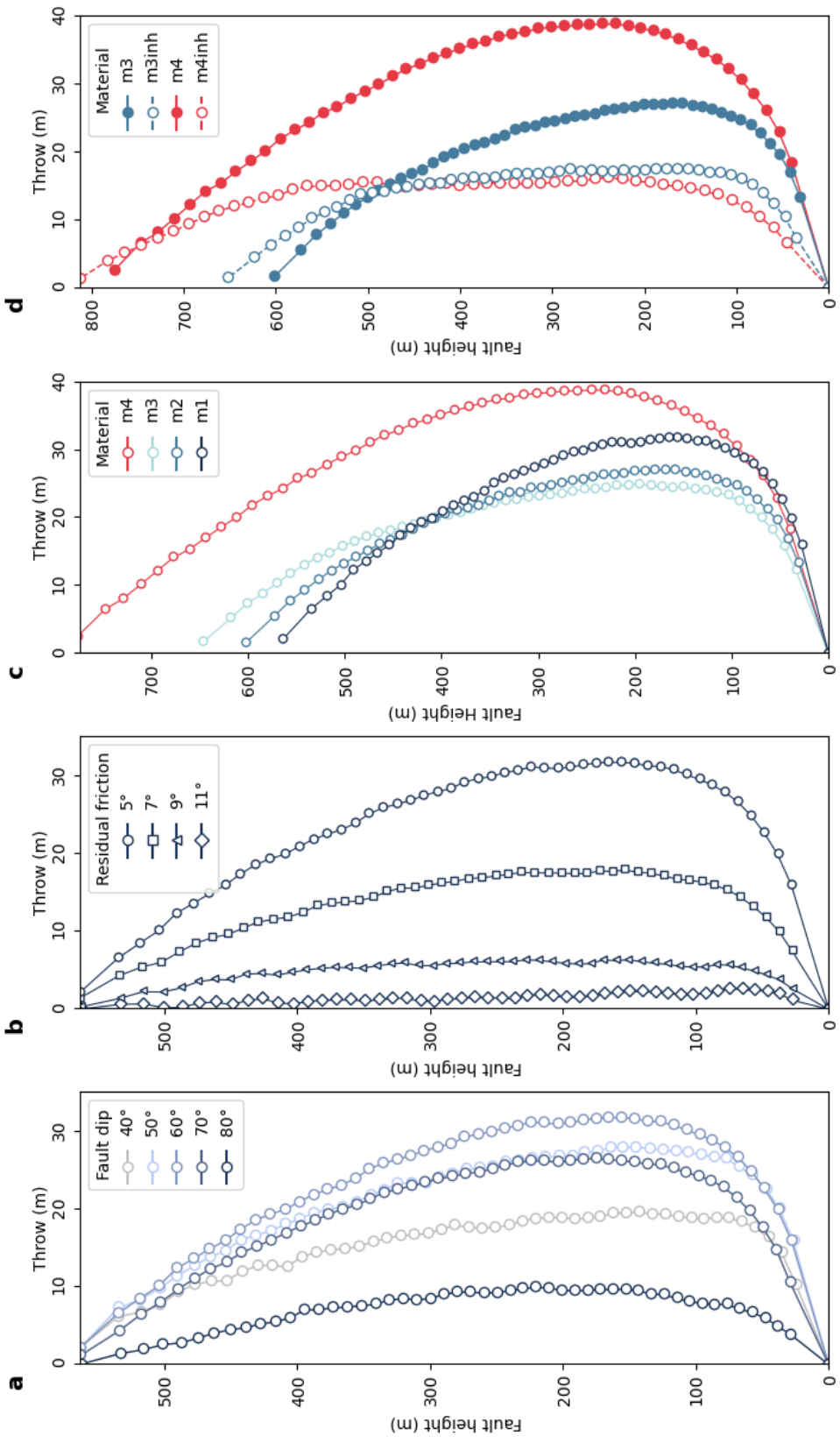


Figure 5.18: Throw versus fault height profiles for faults at the end of the 10 million-year simulation: (a) with propagating dip angles between 40°-80°, hosted in the m1 material with a residual friction angle of 5°; (b) with residual friction angles between 5°-11°, hosted in the m1 material with a propagating dip angle of 60°; (c) hosted in the m1, m2, m3, and m4 materials, with a residual friction angle of 5° and an initial fault dip angle of 60°; (d) hosted in the m3, m3inh, m4, and m4inh materials, with a residual friction angle of 5° and a propagating dip angle of 60°.

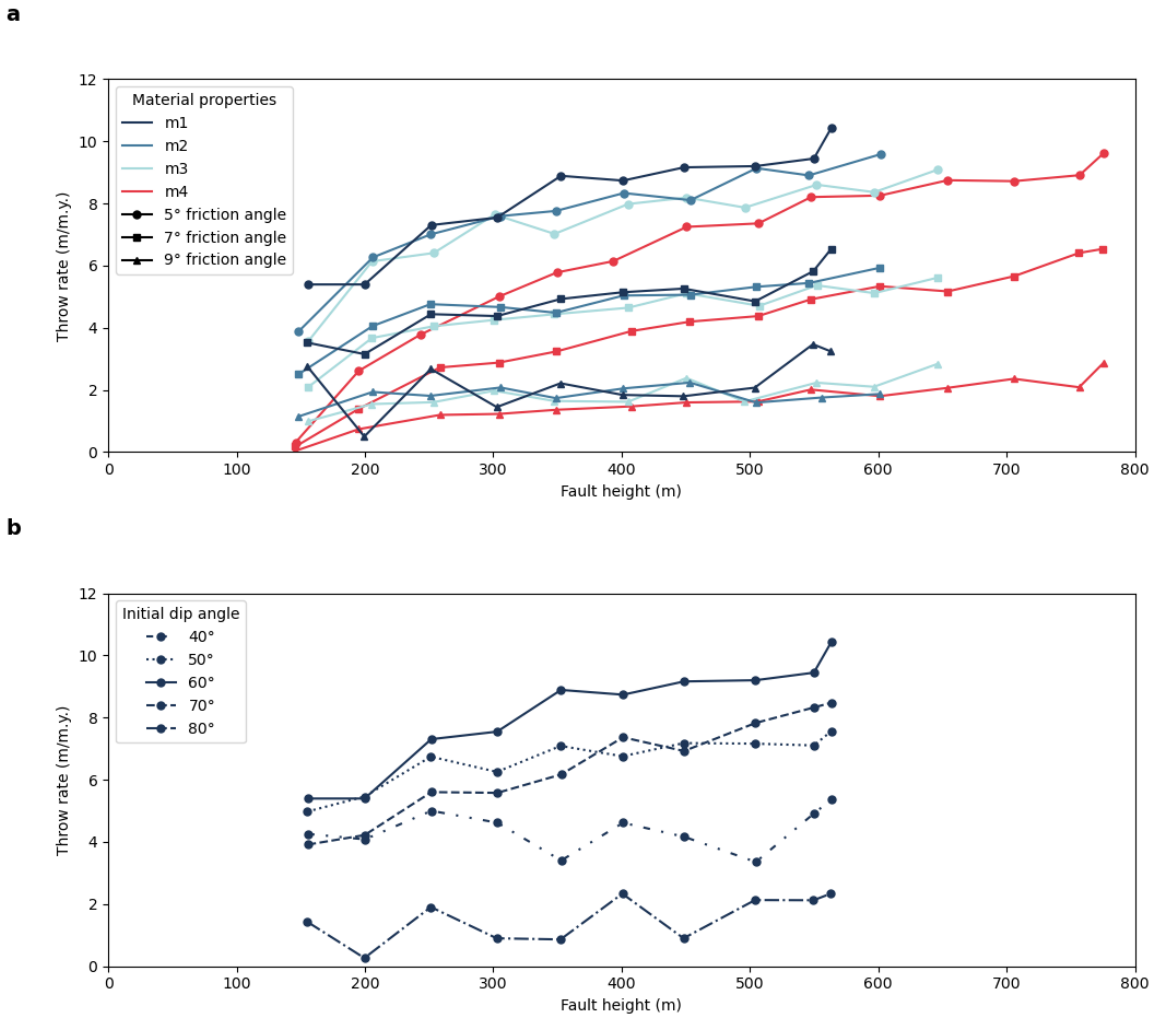


Figure 5.19: Throw rate with respect to fault height measured as the amount of throw accumulated on the stratigraphic marker deposited 1 million-years earlier for: (a) materials m1, m2, m3, and m4 over residual friction angles of 5°, 7°, and 9° on a fault plane with a propagating dip angle of 60°; (b) faults with propagating dip angles of 40°, 50°, 60°, 70°, and 80° hosted in the m1 material with a residual friction angle of 5°.

5.5 Discussion

The purpose of this study was to establish if polygonal fault systems can grow as a result of gravity-driven differential compaction under realistic material property and burial conditions, and if so, to derive which factors are the largest drivers (and inhibitors) of polygonal fault growth. The results of our sensitivity analysis show that gravity-driven differential compaction, facilitated by frictional sliding on a dipping fault plane hosted in laterally-pinned fine-grained sediments, can explain the accrual of polygonal fault throw over physical and material property values recorded from shallowly buried fine-grained sediments in hydrostatic conditions. The empirical scaling relationship between the maximum throw values and heights of polygonal faults (Shin et al., 2010) can be achieved via gravity-driven differential compaction in laterally-pinned hydrostatic conditions at residual friction values less than ~9° on faults with a range of dip angles that are hosted in fine-grained sediments with a range of compaction profiles (Figure 5.4). These results suggest that the accrual of throw on polygonal faults is most sensitive to changes in the residual friction angle.

5.5.1 Upscaling computational models to heterogeneous PFSs

Our modelling strategy did not attempt to replicate the complexity of intersecting polygonal fault geometries (Lonergan et al., 1998a) or heterogeneities between units that comprise a PFS tier (Cartwright et al., 2003; Verschuren, 2019). We characterised our models with a single continuous fault plane with a uniform residual friction angle over its entire surface, however, in reality a single polygonal fault observed at field outcrop scale may comprise a multitude of smaller fractures and splays (Childs et al., 2007, 2009; Fossen, 2016; Tewksbury et al., 2014; Verschuren, 2019) that aggregate to give the appearance of a single plane at the resolution limits of seismic reflection data. These heterogeneities and fault intersections may explain the

differences between the smoothly tapering throw profiles produced in our simulations (Figure 5.18) and the jagged or stepped throw profiles recorded from polygonal faults imaged in seismic reflection data (Neagu et al., 2010a; Morgan et al., 2015; Turrini et al., 2017; Wrona et al., 2017) (Chapter 3). However, despite the relative homogeneity of our models compared to real PFS tiers, our results successfully reproduce the *'C-, M-,* and *L-shaped'* geometries of polygonal fault throw profiles. In addition, the throw rates derived from our models are consistent with those recorded from the upper tips of surface-breaching polygonal faults in the Vøring Basin that are hosted in a tier with similar sedimentation rates to those used in our models (King and Cartwright, 2020) (Chapter 4).

5.5.2 Factors governing the evolution of PFS growth

Polygonal faults may be considered as dewatering structures of shallowly buried fine-grained sediments. Although this study did not explicitly investigate the role of overpressure, elevated fluid pressure may facilitate the episodic growth of some polygonal faults at higher residual friction angles, and contribute to the growth of polygonal faults that span ultra-low permeability fine-grained units which may experience periods of compaction disequilibrium. If, for example, a polygonal fault ceases its growth because of an increase in the fault friction angle, then fluid pressure may build with increasing burial depth in undrained units until the fluid pressure acting on the fault plane reduces the effective mean stress sufficiently to facilitate frictional sliding at low shear stresses (Bolton et al., 1998; Watterson et al., 2000), thus reactivating fault growth. It is worth noting that overpressured mobile units found at the base of fine-grained sedimentary tiers may act as décollement surfaces and have been suggested as a means to nucleate PFSs (Watterson et al., 2000). However, investigating the nucleation of PFSs was beyond the scope of this study, which focused solely on the drivers of post-nucleation growth.

The death of a PFS may occur once its hosting units no longer undergo differential volumetric strain. This may occur from the base of the tier upwards in a burial conveyor-belt like fashion, or in a single fossilisation phase. The slowing and ultimate cessation of differential volumetric strain may occur as frictional sliding is inhibited by an increase in the residual friction angle and/or the slowing of volumetric change of the host units caused by lithification. The upward termination of a PFS may also occur because of a depositional facies change (Cartwright et al., 2003; Jackson et al., 2014), and the growth of individual polygonal faults within a PFS may be inhibited by the intersection of neighbouring faults (Lonergan et al., 1998a). Fluctuations in the overburden loading rate (both erosional and depositional) may also influence the growth of PFSs. Faster sedimentation rates may increase the rate of compaction in drained conditions or drive overpressure in undrained conditions, therefore driving faster throw rates but also greater PFS tier heights (c.f. the empirical scaling relationship established by Shin et al. (2010)). Erosional events or depositional hiatuses may, on the other hand, limit the subsequent accrual of differential compaction driven throw until the pre-erosional maximum effective stress is reached following re-loading, in which time the material physical properties may have changed to inhibit further differential compaction. In summary, the temporal evolution of individual polygonal faults within a tier may be governed by many factors, however, our sensitivity analysis suggests that the growth of polygonal faults is primarily driven by low residual friction angles on dipping fault planes which facilitate gravity-driven differential compaction.

5.5.3 Implications

The results presented in this study strongly suggest that the growth of normal faults hosted in laterally-pinned sedimentary tiers can be solely facilitated by gravity-driven differential compaction at low residual friction angles. A gravity-driven differential

compaction mechanism is likely the overarching driver of the growth of polygonal fault systems universally, where processes such as overpressure and diagenetically-induced volumetric reductions may act as secondary and tertiary contributing factors, respectively, to enhance or reactivate polygonal faults in some circumstances. In addition to the growth of PFSs, a gravity-driven differential compaction mechanism may also explain why up-dip extensional strains are consistently greater than down-dip compressional strains recorded in shallowly buried gravitational-slope fault systems found on continental shelves (Dalton et al., 2015).

5.6 Conclusions

In this study, we modelled the growth of an isolated fault hosted within laterally-pinned conditions with respect to variable material compaction profiles, residual friction angles, and fault dip angles, using a suite of two-dimensional finite element forward models constructed in *ELFEN*, that coupled upward fault propagation with simultaneous sedimentation and compaction of unconsolidated fine-grained granular sediment. Our results show for the first time, that faults hosted in laterally-pinned conditions – such as those that host polygonal fault systems – can accumulate throw solely through gravity-driven differential compaction under realistic physical property and burial conditions.

The main findings of this study are:

1. Polygonal fault systems can grow solely as the result of gravity-driven differential compaction at low residual friction angles.

2. Maximum throw (T_{max}) as a percentage of fault height values recorded from polygonal fault systems globally (~6%) can be achieved at standard fault dip angles and material property values typical of those recorded from fine-grained sediments at residual friction angles <9°.

3. Throw rates derived from our sensitivity analysis (0-10.45 m/m.y.) are consistent with recently recorded ultra-slow throw rates from the upper tips of polygonal faults in the Vøring Basin, Norwegian Sea (1.4-10.9 m/m.y).

Chapter 6

Summary and Discussion

6.1 Introduction

Understanding the growth of polygonal fault systems has proved enigmatic since they were first reported in the open literature in the late 1980's. Several studies have documented the geometries and distributions of polygonal fault systems in basins around the world (Cartwright et al., 2003; Cartwright, 2011, and references therein), however, there have been relatively few kinematic and temporal investigations of the growth of these enigmatic structures (Morgan et al., 2015; Wrona et al., 2017; King and Cartwright, 2020). Without strong temporal and kinematic calibration, the array of different mechanisms that have been suggested to explain the growth of polygonal faults have remained largely theoretical and establishing the main drivers of PFS growth has proved elusive.

The purpose of this thesis was to establish the temporal evolution of the growth of polygonal fault systems. This aim was achieved through: (1) an investigation of the spatial, temporal, and kinematic evolution of a PFS; (2) the documentation of the first throw rates recorded from polygonal faults globally; and (3) numerical modelling of the drivers of PFS growth using the aforementioned kinematic and temporal findings

as constraints and benchmarks for comparison.

6.2 Summary of Results

Results from Chapter 3: The Spatial, Temporal, and Kinematic Evolution of a Polygonal Fault System

Chapter 3 investigated the spatial, temporal, and kinematic evolution of near-surface and surface-breaching polygonal faults located in the Vøring Basin, Norwegian Sea, using high resolution throw measurements recorded from seismic reflection data calibrated by Ocean Drilling Program (ODP) and industry borehole data.

This study coupled insights from fault throw analysis with the documentation of small growth packages within age-calibrated stratigraphy to determine that the PFS has propagated upward from the lower portion of the tier for much of its growth history, where master polygonal faults have been active at or within a few tens of metres of the seabed from at least the late Pliocene. Offset at the diagenetic opal-CT boundary reflection found in the lower third of the PFS tier, which fossilised before the deposition and faulting of the uppermost portion of the PFS tier, suggests that the accrual of fault throw has occurred over the full vertical extent of the polygonal fault planes throughout the kinematic evolution of the PFS. One of the most striking findings from the spatial analysis of fault throw profiles across the wedge shaped stratigraphy of the study area was the consistency with which macro-scale throw gradient patterns can be correlated between neighbouring polygonal faults. These macro-scale gradient changes may be the result of temporal changes in the amount of differential volumetric strain occurring at depth, and/or differences in the physical and mechanical properties of strata that comprises the PFS host tier, and/or sedimentation rate controlled changes in throw gradient. In contrast to the macro-scale throw gradients that can be correlated across the study area, small-scale throw variations exhibited within the macro-scale gradients are not found systematically

at common seismic reflections and they cannot be correlated beyond neighbouring polygonal faults. These small-scale throw variations and steps are predominately associated with fault intersections, relays, conjugates, and antithetics. In addition, some of the small-scale steps may represent short periods of growth inactivity and/or differences in the intrinsic physical properties of the intra-formational units.

The findings from Chapter 3 provided kinematic constraint to investigate the temporal evolution of the later stages of PFS growth in greater detail in Chapter 4 through throw rate analysis of the upper polygonal fault tips. These findings also provided both kinematic constraint and a basis to investigate the influence of physical properties on polygonal fault growth in Chapter 5 through the use of sensitivity analysis in dynamic finite element forward models.

Results from Chapter 4: Ultra-Slow Throw Rates of Polygonal Fault Systems

The aim of Chapter 4 was to establish the first throw rates recorded from a polygonal fault system. This was achieved by measuring the throw of age-calibrated seismic reflections that are offset by the upper tips of 180 near-surface and surface-breaching polygonal faults located in the Vøring Basin, Norwegian Sea, that have been active at the seabed throughout at least the later stages of their growth. This study area was chosen for its combination of surface-breaching polygonal faults reported by previous studies (Neagu et al., 2010a,b; Ireland et al., 2011; Laurent et al., 2012), high-resolution three-dimensional seismic reflection data, and chronostratigraphic calibration provided by Ocean Drilling Program (ODP) hole 644 (Shipboard Scientific Party, 1987).

The main finding of this study was that polygonal faults have ultra-slow throw rates that range between 1.4-10.9 m/m.y. These throw rates are as much as three orders of magnitude slower than those of the fastest-growing tectonic faults. This

finding not only provided the first measurements of the growth rates of polygonal fault systems but also the lowest ever measured for a fault array of any type globally. The rates recorded in this study mark the lower limit of a continuous spectrum of extensional fault displacement rates recorded from tectonic and gravitational slope fault systems. It is worth noting that the polygonal faults analysed in this study are smaller than the tectonic faults analysed in other studies and similarly sized tectonic faults may have similar slow throw rates to those recorded in Chapter 4. In addition, this study found that individual polygonal faults exhibit a range of throw rate profiles through time that range from near linear to singly or multiply stepped, where the short-term throw rates recorded on stepped profiles range from 0-18 m/m.y. Given that the accommodation of multidirectional extensional faults in laterally-pinned conditions requires a bulk volumetric reduction of the host tier, it is perhaps unsurprising that the polygonal fault throw rates derived in this study are ultra-slow because the rates of geological processes that govern volumetric reductions in shallowly buried fine-grained sediments are intrinsically slow.

The findings from Chapter 4 elucidate our understanding of the rate at which polygonal fault systems grow and provided a temporal constraint to benchmark the results of numerical model simulations which were used to investigate the growth of polygonal faults in Chapter 5.

Results from Chapter 5: Numerical Modelling of the Growth of Polygonal Fault Systems

The aim of Chapter 5 was to investigate the growth of polygonal faults by testing the hypothesis that gravity-driven differential compaction can solely drive the propagation and accumulation of throw on pre-existing polygonal faults that are hosted in laterally-pinned unconsolidated sediments. This hypothesis was tested using field-scale finite element simulations in *ELFEN* to undertake a sensitivity analysis of the

amount of throw that accumulates on a single fault that propagates upward synchronously with the deposition of granular sediment with respect to three main variables: (1) material compaction profiles; (2) residual friction angles; and (3) fault dip angles. The kinematic growth model outlined in Chapter 3 was adopted in the model simulations of Chapter 5.

Sensitivity analysis showed that gravity-driven differential compaction, facilitated by frictional sliding on a dipping fault plane that is hosted within laterally-pinned hydrostatic conditions, can explain the accrual of polygonal fault throw over physical and material property values recorded from fine-grained sediments. The empirical scaling relationship between maximum throw (T_{max}) values and polygonal fault heights established by Shin et al. (2010) was achieved in our model simulations over a range of material compaction profiles and fault dip angles on faults with residual friction angles less than ~9°. The results of this sensitivity study also showed that the cessation of the accrual of fault throw occurred at residual friction angles above ~11° and/or when the fault hosting material no longer underwent compaction. In addition, the throw versus height plots and throw rates derived from these numerical modelling simulations resemble those recorded from polygonal faults found in basins around the world. This study did not explicitly investigate the role of fluid overpressure, however, overpressure may act to enhance or reactivate polygonal fault growth in some PFSs if the fluid pressure acting on a fault plane reduces the effective mean stress sufficiently to facilitate frictional sliding at low shear stresses (Bolton et al., 1998; Watterson et al., 2000).

The results from Chapter 5 strongly suggest that the growth of polygonal fault systems is primarily the result of gravity-driven differential compaction. These findings resolve the longstanding PFS growth enigma and elucidate our understanding of these widespread and fascinating geological structures.

6.3 The Evolution of Polygonal Fault Systems

6.3.1 Nucleation

Although this thesis did not attempt to investigate nucleation, it's findings give reason to speculate that differential compaction may not only drive the growth of polygonal faults but may also play a role in their genesis. The findings of this thesis suggest that the growth of pre-existing polygonal faults are driven by the differential compaction of fine-grained sediments that develops in relation to loading, friction, and geometry. However, differential compaction related to mechanical competency contrasts rather than geometry may explain the nucleation of some polygonal faults in a similar fashion to the development of differential compaction faults associated with claystones onlapping granite hills or sandstone bodies (Powers, 1922; Gay Jr, 1989; Laubach et al., 1999), or depositional thickness variations (Carver, 1968; Labute and Gretener, 1969; O'Connor and Gretener, 1974), albeit at a much smaller scale. Davies (2005) and Davies et al. (2009) presented the first evidence to suggest that the formation of some polygonal faults situated in the northeast Atlantic margin may be initiated by differential compaction associated with the irregular topology of the opal-CT diagenetic reaction boundary. It is tempting to postulate that small-scale differential compaction faulting may also arise in shallowly buried fine-grained sediments in association with mechanically competent concretions and nodules or in relation to the pre-existing relief on geological boundaries that directly underlie the base of PFS tiers, both of which may nucleate multi-directional fault surfaces that are sufficient to seed the growth of larger polygonal fault systems. Furthermore, the fractal nature and heterogeneity of polygonal fault systems documented in outcrop studies (Tewksbury et al., 2014; Verschuren, 2019) and recent ultra-high frequency seismic reflection studies (Fry, 2021), suggest that it may be possible that small-scale compositional and

fabric heterogeneities within shallowly buried unconsolidated sediments could offer an intrinsic nucleation site for differential-compaction driven fracture propagation.

The Moeraki Boulders that are found in the onshore outcrop succession of the Canterbury Basin PFS, offshore New Zealand (Morley et al., 2017), are one such example of concretions associated with PFSs (Figure 6.1). These concretions are up to 2-3 metres in diameter and both internal textural studies and isotopic analysis suggest that they formed within the first 100 metres of burial before any significant compaction (Boles et al., 1985; Thyne and Boles, 1989), and therefore, the timing of the growth of mechanically competent concretions is consistent with the early formation of PFSs. Some examples of PFS planforms that inherit the geometries of underlying structures include the Sable Subbasin PFS (Hansen et al., 2004), Makassar Straits PFS (Armandita et al., 2015), Exmouth Plateau PFS (Paganoni et al., 2019), Levant Basin PFS (Ghalayini et al., 2017), and Lower Congo Basin PFS (Morgan et al., 2015).

The nucleation of many PFSs may be driven by a diagenetically-induced volumetric reduction mechanism (Shin et al., 2008; Cartwright, 2011; Roberts et al., 2014). However, it is possible that the nucleation of different PFSs may not be caused by a single universal genetic mechanism. Nucleation has proved to be one of the most challenging aspects of polygonal fault systems to explain, and it is arguably the least understood facet of these enigmatic geological structures.

6.3.2 Propagation and Growth

6.3.2.1 Kinematics and propagation

Detailed kinematic studies of PFSs are limited because of a lack of temporal constraints and physical analogues. However, it has been widely recognised that PFSs develop in the early stages of burial (Cartwright, 1994a; Lonergan et al., 1998a;

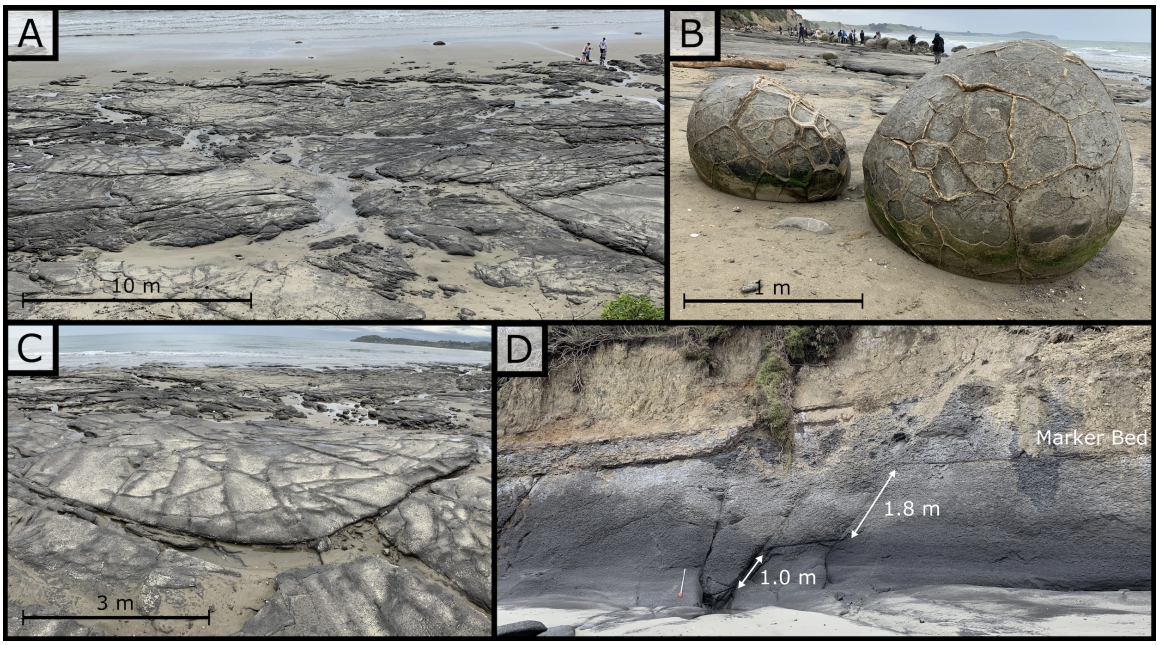


Figure 6.1: Field photos from Hampden Beach, New Zealand, showing the association of large mechanically-competent concretions with the onshore outcrops of the Great Canterbury Basin polygonal fault system. (A) and (C) show the polygonal planform intersections of faults which are traced into adjacent cliffs with offset marker horizons (D). (B) The Moeraki Boulders are spherical in shape and up to 2 metres in diameter. [Photos taken by J. King, 2018, with thanks to CASP and AAPG grants for supporting this fieldwork.]

Berndt et al., 2003; Stuevold et al., 2003; Gay et al., 2004; Morgan et al., 2015). It is likely that in the earliest stages of their growth that polygonal faults propagate radially from their nucleation sites, before their downward tipline propagation is inhibited by either a difference in mechanical properties associated with a change in lithology at the base of the tier or through a detachment of the lower tip into a mobile basal layer (Cartwright et al., 2003; Cartwright, 2011). Polygonal faults may also begin to intersect neighbouring faults in the early phases of their development (Lonergan et al., 1998a). Following an early phase of lateral and lower tip abutment, much of the growth of polygonal faults is likely driven via primarily upward propagation. Upward propagation of polygonal faults has been inferred in several studies (Watterson et al., 2000; Stuevold et al., 2003; Gay and Berndt, 2007; Davies and Ireland, 2011), however, only a handful of studies have investigated the kinematics

of polygonal fault growth in detail (Morgan et al., 2015; Wrona et al., 2017; King and Cartwright, 2020) (Chapter 3). These kinematic studies suggest that at least the largest master polygonal faults, which typically span the entire tier, nucleate in the lower portion of the tier and grow primarily through upward propagation, however, smaller faults within PFS tiers may have different temporal and kinematic growth histories to the master faults which dominate the tier.

The propagation of PFSs has been attributed to 'gravitational loading' of fine-grained sedimentary tiers which have intrinsically low residual friction angles (Goulty, 2001a; Goulty and Swarbrick, 2005). Goulty (2001a) used Mohr-Coulomb theory to show that the residual failure criterion of a pre-existing fault is breached under laterally-confined hydrostatic loading conditions if the fault is hosted within a sediment with a high K_0 value and a sufficiently low residual friction angle (Figure 5.2 A, Chapter 5). Where K_0 is the coefficient of lateral earth pressure 'at rest', calculated as the ratio of the horizontal stress over the vertical stress, which is typically ~0.3-0.4 for coarse-grained sediments and >0.7 for fine-grained sediments (Jones, 1994; Goulty, 2001a; Goulty and Swarbrick, 2005; Casey, 2014). This model provides an elegant framework to explain the upward propagation of polygonal faults with loading, however, it does not explain the accommodation of displacement in laterally-pinned conditions. Laboratory experiments (Shin et al., 2008) and numerical modelling simulations (Roberts et al., 2014) have shown that the propagation (and nucleation) of polygonal faults can also be explained by diagenetically-induced isotropic volumetric reductions, which may also account for of at least a portion of the displacement that accrues in laterally-pinned conditions. It is possible that the 'gravitational loading' and 'diagenetically-induced shear failure' models may both contribute to the propagation of PFSs.

6.3.2.2 PFS growth – accommodating displacement in laterally-pinned conditions

By virtue of geometry, the displacement that accrues over polygonal faults must be accommodated by a differential volumetric change between the footwalls and hanging walls, because PFSs are hosted in laterally-pinned conditions.

If we consider a laterally-pinned volume of granular sediment and incrementally apply an increasing overburden load, the granular sediment will consolidate at a rate proportional to the loading rate provided that the pore fluid can drain in hydrostatic conditions (Terzaghi and Peck, 1948).

If we consider the same laterally-pinned volume of granular sediment, under the same incremental loading and hydrostatic conditions, now with a vertical fault plane in the centre of the volume which has a residual frictional angle that is significantly lower than the peak frictional angle of the unfaulted sediment, then the final state of the sediment volume after consolidation will be the same as in the first unfaulted case because gravity-driven consolidation is uniaxial and in this case parallel to the vertical fault plane.

If, however, we rotate the fault plane so it has a non-vertical dip then the overburden load acts obliquely on the dipping fault plane, and can thus be decomposed (Figure 6.2) into a normal stress (which acts perpendicular to the fault plane) and a shear stress (which acts parallel to the fault plane) (Fossen, 2016), which drives frictional sliding on the fault surface. The amount of frictional sliding, and hence displacement that accrues over the fault surface, in laterally-pinned conditions is determined by three factors: (1) the coefficient of friction on the fault plane; (2) the compressibility of the sediment; and (3) the dip angle of the fault plane – where the greatest amount of frictional sliding occurs when the shear stress is at its maximum, at a 45° angle between the maximum principal stress (overburden) and the orientation of the fault plane (Figure 6.3).

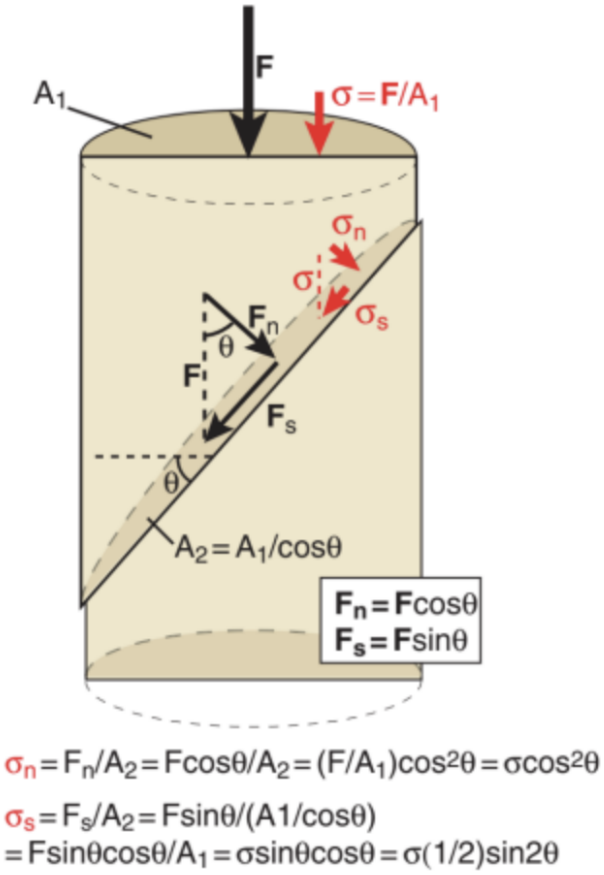


Figure 6.2: The decomposition of an overburden force vector (F) acting on a surface into normal (F_n) and shear (F_s) components. Note that in this illustration the top (hanging wall) block has slid as a rigid unit above a rigid bottom (footwall) block, however, the displacement that accrues over a polygonal fault in laterally-pinned conditions is accommodated by differential compaction of the hanging wall and footwall. From Fossen (2016) with permissions from Cambridge University Press.

This is the premise of the numerical modelling strategy used in Chapter 5 to investigate the growth of polygonal faults. This study found that the throw-height scaling relationship (Shin et al., 2010) and throw rates (King and Cartwright, 2020) of PFSs can be achieved solely by gravity-driven differential compaction facilitated by frictional sliding on a dipping fault plane.

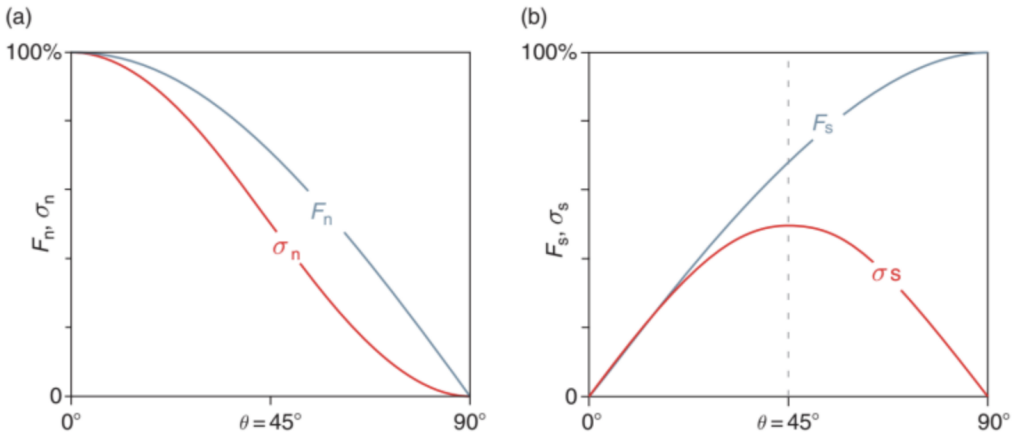


Figure 6.3: The normal components (a) and shear components (b) of the force F acting on a fault surface (see Figure 6.2) plotted as a function of the orientation of the vectors with respect to the fault surface. Note that the shear stress is at its greatest on a fault with a 45° dip angle and maximum shear force is achieved parallel to the fault surface. From Fossen (2016) with permissions from Cambridge University Press.

6.3.2.3 Factors that govern the growth of PFSs

Volume changes in fine-grained sediments

Fine-grained sedimentary sequences, such as those that host PFSs, may achieve changes in volume through mechanical and chemical compaction (Mondol et al., 2007). Mechanical compaction caused by the gravity-driven expulsion of pore fluids may be regarded as the largest component of volume change in many shallowly buried fine-grained unconsolidated sediments with burial, and can therefore be considered the primary driver of the volumetric reduction required to facilitate polygonal fault displacement in laterally-pinned conditions, universally. However, chemical compaction including diagenetic dissolution and reactions such as the transition of opal-A to opal-CT, smectite to illite, and alteration of volcanic ashes (Cartwright, 2011), may contribute to a subordinate but significant portion of the volumetric reduction in some PFS tiers. It is worth noting that uniaxial mechanical compaction generates an orthotropic volumetric reduction, whereas diagenetic reactions may in some cases cause

an isotropic volumetric reduction which may facilitate greater amounts of displacement in laterally-pinned conditions for the same bulk volume change (c.f. Roberts, 2014).

The results of material sensitivity analysis in Chapter 5 revealed that the greatest maximum throw (T_{max}) values as a percentage of the fault height did not scale linearly with the materials that undergo the greatest absolute magnitude of volumetric reduction (Figure 5.4 B, Chapter 5). Instead greater T_{max} to fault height ratios were recorded on faults hosted in laterally-pinned sediments with greater compaction gradients, and the accrual of throw decreased as the compaction gradient decreased.

Polygonal fault dips

Polygonal faults are commonly characterised by listrically dipping fault planes with depth, where shallowly buried upper fault tips can exhibit dips in the range of 50°-80° and deeper buried portions of faults, which have experienced post-propagation compactional flattening (Neagu et al., 2010a), can exhibit dips as low as 30°-50° (Cartwright, 1994a; Cartwright and Lonergan, 1996; Lonergan et al., 1998b; Clausen et al., 1999; Cartwright et al., 2003; Shoulders et al., 2007; Sun et al., 2010).

All else being equal, a 45° fault dip is the optimal angle for maximum frictional sliding (Figure 6.3). Therefore, the incremental accrual of throw on the lower portions of polygonal faults will decrease with burial-induced compactional flattening.

Residual friction angles

One of the main findings of this thesis is that the growth of polygonal fault systems can be explained solely by gravity-driven differential compaction at residual friction angles less than ~9°. Results from sensitivity analysis in Chapter 5 revealed that the accrual of fault throw in laterally-pinned conditions is most sensitive to changes in the residual friction angle (Figure 5.4, Chapter 5).

Several studies have recorded residual friction angles less than 9° in fine-grained

sediments (Table 5.1, Chapter 5). However, there is little direct calibration of residual frictional angles from PFSs. One such example was presented by Goulty and Swarbrick (2005), who used leak-off test results to infer that the residual friction angle of a PFS tier situated in the North Sea was ~5°. Goulty (2001a) and Goulty and Swarbrick (2005) were early advocates of the role of low residual friction angles in the development of PFSs, however, their mechanism dubbed the 'gravitational loading' mechanism was primarily focused on the propagation of polygonal faults rather than on the accrual of displacement.

It may be considered likely that the residual friction angle may change both spatially and temporally across both a PFS and across an individual polygonal fault plane. Spatial differences in the residual friction angle across a sedimentary tier may partially explain the range of T_{max} to height ratios recorded within a single PFS. Changes in the residual friction angle across a fault surface may arise spatially as a result of contrasting material physical properties in layered sedimentary sequences, and temporally as processes such as cementation change the properties of the tier – particularly at depth.

Although this thesis did not investigate mechanisms to facilitate the growth or reactivation of PFSs at higher residual friction angles, it is possible that the growth of some polygonal faults may be aided by processes such as fluid overpressure or diagenetically-induced isotropic volume loss at residual friction angles in excess of 11°.

Fluid overpressure

Overpressure builds in sediments when the pore fluid cannot drain in equilibrium with increasing overburden stresses. Shallowly buried fine-grained sediments have intrinsically low permeability, high compressibility, and high starting porosity and can thus readily develop overpressure when rapidly loaded (Bolton et al., 1998; Swarbrick

et al., 2001).

Elevated fluid overpressure can promote faulting at low values of shear stress by reducing the effective normal stresses (Bolton et al., 1998; Watterson et al., 2000). Therefore, fluid overpressure may facilitate frictional sliding on faults with higher residual friction angles and/or unfavourably oriented dip angles that would otherwise be inactive in laterally-pinned conditions (Collettini and Sibson, 2001; Urlaub et al., 2018). In addition, the transmission of fluids along fault planes may lead to elevated fluid overpressure at the upper tips of polygonal faults (Bolton et al., 1998; Roberts, 2014; Roberts et al., 2014). Elevated tip stresses may facilitate gravitational-loading-driven propagation at higher residual friction angles than ~11° and/or K_0 values less than 0.7.

The development of fluid overpressure in rapidly loaded low-permeability layers may act to facilitate or enhance frictional sliding on active polygonal faults or reactivate the growth of inactive polygonal faults.

6.3.2.4 Growth rates

One of the main objectives of this thesis was to document the first throw rates recorded from a polygonal fault system globally. The throw rates measured in Chapter 4 showed that polygonal faults grow especially slowly when compared to the displacement rates of tectonic and gravitational slope fault systems over similar time periods (Figure 6.4 – reproduced from Chapter 4). However, it should be noted that the polygonal faults analysed in Chapter 4 are smaller than the tectonic fault analysed in other studies and it is possible that similarly sized small tectonic faults may have similar growth rates to those recorded from the Vøring Basin PFS. The finding that polygonal faults have ultra-slow throw rates is not completely unexpected because the geological processes that govern bulk volumetric reductions in shallowly buried fine-grained sediments – required to accommodate fault displacement in laterally-pinned

conditions – are inherently slow. The throw rates derived from the numerical simulations that model the growth of normal fault growth in laterally-pinned conditions in Chapter 5 are remarkably consistent with the rates measured from polygonal faults in Chapter 4. This not only tells us something about the underlying drivers of polygonal fault growth but alongside the empirical throw-height scaling relationship (Shin et al., 2010) and slow sedimentation rates recorded in global PFS tiers (Cartwright and Dewhurst, 1998) also suggests that the ultra-slow throw rates recorded in this thesis are representative of PFSs universally.

In addition to the results presented in this thesis, a preliminary investigation of throw rates from surface-breaching polygonal faults hosted in Pliocene to Recent aged fine-grained sediments of the Lower Congo Basin, offshore Angola, that are imaged in ultra-high resolution seismic reflection lines (the results of which are not included in this thesis due to data confidentiality), reveal throw rates of 2-20 m/m.y. at a 0.15 Ma dated horizon that is buried ~10-20 metres below the seabed. These findings, although anecdotal, are remarkably consistent with the short-term throw rates from the Vøring Basin PFS presented in Chapter 4.

The short-term throw rates (averaged over <1 m.y.) recorded from upper polygonal fault tips in the Vøring Basin, Norwegian Sea, presented in Chapter 4 range from 0-18 m/m.y., whereas longer-term throw rates from the same polygonal faults (averaged over 2.61 m.y.) range between 1.4-10.9 m/m.y., which suggests that the growth rate of polygonal faults fluctuates through time, albeit within a narrow range of values. The small-scale steps exhibited on the throw versus horizon age plots recorded from these polygonal faults (Figure 4.3, Chapter 4) may be interpreted as short periods of growth inactivity. This suggests that polygonal faults may grow through a series of discrete periods of differential compaction driven creep, governed by the four aforementioned factors.

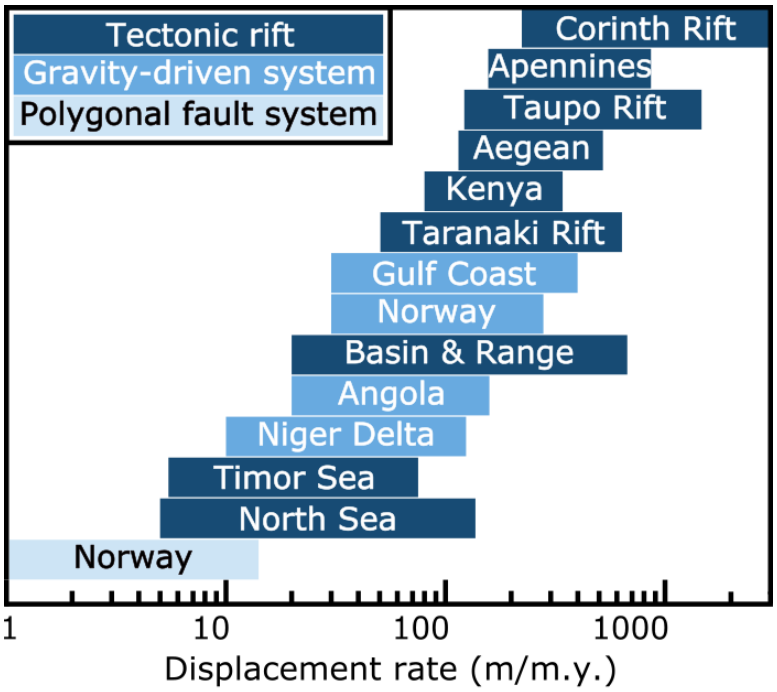


Figure 6.4: Log plot of displacement rates from extensional tectonic, gravitational-slope-driven, and polygonal fault systems (PFSs) from basins around the world. Reproduced from Chapter 4.

6.3.3 Cessation

The growth of polygonal faults may cease temporarily or permanently when the units that comprise PFS tiers stop differentially compacting. This cessation of PFS growth may occur incrementally from the base of the tier in an upward direction, as volumetric changes in the lowermost units may slow as a result of increasing lithification with burial and/or as residual friction angles increase as a result of processes such as cementation. Alternatively, the growth of PFSs as a whole may cease in a single fossilisation event. This may be associated with erosional unloading, which may be followed by a period of reactivation caused by subsequent re-loading (c.f. Gay and Berndt, 2007) or permanent inactivity if the physical properties of the PFS tier change sufficiently during the period of quiescence as a result of diagenesis such that the conditions for differential compaction are no longer achieved. The upward ter-

mination of PFS propagation may arise as a result of a depositional facies change (Cartwright et al., 2003; Carruthers, 2012; Jackson et al., 2014), and the propagation and growth of individual polygonal faults may be arrested by lateral intersections with neighbouring faults (Lonergan et al., 1998a).

The observation that polygonal faults often share a common basal boundary but terminate at a range of different heights within a tier suggests that the growth of PFSs may be a product of survivorship, where master polygonal faults that span the entire tier experienced the 'path of least resistance' throughout their growth histories.

6.4 Future Work

A natural continuation to the research undertaken in this thesis includes: (1) an advanced numerical modelling investigation of fluid pressure, heterogeneities, and three-dimensional intersections on the growth of polygonal faults; and (2) the documentation of throw rates from a large number of different PFSs. In addition, the findings of this thesis elucidate the mechanics of polygonal fault growth, which lays a foundation to quantitatively investigate the sealing capacity of PFSs in petroleum and CO_2 storage systems. Nucleation is also one of the least understood facets of polygonal fault systems and therefore offers a challenging and important area for future studies. Despite the findings of this research there is still much to uncover about these fascinating geological structures.

Chapter 7

Conclusions

The main findings of this thesis are that polygonal fault systems accrue throw at ultra-slow rates, where their growth can be explained solely by gravity-driven differential compaction in laterally-pinned tiers under realistic physical property conditions.

Chapter 3: The Spatial, Temporal, and Kinematic Evolution of a Polygonal Fault System

1. This study investigated the growth of near-surface and surface-breaching polygonal faults in the Vøring Basin, Norwegian Sea, and found that the PFS has propagated upward for much of its growth history, where master faults have been active at or within a few tens of metres of the seabed from at least the late Pliocene.

2. The identification of a series of small hanging wall growth packages that are found sporadically within the upper portions of the age-calibrated PFS tier imply that the master polygonal faults have propagated upwards with sedimentation from at least the late Pliocene.

3. The absence of large syn-sedimentary wedges in the fault hanging walls suggests that the polygonal faults have propagated at a rate approximately equal to the sedimentation rate and that the rate of throw accumulation has not outpaced sedimentation.

4. Offset at the diagenetic opal-CT boundary found in the lower third of the PFS tier, which pre-dates the deposition and faulting of the uppermost portions of the tier, suggests that throw appears to have accrued over the entire vertical extent of the fault planes throughout propagation.

5. Macro-scale throw profile gradients can be correlated across the wedge shaped stratigraphy of the study area, where changes in throw gradients may be the result of temporal changes in the amount of differential volumetric strain occurring at depth and/or differences in the mechanical properties of strata that comprises the PFS host tier, and in some cases fault intersections.

6. Small-scale throw profile variations observed within the macro-scale gradients are not found systematically at common horizons across the study area but they can sometimes be traced to neighbouring faults. These small-scale throw profile steps found in the upper tip regions may be caused by fault intersections and/or represent short periods of growth inactivity and/or differences in the intrinsic physical properties of the intra-formational units.

7. The kinematic growth history of the PFS master faults likely involved:

    i. an initiation phase in the late Paleocene to early Miocene, where the system nucleated within a few tens to hundreds of metres of the paleo-seabed;

    ii. an early phase of radial tipline propagation;

    iii. a period of lower and lateral fault tip abutment, where the lower tips

arrested at a basal boundary and the lateral tips began to intersect neighbouring faults;

iv. a period of upward fault propagation that continues to the present day, where the upper fault tip positions closely track the seabed – sometimes developing small growth packages in the fault hanging walls.

Chapter 4: Ultra-Slow Throw Rates of Polygonal Fault Systems

1. This study derives the first recorded throw rates for a polygonal fault system, from the Vøring Basin in the Norwegian Sea, where throw rates range between 1.4-10.9 m/m.y.

2. Individual polygonal faults exhibit a range of throw rate profiles through time that range from near linear to singly or multiply stepped, where the short-term throw rates recorded on stepped profiles range from 0-18 m/m.y.

3. The ultra-slow throw rates recorded in this study are converted to displacement rates, where they mark the lower limit of a continuous spectrum of extensional fault displacement rates.

4. Polygonal fault displacement rates are as much as three orders of magnitude slower than those of the fastest-growing tectonic faults, and as much as two orders of magnitude slower than those of gravitational slope fault systems.

5. These ultra-slow PFS throw rates are consistent with the slow rates of geological processes that drive differential bulk volumetric reductions in shallowly buried fine-grained sedimentary sequences.

Chapter 5: Numerical Modelling of the Growth of Polygonal Fault Systems

1. This study found that the growth of polygonal faults in laterally-pinned conditions can be explained solely by gravity-driven compaction over a range of material physical property values recorded from fine-grained sediments.

2. Maximum throw (T_{max}) as a percentage of fault height values recorded from polygonal fault systems globally (~6%) can be achieved at standard fault dip angles and material property values typical of those recorded from fine-grained sediments at residual friction angles <9°.

3. The accrual of throw on polygonal faults is most sensitive to changes in the residual friction angle.

4. Throw rates derived from sensitivity analysis are consistent with those recorded from the upper tips of polygonal faults in the Vøring Basin, Norwegian Sea.

5. It is possible that fluid overpressure and diagenetically-induced volumetric reductions, which have been suggested as drivers of PFSs in previous studies, may act to enhance or reactivate the growth of some polygonal fault systems under specific conditions.

6. The death of a PFS may occur once its hosting units no longer undergo differential volumetric strain.

Appendix A

Supplementary Material for "Ultra-Slow Throw Rates of Polygonal Fault Systems"

GSA DATA REPOSITORY ITEM 2020139

A.1 Chronostratigraphic Calibration

The top 250 m of the PFS tier is chronostratigraphically calibrated by eight dated markers from ODP Hole 644 (Figure A.2). Seven of which were uniquely distinguished and mapable across the study area.

A.2 Biostratigraphy – Calcareous Nannofossils

The two youngest stratigraphic markers were biostratigraphically dated by calcareous nannofossil assemblages with the first appearance of E. huxleyi marking the onset of biozone NN21 (0.268 Ma at 22 mbsf), and the last appearance of P. lacunose marking the end of biozone NN19 (0.458 Ma at 51 mbsf) (Shipboard Scientific Party, 1987; Berggren et al., 1995; Cohen and Gibbard, 2017). The respective dating of the start of NN21 and end of NN19 have been updated since the ODP 644 initial reports volume was published, and we use the current biostratigraphic dating framework outlined by the International Commission on Stratigraphy in our analysis (Cohen and Gibbard, 2017). Diatom, silicoflagellate, radiolarian, planktonic and benthic foraminifer assemblages were also examined but did not yield absolute age dates required for our analysis. Similarly, palynological samples yielded paleoenvironmental insight but no direct age-calibration.

A.3 Paleomagnetics

Thirty-four cores from ODP Hole 644 were measured for their natural remanent magnetisation properties on-board the ship using a pass-through cryogenic magnetometer. These results alongside detailed shore-based paleomagnetic analysis of 415 discrete samples using detailed alternating field demagnetisation techniques enabled a complete magnetostratigraphy for the upper Cenozoic that shows exceptional agreement with paleontological analysis (Shipboard Scientific Party, 1987; Bleil, 1989). Major geomagnetic boundaries were identified at 83.45 mbsf (Brunhes-Matuyama, C1N-1/C1R-1) and 225.21 mbsf (Matuyama-Gauss, C2R/C2AN-1) (Figure A.2). Within the Matuyama epoch the top and base Jaramillo were identified at 103.89 mbsf and 111.18 mbsf respectively, and the top and base Olduvai were identified at 166.85 mbsf and 180.81 mbsf respectively (Figure A.2). The depth in meters below seafloor for these geomagnetic reversals was taken at the midpoint between recorded core samples (Bleil, 1989). The absolute ages of the quaternary paleomagenetic reversals documented in ODP 644 have been updated subsequently to the publishing of Shipboard Scientific Party (1987) and Bleil (1989) and are summarised in Singer (2014). We use the updated geomagnetic framework for the respective reversals from Singer (2014) in our analysis.

A.4 Seismic-Well Calibration

In the absence of an absolute seismic velocity tie our dated markers have been converted from meters below seafloor to milliseconds (two-way-travel-time, TWT) using a velocity of 1600 m/s as used by Shipboard Scientific Party (1987) (Figure A.2). The dated horizons have been tied to the seismic at the location of ODP well 644 and mapped to the wiggle apex of the closest seismic reflection. A low velocity estimate of 1500 m/s and a high velocity estimate of 1700 m/s yield a $\pm$ of $<$ 10 ms for the TWT of dated horizons 0.268 Ma, 0.458 Ma, 0.773 Ma, and 1.008 Ma, and therefore these dated horizons are mapped to an accuracy of $\pm$ one seismic reflection. Dated horizons 1.775 Ma, 1.934 Ma, and 2.610 Ma have a $\pm$ TWT conversion greater than 10 ms but less than 20 ms given the low and high velocity estimates of 1500 m/s and 1700 m/s respectively, and are therefore mapped to an accuracy of $\pm$ two seismic reflections. Assuming a sedimentation rate of around 100 m/Ma (Shipboard Scientific Party, 1987) this equates to an error of $\pm$0.1 Ma for the seismic calibration of horizons 0.268 Ma, 0.458 Ma, 0.773 Ma, 1.008 Ma and an error of $\pm$0.2 Ma for the seismic calibration of horizons 1.775 Ma, 1.934 Ma, and 2.610 Ma respectively. These are represented by vertical error bars in Figure 4.3A.

The 1.076 Ma (Base Jaramillo) dated marker cannot be distinguished from the 1.008 (Top Jaramillo) dated marker at the resolution of the seismic data and therefore is not used in our analysis. The 0.773 Ma (Brunhes-Matuyama) dated marker is tied to a laterally discontinuous seismic reflection and is therefore intersected by a small selection of the faults studied. The dated horizons were mapped across the study area using standard 3-D seismic reflection tracking techniques in Schlumberger's Petrel software.

A.5 Measuring Throw Rates

Time-averaged throw rates were calculated as the change in throw of the 2.61 Ma divided by the elapsed time of 2.61 m.y. Whereby, the change in throw is measured as the vertical offset in milliseconds of the age-calibrated seismic reflection taken from the apex of the reflection wiggle. In the shallow stratigraphic section, calibrated by dated horizons, there is limited fault drag, however, where offset reflections are not approximately planar, measurements of throw have been consistently taken to minimise spurious measurement errors by measuring at least one seismic trace in from the fault plane where the wiggle apex on traces either side are stable. Throw values recorded in milliseconds are converted to meters using a velocity of 1600 m/s as outlined above. Throw measurement are accurate to within ± 1 m (cf. Townsend et al. (1998)). We do not apply a decompaction factor to our throw rates (cf. Taylor et al. (2008)) because the ODP Hole 644 porosity-versus-depth plot (Figure A.7) exhibits high porosity values ($> 60\%$) and because the faults have experienced shallow burial conditions with low throw values.

Supplementary Figures

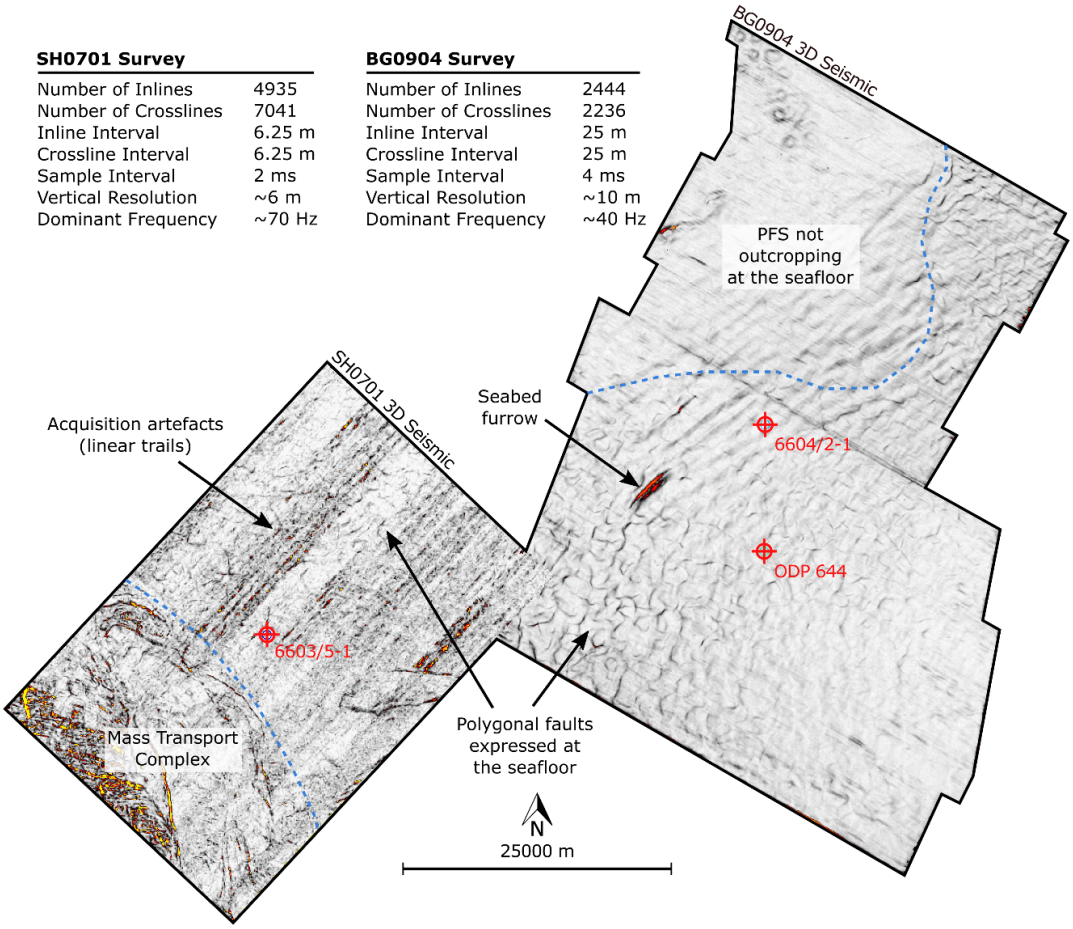


Figure A.1: Seabed maps of the two 3D seismic surveys loacted within the Vøring Basin of the Norwegian Sea showing the seabed expression of polygonal faults. ODP and industry wells used to calibrate the litho- and chronostratigraphy are highlighted in red.

ODP 644 - Summary of Dated Horizons				
Depth (mbsf)	**Depth TWT (ms) v = 1600 m/s**	**Age (Ma)**	**Dating Technique**	**Description**
0	1662.8	0.000	-	Seabed
22.00	1690.3	0.268	Calcareous nannofossils	FAD *E. huxleyi* (NN21)
51.00	1726.6	0.458	Calcareous nannofossils	LAD *P. lacunosa* (NN19/20)
83.45	1767.1	0.773	Paleomagnetics	Brunhes-Matuyama - C1N-1/C1R-1
103.89	1792.7	1.008	Paleomagnetics	Top Jaramillo - C1R-1/C1N-2
111.18	1801.8	1.076	Paleomagnetics	Base Jaramillo - C1N-2/C1R-2
166.85	1871.4	1.775	Paleomagnetics	Top Olduvai - C1R-2/C2N
180.81	1888.8	1.934	Paleomagnetics	Base Olduvai - C2N/C2R
225.21	1944.3	2.610	Paleomagnetics	Matuyama-Gauss - C2R/C2AN-1

Figure A.2: Summary table of dated horizons from ODP 644. See chronostratigraphic calibration section above for detailed description.

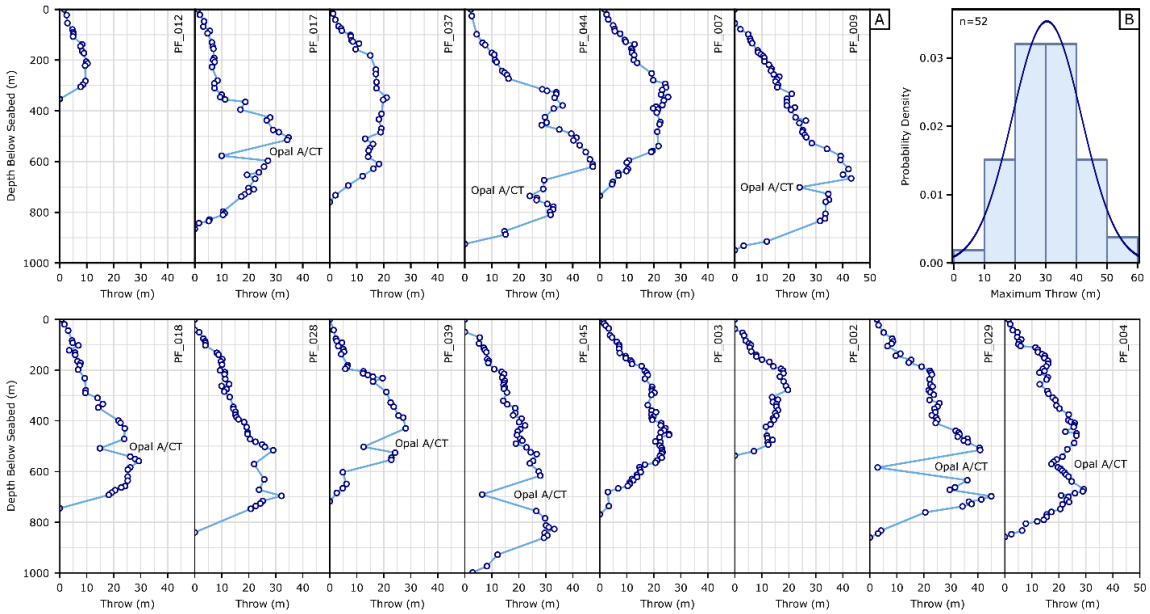


Figure A.3: (A) Throw versus depth plots for the same 14 faults exhibited in Figure 4.3 (main text). (B) Probability density function of maximum throw for 52 faults.

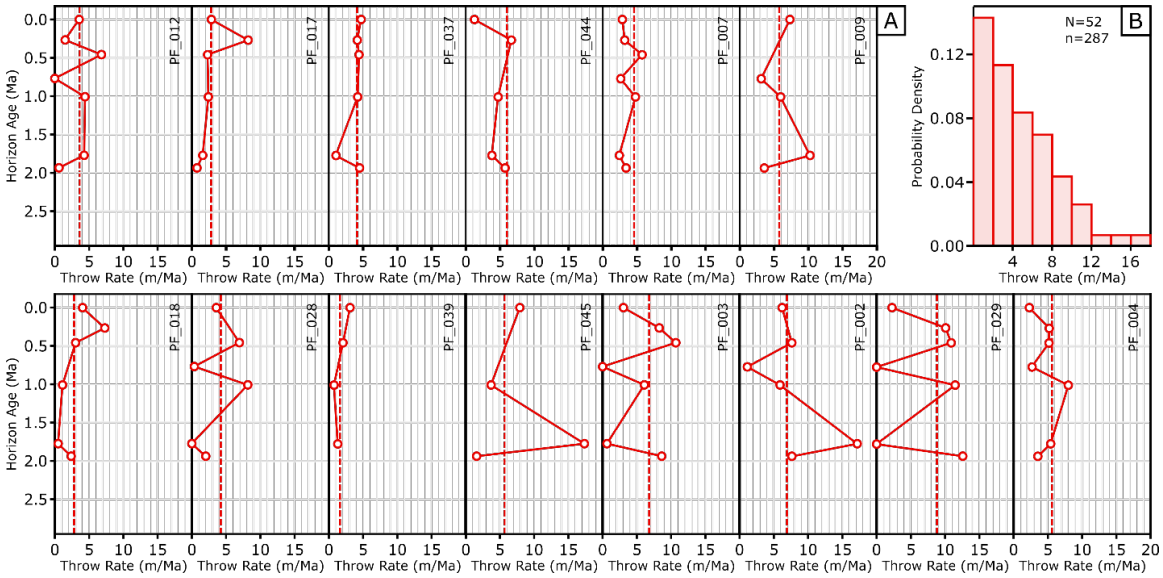


Figure A.4: (A) Throw rate versus horizon age plots for the same 14 faults exhibited in Figure 4.3 (main text). Throw rate is calculated as the change in throw divided by the change in time (horizon age) between adjacent data points of known age. The dashed lines represent the time-averaged throw rate for each fault taken as the throw at the 2.61 Ma horizon divided by time. (B) Probability density function of short-term throw rates (n=287) for 52 faults (N=52).

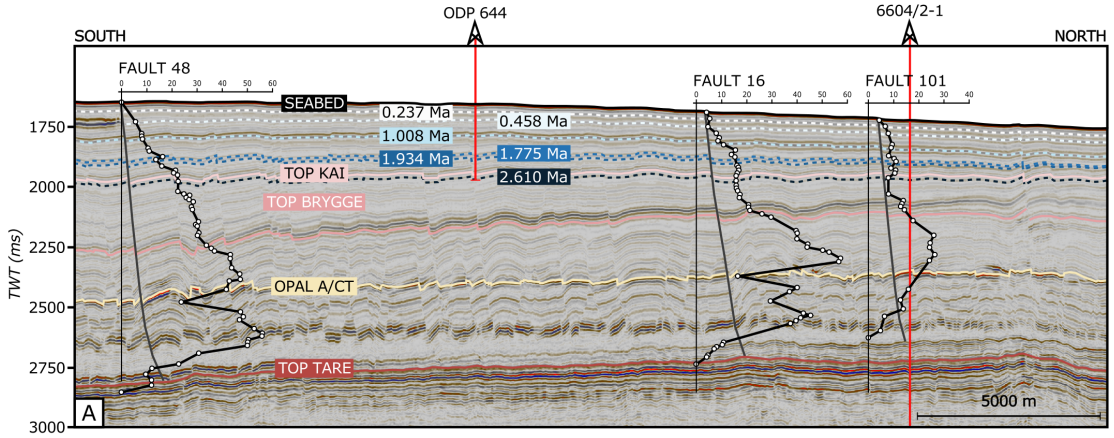


Figure A.5: Extended seismic profile from Figure 4.1B with three throw versus depth plots superimposed.

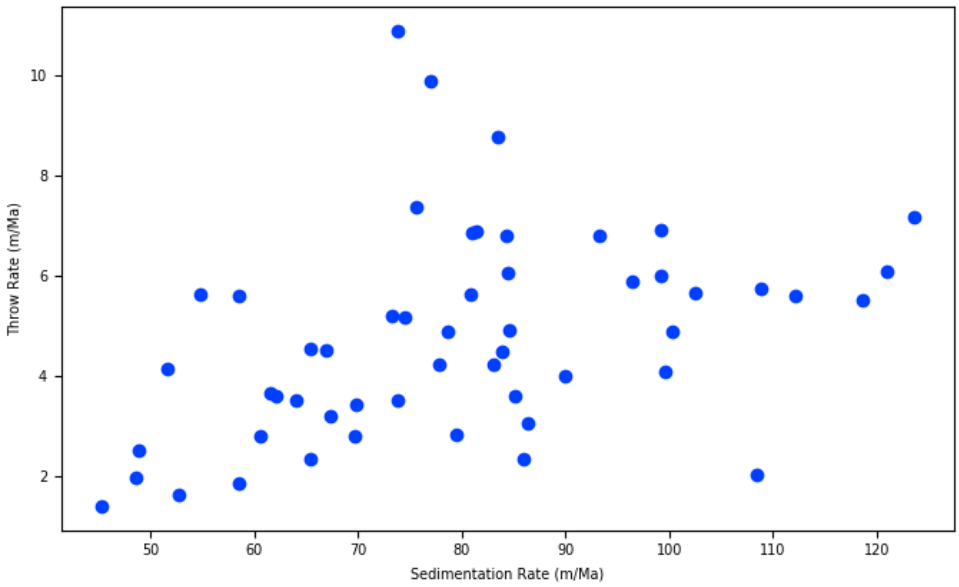


Figure A.6: Time averaged sedimentation rates outpace throw rates by at least one order of magnitude.

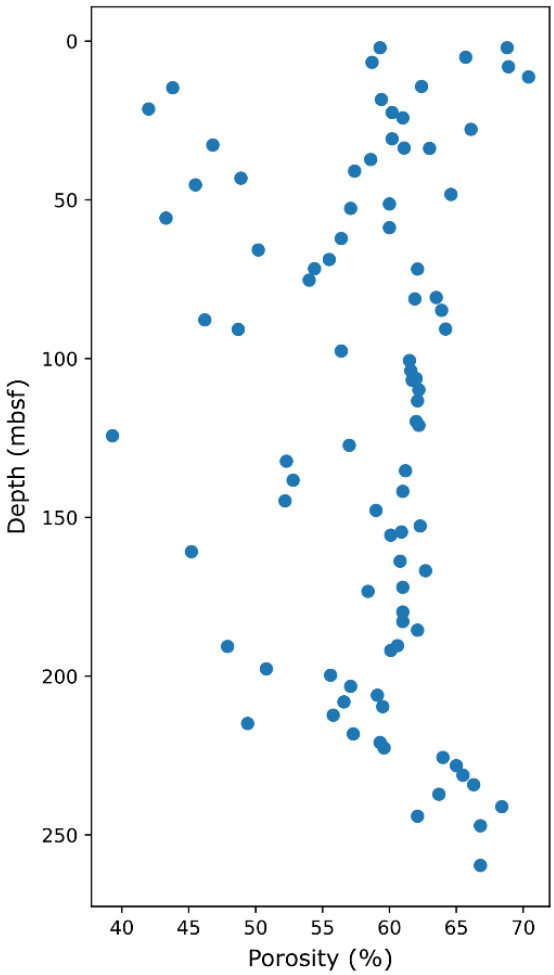


Figure A.7: ODP 644 - porosity versus depth profile from Shipboard Scientific Party (1987). Note this is the same data featured in Figure 3.5, Chapter 3 (main text).

Appendix B

Numerical modelling methodology

This appendix summarises the constitutive modelling methodology employed by *ELFEN* used in Chapter 5. This methodology was used, but not developed, during the work of this thesis. The methodology, equations, testing, and validation of both the computational framework *ELFEN* and the SR3 constitutive model are described and discussed exhaustively in Crook et al. (2003), Perić and Crook (2004), Crook et al. (2006), Rockfield (2010), and Roberts (2014).

B.1 Computational framework

B.1.1 ELFEN

ELFEN uses a quasi-static explicit Lagrangian finite element formulation with automated adaptive remeshing to solve a reduced form of the discretised momentum equation (Rockfield, 2010). At each timestep equilibrium is not enforced and over geological timescales loading occurs slowly enough for inertial terms to be negated (Rockfield, 2010). The underlying computational methods utilised by *ELFEN* are discussed extensively by Perić and Crook (2004), and have been used to solve a host of geological problems ranging from salt tectonics (Nikolinakou et al., 2014a,b) to regional fold and thrust belts (Albertz and Lingrey, 2012), as well as previous studies of polygonal faulting (Roberts et al., 2014; Roberts, 2014). *ELFEN* has the ability to employ several constitutive frameworks. We outline the *SoftRock 3* (SR3) constitutive model below, which was used in the numerical modelling study of this thesis (Chapter 5) because of its explicit incorporation of granular material compaction.

B.2 Constitutive model

The *SoftRock 3* (SR3) constitutive model is a rate independent, single surface, non-associated plasticity model that is an enhanced Modified Cam Clay variant, rooted in critical state soil mechanics (Rockfield, 2010). Critical state soil mechanics theory models the deformation of unconsolidated sediments as a *'frictional fluid'*, where the complicated stochastic grain-to-grain deformations at the micro-scale are assumed to aggregate as a continuous flow at the macro-scale (Schofield and Wroth, 1968).

B.2.1 SoftRock 3 (SR3) state boundary surface

The SR3 state boundary surface, Φ, is a function of three stress invariants:

$$\Phi(p', q, r) = 0 \tag{B.1}$$

where p' is scaled from the first principal invariant of the Cauchy stress tensor I_1, q is scaled from the second principal invariant of the deviatoric stress tensor J_2, and r is a function of J_2 and the third principal invariant of the deviatoric stress tensor J_3. The terms p' and q are commonly referred to as the mean stress and deviatoric stress, respectively.

$$p' = \frac{1}{3}I_1, \qquad q = \sqrt{3J_2}, \qquad r = \left(\frac{27}{2}J_3\right)^{1/3} \tag{B.2}$$

The first invariant of the Cauchy stress tensor, and the second and third invariants of the deviatoric parts of the Cauchy stress tensor are:

$$I_1 = tr[\sigma], \qquad J_2 = \frac{1}{2}s : s, \qquad J_3 = det(s) \tag{B.3}$$

where s is the deviatoric part of the Cauchy stress tensor ($s = \sigma - p'I$, where I is the second order identity tensor, equivalent to the Kronecker delta δ_{ij}). The corresponding infinitesimal strain invariants are:

$$\varepsilon_v^e = tr[\varepsilon^e], \qquad \varepsilon_q^e = \sqrt{\frac{2}{3} e^e : e^e} \tag{B.4}$$

where ε_v^e and ε_q^e are the volumetric and deviatoric components of the infinitesimal elastic strain tensor, respectively.

The SR3 state boundary surface is derived from the deviatoric stress and mean effective stress components of the Cauchy stress tensor and their corresponding infinitesimal strain invariants, and intersects the hydrostatic axis in both tension and compression, and is defined as:

$$\Phi(\sigma, \varepsilon_v^p) = g(\theta, p')q + (p' - p_t') \tan\beta \left(\frac{(p' - p_c')}{(p_t' - p_c')} \right)^{\frac{1}{n}} \tag{B.5}$$

where p' is the effective mean stress, q is the deviatoric stress, ε_v^p is the volumetric plastic strain, θ is the Lode angle (equal to 30°), p_t is the tensile intercept, p_c is the pre-consolidation pressure, β and n are material constants that define the shape of the yield surface in the p'-q plane, and $g(\theta, p)$ controls the shape of the yield function in the deviatoric plane. A useful general expression for the deviatoric correction plane $g(\theta, p)$ is:

$$g(\theta, p') = \left[\frac{1}{1 - \beta^\pi(p')} \left(1 + \beta^\pi(p') \frac{r^3}{q^3} \right) \right]^{N^\pi} \tag{B.6}$$

where N^π is a material constant and β^π is defined by:

$$\beta^{\pi}(p') = \beta_0^{\pi} \exp\left(\beta_1^{\pi} p' \frac{p'_{c0}}{p'_c}\right) \tag{B.7}$$

where β_0^{π} and β_1^{π} are material constants and p_{c0} and p_c are the starting and current pre-consolidation pressures, respectively. The dependency of the yield surface aspect ratio in the deviatoric plane is defined by Equation B.6. The transition from the yield surface to the deviatoric plane is shown in Figure B.1, where the shape of the yield surface can change from a rounded triangular shape at low confining pressures to a more circular shape at higher confining pressures. Equation B.6 is scaled so triaxial compression strength corresponds directly to the strength calibrated using compressive triaxial (CTC) tests and so the strength is reduced in the reduced triaxial extension (RTE) tests:

$$RTE \qquad \theta = -30^{\circ} \qquad \sin 3\theta = -1 \qquad g = \left[(1+\beta^{\pi})/(1-\beta^{\pi})\right]^{N^{\pi}} \tag{B.8}$$

$$\theta = 0^{\circ} \qquad \sin 3\theta = 0 \qquad g = \left[1/(1-\beta^{\pi})\right]^{N^{\pi}} \tag{B.9}$$

$$CTC \qquad \theta = 30^{\circ} \qquad \sin 3\theta = 1 \qquad g = 1 \tag{B.10}$$

The transition from a rounded triangular yield surface at low mean stress to a circular shaped yield surface at high mean stress is enabled by the dependence of β^{π} on the effective mean stress (Figure B.1 B). The evolution of the original yield surface transitional effect with increasing pressure can be kept with the current yield surface status through the introduction of the p_c^0/p_c correction term in Equation B.7.

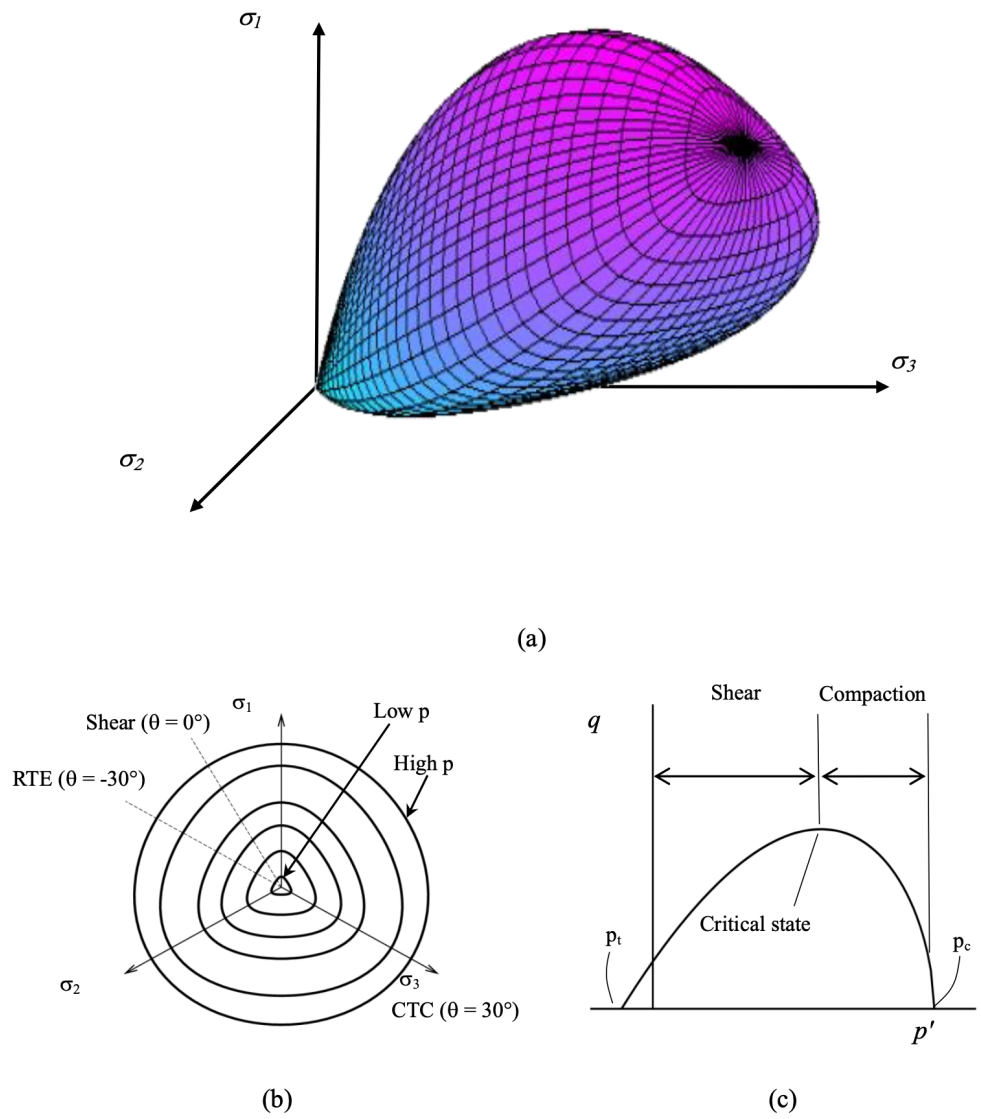


Figure B.1: The SR3 state boundary surface in (a) the principal stress space, (b) the deviatoric plane (π), and (c) the meridian plane ($p' - q$ space). From Roberts (2014).

B.2.2 Flow rule definition

The SR3 plastic strain rate is defined using a non-associated flow rule:

$$\dot{\varepsilon}^p = \dot{\lambda} \frac{\partial \Psi}{\partial \sigma} \tag{B.11}$$

where $\Psi\left(\sigma, \varepsilon_v^p\right)$ is the plastic potential defined as:

$$\Psi\left(\sigma, \varepsilon_v^p\right) = g(\theta, p')q + (p' - p_t') \tan\psi \left(\frac{(p' - p_c')}{(p_t' - p_c')}\right)^{\frac{1}{n}} \tag{B.12}$$

and $\dot{\lambda}$ is the plastic multiplier which determines the magnitude of plastic strain, and is consistent with the Kuhn-Tucker loading/unloading criterion:

$$\Phi(\sigma, q) \leq 0 \qquad \dot{\lambda} \geq 0 \qquad \dot{\lambda}\Phi(\sigma, q) = 0 \tag{B.13}$$

The plastic potential definition has the same form as the state boundary surface having substituted ψ for β (Figure B.2).

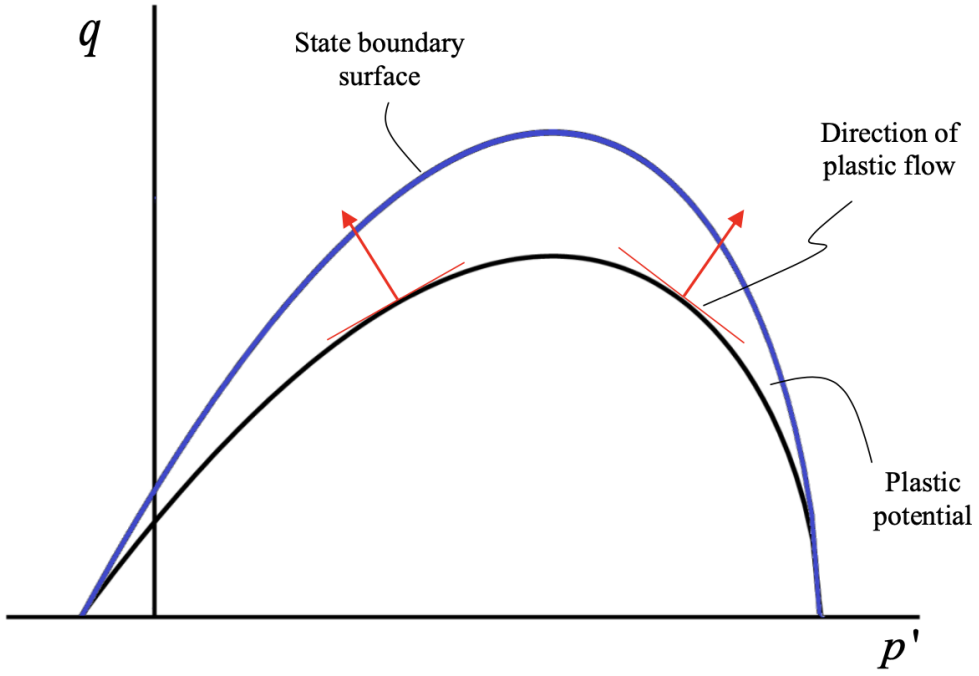


Figure B.2: SR3 plastic potential in the meridian plane showing that the plastic potential has the same form as the state boundary surface. From Roberts (2014).

B.2.3 Volume change

The direction of the plastic strain increment is orthogonal to the plastic potential surface of the SR3 model (Figure B.2). Therefore, the location of the stress point on the plastic potential surface defines the ratio between the incremental shear plastic strain $\delta\varepsilon_q^p$ and the incremental volumetric plastic strain $\delta\varepsilon_v^p$, which determines if the material is dilating or compacting. Extensional plastic flow is expected when the ratio of q/p' is high, where shear bands may be expected to form. Compactive and diffuse deformation is expected when the ratio of q/p' is low. A useful measure for visualisation of dilatancy is the angle β^d between the strain increment vector and the p axis, where:

$$\beta^d = \tan^{-1}\left[\frac{\delta\varepsilon_q^p}{\delta\varepsilon_v^p}\right] = \tan^{-1}\left[\frac{\partial\Psi}{\partial q}\Big/\frac{\partial\Psi}{\partial p}\right] \tag{B.14}$$

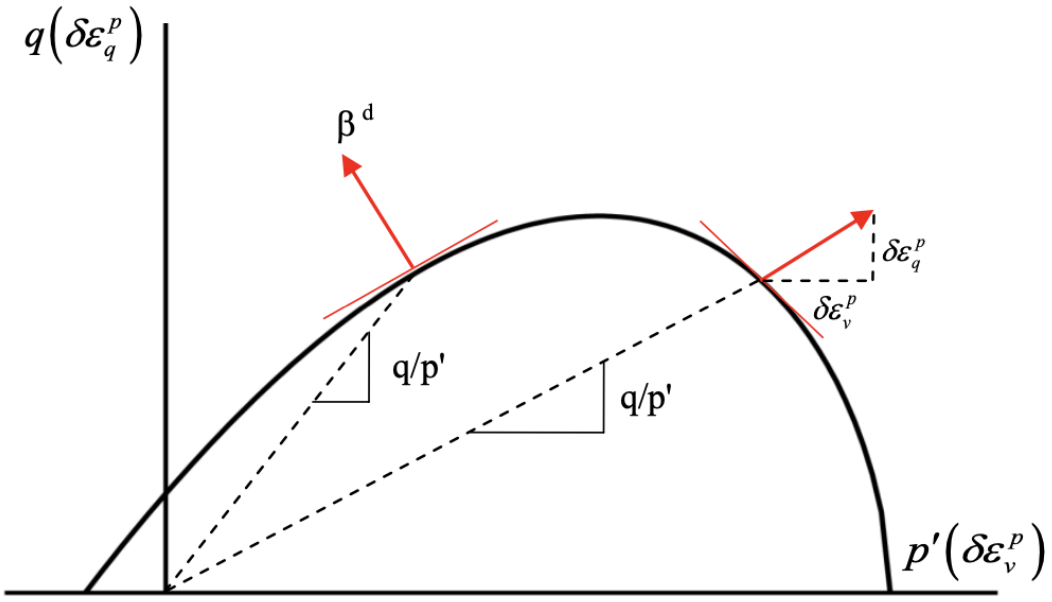


Figure B.3: Definition of the SR3 dilation parameter, β^d. From Roberts (2014).

B.2.4 Hardening law and poro-elasticity

The evolution of the SR3 state boundary surface is governed by a piecewise linear hardening law that relates the volumetric plastic strain (ε_v^p) to the pre-consolidation pressure (p_c) and tensile intercept (p_t) through the Cam Clay hardening parameters λ and κ in the following equations:

$$p_c = p_c\left(\varepsilon_v^p\right), \qquad p_t = p_t\left(\varepsilon_v^p\right) \tag{B.15}$$

$$p_c = p_{c0}\left[\exp\left(\frac{v\varepsilon_v^p}{(\lambda-\kappa)}\right)\right] \tag{B.16}$$

$$p_t = p_{t0}\left[\exp\left(\frac{v\left(\varepsilon_v^p\right)_{max}}{(\lambda-\kappa)}\right)\right] \tag{B.17}$$

where λ and κ are the slopes of the normal consolidation line and unloading-reloading line in v-$\ln p'$ space respectively (Figure B.4), $(\varepsilon_v^p)_{max}$ is the maximum dilational volumetric strain, and v is the specific volume defined as:

$$v = \frac{1}{(1-\phi)} \tag{B.18}$$

where ϕ_t is the porosity at a given timestep (t) defined as:

$$\phi_t = 1 - \frac{1}{e^{\varepsilon_v}}(1-\phi_0) \tag{B.19}$$

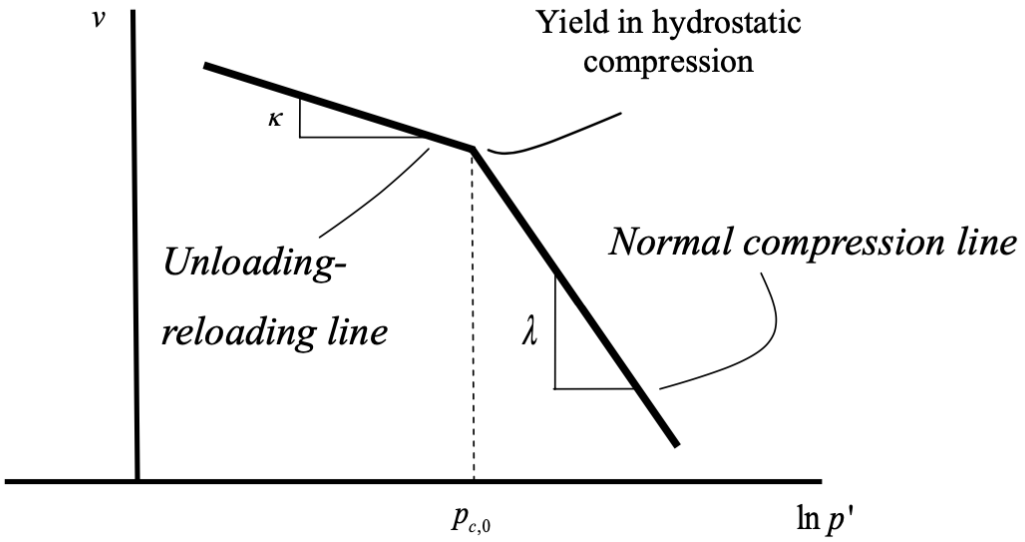


Figure B.4: Relationship between λ and κ and the specific volume of a material with increasing effective mean stress. From Roberts (2014).

where ϕ_0 is the initial porosity and ε_v is the total volumetric strain.

The porous elastic law is defined by two independent nonlinear equations for the material stiffness (E) and Poisson's ratio (ν) respectively, both of which are a function of the effective mean stress (p') that increases with burial depth:

$$E = E_{ref} \left[\frac{p' + A}{B} \right]^n \phi_t^c \tag{B.20}$$

$$\nu = \nu_{min} + (\nu_{max} - \nu_{min}) \times \left(1 - e^{-mp'} \right) \tag{B.21}$$

where E_{ref} is the initial stiffness, ϕ_t is the porosity at time t, ν_{min} and ν_{max} are the Poisson's ratio at low and high p' values respectively, and $A, B, c, m,$ and n are material constants. We note that the vast majority of strain that accumulates

in our models is plastic strain associated with granular compaction, and sensitivity analysis revealed that the modelling results presented in Chapter 5 are insensitive to large changes in both E and ν, over the range of values recorded from fine-grained sediments (Santamarina et al., 2001). This is because the vast majority of gravity-driven compactional strain over the first kilometre or so of burial of high porosity unconsolidated granular sediment is plastic strain rather than elastic strain, which occurs at greater depths once the material is compacted. For completeness, we include the porous elastic law and used a constant Poisson's ratio equal to 0.45 in our models and the stiffness profile exhibited in Figure B.5. This stiffness profile is based on physical property studies of the polygonally faulted Honorobe fine-grained siliceous rocks (Sanada et al., 2009; Miyazawa et al., 2011) and experimental studies of clay aggregates (Mondol et al., 2007). A constant Poisson's ratio of 0.45, is based on values recorded from experimental brine-saturated clay aggregates studies (Mondol et al., 2007). It should be noted that large changes in these values do not influence the volumetric strains in our modelling results (Chapter 5). The elastic property parameters and the SR3 property parameters used in our models are outlined in Table B.1 and Table B.2, respectively. The SR3 friction parameter (β) and dilation parameter (ψ) angles were chosen to yield an equivalent Mohr-Coulomb material peak friction angle of ~30°, and a K_0 burial stress path of 0.7-0.72 (Jones, 1994; Goulty and Swarbrick, 2005; Casey, 2014). It should be noted that the peak friction angle does not determine the fault dip propagation angle in our models because we prescribed fault plane propagation.

B.2.5 Elastoplastic stress update

The final SR3 state boundary function is established following an iterative elastoplastic stress update. The explicit solution of the discretised momentum balance equation (Rockfield, 2010) yields the incremental displacements at each sequential timestep,

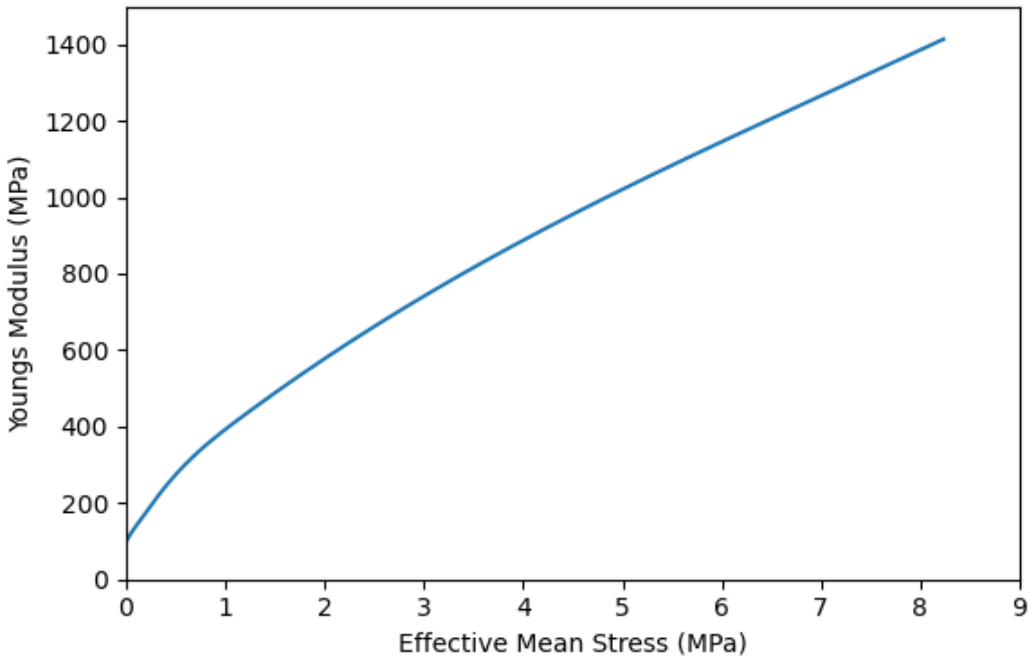


Figure B.5: Young's Modulus (stiffness, E) versus effective mean stress profile used to characterise the elastic properties of all materials used in our sensitivity study.

Elastic Properties	**Value**	**Units**
Young's Modulus (E_{ref})	100	MPa
Poisson's Ratio (ν)	0.45	
Exponent n	0.5	
Constant A	-0.1	MPa
Constant B	-0.4	MPa
Exponent c	-1.9	
Initial Porosity	70	%
Grain Density (ρ_s)	2700	kg/m^3
Fluid Density (ρ_f)	1030	kg/m^3

Table B.1: Elastic property parameter values used in our models.

SoftRock 3 Properties	**Value**	**Units**
Initial tensile intercept (p_{t0})	-0.025	MPa
Initial compressive intercept (p_{c0})	0.2	MPa
Friction parameter (β)	50	Degrees
Dilation parameter (ψ)	55	Degrees
Exponent (n)	1.8	
Deviatoric plane parameter (N^{π})	0.25	
Deviatoric plane parameter (β_0^{π})	0.6	
Deviatoric plane parameter (β_1^{π})	1.00E-04	1/MPa

Table B.2: SoftRock 3 (SR3) property parameter values used in our models.

from which the incremental strains are calculated. The updated components of the Cauchy stress tensor are calculated from the following constitutive equation that relates strains and stresses:

$$\sigma^{Trial} = {}^{t}\sigma + D_{ne}\Delta\varepsilon \tag{B.22}$$

where σ^{Trial} is the provisional calculated stress, D_{ne} is the matrix form of the nonlinear elastic law, $\Delta\varepsilon$ is the incremental strain, and t is the timestep. The stresses at the next timestep (${}^{t+\Delta t}\sigma$) are updated if the provisional stress (σ^{Trial}) lies outside of the state boundary condition according to the following condition:

$${}^{t+\Delta t}\sigma = \begin{cases} {}^{t}\sigma, & \Phi\left(\sigma^{Trial}, \varepsilon_v^p\right) \leq 0 \\ \sigma^{Trial} - D_{ne}\Delta\varepsilon^p, & \Phi\left(\sigma^{Trial}, \varepsilon_v^p\right) > 0 \end{cases} \tag{B.23}$$

The updated incremental stresses are then used to calculate the incremental flow rule (updated Equation B.11) through a fully implicit backward Euler integration,

where the incremental flow rule $\Delta\varepsilon^p$ is defined as:

$$\Delta\varepsilon^p = \Delta\lambda \frac{\partial \Psi}{\partial {}^{t+\Delta t}\sigma} = \Delta\lambda {}^{t+\Delta t}\varphi \tag{B.24}$$

After completion of the stress update, the state boundary function is defined as (updated Equation B.12):

$$\Phi\left({}^{t+\Delta t}\sigma, {}^{t+\Delta t}\varepsilon_v^p\right) = g\left(\theta, {}^{t+\Delta t}p\right) {}^{t+\Delta t}q + \left({}^{t+\Delta t}p - {}^{t+\Delta t}p_t\right) \tan\beta \left(\frac{{}^{t+\Delta t}p - {}^{t+\Delta t}p_c}{{}^{t+\Delta t}p_t - {}^{t+\Delta t}p_c}\right)^{1/n} = 0 \tag{B.25}$$

Once Equations B.23, B.24, and B.25 are satisfied at $t + \Delta t$, the plastic corrector may be formulated into an eight equation system defined as:

$$Y_1 = {}^{t+\Delta t}\sigma - \sigma^{trial} + \Delta\lambda D_{ne}^{t+\Delta t}\varphi \tag{B.26}$$

$$Y_2 = g\left(\theta, {}^{t+\Delta t}p\right) {}^{t+\Delta t}q + \left({}^{t+\Delta t}p - {}^{t+\Delta t}p_t\right) \tan\beta \left(\frac{{}^{t+\Delta t}p - {}^{t+\Delta t}p_c}{{}^{t+\Delta t}p_t - {}^{t+\Delta t}p_c}\right)^{1/n} \tag{B.27}$$

$$Y_3 = \Delta\varepsilon_v^p - \Delta\lambda tr\left({}^{t+\Delta t}\varphi\right) \tag{B.28}$$

where Y_1 is a vector of length 6, and the primary unknowns are the six stress components ${}^{t+\Delta t}\sigma$, the plastic multiplier $\Delta\lambda$, and the incremental volumetric strain $\Delta\varepsilon_v^p$. The system of equations is solved via Newton-Raphson iteration:

$$\begin{bmatrix} \frac{\partial Y_1}{\partial \sigma} & \frac{\partial Y_1}{\partial (\Delta\lambda)} & \frac{\partial Y_1}{\partial (\Delta\varepsilon_v^p)} \\ \frac{\partial Y_2}{\partial \sigma} & \frac{\partial Y_2}{\partial (\Delta\lambda)} & \frac{\partial Y_2}{\partial (\Delta\varepsilon_v^p)} \\ \frac{\partial Y_3}{\partial \sigma} & \frac{\partial Y_3}{\partial (\Delta\lambda)} & \frac{\partial Y_3}{\partial (\Delta\varepsilon_v^p)} \end{bmatrix} \begin{Bmatrix} d\sigma \\ d(\Delta\lambda) \\ d(\Delta\varepsilon_v^p) \end{Bmatrix} = (-1) \begin{Bmatrix} Y_1 \\ Y_2 \\ Y_3 \end{Bmatrix} \tag{B.29}$$

B.2.6 Regularisation of the material softening

A fracture energy regularisation is utilised to scale plastic strain softening based on the element size of the finite element mesh (Crook et al., 2003), expressed as:

$$(\bar{\varepsilon}^p)^{(e)} = (\bar{\varepsilon}^p)^{(m)} \left[\frac{{l_c}^{(m)}}{{l_c}^{(e)}} \right]^n \tag{B.30}$$

where $\bar{\varepsilon}^p$ is an appropriate scalar measure of plastic strain that determines material softening, n is a material constant (equal to 0.65), and ${l_c}^{(m)}$ and ${l_c}^{(e)}$ are the characteristic lengths of the material (0.1 millimetres) and element (5 metres) respectively. This regularisation maintains consistent energy dissipation across the finite element mesh regardless of the element size and is independent of the constitutive model (Crook et al., 2003).

Appendix C

SEGY Peak Picking MATLAB Script

```
function [ZA]=SEGYApexUncertaintyCode_Thesis(dti);

%%% NB: dti = 0.01/sr

%%% NB: Use a manual gain of -13 in Petrel for the point data to sit on the
%%% wiggle apex

%%% histogram(D(:,500), 10000) % Find the discretisation step - half of the
%%% bin spacing

%%% Read in SEGY file
SEGY = read_segy_file('_____.sgy');
D = SEGY.traces; % seismic matrix
```

```
14
15 %%% Set variables
16 H         = SEGY.headers;
17 sr        = SEGY.step;
18 X         = H(7,:)*0.01;
19 Y         = H(8,:)*0.01;
20 [ns,tr]   = size(D);
21 X0        = 1:ns;
22 Xint      = 1:dti:ns;
23 nsi       = length(Xint);
24 ru        = zeros(size(D));
25 ru2       = zeros(size(D));
26 ru3       = zeros(size(D));
27 rl        = zeros(size(D));
28 rl2       = zeros(size(D));
29 rl3       = zeros(size(D));
30 ZA        = [];
31 ZAru      = [];
32 ZAru2     = [];
33 ZAru3     = [];
34 ZArl      = [];
35 ZArl2     = [];
36 ZArl3     = [];
37 ZAv       = [];
38 ZAvru     = [];
39 ZAvru2    = [];
40 ZAvru3    = [];
```

```
41 ZAvrl   = [];
42 ZAvrl2  = [];
43 ZAvrl3  = [];
44
45 %%% Populate the upper (ru) and lower (rl) bound matrices by
       adding/
46 %%% subtracting half of the amplitude discretisation step to
       the amplitude
47 %%% values in D
48 for l = 1:tr-1;
49     for k = 2:ns-2;
50         if D(k,l)>D(k-1,l) && D(k,l)>D(k+1,l)
51             ru(k,l) = D(k,l) - (2175.5/2);
52             rl(k,l) = D(k,l) - (2175.5/2);
53             ru2(k,l) = D(k,l) + (2175.5/2);
54             ru3(k,l) = D(k,l) - (2175.5/2);
55             rl2(k,l) = D(k,l) + (2175.5/2);
56             rl3(k,l) = D(k,l) + (2175.5/2);
57         elseif D(k,l)<D(k-1,l) && D(k,l)<D(k+1,l)
58             ru(k,l) = D(k,l) + (2175.5/2);
59             rl(k,l) = D(k,l) + (2175.5/2);
60             ru2(k,l) = D(k,l) - (2175.5/2);
61             ru3(k,l) = D(k,l) + (2175.5/2);
62             rl2(k,l) = D(k,l) - (2175.5/2);
63             rl3(k,l) = D(k,l) - (2175.5/2);
64         elseif D(k,l)<D(k+1,l)
65             ru(k,l) = D(k,l) + (2175.5/2);
```

```
66              rl(k,l) = D(k,l) - (2175.5/2);
67              ru2(k,l) = D(k,l) + (2175.5/2);
68              ru3(k,l) = D(k,l) + (2175.5/2);
69              rl2(k,l) = D(k,l) - (2175.5/2);
70              rl3(k,l) = D(k,l) - (2175.5/2);
71          elseif D(k,l)>D(k+1,l)
72              ru(k,l) = D(k,l) - (2175.5/2);
73              rl(k,l) = D(k,l) + (2175.5/2);
74              ru2(k,l) = D(k,l) - (2175.5/2);
75              ru3(k,l) = D(k,l) + (2175.5/2);
76              rl2(k,l) = D(k,l) + (2175.5/2);
77              rl3(k,l) = D(k,l) - (2175.5/2);
78          else
79          end
80      end
81  end
82
83  %%% Interpolate sample points for raw data (D -> S), upper (
        ru -> Sru), and
84  %%% lower bounds (rl -> Srl) - Spline Method
85  h = waitbar(0,'Please wait...');
86  %for j=1:tr-1;
87  j=500;
88      waitbar(j/(tr-1),h);
89      % Actual Data
90      F0      = D(:,j);
91      S       = spline(X0,F0,Xint);
```

```
92      S_abs    = abs(spline(X0,F0,Xint));
93      A        = wividia(D(:,500),sr*1e-3,3,0);
94      F0Hz     = bandmax(A,sr*1e-3);
95      SF0Hz    = spline(X0,F0Hz,Xint);
96
97      % Upper Bound
98      F0ru     = ru(:,j);
99      Sru      = spline(X0,F0ru,Xint);
100     Sru_abs  = abs(spline(X0,F0ru,Xint));
101
102     % Upper Bound 2
103     F0ru2    = ru2(:,j);
104     Sru2     = spline(X0,F0ru2,Xint);
105     Sru2_abs = abs(spline(X0,F0ru2,Xint));
106
107     % Upper Bound 3
108     F0ru3    = ru3(:,j);
109     Sru3     = spline(X0,F0ru3,Xint);
110     Sru3_abs = abs(spline(X0,F0ru3,Xint));
111
112     % Lower Bound
113     F0rl     = rl(:,j);
114     Srl      = spline(X0,F0rl,Xint);
115     Srl_abs  = abs(spline(X0,F0rl,Xint));
116
117     % Lower Bound 2
118     F0rl2    = rl2(:,j);
```

```
119     Srl2      = spline(X0,F0rl2,Xint);
120     Srl2_abs  = abs(spline(X0,F0rl2,Xint));
121
122     % Lower Bound 3
123     F0rl3     = rl3(:,j);
124     Srl3      = spline(X0,F0rl3,Xint);
125     Srl3_abs  = abs(spline(X0,F0rl3,Xint));
126
127 %%% Extract points at the interpolated wiggle apex
128    for i = 1:nsi-2;
129        % Actual Data
130        if S_abs(i+1)>S_abs(i) && S_abs(i+1)>S_abs(i+2);
131            if S_abs(i+1)>0;
132                ZAv = [ZAv; (i+1)*sr*dti*-1 S(i+1) SF0Hz(i+1)
                        ];
133            else
134            end
135        else
136        end
137
138        % Upper Bound
139        if Sru_abs(i+1)>Sru_abs(i) && Sru_abs(i+1)>Sru_abs(i
               +2);
140            if Sru_abs(i+1)>0;
141                ZAvru = [ZAvru; (i+1)*sr*dti*-1 Sru(i+1)];
142            else
143            end
```

```
144         else
145         end
146
147         % Upper Bound 2
148         if Sru2_abs(i+1)>Sru2_abs(i) && Sru2_abs(i+1)>Sru2_abs
               (i+2);
149             if Sru2_abs(i+1)>0;
150                 ZAvru2 = [ZAvru2; (i+1)*sr*dti*-1 Sru2(i+1)];
151             else
152             end
153         else
154         end
155
156         % Upper Bound 3
157         if Sru3_abs(i+1)>Sru3_abs(i) && Sru3_abs(i+1)>Sru3_abs
               (i+2);
158             if Sru3_abs(i+1)>0;
159                 ZAvru3 = [ZAvru3; (i+1)*sr*dti*-1 Sru3(i+1)];
160             else
161             end
162         else
163         end
164
165         % Lower Bound
166         if Srl_abs(i+1)>Srl_abs(i) && Srl_abs(i+1)>Srl_abs(i
               +2);
167             if Srl_abs(i+1)>0;
```

```
168                 ZAvrl = [ZAvrl; (i+1)*sr*dti*-1 Srl(i+1)];
169             else
170             end
171         else
172         end
173
174         % Lower Bound 2
175         if Srl2_abs(i+1)>Srl2_abs(i) && Srl2_abs(i+1)>Srl2_abs
               (i+2);
176             if Srl2_abs(i+1)>0;
177                 ZAvrl2 = [ZAvrl2; (i+1)*sr*dti*-1 Srl2(i+1)];
178             else
179             end
180         else
181         end
182
183         % Lower Bound 3
184         if Srl3_abs(i+1)>Srl3_abs(i) && Srl3_abs(i+1)>Srl3_abs
               (i+2);
185             if Srl3_abs(i+1)>0;
186                 ZAvrl3 = [ZAvrl3; (i+1)*sr*dti*-1 Srl3(i+1)];
187             else
188             end
189         else
190         end
191     end
```

```
192     ZA    = [ZA;    ones(length(ZAv),1)*X(j)    ones(length(
            ZAv),1)*Y(j)    ZAv    ones(length(ZAv),1)*j];
193     ZAru  = [ZAru;  ones(length(ZAvru),1)*X(j)  ones(length(
            ZAvru),1)*Y(j)  ZAvru  ones(length(ZAvru),1)*j];
194     ZAru2 = [ZAru2; ones(length(ZAvru2),1)*X(j) ones(length(
            ZAvru2),1)*Y(j) ZAvru2 ones(length(ZAvru2),1)*j];
195     ZAru3 = [ZAru3; ones(length(ZAvru3),1)*X(j) ones(length(
            ZAvru3),1)*Y(j) ZAvru3 ones(length(ZAvru3),1)*j];
196     ZArl  = [ZArl;  ones(length(ZAvrl),1)*X(j)  ones(length(
            ZAvrl),1)*Y(j)  ZAvrl  ones(length(ZAvrl),1)*j];
197     ZArl2 = [ZArl2; ones(length(ZAvrl2),1)*X(j) ones(length(
            ZAvrl2),1)*Y(j) ZAvrl2 ones(length(ZAvrl2),1)*j];
198     ZArl3 = [ZArl3; ones(length(ZAvrl3),1)*X(j) ones(length(
            ZAvrl3),1)*Y(j) ZAvrl3 ones(length(ZAvrl3),1)*j];
199
200 %end
201
202 close (h)
203 np   = length(ZA);
204 npru = length(ZAru);
205 npru2 = length(ZAru2);
206 npru3 = length(ZAru3);
207 nprl = length(ZArl);
208 nprl2 = length(ZArl2);
209 nprl3 = length(ZArl3);
210 ZA   = [ZA (1:np)'];
211 ZAru = [ZAru (1:npru)'];
```

```
212 ZAru2 = [ZAru2 (1:npru2) '];
213 ZAru3 = [ZAru3 (1:npru3) '];
214 ZArl = [ZArl (1:nprl) '];
215 ZArl2= [ZArl2 (1:nprl2) '];
216 ZArl3= [ZArl3 (1:nprl3) '];
217
218 %%% Export as ASCII Tab-Delimited Text File
219 %dlmwrite('------------.txt',ZA,'precision',20,'delimiter','\
    t');
220 %dlmwrite('------------.txt',ZAru,'precision',20,'delimiter
    ','\t');
221 %dlmwrite('------------.txt',ZArl,'precision',20,'delimiter
    ','\t');
222
223 end
224
225 %%% PLOTS
226
227 %%% Plot interpolated wiggles
228 trace = j
229
230 plot(spline(X0,D(:,trace),Xint), 'Color', [0      0.4471
    0.7412], 'LineWidth', 1)  % Actual data - spline curve
231 hold on
232 plot(spline(X0,rl(:,trace),Xint), '--', 'Color', [0.6353
    0.0784      0.1843]) % Lower bound - spline curve
```

```
233 plot(spline(X0,rl2(:,trace),Xint), 'Color', [0.6353 0.0784
        0.1843]) % Lower bound - spline curve
234 plot(spline(X0,rl3(:,trace),Xint), ':', 'Color', [0.6353
    0.0784 0.1843]) % Lower bound - spline curve
235
236 plot(spline(X0,ru(:,trace),Xint), '--', 'Color', [0.1647
    0.3843 0.2745]) % Upper bound - spline curve
237 plot(spline(X0,ru2(:,trace),Xint), 'Color', [0.1647 0.3843
        0.2745]) % Upper bound - spline curve
238 plot(spline(X0,ru3(:,trace),Xint), ':', 'Color', [0.1647
    0.3843 0.2745]) % Upper bound - spline curve
239
240 %%% Plot points
241 scatter(X0*sr*100-(sr*100), D(:,trace), '+', '
    MarkerEdgeColor', [0.7294 0.7294 0.7294]) % Actual data -
    sample points
242
243 scatter(-ZA(:,3)*100,ZA(:,4), 'o', 'MarkerEdgeColor', [0
        0.4471 0.7412], 'MarkerFaceColor', [0.9608 0.9765
        0.9922]) % Actual data - wiggle apex
244 scatter(-ZArl(:,3)*100,ZArl(:,4), 'o', 'MarkerEdgeColor',
    [0.6353 0.0784 0.1843], 'MarkerFaceColor', [0.9843
        0.9686 0.9686]) % Lower bound - wiggle apex
245 scatter(-ZArl2(:,3)*100,ZArl2(:,4), 's', 'MarkerEdgeColor',
    [0.6353 0.0784 0.1843], 'MarkerFaceColor', [0.9843
        0.9686 0.9686]) % Lower bound - wiggle apex
```

```
246 scatter(-ZArl3(:,3)*100,ZArl3(:,4), 'd', 'MarkerEdgeColor',
    [0.6353 0.0784 0.1843], 'MarkerFaceColor', [0.9843
    0.9686 0.9686]) % Lower bound - wiggle apex
247 scatter(-ZAru(:,3)*100,ZAru(:,4), 'o', 'MarkerEdgeColor',
    [0.1647 0.3843 0.2745], 'MarkerFaceColor', [0.9451
    0.9686 0.9490]) % Upper bound - wiggle apex
248 scatter(-ZAru2(:,3)*100,ZAru2(:,4), 's', 'MarkerEdgeColor',
    [0.1647 0.3843 0.2745], 'MarkerFaceColor', [0.9451
    0.9686 0.9490]) % Upper bound - wiggle apex
249 scatter(-ZAru3(:,3)*100,ZAru3(:,4), 'd', 'MarkerEdgeColor',
    [0.1647 0.3843 0.2745], 'MarkerFaceColor', [0.9451
    0.9686 0.9490]) % Upper bound - wiggle apex
250
251 %%% Label points
252 labelpoints(-ZA(:,3)*100, ZA(:,4)+500, ZA(:,3), 'Color'
    , [0 0.4471 0.7412]) % Actual data - wiggle apex
253 labelpoints(-ZA(:,3)*100, ZA(:,4)+750, ZA(:,5)) % Actual
    data - Frequency
254
255 labelpoints(-ZArl(:,3)*100, ZArl(:,4)+500, ZArl(:,3), 'Color'
    , [0.6353 0.0784 0.1843]) % Lower bound - wiggle
    apex
256 labelpoints(-ZArl2(:,3)*100, ZArl2(:,4)+1000, ZArl2(:,3), '
    Color', [0.6353 0.0784 0.1843]) % Lower bound -
    wiggle apex
257 labelpoints(-ZArl3(:,3)*100, ZArl3(:,4)+1500, ZArl3(:,3), '
    Color', [0.6353 0.0784 0.1843]) % Lower bound -
```

```
    wiggle apex
258
259 labelpoints(-ZAru(:,3)*100, ZAru(:,4)+250, ZAru(:,3), 'Color'
    , [0.1647    0.3843    0.2745]) % Upper bound - wiggle
    apex
260 labelpoints(-ZAru2(:,3)*100, ZAru2(:,4)+750, ZAru2(:,3), '
    Color', [0.1647    0.3843    0.2745]) % Upper bound -
    wiggle apex
261 labelpoints(-ZAru3(:,3)*100, ZAru3(:,4)+1250, ZAru3(:,3), '
    Color', [0.1647    0.3843    0.2745]) % Upper bound -
    wiggle apex
```

References

Albertz, M. and Lingrey, S. (2012). "Critical state finite element models of contractional fault-related folding: Part 1. Structural analysis". In: *Tectonophysics* 576, pp. 133–149.

Anderson, E. M. (1905). "The dynamics of faulting". In: *Transactions of the Edinburgh Geological Society* 8.3, pp. 387–402.

Armandita, C., Morley, C. K., and Rowell, P. (2015). "Origin, structural geometry, and development of a giant coherent slide: The South Makassar Strait mass transport complex". In: *Geosphere* 11.2, pp. 376–403.

Barnett, J. A., Mortimer, J., Rippon, J. H., Walsh, J. J., and Watterson, J. (1987). "Displacement geometry in the volume containing a single normal fault". In: *AAPG Bulletin* 71.8, pp. 925–937.

Baudon, C. and Cartwright, J. A. (2008a). "3D seismic characterisation of an array of blind normal faults in the Levant Basin, Eastern Mediterranean". In: *Journal of Structural Geology* 30.6, pp. 746–760.

Baudon, C. and Cartwright, J. A. (2008b). "Early stage evolution of growth faults: 3D seismic insights from the Levant Basin, Eastern Mediterranean". In: *Journal of Structural Geology* 30.7, pp. 888–898.

Baudon, C. and Cartwright, J. A. (2008c). "The kinematics of reactivation of normal faults using high resolution throw mapping". In: *Journal of Structural Geology* 30.8, pp. 1072–1084.

Berggren, W. A., Hilgen, F. J., Langereis, C. G., Kent, D. V., Obradovich, J. D., Raffi, I., Raymo, M. E., and Shackleton, N. J. (1995). "Late Neogene chronology: new perspectives in high-resolution stratigraphy". In: *Geological Society of America Bulletin* 107.11, pp. 1272–1287.

Berndt, C., Bünz, S., and Mienert, J. (2003). "Polygonal fault systems on the mid-Norwegian margin: a long-term source for fluid flow". In: *Geological Society, London, Special Publications* 216.1, pp. 283–290.

Berndt, C., Jacobs, C., Evans, A., Gay, A., Elliott, G., Long, D., and Hitchen, K. (2012). "Kilometre-scale polygonal seabed depressions in the Hatton Basin, NE Atlantic Ocean: Constraints on the origin of polygonal faulting". In: *Marine Geology* 332, pp. 126–133.

BG Group (2012). "Geological end of well report: Gullris 6604/2-1". In: pp. 1–116.

Bishop, A. W., Green, G., Garga, V. K., Andresen, A., and Brown, J. (1971). "A new ring shear apparatus and its application to the measurement of residual strength". In: *Geotechnique* 21.4, pp. 273–328.

Bleil, U. (1989). "Magnetostratigraphy of Neogene and Quaternary sediment series from the Norwegian Sea: Ocean Drilling Program, Leg 104". In: *Eldholm, O., Thiede, J., Taylor, E., et al., Proc. ODP, Sci. Results.* Vol. 104, pp. 829–901.

Blystad, P. (1995). "Structural elements of the Norwegian continental shelf. Part 2: The Norwegian Sea region". In: *NPD Bull.* 8.

Boles, J., Landis, C., and Dale, P. (1985). "The Moeraki Boulders; anatomy of some septarian concretions". In: *Journal of Sedimentary Research* 55.3, pp. 398–406.

Bolton, A., Maltman, A., and Clennell, M. (1998). "The importance of overpressure timing and permeability evolution in fine-grained sediments undergoing shear". In: *Journal of Structural Geology* 20.8, pp. 1013–1022.

Bond, C. E. (2015). "Uncertainty in structural interpretation: Lessons to be learnt". In: *Journal of Structural Geology* 74, pp. 185–200.

Brekke, H., Dahlgren, S., Nyland, B., and Magnus, C. (1999). "The prospectivity of the Vøring and Møre basins on the Norwegian Sea continental margin". In: *Geological Society, London, Petroleum Geology Conference series*. Vol. 5. 1. Geological Society of London, pp. 261–274.

Brekke, H. et al. (2000). "The tectonic evolution of the Norwegian Sea continental margin, with emphasis on the Voring and More basins". In: *Special Publication-Geological Society of London* 167, pp. 327–378.

Brown, A. R. (2011). *Interpretation of three-dimensional seismic data*. Society of Exploration Geophysicists and American Association of Petroleum ...

Buckley, D. and Grant, A. (1985). "Faultlike features in abyssal plain sediments: possible dewatering structures". In: *Journal of Geophysical Research: Oceans* 90.C5, pp. 9173–9180.

Carruthers, D. T. (2012). "Interaction of polygonal fault systems with salt diapirs". PhD thesis. Cardiff University.

Carruthers, D. T., Cartwright, J. A., Jackson, M. P., and Schutjens, P. (2013). "Origin and timing of layer-bound radial faulting around North Sea salt stocks: New insights into the evolving stress state around rising diapirs". In: *Marine and Petroleum Geology* 48, pp. 130–148.

Cartwright, J. A. (1994a). "Episodic basin-wide fluid expulsion from geopressured shale sequences in the North Sea basin". In: *Geology* 22.5, pp. 447–450.

Cartwright, J. A. (1994b). "Episodic basin-wide hydrofracturing of overpressured Early Cenozoic mudrock sequences in the North Sea Basin". In: *Marine and Petroleum Geology* 11.5, pp. 587–607.

Cartwright, J. A. (2011). "Diagenetically induced shear failure of fine-grained sediments and the development of polygonal fault systems". In: *Marine and Petroleum Geology* 28.9, pp. 1593–1610.

Cartwright, J. A., Bouroullec, R., James, D., and Johnson, H. (1998). "Polycyclic motion history of some Gulf Coast growth faults from high-resolution displacement analysis". In: *Geology* 26.9, pp. 819–822.

Cartwright, J. A. and Dewhurst, D. N. (1998). "Layer-bound compaction faults in fine-grained sediments". In: *Geological Society of America Bulletin* 110.10, pp. 1242–1257.

Cartwright, J. A. and Huuse, M. (2005). "3D seismic technology: the geological 'Hubble'". In: *Basin Research* 17.1, pp. 1–20.

Cartwright, J. A., James, D., and Bolton, A. (2003). "The genesis of polygonal fault systems: a review". In: *Geological Society, London, Special Publications* 216.1, pp. 223–243.

Cartwright, J. A. and Lonergan, L. (1996). "Volumetric contraction during the compaction of mudrocks: a mechanism for the development of regional-scale polygonal fault systems". In: *Basin Research* 8.2, pp. 183–193.

Carver, R. E. (1968). "Differential compaction as a cause of regional contemporaneous faults". In: *AAPG Bulletin* 52.3, pp. 414–419.

Casey, B. B. A. (2014). "The consolidation and strength behavior of mechanically compressed fine-grained sediments". PhD thesis. Massachusetts Institute of Technology.

Chand, S., Rise, L., Knies, J., Haflidason, H., Hjelstuen, B., and Bøe, R. (2011). "Stratigraphic development of the south Vøring margin (Mid-Norway) since early Cenozoic time and its influence on subsurface fluid flow". In: *Marine and Petroleum Geology* 28.7, pp. 1350–1363.

Childs, C., Manzocchi, T., Walsh, J. J., Bonson, C. G., Nicol, A., and Schöpfer, M. P. (2009). "A geometric model of fault zone and fault rock thickness variations". In: *Journal of Structural Geology* 31.2, pp. 117–127.

Childs, C., Nicol, A., Walsh, J. J., and Watterson, J. (2003). "The growth and propagation of synsedimentary faults". In: *Journal of Structural geology* 25.4, pp. 633–648.

Childs, C., Walsh, J. J., Manzocchi, T., Strand, J., Nicol, A., Tomasso, M., Schöpfer, M. P., and Aplin, A. C. (2007). "Definition of a fault permeability predictor from outcrop studies of a faulted turbidite sequence, Taranaki, New Zealand". In: *Geological Society, London, Special Publications* 292.1, pp. 235–258.

Clausen, J., Gabrielsen, R., Reksnes, P., and Nysaether, E. (1999). "Development of intraformational (Oligocene–Miocene) faults in the northern North Sea: influence of remote stresses and doming of Fennoscandia". In: *Journal of Structural Geology* 21.10, pp. 1457–1475.

Cohen, K. and Gibbard, P. (2017). *Global chronostratigraphical correlation table for the last 2.7 million years v. 2016a. Cambridge: Subcommission on quaternary Stratigraphy, International Commission on Stratigraphy; 2016.*

Collettini, C. and Sibson, R. H. (2001). "Normal faults, normal friction?" In: *Geology* 29.10, pp. 927–930.

Cowie, P. A. and Scholz, C. H. (1992). "Displacement-length scaling relationship for faults: data synthesis and discussion". In: *Journal of Structural Geology* 14.10, pp. 1149–1156.

Cripps, J. and Taylor, R. (1981). "The engineering properties of mudrocks". In: *Quarterly Journal of Engineering Geology and Hydrogeology* 14.4, pp. 325–346.

Crook, A. J. L., Willson, S., Yu, J., and Owen, D. (2006). "Predictive modelling of structure evolution in sandbox experiments". In: *Journal of Structural Geology* 28.5, pp. 729–744.

Crook, A. J. L., Willson, S., Yu, J. G., and Owen, R. (2003). "Computational modelling of the localized deformation associated with borehole breakout in quasi-

brittle materials". In: *Journal of Petroleum Science and Engineering* 38.3-4, pp. 177–186.

Dalland, A., Worsley, D., and Ofstad, K. (1988). *A lithostratigraphic scheme for the mesozoic and cenozoic and succession offshore mid-and northern norway.* Oljedirektoratet.

Dalton, T. J. S., Paton, D. A., Needham, T., and Hodgson, N. (2015). "Temporal and spatial evolution of deepwater fold thrust belts: Implications for quantifying strain imbalance". In: *Interpretation* 3.4, SAA59–SAA70.

Davies, R. J. (2005). "Differential compaction and subsidence in sedimentary basins due to silica diagenesis: A case study". In: *Geological Society of America Bulletin* 117.9-10, pp. 1146–1155.

Davies, R. J. and Cartwright, J. A. (2002). "A fossilized Opal A to Opal C/T transformation on the northeast Atlantic margin: Support for a significantly elevated palaeogeothermal gradient during the Neogene?" In: *Basin Research* 14.4, pp. 467–486.

Davies, R. J. and Cartwright, J. A. (2007). "Kilometer-scale chemical reaction boundary patterns and deformation in sedimentary rocks". In: *Earth and Planetary Science Letters* 262.1-2, pp. 125–137.

Davies, R. J., Cartwright, J. A., and Rana, J. (1999). "Giant hummocks in deep-water marine sediments: Evidence for large-scale differential compaction and density inversion during early burial". In: *Geology* 27.10, pp. 907–910.

Davies, R. J. and Ireland, M. T. (2011). "Initiation and propagation of polygonal fault arrays by thermally triggered volume reduction reactions in siliceous sediment". In: *Marine Geology* 289.1-4, pp. 150–158.

Davies, R. J., Ireland, M., and Cartwright, J. A. (2009). "Differential compaction due to the irregular topology of a diagenetic reaction boundary: a new mechanism for the formation of polygonal faults". In: *Basin Research* 21.3, pp. 354–359.

Dewhurst, D. N., Cartwright, J. A., and Lonergan, L. (1999). "The development of polygonal fault systems by syneresis of colloidal sediments". In: *Marine and Petroleum Geology* 16.8, pp. 793–810.

Dewoolkar, M. M. and Huzjak, R. J. (2005). "Drained residual shear strength of some claystones from Front Range, Colorado". In: *Journal of Geotechnical and Geoenvironmental Engineering* 131.12, pp. 1543–1551.

Dutton, D. M. and Trudgill, B. D. (2009). "Four-dimensional analysis of the Sembo relay system, offshore Angola: Implications for fault growth in salt-detached settings". In: *AAPG bulletin* 93.6, pp. 763–794.

Eidvin, T., Bugge, T., and Smelror, M. (2007). "The Molo Formation, deposited by coastal progradation on the inner Mid-Norwegian continental shelf, coeval with the Kai Formation to the west and the Utsira Formation in the North Sea." In: *Norwegian Journal of Geology/Norsk Geologisk Forening* 87.

Eidvin, T., Riis, F., and Rasmussen, E. S. (2014). "Oligocene to Lower Pliocene deposits of the Norwegian continental shelf, Norwegian Sea, Svalbard, Denmark and their relation to the uplift of Fennoscandia: A synthesis". In: *Marine and Petroleum Geology* 56, pp. 184–221.

Finch, E., Hardy, S., and Gawthorpe, R. (2003). "Discrete element modelling of contractional fault-propagation folding above rigid basement fault blocks". In: *Journal of Structural Geology* 25.4, pp. 515–528.

Fossen, H. (2016). *Structural Geology*. Cambridge University Press.

Fry, C. R. (2021). "Seafloor analogues: Identifying conventionally sub-seismic structures in polygonal fault systems". PhD thesis. University of Southampton.

Gay, A., Lopez, M., Cochonat, P., and Sermondadez, G. (2004). "Polygonal faults-furrows system related to early stages of compaction-upper Miocene to recent sediments of the Lower Congo Basin". In: *Basin Research* 16.1, pp. 101–116.

Gay, A. and Berndt, C. (2007). "Cessation/reactivation of polygonal faulting and effects on fluid flow in the Vøring Basin, Norwegian Margin". In: *Journal of the Geological Society* 164.1, pp. 129–141.

Gay, A., Lopez, M., Berndt, C., and Seranne, M. (2007). "Geological controls on focused fluid flow associated with seafloor seeps in the Lower Congo Basin". In: *Marine Geology* 244.1-4, pp. 68–92.

Gay Jr, S. P. (1989). "Gravitational compaction, a neglected mechanism in structural and stratigraphic studies: new evidence from Mid-Continent, USA". In: *AAPG bulletin* 73.5, pp. 641–657.

Ghalayini, R., Homberg, C., Daniel, J., and Nader, F. (2017). "Growth of layer-bound normal faults under a regional anisotropic stress field". In: *Geological Society, London, Special Publications* 439.1, pp. 57–78.

Gillespie, P., Howard, C., Walsh, J. J., and Watterson, J. (1993). "Measurement and characterisation of spatial distributions of fractures". In: *Tectonophysics* 226.1-4, pp. 113–141.

Goulty, N. R. (2001a). "Mechanics of layer-bound polygonal faulting in fine-grained sediments". In: *Journal of the Geological Society* 159.3, pp. 239–246.

Goulty, N. R. (2001b). "Polygonal fault networks in fine-grained sediments–an alternative to the syneresis mechanism". In: *First Break* 19.2, pp. 69–73.

Goulty, N. R. (2008). "Geomechanics of polygonal fault systems: a review". In: *Petroleum Geoscience* 14.4, pp. 389–397.

Goulty, N. R. and Swarbrick, R. E. (2005). "Development of polygonal fault systems: a test of hypotheses". In: *Journal of the Geological Society* 162.4, pp. 587–590.

Gradmann, S., Beaumont, C., and Albertz, M. (2009). "Factors controlling the evolution of the Perdido Fold Belt, northwestern Gulf of Mexico, determined from numerical models". In: *Tectonics* 28.2.

Gray, G. G., Morgan, J. K., and Sanz, P. F. (2014). "Overview of continuum and particle dynamics methods for mechanical modeling of contractional geologic structures". In: *Journal of Structural Geology* 59, pp. 19–36.

Hansen, D. M. and Cartwright, J. A. (2006). "The three-dimensional geometry and growth of forced folds above saucer-shaped igneous sills". In: *Journal of Structural Geology* 28.8, pp. 1520–1535.

Hansen, D. M., Shimeld, J. W., Williamson, M. A., and Lykke-Andersen, H. (2004). "Development of a major polygonal fault system in Upper Cretaceous chalk and Cenozoic mudrocks of the Sable Subbasin, Canadian Atlantic margin". In: *Marine and Petroleum Geology* 21.9, pp. 1205–1219.

Hein, J. R., Scholl, D. W., Barron, J. A., Jones, M. G., and Miller, J. (1978). "Diagenesis of late Cenozoic diatomaceous deposits and formation of the bottom simulating reflector in the southern Bering Sea". In: *Sedimentology* 25.2, pp. 155–181.

Henriet, J., De Batist, M., Van Vaerenbergh, W., and Verschuren, M. (1988). "Seismic facies and clay tectonic features of the Ypresian clay in the southern North Sea". In: *Bulletin van de Belgische Vereniging voor Geologie* 97, pp. 457–472.

Henriet, J., De Batist, M., and Verschuren, M. (1991). "Early fracturing of Palaeogene clays, southernmost North Sea: relevance to mechanisms of primary hydrocarbon migration". In: *Generation, accumulation and production of Europe's hydrocarbons* 1, pp. 217–227.

Herrera, M., Lizcano, A., and Santamarina, J. (2007). "Colombian volcanic ash soils". In: *Characterization and engineering properties of natural soils*, pp. 2385–2409.

Higgs, W. and McClay, K. (1993). "Analogue sandbox modelling of Miocene extensional faulting in the Outer Moray Firth". In: *Geological Society, London, Special Publications* 71.1, pp. 141–162.

Ikari, M. J., Kopf, A. J., Hüpers, A., and Vogt, C. (2018). "Lithologic control of frictional strength variations in subduction zone sediment inputs". In: *Geosphere* 14.2, pp. 604–625.

Ireland, M. T., Davies, R. J., Goulty, N. R., and Carruthers, D. (2011). "Structure of a silica diagenetic transformation zone: the Gjallar Ridge, offshore Norway". In: *Sedimentology* 58.2, pp. 424–441.

Ireland, M. T., Goulty, N. R., and Davies, R. J. (2010). "Influence of pore water chemistry on silica diagenesis: evidence from the interaction of diagenetic reaction zones with polygonal fault systems". In: *Journal of the Geological Society* 167.2, pp. 273–279.

Jackson, C. A.-L. (2018). "Chapter Fourteen: Temporal Throw Rate Variability on Gravity-Driven Normal Faults; Constraints from the Gudrun Fault, South Viking Graben, Offshore Norway". In.

Jackson, C. A.-L., Carruthers, D. T., Mahlo, S. N., and Briggs, O. (2014). "Can polygonal faults help locate deep-water reservoirs?" In: *AAPG Bulletin* 98.9, pp. 1717–1738.

James, D., Goulty, N. R., and Swarbrick, R. E. (2006). "Discussion on development of polygonal fault systems: a test of hypotheses". In: *Journal of the Geological Society* 163.1, pp. 221–223.

Jones, M. (1994). "Mechanical principles of sediment deformation". In: *The geological deformation of sediments*. Springer, pp. 37–71.

King, J. J. and Cartwright, J. A. (2020). "Ultra-slow throw rates of polygonal fault systems". In: *Geology* 48.5, pp. 473–477.

Kopf, A., Clennell, B., and Flecker, R. (1998). "49. Relationship between the variation of undrained shear strength, organic carbon content, and the origin and frequency of enigmatic normal faults in fine-grained sediments from advanced piston cores

from the eastern Mediterranean". In: *Proceedings of the Ocean Drilling Program, Scientific Results*. Vol. 160. Ocean Drilling Program, pp. 645–661.

Laberg, J. S., Dahlgren, T., Vorren, T. O., Haflidason, H., and Bryn, P. (2001). "Seismic analyses of Cenozoic contourite drift development in the Northern Norwegian Sea". In: *Marine Geophysical Researches* 22.5, pp. 401–416.

Labute, G. and Gretener, P. (1969). "Differential compactions around a leduc reef - Wizard Lake Area, Alberta." In: *Bulletin of Canadian Petroleum Geology* 17.3, pp. 304–325.

LaGatta, D. P. (1970). *Residual strength of clay and clay-shales by rotation shear tests*. Tech. rep. Harvard University Soil Mechanics Lab.

Laubach, S. E., Schultz-Ela, D. D., and Tyler, R. (1999). "Differential compaction of interbedded sandstone and coal". In: *Geological Society, London, Special Publications* 169.1, pp. 51–60.

Laurent, D., Gay, A., Baudon, C., Berndt, C., Soliva, R., Planke, S., Mourgues, R., Lacaze, S., Pauget, F., Mangue, M., et al. (2012). "High-resolution architecture of a polygonal fault interval inferred from geomodel applied to 3D seismic data from the Gjallar Ridge, Vøring Basin, Offshore Norway". In: *Marine Geology* 332, pp. 134–151.

Lonergan, L. and Cartwright, J. A. (1999). "Polygonal faults and their influence on deep-water sandstone reservoir geometries, Alba Field, United Kingdom central North Sea". In: *AAPG bulletin* 83.3, pp. 410–432.

Lonergan, L., Cartwright, J. A., and Jolly, R. (1998a). "The geometry of polygonal fault systems in Tertiary mudrocks of the North Sea". In: *Journal of Structural Geology* 20.5, pp. 529–548.

Lonergan, L., Cartwright, J. A., Laver, R., and Staffurth, J. (1998b). "Polygonal faulting in the Tertiary of the central North Sea: implications for reservoir geology". In: *Geological Society, London, Special Publications* 127.1, pp. 191–207.

Løseth, H., Gading, M., and Wensaas, L. (2009). "Hydrocarbon leakage interpreted on seismic data". In: *Marine and Petroleum Geology* 26.7, pp. 1304–1319.

Mansfield, C. and Cartwright, J. A. (1996). "High resolution fault displacement mapping from three-dimensional seismic data: evidence for dip linkage during fault growth". In: *Journal of Structural Geology* 18.2-3, pp. 249–263.

McClay, K. (1990). "Extensional fault systems in sedimentary basins: a review of analogue model studies". In: *Marine and Petroleum Geology* 7.3, pp. 206–233.

McKenzie, D. (1978). "Some remarks on the development of sedimentary basins". In: *Earth and Planetary science letters* 40.1, pp. 25–32.

Miyazawa, D., Sanada, H., Kiyama, T., Sugita, Y., and Shijima, Y. (2011). "Poroelastic coefficients for siliceous rocks distributed in the Horonobe area, Hokkaido, Japan". In: *Journal of the Mining and Materials Processing Institute of Japan* 127.3, pp. 132–138.

Mondol, N. H., Bjørlykke, K., Jahren, J., and Høeg, K. (2007). "Experimental mechanical compaction of clay mineral aggregates—Changes in physical properties of mudstones during burial". In: *Marine and Petroleum Geology* 24.5, pp. 289–311.

Moore, D. E. and Lockner, D. A. (2007). "Friction of the smectite clay montmorillonite". In: *The seismogenic zone of subduction thrust faults*, pp. 317–345.

Morgan, D. A., Cartwright, J. A., and Imbert, P. (2015). "Perturbation of polygonal fault propagation by buried pockmarks and the implications for the development of polygonal fault systems". In: *Marine and Petroleum Geology* 65, pp. 157–171.

Morgan, D. A. (2016). "The growth and evolution of polygonal fault tiers". PhD thesis. Cardiff University.

Morley, C., Maczak, A., Rungprom, T., Ghosh, J., Cartwright, J. A., Bertoni, C., and Panpichityota, N. (2017). "New style of honeycomb structures revealed on 3D seismic data indicate widespread diagenesis offshore Great South Basin, New Zealand". In: *Marine and Petroleum Geology* 86, pp. 140–154.

Moscardelli, L., Dooley, T., Dunlap, D., Jackson, M., and Wood, L. (2012). "Deep-water polygonal fault systems as terrestrial analogs for large-scale Martian polygonal terrains". In: *GSA Today* 22.8, pp. 4–9.

Mouslopoulou, V., Walsh, J. J., and Nicol, A. (2009). "Fault displacement rates on a range of timescales". In: *Earth and Planetary Science Letters* 278.3-4, pp. 186–197.

Muir Wood, D. (1990). *Soil behaviour and critical state soil mechanics*. Cambridge University Press.

Muraoka, H. and Kamata, H. (1983). "Displacement distribution along minor fault traces". In: *Journal of Structural Geology* 5.5, pp. 483–495.

Namiki, Y., Tsutsumi, A., Ujiie, K., and Kameda, J. (2014). "Frictional properties of sediments entering the Costa Rica subduction zone offshore the Osa Peninsula: implications for fault slip in shallow subduction zones". In: *Earth, Planets and Space* 66.1, pp. 1–8.

Neagu, R. C., Cartwright, J. A., and Davies, R. J. (2010a). "Measurement of diagenetic compaction strain from quantitative analysis of fault plane dip". In: *Journal of Structural Geology* 32.5, pp. 641–655.

Neagu, R. C., Cartwright, J. A., Davies, R. J., and Jensen, L. (2010b). "Fossilisation of a silica diagenesis reaction front on the mid-Norwegian margin". In: *Marine and Petroleum Geology* 27.10, pp. 2141–2155.

Nelson, J. L. (1992). "Clay mineralogy and residual shear strength of the Santa Clara formation claystone, Saratoga Foothills, California". In: *Bulletin of the Association of Engineering Geologists* 29.3, pp. 299–310.

Nelson, M. A. (2006). "3D geometry and kinematics of non-colinear fault intersections". PhD thesis.

Nicol, A., Walsh, J. J., Manzocchi, T., and Morewood, N. (2005a). "Displacement rates and average earthquake recurrence intervals on normal faults". In: *Journal of Structural Geology* 27.3, pp. 541–551.

Nicol, A., Walsh, J. J., Watterson, J., Nell, P., and Bretan, P. (2003). "The geometry, growth and linkage of faults within a polygonal fault system from South Australia". In: *Geological Society, London, Special Publications* 216.1, pp. 245–261.

Nicol, A., Walsh, J. J., Watterson, J., and Underhill, J. (1997). "Displacement rates of normal faults". In: *Nature* 390.6656, p. 157.

Nicol, A., Watterson, J., Walsh, J. J., and Childs, C. (1996). "The shapes, major axis orientations and displacement patterns of fault surfaces". In: *Journal of Structural Geology* 18.2-3, pp. 235–248.

Nicol, A., Walsh, J. J., Berryman, K., and Nodder, S. (2005b). "Growth of a normal fault by the accumulation of slip over millions of years". In: *Journal of Structural Geology* 27.2, pp. 327–342.

Nikolinakou, M. A., Flemings, P. B., and Hudec, M. R. (2014a). "Modeling stress evolution around a rising salt diapir". In: *Marine and Petroleum Geology* 51, pp. 230–238.

Nikolinakou, M. A., Hudec, M. R., and Flemings, P. B. (2014b). "Comparison of evolutionary and static modeling of stresses around a salt diapir". In: *Marine and Petroleum Geology* 57, pp. 537–545.

O'Connor, M. and Gretener, P. (1974). "Quantitative modelling of the processes of differential compaction". In: *Bulletin of Canadian Petroleum Geology* 22.3, pp. 241–268.

Oehler, D. Z. and Allen, C. C. (2012). "Giant polygons and mounds in the lowlands of Mars: signatures of an ancient ocean?" In: *Astrobiology* 12.6, pp. 601–615.

Ottesen, D., Rise, L., Sletten Andersen, E., Bugge, T., and Eidvin, T. (2009). "Geological evolution of the Norwegian continental shelf between 61° N and 68° N during the last 3 million years." In: *Norwegian Journal of Geology/Norsk Geologisk Forening* 89.4.

Paganoni, M., King, J. J., Foschi, M., Mellor-Jones, K., and Cartwright, J. A. (2019). "A natural gas hydrate system on the Exmouth Plateau (NW shelf of Australia) sourced by thermogenic hydrocarbon leakage". In: *Marine and Petroleum Geology* 99, pp. 370–392.

Peacock, D., Knipe, R., and Sanderson, D. (2000). "Glossary of normal faults". In: *Journal of Structural Geology* 22.3, pp. 291–305.

Peacock, D. and Sanderson, D. (1991). "Displacements, segment linkage and relay ramps in normal fault zones". In: *Journal of Structural Geology* 13.6, pp. 721–733.

Perić, D. and Crook, A. J. L. (2004). "Computational strategies for predictive geology with reference to salt tectonics". In: *Computer Methods in Applied Mechanics and Engineering* 193.48-51, pp. 5195–5222.

Pochat, S., Castelltort, S., Choblet, G., and Van Den Driessche, J. (2009). "High-resolution record of tectonic and sedimentary processes in growth strata". In: *Marine and Petroleum Geology* 26.8, pp. 1350–1364.

Posamentier, H. W. and Kolla, V. (2003). "Seismic geomorphology and stratigraphy of depositional elements in deep-water settings". In: *Journal of sedimentary research* 73.3, pp. 367–388.

Powers, S. (1922). "Reflected buried hills and their importance in petroleum geology". In: *Economic Geology* 17.4, pp. 233–259.

Praeger, T. (2009). "Heterogeneities in fine-grained slope systems and their impact on seal quality". PhD thesis. Cardiff University.

Roberts, D. T., Crook, A. J. L., Cartwright, J. A., Profit, M. L., and Rance, J. M. (2014). "The evolution of polygonal fault systems: Insights from geomechanical forward modeling". In: *48th US Rock Mechanics/Geomechanics Symposium*. American Rock Mechanics Association.

Roberts, D. T. (2014). "A geomechanical analysis of the formation and evolution of Polygonal Fault Systems". PhD thesis. Cardiff University.

Rockfield (2010). *ELFEN Forward Modeling User Manual*.

Sanada, H., Niunoya, S., Matsui, H., and Fujii, Y. (2009). "Influences of sedimentary history on the mechanical properties and microscopic structure change of Horonobe siliceous rocks". In: *Journal of the Mining and Materials Processing Institute of Japan* 125.10_11, pp. 521–529.

Santamarina, J. C., Klein, K., and Fam, M. (2001). "Soils and Waves: Particulate Materials Behaviour, Characterisation and Process Monitoring". In: *Journal of Soils and Sediments* 1.2, p. 196.

Scheck-Wenderoth, M., Raum, T., Faleide, J., Mjelde, R., and Horsfield, B. (2007). "The transition from the continent to the ocean: a deeper view on the Norwegian margin". In: *Journal of the Geological Society* 164.4, pp. 855–868.

Schofield, A. and Wroth, P. (1968). *Critical state soil mechanics*. McGraw-hill.

Schöpfer, M. P., Abe, S., Childs, C., and Walsh, J. J. (2009). "The impact of porosity and crack density on the elasticity, strength and friction of cohesive granular materials: Insights from DEM modelling". In: *International Journal of Rock Mechanics and Mining Sciences* 46.2, pp. 250–261.

Schultz-Ela, D. D. (2003). "Origin of drag folds bordering salt diapirs". In: *AAPG bulletin* 87.5, pp. 757–780.

Shin, H., Santamarina, J. C., and Cartwright, J. A. (2008). "Contraction-driven shear failure in compacting uncemented sediments". In: *Geology* 36.12, pp. 931–934.

Shin, H., Santamarina, J. C., and Cartwright, J. A. (2010). "Displacement field in contraction-driven faults". In: *Journal of Geophysical Research: Solid Earth* 115.B7.

Shipboard Scientific Party (1987). "Site 644: Norwegian Sea". In: *Eldholm, O., Thiede, J., Taylor, E., et al., Proceedings of the Ocean Drilling Program, Initial Reports*, pp. 751–771.

Shipboard Scientific Party (1990). "Site 762: Exmouth Plateau". In: *Haq, B.U., von Rad, U., O'Connell, S., et al., Proceedings of Ocean Drilling Program, Initial Reports, 1990* 122, pp. 213–288.

Shipboard Scientific Party (1996). "Site 982: Rockall Trough". In: *Jansen, E., Raymo, M.E., Blum, P., et al., Proceedings of Ocean Drilling Program, Initial Reports, 1996* 122, pp. 91–138.

Shipboard Scientific Party (2001). "Site 1173: Nankai Trough". In: *Moore, G.F., Taira, A., and Klaus, A., et al., Proceedings of Ocean Drilling Program, Initial Reports, 2001* 190, pp. 1–147.

Shoulders, S. J., Cartwright, J. A., and Huuse, M. (2007). "Large-scale conical sandstone intrusions and polygonal fault systems in Tranche 6, Faroe-Shetland Basin". In: *Marine and Petroleum Geology* 24.3, pp. 173–188.

Singer, B. (2014). *A quaternary geomagnetic instability time scale. Quat. Geochronol. 21, 29e52.*

Skogseid, J., Pedersen, T., Eldholm, O., and Larsen, B. T. (1992). "Tectonism and magmatism during NE Atlantic continental break-up: the Vøring Margin". In: *Geological Society, London, Special Publications* 68.1, pp. 305–320.

Stuevold, L. M., Faerseth, R. B., Arnesen, L., Cartwright, J. A., and Möller, N. (2003). "Polygonal faults in the Ormen Lange field, Møre basin, offshore mid Norway". In: *Geological Society, London, Special Publications* 216.1, pp. 263–281.

Sun, Q., Wu, S., Lü, F., and Yuan, S. (2010). "Polygonal faults and their implications for hydrocarbon reservoirs in the southern Qiongdongnan Basin, South China Sea". In: *Journal of Asian Earth Sciences* 39.5, pp. 470–479.

Swarbrick, R. E., Osborne, M. J., and Yardley, G. S. (2001). "AAPG Memoir 76, Chapter 1: Comparision of Overpressure Magnitude Resulting from the Main Generating Mechanisms". In.

Taylor, S. K., Nicol, A., and Walsh, J. J. (2008). "Displacement loss on growth faults due to sediment compaction". In: *Journal of Structural Geology* 30.3, pp. 394–405.

Terzaghi, K. and Peck, R. B. (1948). *Soil mechanics in engineering practice*. Chapman and Hall, London.

Tewksbury, B. J., Hogan, J. P., Kattenhorn, S. A., Mehrtens, C. J., and Tarabees, E. A. (2014). "Polygonal faults in chalk: Insights from extensive exposures of the Khoman Formation, Western Desert, Egypt". In: *Geology* 42.6, pp. 479–482.

Thyne, G. D. and Boles, J. R. (1989). "Isotopic evidence for origin of the Moeraki septarian concretions, New Zealand". In: *Journal of Sedimentary Research* 59.2, pp. 272–279.

Townsend, C., Firth, I., Westerman, R., Kirkevollen, L., Hårde, M., and Andersen, T. (1998). "Small seismic-scale fault identification and mapping". In: *Geological Society, London, Special Publications* 147.1, pp. 1–25.

Turrini, L., Jackson, C. A.-L., and Thompson, P. (2017). "Seal rock deformation by polygonal faulting, offshore Uruguay". In: *Marine and Petroleum Geology* 86, pp. 892–907.

Urlaub, M., Geersen, J., Krastel, S., and Schwenk, T. (2018). "Diatom ooze: Crucial for the generation of submarine mega-slides?" In: *Geology* 46.4, pp. 331–334.

Vendeville, B., Cobbold, P., Davy, P., Choukroune, P., and Brun, J. (1987). "Physical models of extensional tectonics at various scales". In: *Geological Society, London, Special Publications* 28.1, pp. 95–107.

Verschuren, M. (1992). “An integrated 3D approach to clay tectonic deformation”. PhD thesis.

Verschuren, M. (2019). “Outcrop evidence of polygonal faulting in Ypresian marine clays (Southern North Sea Basin) leads to a new synthesis”. In: *Marine Geology* 413, pp. 85–98.

Walsh, J. J., Nicol, A., and Childs, C. (2002). “An alternative model for the growth of faults”. In: *Journal of Structural Geology* 24.11, pp. 1669–1675.

Walsh, J. J. and Watterson, J. (1987). “Distributions of cumulative displacement and seismic slip on a single normal fault surface”. In: *Journal of Structural Geology* 9.8, pp. 1039–1046.

Walsh, J. J. and Watterson, J. (1988). “Analysis of the relationship between displacements and dimensions of faults”. In: *Journal of Structural Geology* 10.3, pp. 239–247.

Walsh, J. J. and Watterson, J. (1989). “Displacement gradients on fault surfaces”. In: *Journal of Structural Geology* 11.3, pp. 307–316.

Wan, Y. and Kwong, J. (2002). “Shear strength of soils containing amorphous clay-size materials in a slow-moving landslide”. In: *Engineering Geology* 65.4, pp. 293–303.

Watterson, J., Walsh, J. J., Nicol, A., Nell, P., and Bretan, P. (2000). “Geometry and origin of a polygonal fault system”. In: *Journal of the Geological Society* 157.1, pp. 151–162.

Watterson, J. (1986). “Fault dimensions, displacements and growth”. In: *Pure and Applied Geophysics* 124.1-2, pp. 365–373.

Wibberley, C. A., Petit, J.-P., and Rives, T. (1999). “Mechanics of high displacement gradient faulting prior to lithification”. In: *Journal of Structural Geology* 21.3, pp. 251–257.

Widess, M. (1973). “How thin is a thin bed?” In: *Geophysics* 38.6, pp. 1176–1180.

Wood, L. C. (1974). "Seismic data compression methods". In: *Geophysics* 39.4, pp. 499–525.

Wrona, T., Magee, C., Jackson, C. A.-L., Huuse, M., and Taylor, K. G. (2017). "Kinematics of polygonal fault systems: observations from the northern North Sea". In: *Frontiers in Earth Science* 5, p. 101.

Yilmaz, Ö. (2001). *Seismic data analysis: Processing, inversion, and interpretation of seismic data*. Society of exploration geophysicists.

Yin, H., Zhang, J., Meng, L., Liu, Y., and Xu, S. (2009). "Discrete element modeling of the faulting in the sedimentary cover above an active salt diapir". In: *Journal of Structural Geology* 31.9, pp. 989–995.